Universitat d'Alacant
Universidad de Alicante

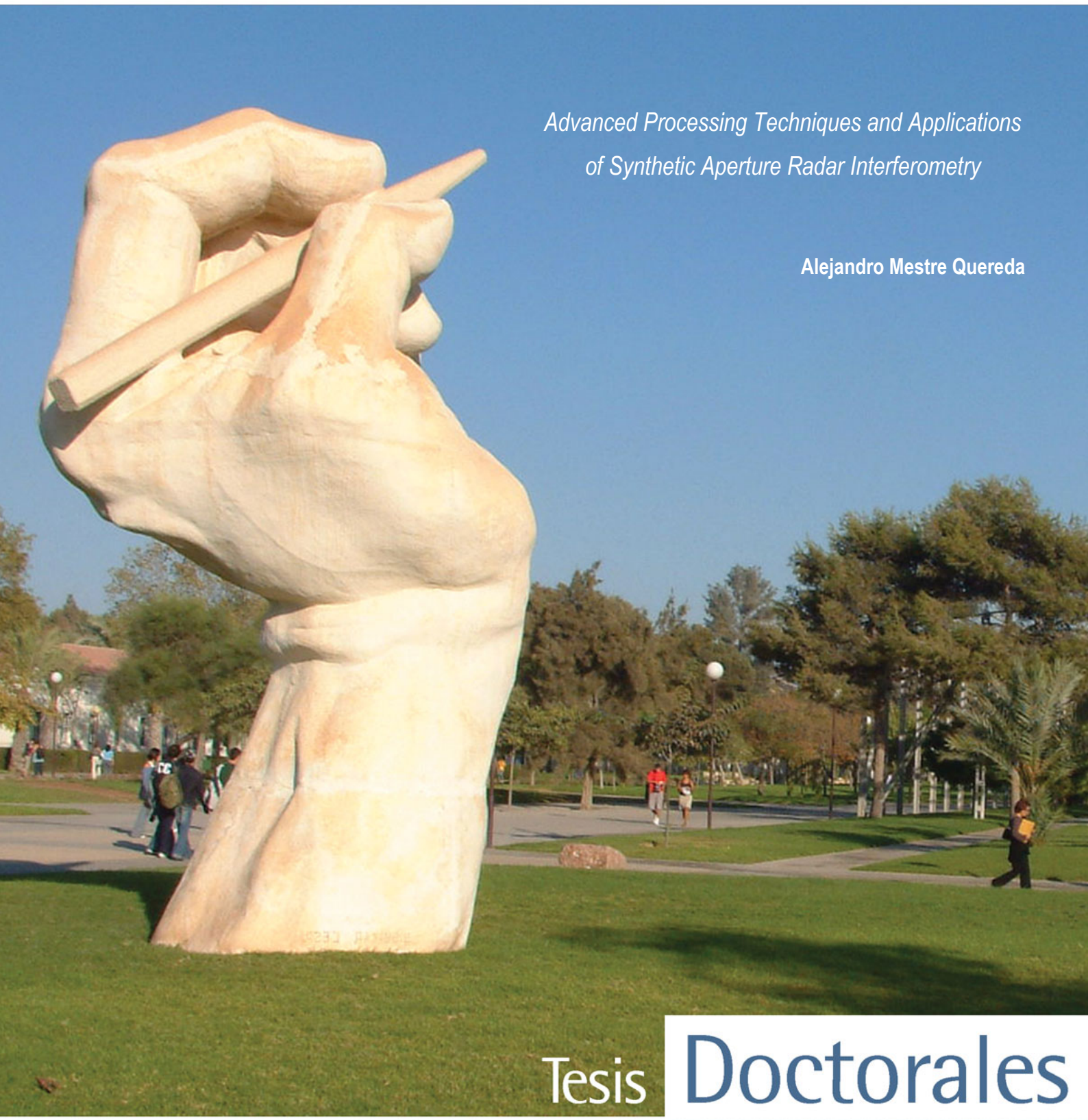

Advanced Processing Techniques and Applications of Synthetic Aperture Radar Interferometry

Alejandro Mestre Quereda

Tesis Doctorales

www.eltallerdigital.com

UNIVERSIDAD de ALICANTE

Universitat d'Alacant
Universidad de Alicante

University Institute for Computer Research

Advanced Processing Techniques and Applications of Synthetic Aperture Radar Interferometry

Alejandro Mestre Quereda

Thesis Advisor
Juan Manuel López Sánchez

A thesis presented to the University of Alicante
in partial fulfillment of the requirements
for the degree of
Doctor of Philosophy
in the subject of
Signal Theory and Communications

PhD Program in Computer Science

Alicante, Spain
September 2019

Work supported by the Spanish Ministry of Economy, Industry and Competitiveness, Research State Agency (AEI) and European Regional Development Funds (ERDF) under project TEC 2017-85244-C2-1-P, by the European Space Agency under project ESA/AO/1-8306/15/I-NB 'SEOM – S14SCI Land', and by HISDESAT Servicios Estratégicos S.A under project Hisdesat1-18I

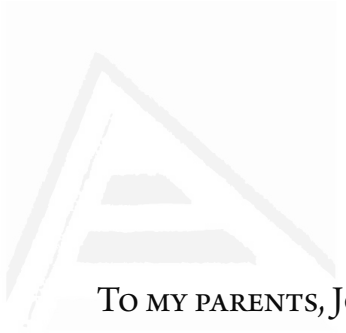

To my parents, José Luis and Luisa María

I would like to express my acknowledgment to all institutions and organizations that provided all the images and other types of data that made this work possible.

- Special thanks to DARES Technology for processing the large stack of Sentinel-1 images and the EURAC Research Sentinel Alpine Observatory and the Institute for Earth Observation for providing the infrastructure and the access to the data.
- All RADARSAT-2 images were provided by MDA and CSA in the framework of project SOAR 5087. *RADARSAT-2 Data and Products MacDonald, Dettwiler and Associates Ltd. (2008) – All Rights Reserved. RADARSAT is an official trademark of the Canadian Space Agency (CSA).*
- Spotlight TerraSAR-X image of Alicante has been provided by the Central Aerospace Center (DLR) in the framework of project GEO0583 of the TerraSAR-X scientific programme.
- PAZ image of the Mojave Desert has been provided by HISDESAT Servicios Estratégicos in the framework of project HISDESAT1-18I.
- The UAVSAR differential interferogram of Hawaii has been provided by NASA-Jet Propulsion Laboratory.

This work was supported by the Spanish Ministry of Economy, Industry and Competitiveness, Research State Agency (AEI) and European Regional Development Funds (ERDF) under project TEC 2017-85244-C2-1-P, by the European Space Agency under project ESA/AO/1-8306/15/I-NB 'SEOM – S14SCI Land', and by HISDESAT Servicios Estratégicos S.A under project HISDESAT1-18I.

Acknowledgments

This thesis is the result of three years of research carried out as a member of the Signals, Systems and Telecommunication Group (SST) of the University of Alicante. These last few lines put an end to the writing of this work. With them, I would like to acknowledge to everyone who directly or indirectly helped my throughout my PhD

First and foremost, I would like to express my deepest appreciation to my supervisor, Juan M. López Sánchez, for providing me the opportunity to carry out this work. His guidance, dedication and continuous support turned the course of this thesis into a challenging, yet exciting, venture. Undoubtedly, his advice on both my research as well as on my career have been priceless. I am grateful to consider him a friend, more than an academic supervisor. It is a real pleasure working with you.

I would like to thank the members and colleagues of the SST group (David, Jesús and Miguel), and also Basilio, for their encouragement, for the nice and fun moments we shared during these years and for making my time at the university truly enjoyable.

Thanks also go to all my colleagues at the SST laboratory, for providing a pleasant and stimulating work environment.

Beyond the world of SAR, I would like to acknowledge many other people who also helped me during these years. Thanks, once again, to my beloved family and especially to my mother Luisa María and my sister Laura, for always being there. Your unconditional support and understanding are priceless. Special thanks to my father José Luis, to whose memory I dedicate my PhD Thesis. He would have been really proud to see me growing as a scientist.

Huge thanks to all my lifelong friends for the uncountable funny moments we have shared and the laughs we have had throughout the years.

Thanks, finally, to my training partners and the rest of our athletics team members, for the amazing moments during competitions and the long and tough days of training.

Alejandro Mestre Quereda.
Alicante, July 2019.

Contents

List of Figures

List of Tables

Técnicas de Procesado y Aplicaciones Avanzadas de la Interferometría con Radar de Apertura Sintética

Resumen

Introducción, Contexto y Motivación

La teledetección hace referencia a la adquisición y análisis de información de objetos o fenómenos a distancia sin que exista un contacto material directo con ellos. Esto requiere del diseño de instrumentos capaces de recoger y procesar señales, tales como ondas electromagnéticas o acústicas, que interaccionan con la materia y proporcionan datos relacionados con las propiedades físicas del objeto sobre el que inciden. Actualmente, la teledetección se asocia con el estudio de las dinámicas de nuestro planeta Tierra y de los complejos procesos asociados a las mismas, llevado a cabo mediante el procesado de datos adquiridos por sistemas aéreos o espaciales en forma de imágenes. Al estudiar la Tierra mediante dichos sistemas, se suele hablar de Observación de la Tierra, e incluye una enorme variedad de técnicas y herramientas cuyo objetivo consiste en mejorar el conocimiento que tenemos de nuestro planeta a escala global.

Los avances en teledetección, especialmente desde mediados de la década del año 2000, han demostrado el enorme potencial que esta tecnología ofrece para monitorizar la superficie de la Tierra. En este sentido, se ha desarrollado una gran cantidad de aplicaciones para múltiples áreas, tanto de ámbito civil como militar e, indudablemente, se seguirán desarrollando nuevas aplicaciones en el futuro. Tanto es así que hoy en día la teledetección juega un papel crucial en diversas áreas científicas y de la ingeniería. Entre otras aplicaciones, la teledetección permite la generación de Modelos Digitales de Elevación (MDE), muy usados en topografía y cartografía. Es ampliamente empleada en ciencias geofísicas para el análisis de sucesos geológicos (erupciones volcánicas, terremotos, etc.), así como para la gestión del riesgo de desastres. También, se emplean técnicas de teledetección en meteorología para la estimación del clima, su evolución y su evidente impacto sobre la biodiversidad. Otro ejemplo de aplicación de métodos de teledetección estaría relacionado con la monitorización de cambios terrestres y medioambientales provocados por el avance de la civilización moderna, incluyendo el mapeado 2-D, 3-D o 4-D (espacio y tiempo) de la superficie del terreno, o la detección de cambios (para controlar la deforestación o la desertificación) y un largo etcétera.

Una forma de clasificar los sistemas de teledetección es en función de su fuente de iluminación, de modo que diferenciamos sistemas activos y pasivos. Un sistema activo consta de su propia fuente de iluminación, de modo que emite radiación electromagnética hacia el medio y mide la señal que le es devuelta (reflejada). Por el contrario, un sistema pasivo detecta únicamente aquellas señales reflejadas de manera natural que provienen de una fuente de iluminación externa al sensor, como la radiación solar. Una segunda manera de clasificar estos sistemas es en función de la banda del

espectro electromagnético empleada, distinguiéndose sistemas de microondas y sistemas ópticos. Esta tesis se centra en los sistemas de Radar de Apertura Sintética (abreviado SAR), que son sistemas activos que operan en la banda de microondas del espectro electromagnético. Los sistemas SAR constituyen uno de los sistemas más ampliamente usados en teledetección, debido a su amplia cobertura y a su capacidad de operar con independencia de la situación climática. Los SAR se montan sobre plataformas móviles, que pueden ser aéreas (un avión o un helicóptero) o espaciales (un satélite), siendo esta última la configuración que mayor impacto e interés ha tenido en este ámbito dada la gran cobertura espacial que proporciona. La característica principal de estos sistemas radar es que aprovechan el movimiento de la plataforma en los que están situados para sintetizar una antena mucho mayor a la realmente empleada. Esto se conoce como principio de apertura sintética, y permite un aumento drástico de la resolución espacial de las imágenes generadas.

Desde el lanzamiento del primer SAR orbital, SEASAT, en 1978, el número de misiones operacionales (lanzamientos) llevadas a cabo por diferentes estados y organizaciones intergubernamentales ha ido en aumento, especialmente desde principios de los años 90. De hecho, el número de misiones no sólo ha aumentado, sino que ha ido aumentado cada vez más rápido. Esto demuestra el auge que han experimentado los sistemas SAR así como el interés común en desarrollar y mejorar el enorme potencial que estos sistemas ofrecen en el ámbito de observación de la Tierra. En este sentido, las mejoras en la vida útil de nuevos sistemas, la resolución de las imágenes, la cobertura espacial, el tiempo de revisita o la adquisición de imágenes en múltiples polarizaciones, asentaron las bases para el desarrollo de técnicas avanzadas tales como la Interferometría o la Polarimetría SAR, sobre las que trata el presente trabajo. Cabe destacar que el desarrollo de nuevas técnicas y aplicaciones se ha visto favorecido por un mejor acceso a los datos. En concreto, la política de acceso libre del programa Comisión Europea, representa un cambio de paradigma en este sector, ya que permite obtener libremente y desde cualquier parte del mundo, imágenes SAR y datos de otros sensores que pueden analizarse y procesarse para cualquier fin.

La Interferometria SAR (InSAR) se desarrolló con el objetivo de extraer la topografía de una determinada escena. Inicialmente descrita en 1974, esta técnica empezó a cobrar interés a finales de los años 80, consolidándose definitivamente con el lanzamiento del primer satélite europeo ERS-1 en 1991, ya que una mayor cantidad de datos radar comenzó a estar disponible para usos científicos. La interferometría se basa en combinar, al menos, dos imágenes SAR adquiridas desde dos posiciones ligeramente distintas. Esta diferencia de posición es la que proporciona sensibilidad a las alturas y permite extraer la topografía. Así, se han podido generar modelos digitales de elevación a escala global, tales como el SRTM (Shuttle Radar Topographic Mission) de la NASA o el DEM de TanDEM-X (del Centro Espacial Alemán, DLR).

Mientras que la interferometría convencional permite obtener la topografía del terreno, la denominada Interferometría Diferencial (DInSAR) va un paso más allá y se centra en el análisis de deformaciones de la superficie terrestre sucedidas durante la adquisición de múltiples imágenes. En otras palabras, si la topografía es conocida, la interferometría diferencial permite monitorizar cam-

bios o deformaciones relativas entre imágenes SAR. Esta extensión diferencial de la interferometría es hoy en día una técnica tremendamente potente y ampliamente empleada en múltiples áreas, especialmente en el ámbito de la ingeniería civil, geológica, etc. Por ejemplo, permite estimar subsidencias (hundimientos) o elevaciones del terreno así como deslizamientos de tierra. Permite también analizar fuertes deformaciones de la corteza terrestre causadas por la actividad tectónica. El enorme potencial de la interferometría diferencial es su capacidad para obtener medidas de deformación muy precisas (del orden de 1cm) en grandes extensiones del terreno o áreas directamente no accesibles, lo que supone una evidente ventaja frente a métodos de medida convencionales (*in-situ*). Conviene mencionar que en los últimos años se han desarrollado múltiples técnicas ligadas a la interferometríal diferencial. Entre ellas, destaca la denominada PSI (*Permanent Scatterer Interferometry*), que es una rama de la interferometría diferencial centrada el procesar únicamente ciertos píxeles de alta calidad denominados dispersores persistentes (*permanent scatterers*) . Procesando series de imágenes SAR, los algoritmos y métodos de PSI proporcionan medidas muy robustas y precisas de la deformación o movimiento del terreno sobre dichos píxeles estables en áreas extensas.

Los sistemas SAR convencionales se diseñaron para generar imágenes de reflectividad de una escena empleando una única polarización de las señales electromagnéticas transmitidas y recibidas. El estudio de cómo la polarización de dichas señales interacciona con la materia se denomina Polarimetría. En el ámbito concreto del SAR, se conoce como Polarimetría SAR (o PolSAR) al estudio, análisis y explotación del estado de polarización de señales para aplicaciones radar. Inicialmente introducida a principios de los años 50, la polarimetría radar comenzó a cobrar interés sobre todo a partir de los años 70, en los que se demostró el potencial de la polarimetría para caracterizar blancos de radar. Como resultado de estas investigaciones, el interés en la polarimetría aumentó considerablemente. Tanto es así que hoy en día, la polarimetría radar constituye una de las líneas de investigación más importantes relacionadas con la teledetección mediante SAR. Entre sus múltiples aplicaciones, destacan la monitorización de bosques, la estimación de la altura de la vegetación, análisis de la biomasa (cantidad de masa vegetal), etc. Además, el aumento del número de satélites con capacidad polarimétrica, tales como RADARSAT-2, TerraSAR-X, Sentinel-1 o PAZ, lanzados en los últimos años, justifica el interés en desarrollar nuevas técnicas y aplicaciones basadas en polarimetría.

Mientras que la interferometría permite estimar alturas o deformaciones, la polarimetría permite caracterizar blancos del radar extrayendo propiedades físicas adicionales. Ambas técnicas son, de hecho, complementarias. Desde finales de los años 90, surgió la idea de combinar la información proporcionada por cada una de las dos técnicas. En este sentido, la Interferometría SAR Polarimétrica (PolInSAR), cuyas bases fueron asentadas en 1998, constituye una extensión de la interferometría escalar convencional y trata de solventar algunas de sus limitaciones debidas al empleo de una polarización fija, explotando la diversidad de canales polarimétricos que proporcionan sensibilidad a la geometría y forma de los blancos del radar. Además, estudios recientes han demostrado el potencial de juntar ambas técnicas en aplicaciones diferenciales. Así, la incorporación de datos en polarización dual (dos polarizaciones) o en polarización completa (cuatro polarizaciones), proporcionados por

nuevos sensores radar, ha demostrado ser de gran utilidad para la monitorización de deformaciones mediante interferometría diferencial, especialmente cuando se dispone de series temporales de imágenes.

Además de los avances tanto en interferometría como en polarimetría, el mapeado de la superficie terrestre empleando imágenes SAR ha experimentado un gran progreso en los últimos años. En este sentido, la clasificación de la cobertura terrestre con imágenes radar pertenece a la disciplina del reconocimiento de patrones, que es la ciencia que trata de clasificar objetos en múltiples categorías o clases atendiendo a sus propiedades. Su objetivo es extraer características de objetos y, por tanto, proporcionar información específica de un determinado sistema o conjunto de datos. Dicha clasificación suele llevarse a cabo con algoritmos de Aprendizaje Automático (*Machine Learning*), propios del ámbito de la Inteligencia Artificial. De forma general, el aprendizaje automático fue concebido desde la hipótesis de que los ordenadores pueden "aprender" directamente de los datos sin necesidad de haber sido específicamente programados para una determinada tarea. Buscando patrones en cantidades enormes de datos, los algoritmos de aprendizaje pueden readaptarse y predecir la evolución de un determinado sistema o los valores asociados a nuevas observaciones. Las aplicaciones del aprendizaje automático son hoy en día innumerables. Visión artificial, ingeniería del software, ayudas al diagnóstico médico, economía o lingüística son solamente algunos ejemplos. En el ámbito concreto del SAR o la teledetección en general, los algoritmos de aprendizaje automático permiten clasificar las observaciones proporcionadas por los sensores, y permiten generar mapas extensos de la cobertura terrestre, su uso, así como de la vegetación. Cabe destacar que para que nuestro ecosistema y medioambiente sean debidamente gestionados, es necesario un conocimiento apropiado sobre la distribución de áreas naturales, de recursos hídricos o del estado del suelo. Esto queda claramente representado por el programa CORINE Land-Cover (Coordination of Information on the Environment Land-Cover) creado por el Consejo Europeo en 1985 bajo propuesta de la Comisión Europea, cuyo objeto es generar un inventario digital sobre la cobertura terrestre y su uso en todos los países de la Unión Europea.

Objetivos

El objetivo principal de esta tesis consiste en proponer y evaluar una serie de mejoras relacionadas con la interferometría SAR, mediante el desarrollo de nuevos algoritmos y métodos relacionados con diferentes etapas de procesado. Por otro lado, se pretende demostrar también el potencial que la interferometría ofrece en el ámbito de la clasificación de tipos de cultivos. A continuación, se resume brevemente cada una de las contribuciones realizadas.

En primer lugar, esta tesis trata de solventar diferentes limitaciones de la interferometría ligadas a los efectos de la decorrelación o ruido presentes en los datos. Como se ha comentado previamente, la interferometría se basa en combinar dos imágenes de una misma zona, lo que da lugar a una nueva imagen denominada interferograma. Mientras que la amplitud del interferograma no contiene información útil (más allá de la que ya contienen las imágenes por separado), la fase del interferograma es el producto clave de esta técnica ya que contiene la información de distancia entre el satélite y el terreno. La calidad de dicha fase constituye el elemento central a partir del cual se pueden generar todos los productos de interés para aplicaciones basadas en interferometría o su extensión diferencial. Cabe destacar que la minimización del ruido es obligatoria prácticamente en cualquier ámbito o aplicación que involucre un procesado digital de señales, tales como imágenes médicas, señales de audio, etc. La reducción del ruido se lleva a cabo mediante el diseño de algoritmos de filtrado que tratan de mejorar la calidad de la parte útil de la señal, a la vez que se minimizan los efectos de algún tipo específico de ruido. En el ámbito concreto de la interferometría SAR, puede demostrarse que existe una variedad de factores de decorrelación que degradan la calidad de los datos. Uno de ellos es debido a la diferencia en la geometría de adquisición entre las dos imágenes empleadas para generar un interferograma. Esta geometría diferente induce un desplazamiento entre los espectros de las dos imágenes, de manera que únicamente la parte común contiene información útil, pudiéndose considerar el resto como ruido. Otra importante fuente de decorrelación es debida a cambios significativos entre las imágenes. Es decir, si la escena ha cambiado entre las dos imágenes (por ejemplo, debido a cambios en la vegetación) aparecerán fases extremadamente ruidosas dado que la respuesta de algunos elementos dentro de la imagen es diferente. Esta decorrelación se denomina decorrelación temporal.

En base a estas limitaciones, se han desarrollado nuevos métodos de reducción de los efectos del ruido con el objetivo de mejorar la calidad de la fase. A continuación, se describen brevemente.

- Un nuevo filtro que trata de limitar la decorrelación geométrica en la dimensión rango. El filtrado en rango es una etapa bien conocida dentro del procesado interferométrico que trata de limitar la anteriormente introducida decorrelación geométrica entre dos imágenes empleadas para generar un interferograma. Se ha desarrollado un algoritmo mejorado que emplea información topográfica para adaptar automáticamente el filtrado a cualquier tipo de superficie, de modo que se optimizan los resultados con respecto a métodos convencionales, en los que no se consigue filtrar adecuadamente en zonas con topografía. Nótese que esta etapa de filtrado

en rango suele considerarse una etapa de pre-procesado, ya que modifica la respuesta espectral de cada imagen por separado y se lleva a cabo antes de la generación de interferogramas.

- Un filtro para la fase interferométrica final. Cuando se genera un interferograma, puede que la calidad de su fase no sea lo suficientemente buena para su procesamiento posterior debido a los efectos de decorrelación temporal anteriormente explicados. En este sentido, prácticamente cualquier interferograma contiene áreas extremadamente ruidosas que pueden afectar a la calidad de los resultados finales, haciéndose necesaria la reducción del ruido en dichas zonas. Este filtro, aunque inicialmente diseñado para aplicaciones geofísicas (es decir, para interferogramas diferenciales ligados a sucesos geológicos) puede aplicarse sobre cualquier interferograma gracias a su adaptación tanto al nivel de ruido como a características de la imagen. El objetivo final de este filtro es reducir el nivel de ruido en su totalidad, a la vez que se mantienen detalles de la fase que contienen información útil.

En segundo lugar, se han evaluado diferentes métodos de optimización polarimétrica en pares interferométricos de imágenes. La interferometría diferencial SAR polarimétrica (PolDInSAR) trata de incluir la polarimetría en aplicaciones diferenciales de la interferometría. Hasta la fecha, esta técnica únicamente ha sido evaluada con series temporales, es decir, cuando se dispone de un número elevado de imágenes que se combinan en un número elevado de interferogramas. Sin embargo, no se ha probado con interferogramas aislados, que es el caso típico de las aplicaciones geofísicas ligadas a eventos como terremotos o erupciones volcánicas. Por consiguiente, el segundo objetivo de la presente tesis consiste en comprobar si se puede mejorar la calidad de la fase interferométrica en pares interferométricos mediante la aplicación de algoritmos de optimización basados en polarimetría.

Por último, el tercer objetivo de la tesis se centra en nuevas aplicaciones finales de la interferometría SAR y, concretamente, en la explotación de datos InSAR para la clasificación de tipos de cultivos (generación de mapas temáticos de tipos de cultivos). De forma tradicional, los algoritmos de clasificación emplean datos obtenidos de sensores ópticos o multi-espectrales, dada su mayor sensibilidad a las propiedades de los cultivos (como su humedad, la cantidad de clorofila en sus hojas, etc.). Sin embargo, debido a la banda de trabajo de estos sensores, el número de imágenes disponibles puede ser limitado en algunas ocasiones (por ejemplo, debido a la presencia de nubes o niebla en algunas adquisiciones.). Por consiguiente, el empleo de imágenes SAR, adquiridas independientemente de las condiciones climáticas, supone una evidente ventaja para este tipo de aplicación. Cabe destacar que los algoritmos de clasificación basados en imágenes radar suelen emplear como entrada la intensidad de las propias imágenes. Es decir, emplean datos radiométricos obtenidos a partir de la reflectividad de las imágenes. Sin embargo, esta tesis trata de demostrar que los datos interferométricos y, concretamente, series multi-temporales de coherencia, pueden emplearse de forma alternativa o complementaria para esta aplicación.

Resultados

Todas las técnicas de procesado desarrolladas durante la tesis muestran resultados satisfactorios. En todos los casos, se han demostrado las limitaciones y/o desventajas que presentan los métodos convencionales en cada ámbito específico, justificándose las ventajas que ofrecen los métodos propuestos. A continuación, se presenta un resumen global de los resultados obtenidos así como una discusión sobre los mismos.

En primer lugar, se ha demostrado que los métodos tradicionales de filtrado en rango no consiguen reducir de forma óptima la decorrelación geométrica en aquellas zonas con una topografía variable. El método conocido como adaptativo se basa en estimar el desplazamiento espectral entre imágenes mediante la generación de un interferograma temporal. El máximo valor del espectro se corresponde directamente con dicho desplazamiento. Si bien tiene la ventaja de no requerir información externa o auxiliar, presenta evidentes limitaciones. Por un lado, puede comprobarse que la frecuencia de las franjas asociadas a la topografía coincide con la componente dominante del espectro del interferograma, lo que acarrea incertidumbre en la estimación del desplazamiento espectral. Por otro lado, este método es muy dependiente de la calidad original de los datos, de manera que con interferogramas muy ruidosos el algoritmo adaptativo es totalmente ineficaz.

Otro filtro convencional emplea información orbital para calcular el desplazamiento espectral entre imágenes. Es decir, se emplea directamente información de la geometría de adquisición de ambas imágenes. A pesar de estar menos limitado ya que el desplazamiento se calcula de forma externa, el filtrado no es óptimo si no se emplea información topográfica, especialmente en aquellas áreas en las que la superficie del terreno varía rápidamente.

El desarrollo de filtros que incluyan información sobre las pendientes locales del terreno es absolutamente necesario. En este sentido, los resultados obtenidos muestran que el método desarrollado consigue adaptarse correctamente a cualquier tipo de superficie, mejorando los resultados de todos y cada uno de los métodos ya conocidos. Se ha demostrado que se consigue eliminar en mayor medida la decorrelación geométrica mediante la explotación completa de la información proporcionada por un DEM externo. Asimismo, el algoritmo propuesto es capaz de conseguir una fase más limpia e incluso, recuperar información útil en zonas con topografía en las que los demás métodos resultan ineficaces.

En segundo lugar, el filtro de fase desarrollado ha sido evaluado tanto con datos simulados como con datos reales. La ventaja de emplear simulaciones es que podemos proporcionar más medidas cuantitativas de calidad del filtrado al conocer la fase real (es decir, sin ruido). El filtro propuesto se ha comparado con cuatro filtros distintos, siendo el denominado filtro de Goldstein el más conocido y más ampliamente empleado en este ámbito. Los demás son variaciones de este filtro original que incluyen diferentes cambios y mejoras en su formulación. Con respecto a las simulaciones, se han generado cuatro interferogramas con distintos niveles de ruido (desde un nivel intermedio hasta un nivel extremadamente alto con el que la señal se encuentra prácticamente enmascarada por el

ruido). Con respecto a los datos reales, se han procesado tres interferogramas correspondientes a tres sucesos geológicos distintos y de diferentes sensores radar. En todos los casos, se muestra que el filtro propuesto ofrece los mejores resultados. En efecto, se ha demostrado que, cualitativamente, se consigue reducir en mucha mayor medida el nivel de ruido original en cada uno de los interferogramas a la vez que se consigue preservar detalles (franjas) útiles en la fase. Las fases filtradas son mucho más limpias y continuas espacialmente (suaves), lo que resulta enormemente ventajoso para etapas posteriores del procesado y, especialmente, para la etapa de desenrollado de fase. Del mismo modo, las medidas cuantitativas de la calidad del filtrado muestran que el método propuesto mejora considerablemente los resultados de los demás. Concretamente, se consigue reducir prácticamente en su totalidad los denominados residuos de fase, que se corresponden con píxeles inconsistentes asociados a valores de fase erróneos.

En tercer lugar, los métodos de optimización polarimétrica no muestran unos resultados tan buenos como se podía esperar inicialmente, y la mejora en la calidad de la fase en interferogramas aislados está muy limitada. Se ha llegado a la conclusión de que la reducción del ruido con esta técnica se consigue gracias al promediado espacial de muestras (multilook) empleado para calcular la coherencia interferométrica, mientras que la propia optimización no proporciona una mejora adicional. No obstante, se ha podido comprobar que la optimización muestra resultados muy variables en función de este número de muestras promediadas. En este sentido, pequeños promediados (pocas muestras) proporcionan un aumento de coherencia muy grande (especialmente si se emplea un multilook de 3×3 píxeles), aunque el nivel de ruido en el interferograma se mantiene elevado. Sin embargo, el uso de promediados más grandes, a pesar de conseguir reducir en mayor medida el ruido, no proporcionan una mejora clara frente a los canales polarimétricos convencionales.

Dentro de este mismo ámbito, se ha seguido una metodología alternativa en la que se realiza una optimización individual de cada píxel, pero nunca se hace un promediado efectivo del interferograma. La idea de este último test consiste en verificar si efectivamente el algoritmo de optimización permite aumentar la calidad de la fase sin aplicar ningún filtrado (promediado). Para ello, se extraen matrices de 3×3 píxeles en las que siempre se optimiza el píxel central. Los resultados muestran que, finalmente, esta estrategia sí que consigue mejorar sustancialmente la calidad de la fase original, demostrando que la optimización polarimétrica resulta útil. Los resultados muestran que el nivel de ruido se reduce sustancialmente, únicamente manteniéndose elevado en aquellas zonas extremadamente ruidosas inicialmente. La principal ventaja de esta técnica es que no existe el riesgo de que disminuya la resolución original del interferograma, lo que supone una ventaja evidente frente a algunos métodos de filtrado.

Por último, la clasificación de tipos de cultivos se ha llevado a cabo en una zona agrícola localizada al suroeste de Sevilla (Andalucía, España), denominada BXII. En dicha zona, se dispone de 17 tipos de cultivos diferentes, siendo el algodón y el tomate los más abundantes. El proceso de clasificación consiste en emplear datos InSAR de Sentinel-1 del año 2017, usando el algoritmo de Bosques Aleatorios (Random Forests), muy conocido en el ámbito del aprendizaje automático. Concreta-

mente, se han empleado las coherencias generadas con una línea de base temporal corta (es decir, poca separación temporal entre imágenes) de 6, 12 y 18 días, y provenientes de las dos polarizaciones de Sentinel-1 (VV y VH).

Los resultados de clasificación son globalmente muy buenos, obteniéndose una precisión global entre el 70 y el 80%. Se observa que el mejor resultado se obtiene cuando se emplean las coherencias de la línea de base más corta (6 días). Esto era de esperar ya que los datos asociados se ven menos afectados por la decorrelación temporal. El uso simultáneo de coherencias de múltiples líneas de base no aporta ninguna mejora, de modo que la inclusión de más información temporal no tiene ninguna ventaja en este ámbito específico. Con respecto a la influencia de la polarización, se ha demostrado que las coherencias del canal VV proporcionan un resultado sustancialmente mejor. Esto tiene sentido dado que se sabe que el canal VV dispone de una mayor relación señal a ruido (SNR) que el VH. Sin embargo, los resultados muestran que el empleo de las coherencias de ambos canales conjuntamente proporciona un mejor resultado (la precisión global aumenta en torno al 1-2% con respecto al uso del canal VV únicamente). Conviene mencionar que sólo 4 clases de las 17 muestran una mala clasificación, es decir, se identifican peor y se confunden con algún otro tipo de cultivo. El análisis de la evolución temporal de la coherencia asociada a estos cultivos nos permite observar el motivo de esta mala clasificación. En efecto, se ha demostrado que aquellos cultivos que presentan una evolución temporal de coherencia similar a otros (es decir, muestran el mismo patrón de crecimiento/disminución en sus valores a lo largo del tiempo) son los que presentan la mayor confusión.

Principales Conclusiones

En la presente tesis se han desarrollado diferentes métodos avanzados ligados a la interferometría radar. En base a todos los resultados mostrados a lo largo de este trabajo, puede decirse que los objetivos inicialmente propuestos se han cumplido satisfactoriamente. A continuación, se resumen las principales conclusiones derivadas de los resultados obtenidos en cada ámbito específico.

Se ha demostrado que los métodos convencionales de filtrado en rango tienen dificultades para eliminar los efectos de decorrelación geométrica en escenas con topografía. El método propuesto consigue solventar todas las limitaciones de los métodos conocidos mediante la explotación completa de la topografía de la escena. Se ha podido comprobar que el tamaño de las ventanas empleado en el filtrado afecta considerablemente a la calidad de los resultados. En efecto, ha quedado demostrado que áreas con topografía muy variable se filtran mejor con ventanas pequeñas (16 y 32 píxeles) mientras que las zonas llanas se ven beneficiadas por bloques de mayor tamaño (64 o 128 píxeles). El filtro propuesto evalúa todos los tamaños de ventana posible y escoge la mejor solución, de manera que se adapta automáticamente a cualquier tipo de superficie y se maximiza la calidad del filtrado.

Se ha visto también que debido a las fuentes de decorrelación restantes, prácticamente cualquier interferograma presenta ciertas áreas muy ruidosas en las que no hay medidas de fase útiles. Los resultados del filtro de fase propuesto demuestran que el método desarrollado va un paso más allá con respecto a los métodos convencionales. Así, se ha demostrado que el filtro consigue reducir en gran medida los efectos del ruido, a la vez que se mantienen detalles de fase útiles. Conseguir esto de forma simultánea es probablemente la tarea más difícil en el ámbito de filtrado del interferograma. Estos dos objetivos se consiguen mediante 1) filtrar iterativamente la fase ruidosa original, 2) adaptarse localmente al nivel de ruido del interferograma y 3) suavizar espacialmente los valores de fase ruidosos estimados. Además, una característica importante del filtro propuesto es que es completamente no paramétrico, es decir, no requiere especificar manualmente ninguno de sus parámetros, a excepción del tamaño inicial del bloque de filtrado. En este sentido, interferogramas muy ruidosos se verán beneficiados por un tamaño inicial grande (por ejemplo, de 256×256 píxeles como se ha propuesto), y un mayor número de iteraciones. Por el contrario, interferogramas de mejor calidad requerirán menos iteraciones. Sin embargo, aunque se fije un tamaño de bloque inicial grande para filtrar interferogramas poco ruidosos, únicamente repercutirá sobre el tiempo de computación y no en el resultado final, ya que el filtro se adapta siempre al nivel de ruido del bloque.

El análisis de los métodos de optimización polarimétrica en interferogramas aislados muestra que la mejora en la calidad de la fase viene, principalmente, del promediado espacial empleado para calcular la coherencia. Se ha podido comprobar que la propia optimización no ofrece una mejora adicional a no ser que se emplee la metodología alternativa propuesta, en la que se optimiza cada píxel individualmente sin promediar el interferograma original. En este caso, se ha visto que se reduce el nivel de ruido de forma aceptable. Los resultados muestran que se consigue suavizar espacialmente la fase en áreas no excesivamente ruidosas a la vez que se mejora la calidad de las franjas de fase. Sin

embargo, la mejora en la calidad de los datos sigue limitada en aquellas zonas extremadamente ruidosas. Conviene mencionar que esta metodología tiene la ventaja de que la resolución original del interferograma nunca se reduce.

Por último, se ha demostrado que los datos InSAR constituyen un observable útil que puede ser empleado para clasificar cultivos mediante algoritmos de aprendizaje automático. La conclusión general es que la coherencia multitemporal ofrece resultados más que aceptables, con una precisión global que varía entre el 70 y el 80% en función de los datos de entrada del clasificador. Concretamente, el mejor resultado se obtiene cuando se emplean las coherencias de la línea de base temporal más corta (en este caso, 6 días) y de dos canales polarimétricos (en este caso, VV y VH), simultáneamente.

Se ha demostrado también la importancia que tiene un muestreo correcto de los datos proporcionados al modelo de entrenamiento. En este sentido, se ha visto que si el conjunto de entrenamiento está desbalanceado (es decir, no todas las clases presentan un número similar de muestras), el clasificador tiende a favorecer las clases mayoritarias, mientras que las clases minoritarias se clasifican peor. El problema del desequilibrio de clases se ha resuelto submuestrando cada tipo de cultivo de forma de cada uno de ellos tenga exactamente el mismo número de píxeles. Al hacer esto, los resultados mejoran drásticamente de forma que cada una de las clases se identifica mejor. Por último, se ha podido comprobar que el clasificador identifica peor aquellas clases cuya variación temporal de coherencia presenta el mismo patrón (es decir, presenta la misma tendencia de aumento y disminución en sus valores en el tiempo).

1 Introduction

1.1 Motivation

Remote Sensing refers to the acquisition and analysis of information of distant objects or phenomena without directly interacting with them. To retrieve the information, instruments are designed to gather signals, such as electromagnetic or acoustic waves, which come from its interaction with matter and contain significant data related to the object physical properties. In its current state, remote sensing is generally associated with the study of complex processes and dynamics of our planet Earth, by means of processing data gathered by aerial or space-borne systems in the form of electromagnetic images. When studying the Earth with such systems, we usually use the term Earth Observation, which involves a wide variety of techniques and tools the goal of which is to improve the knowledge we have of our planet at a global scale.

Advances in remote sensing technology, especially since the mid-2000s, have drastically increased the potential of remote sensed data to monitor the Earth surface in multiple areas. A large number of applications, related to both civil and military domains, have been developed in the latest years and, certainly, new ones will appear in the future. Nowadays, remote sensing plays a crucial role in many scientific and engineering topics [1], including topography and cartography with the generation of Digital Elevation Models (DEM). It is widely employed in geoscience for assessing geo-hazards (volcanic eruptions, earthquakes, etc.) and disaster risk management. Also, remote sensing techniques are used in meteorology by estimating the climate and its evolution, and its subsequent impact on biodiversity. Moreover, it can also be exploited to monitor terrestrial and environmental changes

caused by modern civilization, including 2-D, 3-D and 4-D (space and time) land mapping, change detection (for deforestation and desertification monitoring), etc.

Remote sensing technologies can be classified either according to its source of illumination (energy radiation) or to the working frequency of the system. In the first case, a system is called *active* if it has its own source of illumination. Particularly, it sends electromagnetic radiation to a target and measures the backscattered signal returned to the sensor. Contrarily, a *passive* system can only detect backscattered signals that are reflected naturally from a source other than the sensor, as the light emitted by the Sun. These sensors are useful to detect ultraviolet, visible and infrared radiations or thermal radiation generated by all matter with a temperature higher than absolute zero. We also classify the sensors according to the band of the electromagnetic spectrum employed. We distinguish between microwave (frequency ranging from 300 MHz to 30 GHz) and optical systems. This thesis focuses on *Synthetic Aperture Radar* (hereafter called SAR) systems, which are a specific type of radar (*RAdio Detection And Ranging*). SAR are active systems which work on the microwave band of the electromagnetic spectrum. They constitute one of the most important and remarkable instruments for remote sensing due to its wide coverage and its weather-independent capability, and also because they can operate indistinctly during day and night. SAR are mounted on moving platforms, which can be either airborne (the sensor is placed on a plane or a helicopter) or space-borne (the sensor is placed on a satellite which is in orbit around the Earth). The SAR system moves along its trajectory transmitting and receiving signals in a side-looking fashion. All these signals are processed in such a way that a larger antenna is "synthesized". This is referred to as the synthetic aperture principle and allows an increase of the image resolution in the flight direction.

Since the launch of the first orbital SAR, SEASAT, in 1978, the number of operational missions carried out by different states and intergovernmental organizations has experienced a significant growth, especially since the beginning of the 90's [2] [3] [4]. As shown in Table 1.1, the number of missions has not only increased, but has increased more quickly over time, showing the common interest in developing and enhancing the huge potential that SAR systems offer for observing the Earth and its characteristics. As a visual example, Figure 1.1 shows the substantial improvement of spatial resolution between a SAR image acquired in the early 90's and an image acquired in 2008. Improvements in terms of mission's life span, images' resolution, coverage, revisiting time (6 days for Sentinel-1 A/B, 11 days for TerraSAR-X and PAZ), or polarization diversity, paved the way for the development of advanced techniques derived from the exploitation of the data, such as SAR Interferometry and Polarimetry, which are introduced in the following paragraphs. It is important to note that the development of new techniques and products has also been favored by a better access to the data. Specifically, the Copernicus Open Access Hub, a platform developed by the European Space Agency, represents a paradigm change in Earth observation, since it provides completely free and worldwide open access to different SAR products which can be directly downloaded and processed for scientific purposes.

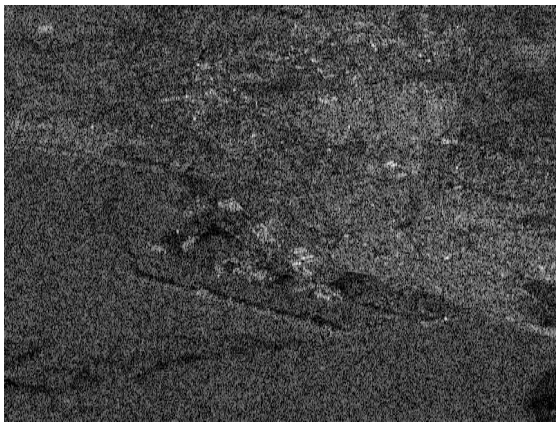

(a) Image acquired by satellite ERS-1 in date 1995-10-15 (around 3×22 meters resolution) in Stripmap mode.

(b) Image acquired in date 2008-05-13 by satellite TerraSAR-X in Spotlight mode (2 m resolution).

Figure 1.1: Comparison between two SAR intensity images acquired over the city of Alicante (Spain).

Satellite name	Operator	Polarization	Mission duration
SEASAT	NASA / JPL / Caltech (USA)	Single	June 1978 - October 1978
SIR-A	NASA / JPL (USA)	Single	November 1981 - November 1981
SIR-B	NASA / JPL (USA)	Single	October 1984 - October 1984
SIR-C/X-SAR	NASA / JPL (USA)	Dual	April 1994 - October 1994
ERS-1	ESA (Europe)	Single	July 1991 - March 2000
ERS-2	ESA (Europe)	Single	July 1995 - September 2011
ENVISAT	ESA (Europe)	Dual	March 2002 - April 2012
TerraSAR-X	DLR (Germany)	Dual	June 2007 - present
RADARSAT-2	CSA (Canada)	Full	December 2007 - present
Cosmo-Skymed	ASI (Italy)	Full	June 2007 - present
TanDEM-X	DLR (Germany)	Dual	June 2010 - present
Sentinel 1-A	ESA (Europe)	Dual	April 2014 - present
Sentinel 1-B	ESA (Europe)	Dual	April 2016 - present
PAZ	HISDESAT (Spain)	Dual	February 2018 - present

ESA refers to the European Space Agency, NASA refers to the National Aeronautics and Space Administration, CSA is the abbreviation of Canadian Space Agency, ASI is the abbreviation of Italian Space Agency and DLR refers to the German Aerospace Center.

Table 1.1: Launch dates of some European and North-American space-borne SAR missions since the launch of SEASAT in 1978.

SAR Interferometry, abbreviated InSAR, was developed with the goal of retrieving the topography of an area. Although the basics of interferometry were initially described in 1974 [5], the technique became more popular in the late 80's [6] [7] [8] [9], and its robustness consolidated with the launch of the European satellite ERS-1 in 1991, since a large amount of SAR data became available for scientific analysis. SAR Interferometry is based in combining, at least, two different images acquired from two slightly different positions. If the images were acquired using two antennas simultaneously, we would use the term single-pass interferometry. If both images were acquired at different times, we would talk about repeat-pass interferometry. By extracting the topography, InSAR allowed the generation of global DEM's, such as the NASA Shuttle Radar Topographic Mission (SRTM) [10] or the global TanDEM-X DEM [11]. In this context, a major step forward with respect to classical InSAR applications is related to the estimation of changes in the Earth surface. If the topography of an area is known, Differential SAR Interferometry (abbreviated DInSAR) allows to monitor relative surface deformations between different SAR acquisitions [12] [13] [14]. DInSAR is nowadays established as a very powerful advanced technique used in multiple areas. It is used in civil engineering for estimating surface subsidence or uplifts caused by underground mining or water extraction or for landslide monitoring. It is also widely used in geophysics to analyze crustal deformation caused by tectonic activities, such as volcanic eruptions and earthquakes. This technique provides accurate measurements (up to less than 1 cm) over large spatial extents, making it advantageous in comparison to conventional *in-situ* methods. Innovative DInSAR algorithms using large stacks of images have recently been developed. The family of techniques known as PSI (Permanent Scatterer Interferometry) is a branch of differential interferometry which is able to measure ground motion very accurately on certain pixels previously selected as reliable (permanent scatterers). By processing multiple SAR acquisitions, PSI has proved to be very powerful for monitoring ground displacements over time, providing accurate deformation time series over such permanent scatterers [15] [16] [17] [18] [19].

Conventional SAR systems were designed to generate reflectivity images using a single combination of polarizations of transmitted and received electromagnetic signals. Polarimetry is based on analyzing the polarization state of electromagnetic fields, which is modified after the interaction with scatterers. Consequently, SAR Polarimetry (abbreviated PolSAR) concerns the use of polarimetry in radar applications, being initially introduced with the work of G.W. Sinclair [20]. Later on, throughout the 50's and 60's, important works related to backscatter theory were carried out [21] [22] [23] [24]. A major contribution was done by Hyunen in 1970 [25], where he applied previous researches related to polarization to radar targets. As a result of his work, interest in SAR polarimetry increased [26]. Polarimetry constitutes today a major topic in SAR remote sensing, due to the numerous applications it offers in different fields, including agriculture (crop mapping), forest monitoring, tree height retrieval, land use, etc. Furthermore, the number of SAR satellites with polarimetric capabilities has grown significantly in the last decades. Modern and currently operating SAR systems, such as RADARSAT-2, TerraSAR-X, Sentinel-1 or PAZ are able to collect data at

different polarizations, proving the interest in developing PolSAR techniques and applications.

While interferometry allows to detect relative height (or motion) of radar targets, polarimetry deals with the physical properties of scatterers, and is able to retrieve additional features of them by analyzing the polarization information contained in backscattered signals. Both techniques are, in fact, complementary. Since the end of the 90's, the idea of combining the information provided by polarimetry and interferometry emerged. Polarimetric SAR Interferometry (abbreviated PolInSAR), introduced in 1998, constitutes an extension of conventional scalar interferometry, leading to solve the limitations or inaccuracies of interferometric systems operating with a fixed polarization (such as a better estimation of the height location of targets), by exploiting the sensitivity of polarimetry to the shape or geometry of scatterers [27] [28]. Moreover, recent studies have also shown the potential of including polarimetry in differential applications. Polarimetric Differential SAR Interferometry (abbreviated PolDInSAR) has demonstrated to outperform classical DInSAR techniques. The integration of fully or dual polarimetric data into DInSAR processing algorithms has shown to greatly improve the quality of motion/deformation maps in both accuracy and spatial density, especially when multi-temporal data-sets are considered, as in the framework of the previously introduced PSI [29] [30] [31] [32] [33].

Besides the major improvements carried out in both InSAR and PolSAR, the mapping of the Earth surface with SAR imagery has also experienced an outstanding progress during the last years. Image classification using remote sensed data belongs to the general field of pattern recognition. Pattern recognition is the scientific discipline which tries to classify objects into different categories or classes according to its properties. Its goal is to derive features of such classified objects and yield useful information of a given system or data set. Pattern recognition problems are approached by machine learning algorithms, which fall into the field of Artificial Intelligence [34]. Broadly speaking, machine learning was born with the theory that computers (machines) can "learn" directly from data without being explicitly programmed to perform tasks. By looking for patterns through large amounts of data, machine learning algorithms are able to re-adapt themselves and predict the evolution of complex systems or the value of new observations. Machine learning applications are nowadays innumerable. Computer vision, software engineering, medical diagnosis, economics, linguistics or marketing are just some examples. In the context of SAR and remote sensing, machine learning algorithms allow to classify what the sensor is observing and, consequently, they allow to compile land-cover and vegetation maps of vast areas. If our ecosystem and natural environments are to be properly managed, appropriate knowledge of the state and distribution of natural areas, the quantity of water resources or the state of the soil is mandatory, and satellite datasets are very suitable to this end. Finally, the global concern over land-use management is clearly represented by the CORINE-Land-Cover (Coordination of Information on the Environment - Land-Cover) programme created in 1985 by the European Council under proposal of the European Commission [35], whose main aim is to establish a digital inventory on land-cover of all European Union members.

1.2 Objectives

Once the reader has been properly oriented to the topics this work deals with, its main objectives can be introduced. This PhD is intended to provide improvements in different steps of the interferometric processing, by the development of new algorithms and methods. Also, the work investigates innovative InSAR applications related to the classification of crops. Each contribution is briefly described in the following paragraphs.

In first place, this thesis addresses an issue intrinsically related to the interferometric processing, which is the inherent decorrelation or noise present in InSAR stacks in repeat-pass mode. As stated previously, interferometry is based on combining two images of the same area, resulting in a new image denoted as interferogram. As complex signals, interferograms have both amplitude and phase information. While amplitude is related to the power of radar targets, the interferometric phase contains the distance difference between the satellite antenna and the ground targets in both acquisitions. InSAR just exploits this phase difference, since the amplitude does not provide meaningful information related to distances. Consequently, the accuracy and the quality of phase data represent the key-element in both InSAR and DInSAR processing algorithms, and the reduction or suppression of decorrelation effects is strictly mandatory to provide reliable products derived from these two techniques. It is worth mentioning that noise reduction is compulsory in (almost) all fields that treat digital signals, such as medical images, audio signals, etc. Noise reduction is achieved by designing filtering algorithms which try to enhance the quality of the signals by reducing the influence of specific types of noise. In the context of SAR, multiple sources of noise are present in interferometric images. Although an analysis of the multiple sources will be carried out in Chapter 2.2, a basic and initial distinction can be drawn as follows. An important source of noise is due to the InSAR principle itself. More specifically, it is due to the fact that each image has its own acquisition geometry. This different geometry induces an spectral misalignment between the images, leading to an inevitable increase of decorrelation and loss of quality in the future phase. Since this source of noise cannot be avoided, specific algorithms are to be designed to remove this type of noise. Another important source is more related to the characteristics of the scene. If the scene changed significantly between both images (for instance, due to changes in the vegetation), an important decorrelation would inevitably appear since the response of the scatterers between the images would differ. Accordingly, one of the main objectives of this thesis deals with the development of improved denoising algorithms for InSAR/DInSAR applications. More precisely, two different filters are proposed:

- A filter which addresses the problem of the spectral misalignment in range direction. Range filtering is a commonly-used pre-processing step in SAR interferometry. Its goal is to remove, from the two images used to generate an interferogram, the non-common frequency bands in range dimension, as they cause a loss of correlation and deteriorate the quality of interferometric products. This work presents a refined method which correctly adapts to the local topography and is able to optimize the filtering performance. Note that range filtering is per-

formed prior to interferogram formation, so its output corresponds to two filtered images, the spectral properties of which have been enhanced for interferometric purposes.

- An innovative filter for the final interferometric phase. Once an interferogram is generated, it may not be directly suitable for its further processing due to the remaining noise in the data. Consequently, without accurate and robust filtering processes, final InSAR or DInSAR products may be completely unfeasible to obtain. This filter has originally been conceived to eliminate the noise in differential interferograms used in geophysical applications, that is, interferograms which map any kind of tectonic activities (such as volcanic eruptions or earthquakes). However, its use can be extended to any kind of interferogram, thanks to its adaptation to both the noise level and image features. The goal of the proposed method is to reduce the noise at all levels while simultaneously preserving fine phase details which contain useful information.

Secondly, this thesis explores some specific aspects of PolDInSAR when only one date is analyzed (not time series as in PSI). As previously stated, PolDInSAR deals with the inclusion of polarimetry in differential interferometry applications, and it has shown to outperform the results obtained with conventional single-polarized DInSAR. Its benefits have intensively been analyzed in the framework of PSI, that is, when a large stack of images (resulting in a large number of interferograms) is to be processed. However, its potential has not been evaluated with isolated interferograms. In this thesis, an exhaustive analysis of the inclusion of polarimetry in differential applications based on a single interferogram has been carried out. Consequently, the second objective of this work consists in evaluating the potential role of polarimetry in improving the quality of isolated InSAR pairs. To this end, different polarimetric optimization methods, parameters and criteria have been implemented and tested with the goal of generating an optimum interferogram the phase of which is more suitable for its future processing.

Finally, the third objective is related to new final applications of interferometric data, and more precisely in crop-type mapping or classification. Conventional crop classification employs as input features optical/multi-spectral data, due its high sensitivity to crop properties (such as the moisture or the chlorophyll in the leaves). However, due to the passive nature of optical sensors, the number and/or the quality of images may be insufficient in some cases (for instance, because of clouds, haze or darkness during winter). In this regard, alternative approaches using SAR data progressively gained attraction. Classical SAR-based mapping methods are radiometric, that is, the backscatter intensity of a series of images is used as input to classification algorithms. The third goal of this work is to prove that InSAR is also sensitive to the temporal evolution of crops and, hence, that it constitutes an alternative or a complement to conventional radiometric information for crop-type classifications.

1.3 Structure of the Thesis

The contents of the manuscript are divided into 5 chapters, being the first one this introduction used to contextualize and provide the reader with basic information for the rest of the work, as well as to explain the main objectives of the research.

Chapter 2 provides the theoretical background needed to ease the comprehension of the subsequent chapters. A revision of the main concepts of SAR imaging is presented. In addition, the fundamentals of SAR interferometry, including the differential extension, and SAR polarimetry are introduced. The basic formulation of PolInSAR is also reviewed, including all mathematical considerations which generalize the conventional single-polarized InSAR formulation to the diversity of polarimetric channels. This is mandatory to understand the different optimization algorithms for PolDInSAR processing, from the mathematical point of view, implementation aspects and computational complexity. In the last section of the chapter, an overview of image classification is provided. In this regard, it is worth mentioning that image classification can be approached as a machine learning problem, where a set of objects (classes) within the images are to be recognized and classified according to a known model. Among the wide variety of machine learning algorithms, we have specifically used Random Forests, which is an ensemble approach known to provide good classification accuracies. A revision of this algorithm is also done in Chapter 2.

Chapter 3 and 4 constitute the core of the thesis. In the third chapter, the main contributions to InSAR/DInSAR processing developed throughout the PhD are explained and justified in detail. Each contribution concerns different key steps within the interferometric processing chain, although they have the common goal of enhancing the quality of the data. The contribution related to range filtering is regarded as a pre-processing step, i.e., it is performed before interferogram formation. That is, range filtering employs two SAR images as input, and outputs the same images but which are more suitable for future interferometric processing. Contrarily, both the proposed interferogram filter and the PolDInSAR phase quality optimization approach are related to final processing steps. Chapter 3 includes a variety of results, coming from simulated and real datasets, and yields conclusions derived from the different innovative methods and algorithms which are presented. All contributions are compared with conventional, state-of-the-art techniques to prove both the limitations of already-existing methods and the advantage of the proposed ones.

Whereas Chapter 3 deals with processing, Chapter 4 deals with application. A novel method for mapping cropland distribution by exploiting multi-temporal coherence data obtained from a large stack of interferometric images is presented. A deep evaluation of the performance of InSAR data is carried out by analyzing the influence of multiple temporal baselines and the combination of different polarizations.

Main conclusions of the thesis are summarized in Chapter 5. Additionally, some suggestions for future work are also provided. Finally, a complete list of publications in indexed journals and conference proceedings, generated during the work carried out for this thesis, is presented in Appendix A.

2

Theoretical Basis

In this chapter we review the fundamental principles of SAR systems, their applications and shortcomings which are involved in this thesis. Starting from the basic concepts of image acquisition and generation in Section 2.1, we introduce SAR interferometry and the differential extension in Sections 2.2 and 2.3. Interferometry is based on combining multiple SAR images from the same area and generate new images called interferograms, which contain the phase difference between the two images. An explanation on how this phase is sensitive to the topography of a surface or its changes over time is included. The multiple sources of decorrelation and the concept of interferometric coherence, as an indicator of the phase quality, are also introduced.

Section 2.4 gives a general review of SAR polarimetry. Polarimetry analyses how the polarization of electromagnetic waves is modified after the interaction with objects. These modifications depend on the physical and geometrical properties of scatterers. In this section, the so-called Scattering Matrix (or Sinclair Matrix) is introduced. This matrix is the fundamental representation of PolSAR data since it contains all the information related to each polarization state.

Once the mathematical background of InSAR and PolSAR have been reviewed, we can introduce the formulation of PolInSAR [1] in Section 2.5. PolInSAR coherently combines both interferometric and polarimetric information, in such a way that the complementary potentials of both techniques are exploited. Finally, in Section 2.6, basics of both image classification strategies and machine learning algorithms related to this work are described.

[1] The formulation of PolDInSAR is identical to PolInSAR, with the exception that the topographic component has been subtracted from phase data prior to the formation of the data structures and matrices.

2.1 SAR Systems

2.1.1 Fundamentals of SAR Imaging

Radar systems have been used for the observation and remote detection of objects since World War II. By means of sending electromagnetic radiations and receiving its echoes, a conventional radar can determine the location, the distance and the speed of its targets. A SAR constitutes an extension of a conventional radar since it offers an outstanding improvement in terms of geometric resolution. Accordingly, with the use of pulse compression techniques and the synthetic aperture principle, SAR systems are able to obtain high-resolution reflectivity images (similar to maps) of areas with different backscattering properties, and with the use of relatively small antennas [36].

SAR systems operate with electromagnetic radiation in the microwave band, which is a specific band of the electromagnetic spectrum, the frequency of which ranges from 1 to 100 GHz (i.e., wavelengths from 0.3 m to 3 mm). However, SAR are commonly restricted to frequencies ranging from 1 to 40 GHz. Wavelength (or wave frequency) affects the interaction between the signal and the target, so that higher frequencies interact with higher surface layers while lower frequencies penetrate deeper into the media. Table 2.1 shows some usually-employed bands and their corresponding frequency and wavelength.

Band	**Frequency** (*GHz*)	**Wavelength** (*cm*)
P	0.3 – 1	100 – 30
L	1 – 2	30 – 15
S	2 – 4	15 – 7.5
C	4 – 8	7,5 – 3.8
X	8 – 12.5	3,8 – 2.4
Ku	12.5 – 18	2,4 – 1.7
K	18 – 26.5	1,7 – 1.1
Ka	26.5 – 40	1.1 – 0.8

Table 2.1: Frequency bands usually employed in SAR systems.

Either it is space-borne or air-borne, the SAR illuminates the Earth surface in a side-looking fashion as shown in Figure 2.1. The SAR moves jointly with the platform along its flight trajectory, sending microwave pulses at a certain *Pulse Repetition Frequency* (PRF) and receiving each backscattered pulse from the Earth surface. The illuminated scene is swept across and, simultaneously, scanned in the along-track direction, generating a 'raw' data matrix of the scene. The flight direction (represented by 'x' dimension in Figure 2.1) is defined as the 'along-track' or azimuth direction, while the across-track (or ground-range) direction (represented by dimension 'y') is denoted as range.

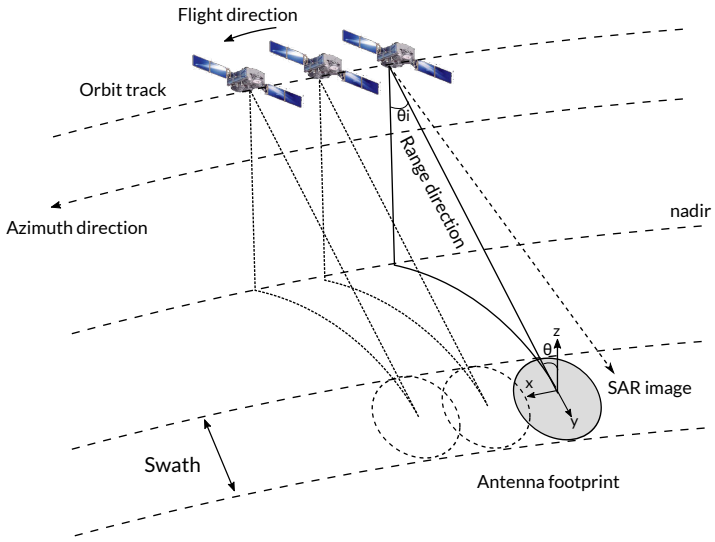

Figure 2.1: SAR imaging geometry.

The backscattered signals reach the receiver antenna after a delay which depends on the distance d between the sensor and the scatterer,

$$\Delta t = \frac{2d}{c}, \tag{2.1}$$

being c the speed of light in vacuum (approximately 300.000 km/s).

The resolution of an imaging system can be defined as the determination if only one or more than one target is observed. In the case of SAR, we have a two-dimensional resolution. On the one hand, the resolution in range dimension δ_r is related to pulse duration τ or to signal bandwidth B_W,

$$\delta_r = \frac{c\tau}{2} = \frac{c}{2B_W}. \tag{2.2}$$

Equation 2.2 clearly states that, to obtain a fine resolution in range, short pulses (in terms of duration) would be needed. Conversely, in order to obtain a high Signal-to-Noise Ratio (SNR), high energy pulses have to be emitted, which is unfeasible if the pulses' duration are short. To overcome this limitation, a linearly frequency modulated signal (chirp) is transmitted [36] [2], which can be longer in time and cover the desired bandwidth. These chirp pulses are compressed and convolved with a reference range function, resulting in a range-compressed image.

On the other hand, in principle, the resolution in azimuth dimension is directly related to the physical size L of the antenna and its half-power beam width β, which are directly proportional,

$$\beta = \frac{\lambda}{L}, \tag{2.3}$$

being λ the wavelength. The azimuth resolution δ_a is given by

$$\delta_a = r_0 \frac{\lambda}{2L}, \tag{2.4}$$

where r_0 is the range distance to the ground. By observing Equation 2.4, because of the long distance r_0 (especially in space-borne systems), it can be deduced that fine resolutions cannot be obtained unless extremely huge antennas are used, which is, once again, unfeasible. The generation of a *synthetic antenna* allows to greatly improve the azimuth resolution. The idea is to 'synthesize' an effective longer antenna by means of signal processing rather than to actually use longer physical antennas. This longer antenna is synthesized by taking advantage of the motion of the platform where the sensor is deployed, so that the antenna takes up several positions along the platform trajectory. A signal is transmitted at each of these positions and each received signal is sequentially stored (it is crucial that the amplitude and the phase of each received signal is properly preserved). All these stored signals resemble the signals which would have been obtained by using a linear array of antennas, but only a single radiating element is used. The new effective half-power beamwidth of the synthetic aperture is given by

$$\beta_{sa} = \frac{\lambda}{L_{sa}} \tag{2.5}$$

where L_{sa} is the effective length of the synthetic aperture, i.e., the path length during the SAR receives signal from ground targets,

$$L_{sa} = r_0 \frac{\lambda}{L}, \tag{2.6}$$

which provides the new azimuth resolution,

$$\delta_{a_{sa}} = r_0 \frac{\lambda}{2L_{sa}}. \tag{2.7}$$

By inserting Equation 2.6 into 2.7, we obtain that the azimuth resolution does not depend on either the ground range distance or the wavelength, and that it only depends on the antenna size L,

$$\delta_{a_{sa}} = r_0 \frac{\lambda}{2L_{sa}} = \frac{\lambda r_0 L}{2r_0 \lambda} = \frac{L}{2}. \tag{2.8}$$

Moreover, Equation 2.8 paradoxically indicates that finer azimuth resolutions are obtained with smaller rather than larger antennas, which is a truly spectacular result and motivated the research on SAR.

2.1.2 Image Description

The data acquisition process presented in the previous section allows the obtaining of series of data denoted as *raw* data, which are not directly related to the final reflectivity of the scanned area but they contain information of point targets which is spread throughout all received signals during the synthetic aperture time. The generation of such final reflectivity image from the raw data, known as *focusing*, is clearly non-trivial, and consists in a two-step method where a relative amount of specific processing is required [37] [38].

In order to derive the SAR image equations, the impulse response of the system must be known. A simplified approach can be derived by considering the imaging geometry of Figure 2.2, where a

single-point (or deterministic) scatterer P is located in space at coordinates (x', y', z').

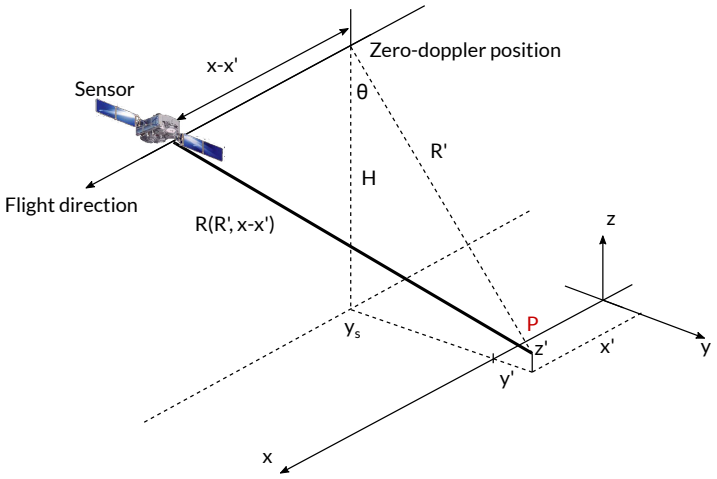

Figure 2.2: SAR measurement of a single-point scatterer.

The sensor is located at (x, y_s, H), where the x dimension can be described in time as a function of the flight speed v, yielding $x = vt$. The distance between the sensor and the scatterer is

$$R(R', x - x') = \sqrt{R'^2 + (x - x')^2}. \tag{2.9}$$

According to this geometry, the response of the point scatterer in the SAR image (centered at its zero-Doppler coordinates) is given by the convolution of the intensity of the scatterer and the impulse response function of the SAR system [39],

$$S(x, r) = \sigma_S(x', y')\delta(x - x', y - y', z - z')h(x - x', r - R') \cdot \exp\left(-j\frac{4\pi}{\lambda}R'\right), \tag{2.10}$$

where σ_S is the complex reflectivity of the point target and $h(x, R)$ corresponds to the two-dimensional (range and azimuth) impulse responses which are related to the imaging resolution in both azimuth (d_{sa}) and range (d_r),

$$h(x, R) = \text{sinc}\left(\frac{x}{\delta_{sa}}\right)\text{sinc}\left(\frac{R}{\delta_r}\right). \tag{2.11}$$

In order to derive a complete mathematical formulation of a SAR image, different concepts have to be introduced. The *resolution cell* is defined as the area given by $d_{sa} \times d_r$ (that is, the area given by the SAR impulse response). In a real scenario, there is not just an individual scatterer but an ensemble of point scatterers within the resolution cell. It is important to note that this happens since the dimension of the resolution cell (order of meters) is significantly larger than the signals' wavelength (centimeters). In other words, all received echoes are not due to an individual scatterer, but are the result of the combination of an arbitrarily number of individual point scatterers within the resolution cell. Contrarily to the deterministic behavior of a point scatterer described by the image model of Equation 2.10, the response of this ensemble of individual scatterers is completely random. Thus, to derive a general expression of a SAR image, different assumptions have to be made. Firstly, we

assume that the scatterer did not move while it was illuminated (the scene remains stationary during its acquisition). The second assumption refers to linearity [39], that is, the total scattered field results from the linear superposition of each field of each individual scatterer.

The general expression of the SAR image model is derived as follows. We consider an ensemble of scatterers $E(x, y, z)$ located in a 3D space, or volume V. The projection of E into the 2D cylindrical zero-Doppler radar coordinates gives the complex reflectivity of the distributed target,

$$E(x, R) = \int_V E(x, y' + R\sin(\theta), z' - R\cos(\theta))\, R\, d\theta, \tag{2.12}$$

where θ is the incidence angle. The SAR image expressed in azimuth x and slant-range R coordinates is

$$S'(x, R) = \int_V E(x, y' + R\sin(\theta), z' - R\cos(\theta))\ \exp(-j\frac{4\pi}{\lambda}R)\, h(x - x', R - R')\, dV. \tag{2.13}$$

where $dV = dx'\, dy'\, dz'$.

In practice, it becomes completely unfeasible to describe the distributed scattering process by means of the SAR image model of Equation 2.13. Accordingly, a statistical model which assumes that N individual scatterers are within the resolution cell is assumed, so that Equation 2.13 can be transformed into

$$S(x, R) = \sum_{n=1}^{N} \sigma_n(x_n, R_n)\, h(x - x_n, R - R_n), \tag{2.14}$$

where $\sigma_n(x_n, R_n) = \sqrt{\sigma_n}\, e^{j\theta_n}$ is the *radar cross-section* [40] [41] and the impulse response of each scatterer can be expressed as

$$h(x - x_n, R - R_n) = h_n\, e^{j\varphi_n}. \tag{2.15}$$

According to Equation 2.14, the complex SAR image S is of the form

$$S = \sum_{n=1}^{N} A_n\, e^{j\varphi_n}, \tag{2.16}$$

where A_n is the amplitude of the n scatterer and φ_n its phase within the resolution cell. Visually, the complex reflectivity resulting from the contribution of each elementary scatterer can be illustrated in the complex plane as in Figure 2.3.

Due to the random distribution of the scatterers within a resolution cell, the signals of these scatterers may interfere constructively or destructively. Such effect gives a granular aspect to the images with significantly important random spatial variations between pixels. This phenomenon corresponds to the so-called *speckle* which will be described in Subsection 2.1.3.

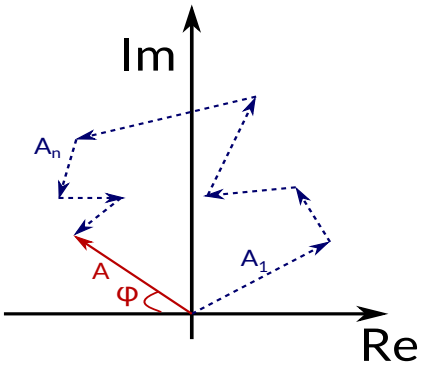

Figure 2.3: Coherent integration of an ensemble of scatterers resulting in the final SAR complex reflectivity.

2.1.3 Speckle

Although it is misleadingly considered as noise since it degrades the quality of SAR images, speckle is purely related to the radar echoes and the coherent nature of SAR imaging. The superposition of all point scatterers within a resolution cell makes that the derivation of a speckle noise model can only be done statistically, with a set of multiple assumptions:

- The number of elementary scatterers is large and they are statistically independent, i.e., none of them has a dominant contribution.
- The amplitude A_n of the n scatterer is independent from its phase (i.e., they are random variables).
- The phase lies within the interval $[-\pi,\ \pi]$.

Under these hypotheses, the Central Limit Theorem allows us to split Equation 2.16 as the summation of its real and imaginary parts, i.e.,

$$S = \sum_{n=1}^{N} \mathrm{Re}(A_n\, e^{j\varphi_n}) + j \sum_{n=1}^{N} \mathrm{Im}(A_n\, e^{j\varphi_n}), \tag{2.17}$$

where the real and imaginary parts of the image are

$$\begin{aligned} \mathrm{Re}(S) &= \sum_{n=1}^{N} A_n\ \cos(\varphi_n), \\ \mathrm{Im}(S) &= \sum_{n=1}^{N} A_n\ \sin(\varphi_n), \end{aligned} \tag{2.18}$$

and follow a zero-mean Gaussian distribution with σ standard deviation, denoted as $\mathcal{N}(0, \sigma^2)$ [42]

$$\mathrm{pdf}_{Re(S)} = \mathrm{pdf}_{Im(S)} = \frac{1}{\sqrt{2\pi\sigma^2}}\ \exp\left(\frac{-A^2}{2\sigma^2}\right). \tag{2.19}$$

From Equation 2.19, we can derive the expressions of the *probability density functions* (pdf) of the amplitude, the phase and the intensity of a distributed scatterer (being the latter defined as the square of the amplitude, i.e., the intensity $I = A^2$), within a *single-look complex* (SLC) SAR image, as

$$\mathrm{pdf}_A = \frac{A}{\sigma} \exp\left(\frac{-A^2}{2\sigma^2}\right), \tag{2.20}$$

$$\mathrm{pdf}_I = \frac{1}{2\sigma^2} \exp\left(\frac{-I}{2\sigma^2}\right), \tag{2.21}$$

$$\mathrm{pdf}_\varphi = \frac{1}{2\pi}. \tag{2.22}$$

Each magnitude is statistically described with a different type of distribution. The pixel amplitude and intensity follow a *Rayleigh* and an exponential distribution respectively, whereas the phase follows a uniform distribution within $[-\pi, \pi]$. A visual representation of each distribution is represented in Figure 2.4. Since the phase is uniformly distributed within its definition domain, there is no information that can be extracted from it due to the randomly distributed scatterers. It follows that the phase of a single SAR image is uninterpretable and cannot be exploited, as shown in Figure 2.5. However, ground scattering hopefully cancels out when the phase difference between a set of SAR images is calculated. This fact allows the exploitation of the phase difference, which constitutes the base for InSAR processing and will be analyzed in detail in Section 2.2 and 2.3.

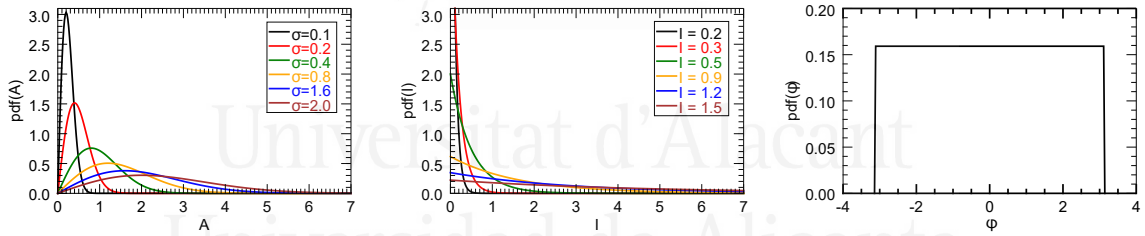

(a) Amplitude. **(b)** Intensity. **(c)** Phase.

Figure 2.4: Probability density functions of amplitude, intensity and phase of a SLC image over distributed scatterers.

Speckle reduction or *despeckling* can be achieved by *multilooking*, which, basically, consists in averaging independent pixels or *looks* of the intensity image. Although it causes a loss of spatial resolution, multilook greatly improves both the radiometric estimation and the interpretability of the image by reducing the noise variance. Speckle reduction is an important topic in SAR imagery, and a wide variety of methods and algorithms have been developed in the latest years. The most simple method is the previously explained multilook, but there undoubtedly exist more sophisticated methods. The Lee Filter [43] [44], the adaptive and Intensity-driven filter (IDAN) [45], Non-Local method [46], or the Binary Partition Tree-based approach [47] are just some of such improved algorithms for speckle suppression. Finally, Figure 2.6 provides an example of speckle reduction filters.

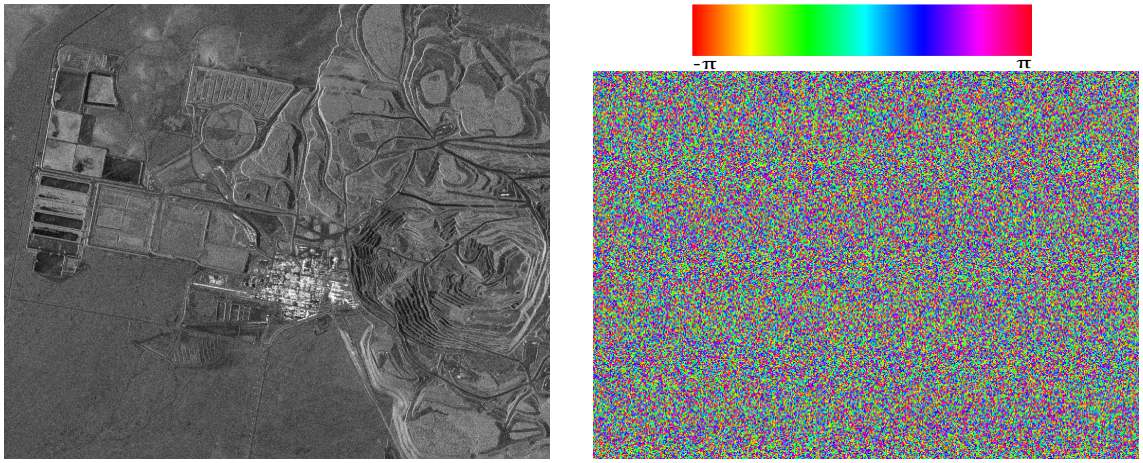

(a) Intensity. **(b)** Phase.

Figure 2.5: Intensity and phase of a SAR image. The phase of a single image is completely noisy and provides no information. The scene corresponds to a PAZ image of the Mojave Desert (USA).

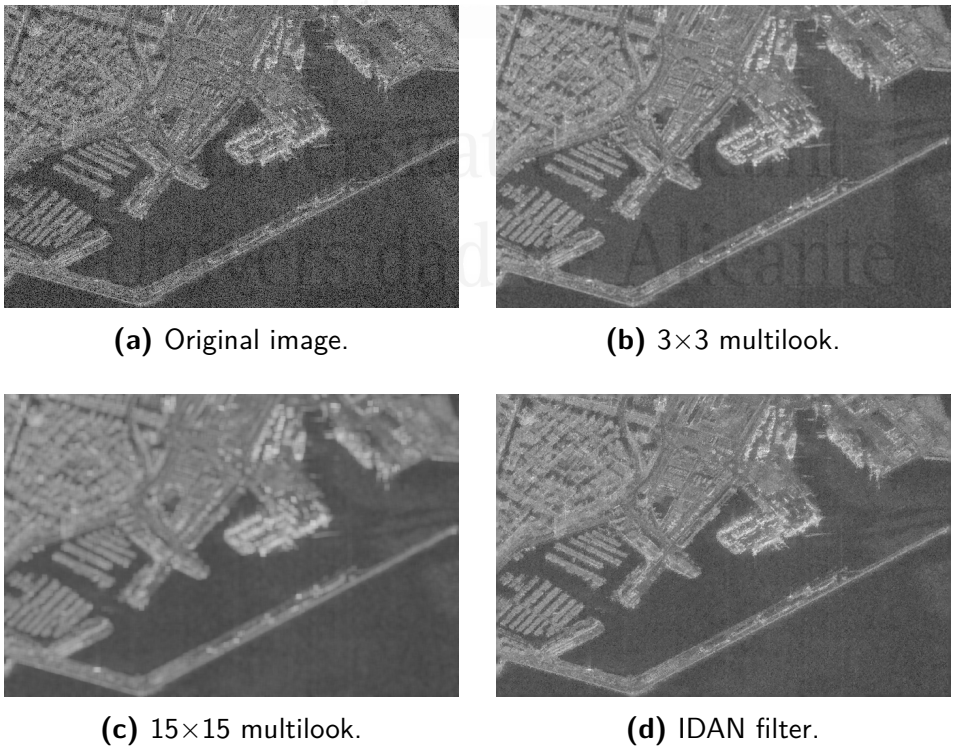

(a) Original image. **(b)** 3×3 multilook.

(c) 15×15 multilook. **(d)** IDAN filter.

Figure 2.6: Speckle reduction in a SAR image intensity by different methods.

2.2 SAR Interferometry

SAR interferometry was conceived with the goal of retrieving the topography of an area. As previously indicated, the technique requires, at least, two SAR images from the same area acquired from two slightly different positions. Both images can be acquired either simultaneously using two different antennas in single-pass mode, or at different times (repeat-pass mode). A critical step in InSAR processing is image coregistration [48] [49]. The goal of this step is to align or resample both images to the same geometry, so that there is a 'pixel match' and the amplitude or the phase to be extracted comes from the same ground area. Coregistration requires the selection of a 'reference image', usually referred as 'master image' and the rest of images (usually called 'slaves') are resampled to the master's geometry. Very high accuracies, at sub-pixel resolution are required at this step, usually in the order of 1/16 pixel. Note that, aside from InSAR, a large number of applications could not be implemented, such as the analysis of time series, change detection, etc., without properly coregistering a set of images.

InSAR imaging geometry can be illustrated as in Figure 2.7. The separation between both sensors (or orbits) is called the *interferometer baseline* (denoted as B in Figure 2.7), and can be divided into two components. The *perpendicular or normal baseline* $B_\perp$ is the component perpendicular to the *Line of Sight* (LOS), while the *parallel baseline* $B_\parallel$ is the component along the LOS.

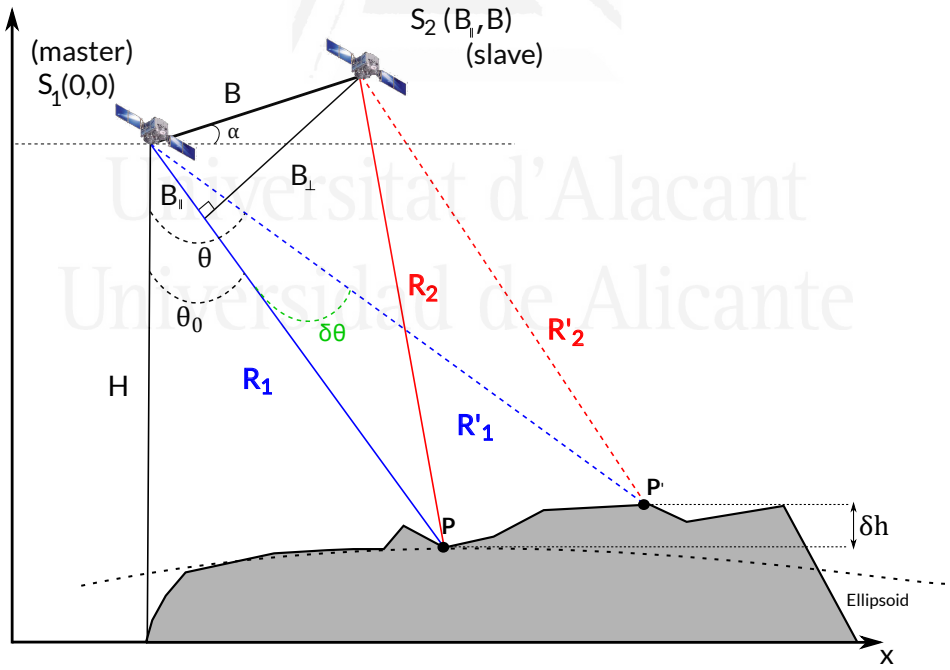

Figure 2.7: InSAR imaging geometry.

The angular separation between both sensor positions is denoted the slope angle α and the path length difference $\Delta R = R_2 - R_1$, directly related to the phase difference between both images, can be calculated to estimate the height at each image pixel.

Once both images have been properly registered, they can be 'interfered' simply by performing a

complex conjugate multiplication (pixel by pixel). This complex product yields a new image called interferogram. Thus, denoting as S_1 and S_2 two SAR images,

$$\begin{aligned} S_1(x,r) &= |S_1(x,r)| \exp\ (j\,\varphi_1(x,r)), \\ S_2(x,r) &= |S_2(x,r)| \exp\ (j\,\varphi_2(x,r)), \end{aligned} \tag{2.23}$$

where (x,r) are the image spatial coordinates (i.e., line and pixel), the complex interferogram I is defined as

$$I(x,r) = S_1(x,r)\ \cdot\ S_2^*(x,r) = A \exp\ (j\Delta\Phi). \tag{2.24}$$

Interferometry exploits the phase difference $\Delta\Phi$ since, as we will see in the following, it is related to the topography of the illuminated area.

The phase of each image S_1 and S_2 that form an interferogram is given by

$$\begin{aligned} \varphi_1 &= -\frac{4\pi}{\lambda} R_1 + \psi_1, \\ \varphi_2 &= -\frac{4\pi}{\lambda} R_2 + \psi_2, \end{aligned} \tag{2.25}$$

where λ is the radar wavelength, R_1 and R_2 are the range distances to the ground, and ψ_1 and ψ_2 model the phase term contribution from the random ground scattering in each image. It is important to point out that noise components due to both the acquisition system and atmospheric disturbances have been neglected. Assuming that ground scattering properties did not change significantly between the acquisition of both images, i.e. $\psi_1 \approx \psi_2$, the phase difference or *interferometric phase* (or simply called the phase in InSAR context) is

$$\Delta\Phi = \varphi_1 - \varphi_2 = -\frac{4\pi}{\lambda}(R_1 - R_2) = -\frac{4\pi}{\lambda}\,\Delta R. \tag{2.26}$$

Note that phase values still belong to $[-\pi, \pi]$, i.e., they are 'wrapped' to that interval. By means of geometrical relations, it is possible to derive the topographic height difference between two generic points P and P' from the corresponding interferometric phase measurements at each point. Range distance R_2 in Figure 2.7 can be expressed as

$$R_2^2 = R_1^2 + B^2 + 2R_1\,B\cos\left(\frac{\pi}{2} - \theta - \alpha\right). \tag{2.27}$$

The cosine law yields

$$\cos\left(\frac{\pi}{2} - \theta - \alpha\right) = \sin(\theta - \alpha), \tag{2.28}$$

so

$$\sin(\theta - \alpha) = \frac{R_2^2 - R_1^2 - B^2}{2R_1 B}. \tag{2.29}$$

Since the baseline B is small in comparison to the range distances, we can derive the following ap-

proximation (known as *far-field approximation*)

$$B\sin(\theta - \alpha) \approx \Delta r. \tag{2.30}$$

Due to the ambiguity in wrapped phase values and orbits inaccuracies, the expression of ΔR cannot be derived from the geometry [42]. However, the increment in δR between points P and P' can be measured precisely as

$$\partial\Delta R = B\cos(\theta - \alpha)\delta\theta, \tag{2.31}$$

where the *off-nadir angle* θ_0, which corresponds to the inclination of the sensor with respect to the nadir, is known. Consequently, the change in the phase between P and P' is

$$\partial\Delta\Phi = -\frac{4\pi}{\lambda}\,\partial\Delta R. \tag{2.32}$$

Combining Equations 2.31 and 2.32 we obtain the relation between a change in the interferometric phase and a change in the look-angle as

$$\partial\Delta\Phi = -\frac{4\pi}{\lambda}\,B\cos(\theta_0 - \alpha)\delta\theta, \tag{2.33}$$

and the relation between δh and $\partial\Delta\Phi$ is

$$\delta h = -\frac{-\lambda R_1' \sin(\theta_0)}{4\pi B_\perp}\partial\Delta\Phi. \tag{2.34}$$

Then, we can derive an expression which relates the topography δh and the interferometric phase difference between two points as

$$\partial\Delta\Phi = -\frac{4\pi}{\lambda}\left(-\frac{B_\perp}{R_1' \sin(\theta)}\,\delta h\right). \tag{2.35}$$

Finally, combining the previous Equations 2.33, 2.34 and 2.35, the expression of the interferometric phase is

$$\Delta\Phi = \frac{4\pi}{\lambda}\left(B\sin(\theta - \alpha) - \frac{B_\perp}{R_1 \sin(\theta)}\,\delta h\right). \tag{2.36}$$

Thus, Equation 2.36 shows that, if we know the spatial baseline in slant-range direction ($B_\perp$), the interferometric phase measurements are directly related to the topography of an illuminated area. In other words, the normal baseline between the orbits provides the sensitivity from which the topography can be extracted. In fact, the larger is the normal baseline is, the more sensitive or accurate the estimation of the topography will be. By looking at Equation 2.36, we can distinguish two different terms, so that the interferometric phase can be divided into two contributions,

$$\Delta\Phi = \Delta\Phi_{flat} + \Delta\Phi_{topo}. \tag{2.37}$$

The *flat-earth* component $\Delta\Phi_{flat}$ is due to the fact that two points located at the same height do not have the same interferometric phase value since the look angles of each acquisition are slightly different. As a consequence, even a completely flat terrain (i.e., in the absence of topography) will have an important phase contribution. Visually, the flat-earth phase is shown as a linear phase component with fringes which are parallel to the flight direction. This term can easily be estimated and subtracted by means of the geometrical information of each SAR acquisition. Its expression is

$$\Delta\Phi_{flat} = \frac{4\pi}{\lambda} B \sin(\theta - \alpha) = \frac{4\pi}{\lambda} \frac{B_\perp}{R_1 \tan(\theta)} \Delta R. \tag{2.38}$$

The second term $\Delta\Phi_{topo}$ is the *topographic component*. If the terrain is not flat, this phase component is modulated by the topography, i.e., it is associated with local height changes. Its expression is

$$\Delta\Phi_{topo} = \frac{4\pi}{\lambda} \frac{B_\perp}{R_1 \sin(\theta)} \delta h. \tag{2.39}$$

Evidently, the goal of InSAR is to isolate this last term from the original interferogram in which the flat-earth and the topographic phase are superimposed.

The interferometric process is illustrated with the example of Figure 2.8. Two images corresponding to the Mount Etna volcano (Italy) acquired with Sentinel-1 satellite have been used (images were acquired on dates 2018-07-07 and 2018-07-19). Once both images have been coregistered, an interferogram can be computed according to Equation 2.24. Figure 2.8 (b) shows such raw interferogram simply obtained by the complex product of both images. As it can be observed, the flat-earth component clearly 'dominates' and a linear pattern of fringes appear throughout the phase. It is important to note that this component provides information about the interferogram, but it does not contain useful information about the topography of the scene. The flat-earth phase can be estimated according to Equation 2.38 (Figure 2.8 (c)) and then it can be subtracted from the original interferogram, yielding a phase which is directly related to the topography of the area. This is represented in Figure 2.8 (d). The remaining interferometric fringes represent the strong topography which is present around the volcano, and can be understood as isolines, i.e., each color inside a fringe is located at the same height.

Finally, an important aspect should be addressed. Since all phase values are wrapped to $[-\pi, \pi]$, a phase *unwrapping* process must be performed to obtain a final DEM. Phase unwrapping consists in recovering absolute and unambiguous phase data from the original wrapped measurements, so that a conversion from the absolute phase to the topographic height can be directly performed. A wide variety of phase unwrapping methods and algorithms can be found in literature [50]. Also, a more sophisticated method based on a Statistical-cost Network-Flow (SNAPHU) is proposed in [51]. The major problem of unwrapping is related to the noise and the multiple decorrelation factors that degrade the quality of interferograms, to the point that the task may become unfeasible with very noisy data. In this regard, each processing contribution explained in Chapter 3 is directly linked with phase unwrapping, since each contribution is conceived with the goal of improving the quality

of the phase and, hence, with the goal of making the phase unwrapping process easier for both InSAR or DInSAR applications.

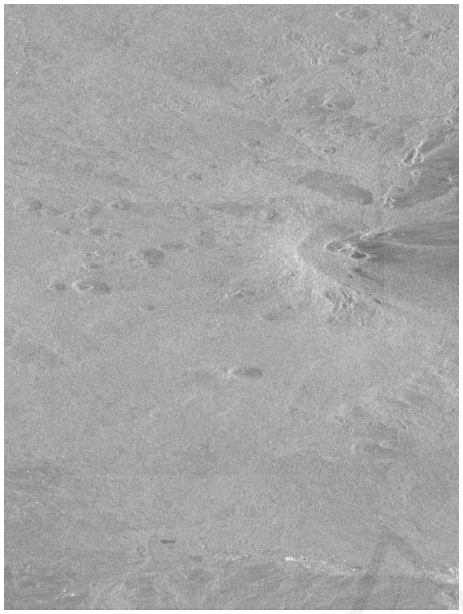

(a) Master image intensity.

(b) Original interferogram as complex product of two coregistered images. The phase contains both the flat-earth and the topographic components.

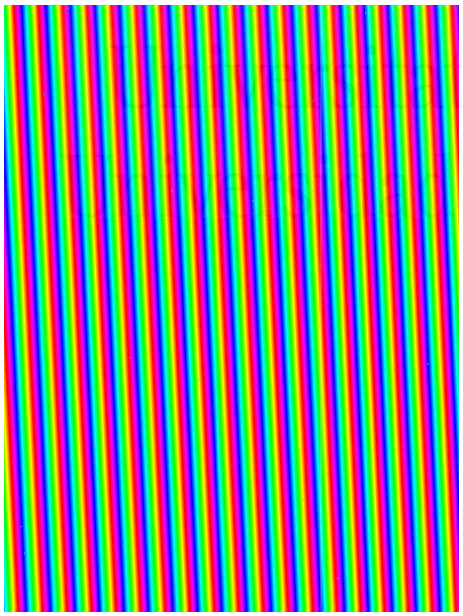

(c) Computed flat-earth reference phase.

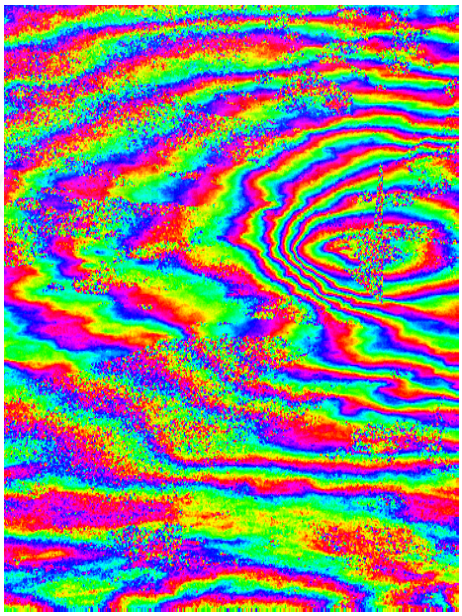

(d) Resulting phase after subtracting the flat-earth component.

Figure 2.8: Interferogram generation.

2.3 Differential SAR Interferometry

The formulation of (conventional) interferometry described in Section 2.2 assumes that the ground surface is stationary (i.e., it has not changed) between each SAR acquisition. However, this is not always true, since there can be displacements in the imaged surface. The clearest example of such displacement, or motion, may be represented by the violent shaking of the Earth surface caused by an earthquake, where there is a massive movement of the Earth's crust. Since interferometry is sensitive to topography, it is also sensitive to topographic displacements that happened in the time lapse between the two acquired images. As a consequence, the interferometric phase in Equation 2.36 can be reformulated as follows,

$$\begin{aligned} \Delta\Phi &= \Delta\Phi_{flat} + \Delta\Phi_{topo} + \Delta\Phi_{disp} + \Delta\Phi_{atmos} + \Delta\Phi_{noise}, \\ \Delta\Phi &= \frac{4\pi}{\lambda R_1}\frac{B_\perp \Delta R}{\tan\theta} + \frac{4\pi}{\lambda R_1}\frac{B_\perp \delta h}{\sin\theta} + \frac{4\pi}{\lambda}\Delta_{disp} + \Delta\Phi_{atmos} + \Delta\Phi_{noise}. \end{aligned} \tag{2.40}$$

The term $\Delta\Phi_{disp}$ represents the additional contribution to the interferometric phase when there is a surface displacement. Additionally, note that noise contributions due to the atmosphere and the system noise have been included to show the generic expression of the interferometric phase containing all possible contributions.

Differential SAR interferometry (DInSAR) is an extension of conventional InSAR which focuses on the displacement contribution to the phase. In order to isolate the displacement component, both the reference phase and the topography must be removed. To this end, usually an external DEM is used to synthesize the local topography of the imaged area. Since the orbital geometry is known, the topographic component can be easily derived according to Equation 2.39 and the data provided by the external DEM. This process is generally referred to as creating a *synthetic* interferogram with both the flat-earth and the topographic components, that are then subtracted from the original interferogram to generate a *differential interferogram* the phase of which is directly related to the relative motion of the ground. Once both terms have been subtracted, the resulting differential phase, in absence of noise and atmospheric effects, is due to the deformation of the Earth surface between the two images,

$$\Delta\Phi_{diff} = \frac{4\pi}{\lambda}\rho, \tag{2.41}$$

being ρ the ground displacement in the line of sight of the satellite. As introduced in Section 2.2, the differential phase should be unwrapped to obtain absolute measurements of the ground motion.

DInSAR is nowadays a well-established tool for measuring changes in large areas with high accuracy. A wide variety of displacements can be monitored, ranging from the slow ground subsidence (due, for instance, to groundwater extraction) [31] [52] [53] [54] to the fast and violent surface movement caused by tectonic and volcanic activities [12] [9].

As an example, a differential interferogram mapping the Mount Etna's volcanic eruption (Italy) that took place in May 2008, is shown. Images were acquired on dates 2008-/05-05 and 2008-05-29 by RADARSAT-2 satellite. Once both images have been coregistered, an interferogram can be formed as shown in Figure 2.9(c). As in the previous example of Figure 2.8, the flat-earth component has a clear predominance throughout the scene, except in the central part of the image. Figure 2.9(d) shows the resulting interferogram after subtracting the reference phase. At this stage, phase measurements contain both the topographic and the displacements contributions. The synthesized topographic component is represented in Figure 2.9(e). Note the strong influence that the topography has throughout the image, which was expected since the imaged area is mountainous. As a consequence, a lot of fringes are present when the topographic phase is computed (Figure 2.9(e)). After subtracting the topographic phase component, we obtain the differential phase and the remaining fringes represent the strong surface deformation caused by the eruption. In fact, each fringe corresponds to a ground motion of approximately 2.77 cm (half of the sensor's wavelength which is 5.5468 cm).

A major limiting factor of SAR interferometry is *decorrelation*, which is present in almost every interferogram (for instance, it is clearly visible in some areas of Figure 2.9(f)). If the signals of master and slave images decorrelate, no measurement is possible and neither a DEM generation nor the estimation of ground displacements can be done accurately. Consequently, decorrelation can be regarded as the most critical factor towards a successful generation of InSAR and DInSAR final products. An analysis of the different sources of decorrelation that degrade the quality of the phase will be carried out in Subsection 2.3.1, since the whole Chapter 3 addresses this limitation of InSAR imagery.

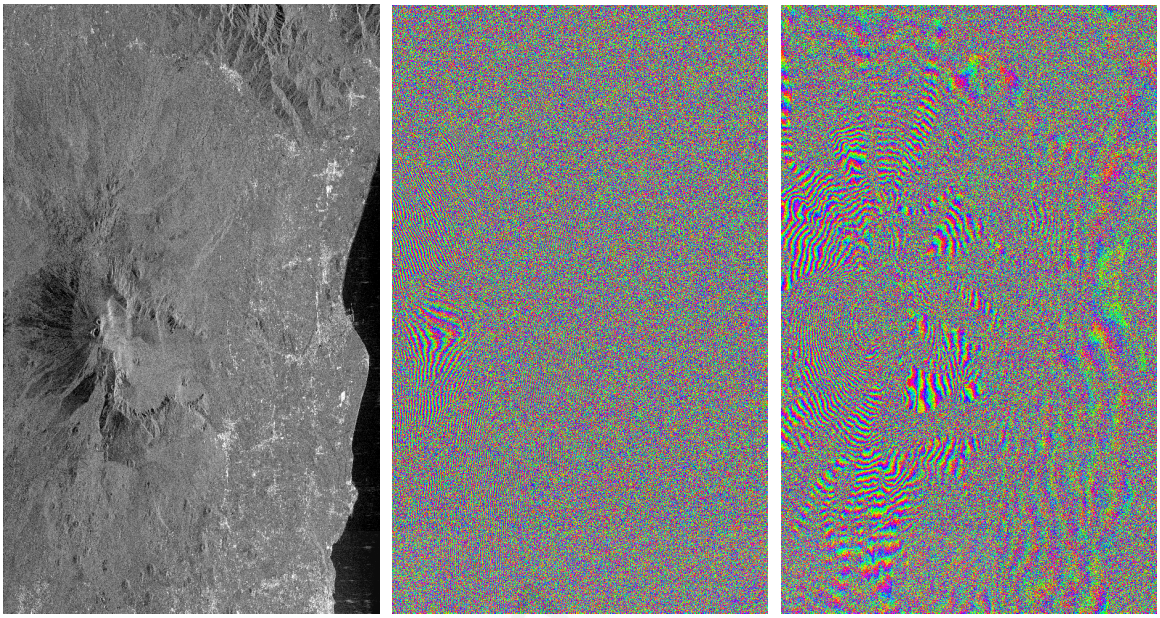

(a) Intensity image. **(b)** Original interferogram. **(c)** Interferogram after flat-earth phase subtraction.

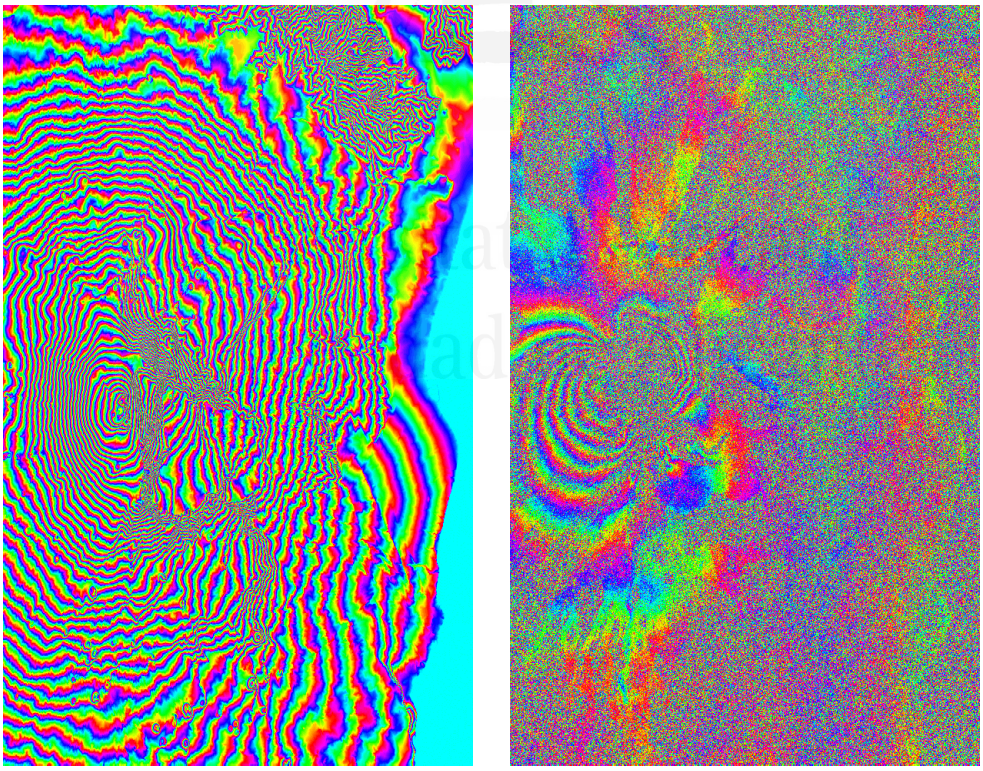

(d) Topographic phase. **(e)** Differential interferogram.

Figure 2.9: Differential interferogram formation.

2.3.1 Sources of Decorrelation

The interferometric phase constitutes a delicate product from which a wide variety of applications, including the previously explained InSAR and DInSAR, can be derived. As a consequence, it is important to have an estimator of the phase quality. The so-called *interferometric coherence* (or simply coherence) is the most widely used measure of the phase quality. Coherence yields the amount of normalized complex correlation between two SAR images and is defined as

$$\hat{\gamma} = \frac{E\{S_1 S_2^*\}}{\sqrt{E\{S_1 S_1^*\} \cdot E\{S_2 S_2^*\}}}, \tag{2.42}$$

where $E\{\cdot\}$ is the expectation operator and S_1 and S_2 are two complex and coregistered SAR images (master and slave images). For practical purposes and under the assumption that signals S_1 and S_2 have an ergodic behavior, the expectation operator is usually substituted by a spatial average of an ensemble of pixels inside a window [55]. Equation 2.42 therefore becomes

$$\gamma = \frac{\frac{1}{N}\sum_{n=1}^{N} S_1 S_2^*}{\sqrt{\frac{1}{N}\left(\sum_{n=1}^{N} S_1 S_1^* \sum_{n=1}^{N} S_2 S_2^*\right)}} \qquad (N > 1), \tag{2.43}$$

where N is the number of samples in the window. Note that the process of averaging a certain number of pixels is equivalent to the multilook described in Subsection 2.1.3, which, again, has the drawback of a resolution loss. Additionally, it is important to point out that the coherence cannot be estimated on a pixel basis, i.e., the number of samples or *multilook number* N must be different to 1. The magnitude of Equation 2.43, which ranges between 0 and 1, is usually employed as the estimator of the phase quality, that is, we employ $|\gamma| \in [0, 1]$. Lower values of $|\gamma|$ (close to 0) mean that signals S_1 and S_2 are decorrelated and the phase at those points is noisy. On the contrary, coherence values close to 1 identifies high quality phase measurements, since both signals are correlated.

Deeper analysis of the coherence and its relation with the quality of phase measurements have been carried out in a statistical framework. More specifically, the pdf of the phase is related to the coherence as [43]

$$\begin{aligned} \mathrm{pdf}(\varphi) = {} & \frac{\Gamma(N+1/2)(1-|\gamma|^2)^N \gamma \cos(\varphi-\varphi_0)}{2\sqrt{\pi}\Gamma(N)(1-|\gamma|^2\cos^2(\varphi-\varphi_0))^{N+1/2}} \\ & + \frac{(1-|\gamma|^2)}{2\pi} F_1(N, 1; 1/2; \gamma^2\cos^2(\varphi-\varphi_0)), \end{aligned} \tag{2.44}$$

where N is the multilook number, Γ is the Gamma function, F_1 is the Gauss hypergeometric function and the expected phase φ_0 can be set to zero without loss of generality.

From Equation 2.44, we can derive the phase variance σ_φ^2 as a meaningful measure of the phase noise as follows

$$\sigma_\varphi^2 = \int_\varphi (\varphi - \varphi_0)^2 \, \mathrm{pdf}(\varphi) \mathrm{d}\varphi. \tag{2.45}$$

Based on 2.44 and 2.45, Figure 2.10 shows the phase standard deviation as a function of coherence for a different number of looks. As it can be observed, higher coherence values are associated with a lower standard deviation and vice-versa. In addition, it is shown that multilooking improves the phase accuracy, but it entails the risk of losing too much spatial resolution.

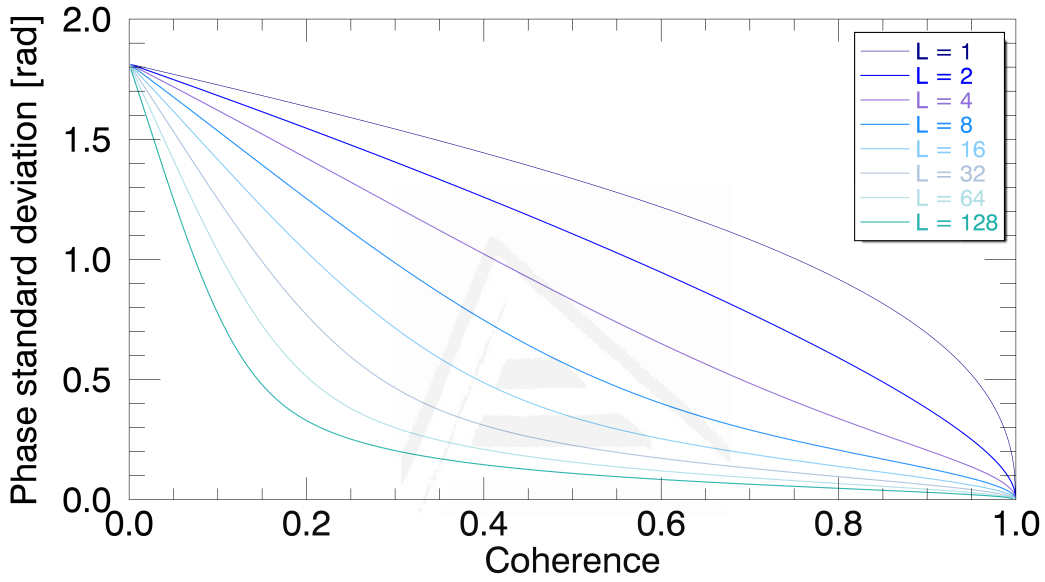

Figure 2.10: Phase standard deviation as a function of coherence and a number of looks.

Figure 2.11(a) shows an example of coherence map of the Etna area. Coherence has been estimated using a 5×5 multilook. It can be clearly seen that areas with a good phase have high coherence values, whereas noisy areas exhibit coherences which are almost 0.

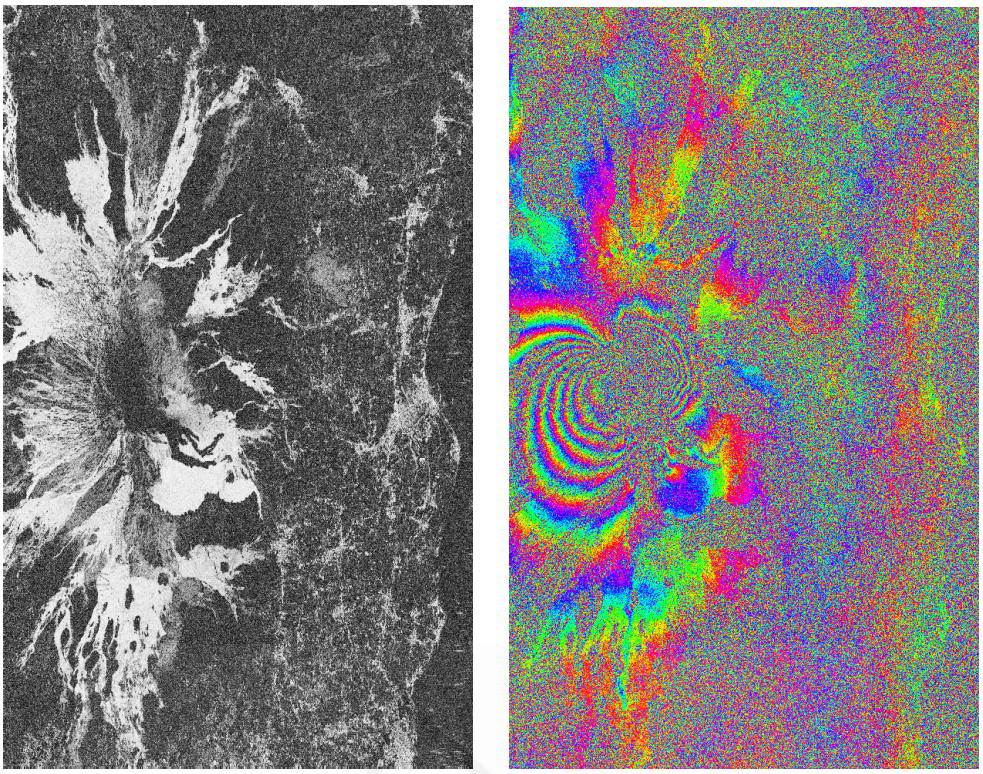

(a) Coherence map of the area of the Mount Etna estimated using a 5×5 multilook.

(b) Differential phase.

Figure 2.11: Interferometric coherence as an indicator of the phase quality.

The total coherence follows a *multiplicative model* of decorrelation factors [56], and it can be decomposed as a set of different contributions:

$$\gamma = \gamma_{coreg} \cdot \gamma_{geom} \cdot \gamma_{Doppler} \cdot \gamma_{vol} \cdot \gamma_{temp} \cdot \gamma_{thermal}, \tag{2.46}$$

where

- γ_{coreg} (Miss-registration decorrelation) is the decorrelation induced by miss-registration errors during the coregistration step.

- γ_{geom} (Geometrical decorrelation) is an important decorrelation factor caused by the different incidence angles of each SAR acquisition used to generate an interferogram. The different incidence angles introduce a frequency shift in the range dimension between the two images spectra, i.e., the ground reflectivity spectrum of the first image is shifted in the second image. As a result, both images have a common band, which is useful from the interferometric point of view, but also a non-common band which introduces decorrelation. This specific noise contribution is addressed with the proposed range filter method which will be detailed in Chapter 3.

- $\gamma_{Doppler}$ (Doppler decorrelation) is a noise source caused by Doppler frequency variations between the images. It is similar to the previous geometrical decorrelation but in azimuth dimension. It can be reduced by an appropriate filtering process.

- γ_{vol} (Volume decorrelation) is also a consequence of using two different images with different look angles. A coherence degradation appears since there is an uncertainty in the phase due to the presence of scatterers at different heights inside the resolution cell. It cannot be avoided but is useful for some applications, like vegetation height retrieval.

- γ_{temp} (Temporal decorrelation) is due to changes in the physical and geometrical properties of the imaged area between each survey. The clearest example of this source of noise is represented by changes in vegetated or forest areas, where the vegetation water content or the soil moisture change. It cannot be avoided. Temporal decorrelation is a major limitation of SAR interferometry and can be clearly identified in the example of Figure 2.11 throughout the phase image.

- $\gamma_{thermal}$ (Thermal noise) is a decorrelation factor induced by the thermal noise in all electronic systems, including SAR. It may be significant only in areas with a very low backscattering. Its expression is a measure of the signal-to-noise ratio (SNR) of the system,

$$\gamma_{thermal} = \frac{SNR}{SNR + 1}. \tag{2.47}$$

As a summary, the interferometric processing chain is illustrated with the flow diagram of Figure 2.12.

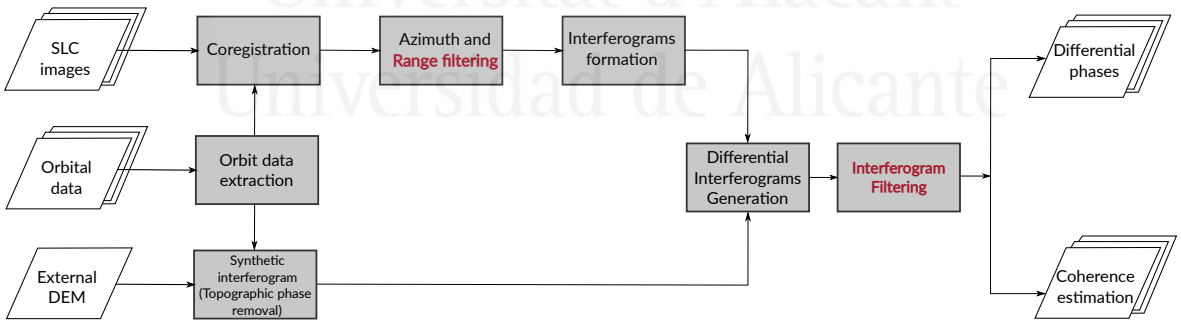

Figure 2.12: Flow diagram of the interferometric processing chain. Blocks highlighted in red color represent the steps in which a processing contribution has been done.

2.4 SAR Polarimetry

Polarimetry analyses how the polarization of an electromagnetic wave is modified when it interacts with an object or the media. When the signal interacts with a particular target, a part of its energy is absorbed and the rest is re-radiated as a new signal with new properties. As a consequence, polarimetry addresses the question of how these changes between the incident and the received wave are suitable for characterizing the target and its features.

Historically, SAR systems transmitted electromagnetic signals which were linearly polarized in a single direction, which could be horizontal (H) or vertical (V), and they received the backscattered signal either in the same or in the opposite polarization. This combination of transmitted-received polarization is referred to as *polarimetric channel*, and, therefore, it can be *HH*, *VV*, *HV* or *VH*. As stated in Chapter 1, PolSAR systems gather different images as a result of multiple combinations of polarization states. Specifically, a *full or quad-polarimetric* SAR system acquires four images corresponding to every possible combination of transmitted and received polarization, i.e., *HH*, *VV*, *VH* and *VV*. If the system obtains just two combinations, it is called *dual-polarimetric*.

Electromagnetic radiations propagate in space in the form of two vectorial waves which are mutually linked, one wave corresponds to the electrical field $\vec{E}(\vec{r},t)$ and the other one corresponds to the magnetic field $\vec{H}(\vec{r},t)$. Both fields are described as a function of time t and position $\vec{r}$, and are related by the Maxwell Equations [57],

$$\begin{aligned} \operatorname{div}\vec{E} &= 0, \\ \operatorname{div}\vec{H} &= 0, \end{aligned} \tag{2.48}$$

$$\begin{aligned} \operatorname{rot} E &= -\frac{\partial \vec{H}}{\partial t}, \\ \operatorname{rot}\vec{H} &= \varepsilon_0\mu_0\frac{\partial \vec{E}}{\partial t}, \end{aligned} \tag{2.49}$$

where $\varepsilon_0 = 8.8544 \cdot 10^{-12} \cdot N^{-1} \cdot m^{-2} \cdot C^2$ is the vacuum permittivity and $\mu_0 = 1.2566 \cdot 10^{-6} \cdot m \cdot kg \cdot C^{-2}$ is the vacuum permeability, so that the electromagnetic waves propagate in vacuum at the speed of light c,

$$c = \frac{1}{\sqrt{\varepsilon_0 \cdot \mu_0}} \approx 3 \cdot 10^8 m/s. \tag{2.50}$$

Electromagnetic waves are transverse, that is, the vibration is normal to the direction of propagation. Thereby, in a planar electromagnetic wave which propagates in the x direction, both the electrical $\vec{E}$ and magnetic fields $\vec{H}$ are normal to that direction and, at the same time, each field is normal to each other, as represented in Figure 2.13. Taking this into account, the 3-D equations defined in 2.48 can be simplified by fixing the direction of propagation, say x, and therefore we can reduce the wave field equations to a 2-D space in dimensions y and z. The equations that describe the propagation of

the electric field in such dimensions are given by

$$\begin{aligned} E_y &= A_y \cos\left[\omega\left(t - \frac{x}{c}\right) + \varphi_y\right], \\ E_z &= A_z \cos\left[\omega\left(t - \frac{x}{c}\right) + \varphi_z\right], \end{aligned} \tag{2.51}$$

and

$$\vec{E}(x,t) = E_y\vec{u}_y + E_z\vec{u}_z, \tag{2.52}$$

where $\vec{u}_y$ and $\vec{u}_z$ are the unitary vectors in dimensions y and z, respectively. If we impose $\delta = \varphi_z - \varphi_y$, we arrive to the expression of the *polarization ellipse* which can be represented as in Figure 2.14,

$$\frac{E_y^2}{A_y^2} + \frac{E_z^2}{A_z^2} - 2\frac{E_yE_z}{A_yA_z}\cos\delta = \sin^2\delta. \tag{2.53}$$

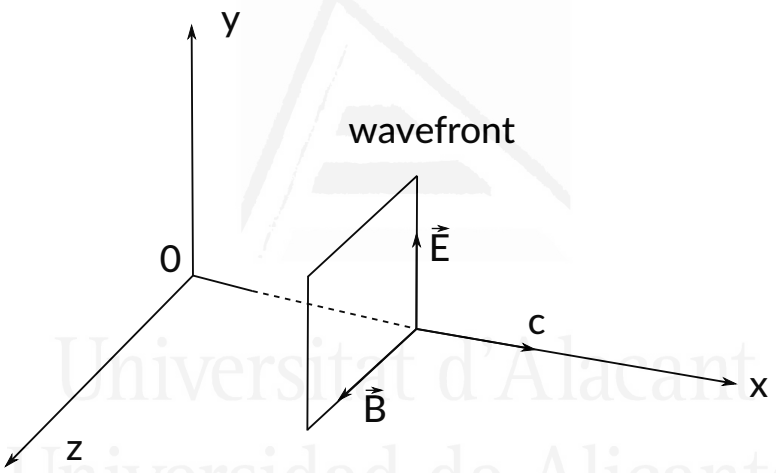

Figure 2.13: Propagation of an electromagnetic wave.

The polarization state is defined by [58]

- Orientation $\varphi \in \left[\frac{-\pi}{2}, \frac{\pi}{2}\right]$ is the inclination of the major axis of the ellipse.

- Ellipticity $\tau \in \left[\frac{-\pi}{4}, \frac{\pi}{4}\right]$ which represents the shape of the ellipse. Its sign defines the polarization direction (i.e., in which direction the ellipse is turning). By convention, if $\tau < 0$ the electric field vector turns clockwise and if $\tau > 0$ it turns counterclockwise.

- The amplitude of the polarization ellipse, defined as a function of the length of the major and minor axes of the ellipse,

$$A = \sqrt{E_{0y}^2 + E_{0z}}. \tag{2.54}$$

- The absolute phase of the ellipse φ which can be defined from its geometry as

$$\varphi = \frac{1}{2} \arg\left(\vec{p}^2 - \vec{q}^2 - 2j\,\vec{p}\vec{q}\right) + n\pi, \tag{2.55}$$

being $\vec{p}$ and $\vec{q}$ the conjugate diameters of the polarization ellipse [58].

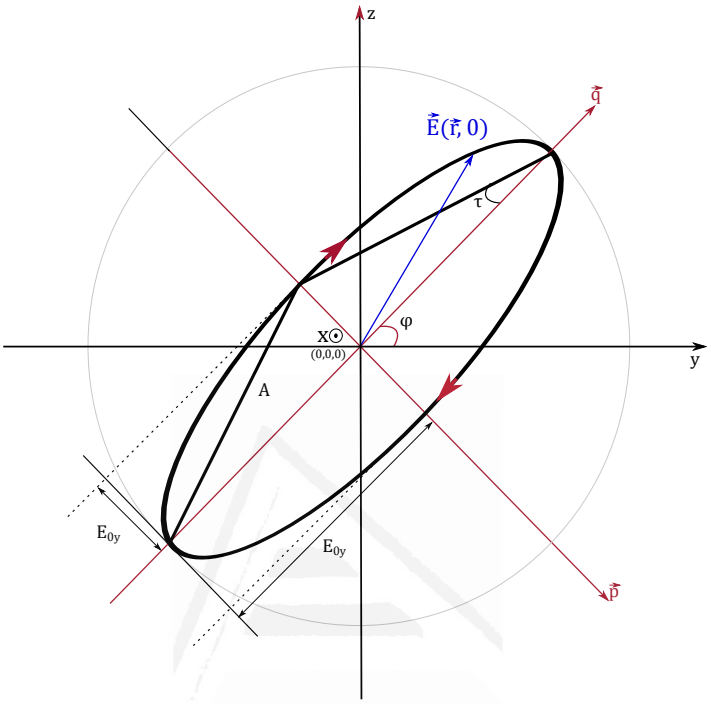

Figure 2.14: Polarization ellipse for an electromagnetic wave propagating on dimension x and at $(x, t) = (0, 0)$.

Another way to describe the electrical field is by means of the *Jones Vector*. The idea of this representation is to divide the space-time domain expression of $\vec{E}(x, t)$ as

$$\underline{\vec{E}} = \begin{bmatrix} E_y \\ E_z \end{bmatrix} = \begin{bmatrix} E_{0y}\, e^{j\varphi_y} \\ E_{0z}\, e^{j\varphi_z} \end{bmatrix}, \tag{2.56}$$

so that we have a representation of the electrical field in the orthogonal (or polarization) base $\{y, z\}$ which is independent from time. In terms of the polarization ellipse previously described, Equation 2.56 becomes

$$\underline{\vec{E}} = A\, e^{j\varphi} \begin{bmatrix} \cos\varphi & -\sin\varphi \\ \sin\varphi & \cos\varphi \end{bmatrix} \begin{bmatrix} \cos\tau \\ j\sin\tau \end{bmatrix}. \tag{2.57}$$

Once we have briefly reviewed general concepts regarding the propagation of electromagnetic waves, we can address the formulation of how radar targets are described from a polarimetric or scattering point of view. As previously mentioned, when the radar transmits signals to the ground surface, part of the transmitted energy is absorbed, part is backscattered and received, and most of the energy is scattered in other directions (different from backscattering). Formerly, this is described

with Equation 2.58

$$\vec{E}^S = \frac{e^{-jkr}}{r}\mathbf{S}\vec{E}^I, \tag{2.58}$$

where $\vec{E}^S$ and $\vec{E}^I$ represent the scattered and the incident electromagnetic fields respectively, k is the wavelength number $\left(\frac{2\pi}{\lambda}\right)$, r is the range distance to the target, and $\mathbf{S} \in \mathbf{Mat}_2(\mathbb{C})$ is the scattering matrix. This matrix describes the scattering behavior of a particular target, by relating the Jones vector of the incident field to the one of the scattered field. By using an orthogonal basis $\{\hat{h}, \hat{v}\}$ and a given coordinate system which is the same for transmitting and receiving, the scattering matrix can be expressed as

$$\begin{bmatrix} E_h^S \\ E_v^S \end{bmatrix} = \frac{e^{-jkr}}{r} \begin{bmatrix} S_{hh} & S_{hv} \\ S_{vh} & S_{vv} \end{bmatrix} \begin{bmatrix} E_h^I \\ E_v^I \end{bmatrix}. \tag{2.59}$$

Each element of $\mathbf{S}$ can be differentiated by its index, so that the first index refers to the scattered polarization and the second one refers to the incident polarization (for instance, the element S_{hv} corresponds to the complex backscattering coefficient obtained by transmitting with horizontal polarization and receiving with vertical polarization). Diagonal elements of the matrix are the *copolar* terms, since they represent the scattering coefficients obtained using the same polarization for transmitting and receiving. Off-diagonal elements are the *cross-polar* coefficients, since they come from different polarizations in transmission and reception. The total power backscattered by the target, called SPAN, can be obtained from $\mathbf{S}$ as

$$SPAN = |S_{hh}|^2 + |S_{hv}|^2 + |S_{vh}|^2 + |S_{vv}|^2. \tag{2.60}$$

The scattering matrix can be vectorized by projecting it onto a group a matrices yielding the so-called *target vector* $\mathbf{k} \in \mathbb{C}^4$,

$$\mathbf{k} = \frac{1}{2}Tr(\mathbf{S}\Psi) = \begin{bmatrix} k_1 \\ k_2 \\ k_3 \\ k_4 \end{bmatrix} \tag{2.61}$$

where $\mathrm{Tr}\{\cdot\}$ refers to the *trace* operator (the sum of the elements of the main diagonal), and Ψ defines a group of complex orthogonal matrices of size 2×2. The lexicographic basis consists in a straightforward ordering of the elements of $\mathbf{S}$ with

$$\{\Psi_L\} = \left\{ \begin{bmatrix} 2 & 0 \\ 0 & 0 \end{bmatrix}, \begin{bmatrix} 0 & 2 \\ 0 & 0 \end{bmatrix}, \begin{bmatrix} 0 & 0 \\ 2 & 0 \end{bmatrix}, \begin{bmatrix} 0 & 0 \\ 0 & 2 \end{bmatrix} \right\} \tag{2.62}$$

which yields the target vector $\mathbf{k}_{4L} \in \mathbb{C}^4$

$$\mathbf{k}_{4L} = [S_{hh}, S_{hv}, S_{vh}, S_{vv}]^T. \tag{2.63}$$

Another projection can be done by means of the *Pauli matrices*, named after the theoretical physicist Wolfgang Pauli and which arise in his treatment of spin in quantum mechanics. The set of Pauli matrices is

$$\{\Psi_P\} = \left\{ \sqrt{2}\begin{bmatrix} 1 & 0 \\ 0 & 1 \end{bmatrix}, \sqrt{2}\begin{bmatrix} 1 & 0 \\ 0 & -1 \end{bmatrix}, \sqrt{2}\begin{bmatrix} 0 & 1 \\ 1 & 0 \end{bmatrix}, \sqrt{2}\begin{bmatrix} 0 & -i \\ i & 0 \end{bmatrix} \right\} \tag{2.64}$$

which yields the target vector $\mathbf{k}_{4P} \in \mathbb{C}^4$

$$\mathbf{k}_{4P} = \frac{1}{\sqrt{2}}[S_{hh} + S_{vv}, S_{hh} - S_{vv}, S_{hv} + S_{vh}, i(S_{hv} - S_{vh})]^T. \tag{2.65}$$

The advantage of using this set of matrices is that the obtained target vector is more related to the physical scattering mechanism than by employing the lexicographic basis. In this regard, the first element of the Pauli basis, i.e., channel $HH + VV$ can be associated with surface scattering, where the contribution of channel HH is in phase with VV and both present similar amplitudes. The second element $HH - VV$ corresponds to a double-bound scattering mechanism, which, for instance, can be originated from human-made structures such as buildings. The last two elements of the Pauli channels represent a volume scattering [58], which is typically originated from vegetation canopy. This is represented in Figure 2.15.

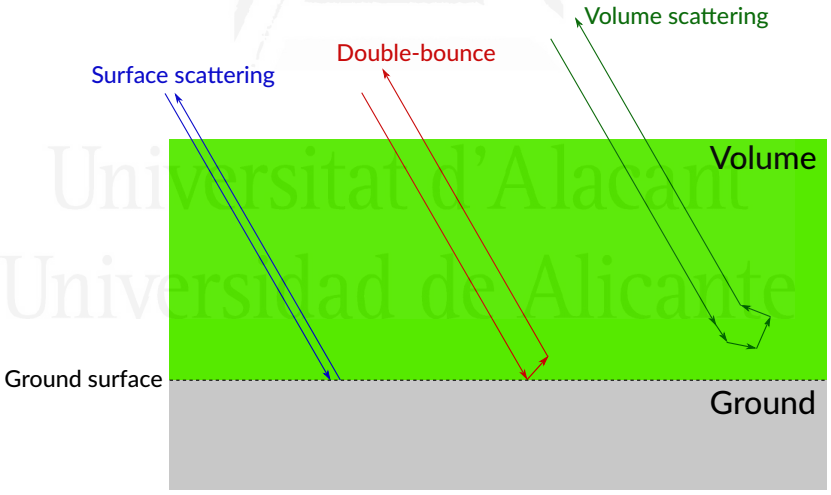

Figure 2.15: Different scattering mechanisms.

Both vectorial representations are related by means of a unitary matrix transformation $\mathbf{A}_4 \in \mathbf{U}_4(\mathbb{C})$, so that

$$\mathbf{k}_{4L} = \mathbf{A}_4\mathbf{k}_{4P} = \frac{1}{\sqrt{2}}\begin{bmatrix} 1 & 1 & 0 & 0 \\ 0 & 0 & 1 & -i \\ 0 & 0 & 1 & i \\ 1 & -1 & 0 & 0 \end{bmatrix}\mathbf{k}_{4P}. \tag{2.66}$$

Additionally, if the SAR system is *monostatic*, that is, if the transmitter and the receiver are collo-

cated, the reciprocity theorem implies that $\mathbf{S}$ is symmetric, i.e., $S_{hv} = S_{vh}$.

Thus, target vectors can be simplified as

$$\mathbf{k}_{3L} = [S_{hh}, \sqrt{2}S_{hv}, S_{vv}]^T, \tag{2.67}$$

$$\mathbf{k}_{3P} = \frac{1}{\sqrt{2}}[S_{hh} + S_{vv}, S_{hh} - S_{vv}, 2S_{hv}]^T. \tag{2.68}$$

Evidently, Equations 2.67 and 2.68 are not valid for *bistatic* systems where the transmitter and the receiver are separated. In that case, Equations 2.63 and 2.65 must be used.

Target vectors represent an extension of a 1-D (single) backscattering coefficient to the diversity of polarization states gathered by PolSAR systems, i.e., the 2×2 scattering matrix. An analysis of these multidimensional data can be carried out by means of second order polarimetric statistics. Considering the lexicographic base and a bistatic system, the covariance matrix $\mathbf{C}_4 \in \mathbf{Mat}_4(\mathbb{C})$ is defined as

$$\mathbf{C}_4 = E\{\mathbf{k}_{4L}\mathbf{k}_{4L}^H\} = \begin{bmatrix} E\{S_{hh}S_{hh}^*\} & E\{S_{hh}S_{hv}^*\} & E\{S_{hh}S_{vh}^*\} & E\{S_{hh}S_{vv}^*\} \\ E\{S_{hv}S_{hh}^*\} & E\{S_{hv}S_{hv}^*\} & E\{S_{hv}S_{vh}^*\} & E\{S_{hv}S_{vv}^*\} \\ E\{S_{vh}S_{hh}^*\} & E\{S_{vh}S_{hv}^*\} & E\{S_{vh}S_{vh}^*\} & E\{S_{vh}S_{vv}^*\} \\ E\{S_{vv}S_{hh}^*\} & E\{S_{vv}S_{hv}^*\} & E\{S_{vv}S_{vh}^*\} & E\{S_{vv}S_{vv}^*\} \end{bmatrix}. \tag{2.69}$$

Its equivalent for a monostatic system is given by $\mathbf{C}_3 \in \mathbf{Mat}_3(\mathbb{C})$ as

$$\mathbf{C}_3 = E\{\mathbf{k}_{3L}\mathbf{k}_{3L}^H\} = \begin{bmatrix} E\{S_{hh}S_{hh}^*\} & \sqrt{2}E\{S_{hh}S_{hv}^*\} & E\{S_{hh}S_{vv}^*\} \\ \sqrt{2}E\{S_{hv}S_{hh}^*\} & E\{S_{hv}S_{hv}^*\} & \sqrt{2}E\{S_{hv}S_{vv}^*\} \\ E\{S_{vv}S_{hh}^*\} & \sqrt{2}E\{S_{vv}S_{hv}^*\} & E\{S_{vv}S_{vv}^*\} \end{bmatrix}. \tag{2.70}$$

Considering the Pauli basis, we define the coherency matrix for the bistatic case, $\mathbf{T}_4 \in \mathbf{Mat}_4(\mathbb{C})$, and monostatic case $\mathbf{T}_3 \in \mathbf{Mat}_3(\mathbb{C})$

$$\mathbf{T}_4 = E\{\mathbf{k}_{4P}\mathbf{k}_{4P}^H\}, \tag{2.71}$$

$$\mathbf{T}_3 = E\{\mathbf{k}_{3P}\mathbf{k}_{3P}^H\}. \tag{2.72}$$

The covariance and the coherency matrices are related as follows,

$$\mathbf{T}_4 = \frac{1}{2}\begin{bmatrix} 1 & 0 & 0 & 1 \\ 1 & 0 & 0 & -1 \\ 0 & 1 & 1 & 0 \\ 0 & i & -i & 0 \end{bmatrix} \mathbf{C}_4 \begin{bmatrix} 1 & 1 & 0 & 0 \\ 0 & 0 & 1 & i \\ 0 & 0 & 1 & -i \\ 1 & -1 & 0 & 0 \end{bmatrix}, \tag{2.73}$$

$$\mathbf{T}_3 = \frac{1}{2}\begin{bmatrix} 1 & 0 & 1 \\ 1 & 0 & -1 \\ 0 & \sqrt{2} & 0 \end{bmatrix} \mathbf{C}_3 \begin{bmatrix} 1 & 1 & 0 \\ 0 & 0 & \sqrt{2} \\ 0 & -1 & 0 \end{bmatrix}. \tag{2.74}$$

Finally, a simple way of visualizing the polarimetric diversity and, simultaneously, recognizing by naked eye the scattering mechanism that dominates in a particular area, is to generate a false color-coded RGB image. By assigning each element of the target vector to a primary color component, we can check that the response of each channel varies in distinct types of zones. Using the Pauli basis, we can directly assign each element of the target vector in Equation 2.68 to a color as follows,

$$\begin{aligned} S_{HH} - S_{VV} &= \text{Red}, \\ S_{2HV} &= \text{Green}, \\ S_{HH} + S_{VV} &= \text{Blue}\,. \end{aligned} \tag{2.75}$$

This is illustrated with Figure 2.16. It can be observed that in urban areas there is a clear predominance of channel $HH + VV$ (coded in red color), due to the human-made structures which contribute to a double-bounce scattering mechanism. In vegetated zones, there is a major contribution from channel $2HV$ associated with a volume scattering, and blue areas correspond to bare surfaces where the lava flow has burned the vegetation that was present. Thus, a surface scattering associated with channel $HH - VV$ dominates.

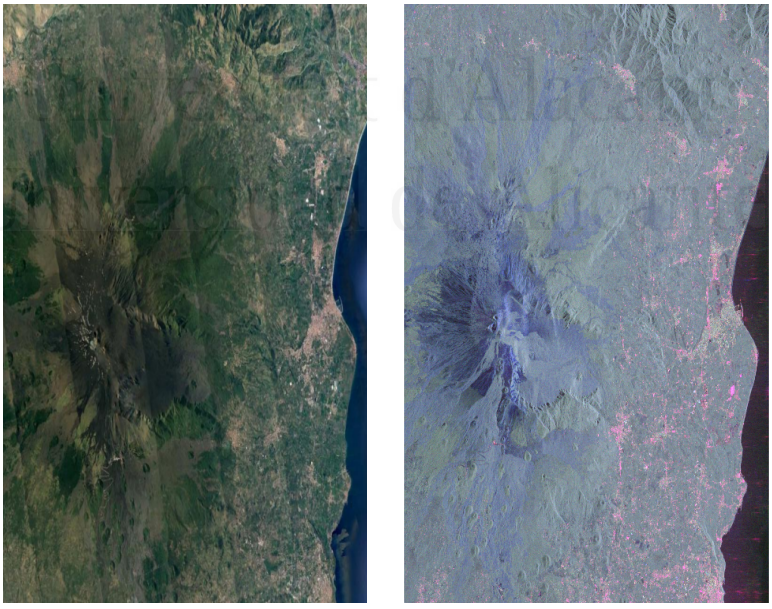

(a) Google-Earth™ optical image.

(b) Pauli RGB color-coded image with $R = S_{HH} - S_{VV}$, $G = 2S_{HV}$, $B = S_{HH+VV}$.

Figure 2.16: Polarimetric representation of the Mount Etna area using the Pauli basis.

2.5 Polarimetric (Differential) SAR Interferometry

Polarimetric SAR Interferometry aims to combine the sensitivity of InSAR to topography, i.e. to the vertical coordinate in the scene, with the polarized multichannel data which are sensitive to the target physical features, i.e., dielectric constant, morphology, etc.

The first formulation of PolInSAR was presented in [27] by introducing a multidimensional complex space which contains all polarimetric and interferometric information. Thus, PolInSAR requires the definition of a general framework in which we are able to generate interferograms (which come from the combination of complex scattering coefficients of two images, as in the single-polarization case) but in which we also take into account all polarization diversity. As a consequence, we can analyze the relation between 'interferometric measurements' (such as the phase or the coherence), with 'polarimetric measurements' (a specific polarization).

Let $\mathbf{k}_1$ and $\mathbf{k}_2$ be the two target vectors containing the polarimetric scattering associated with two generic images S_1 and S_2. The coherence matrix (or covariance matrix if the lexicographic base is used) $\mathbf{T}_6 \in \mathbf{Mat}_6(\mathbb{C})$ can be defined as follows,

$$\mathbf{T}_6 = E\left\{ \begin{bmatrix} \mathbf{k}_1 \\ \mathbf{k}_2 \end{bmatrix} \begin{bmatrix} \mathbf{k}_1{}^{*T} & \mathbf{k}_2{}^{*T} \end{bmatrix} \right\}, \tag{2.76}$$

where ^{*T} refers to conjugate transpose. The matrix can be reformulated as

$$\mathbf{T}_6 = \begin{bmatrix} \mathbf{T}_{11} & \mathbf{\Omega}_{12} \\ \mathbf{\Omega}_{12}^{*\mathrm{T}} & \mathbf{T}_{22} \end{bmatrix}, \tag{2.77}$$

where matrices $\mathbf{T}_{ii} \in \mathbf{Mat}_3(\mathbb{C})$ $(i = 1, 2)$ and matrix $\mathbf{\Omega}_{12} \in \mathbf{Mat}_3(\mathbb{C})$ are defined as

$$\begin{aligned} \mathbf{T}_{11} &= E\{\mathbf{k}_1 \mathbf{k}_1^{*\mathrm{T}}\}, \\ \mathbf{T}_{22} &= E\{\mathbf{k}_2 \mathbf{k}_2^{*\mathrm{T}}\}, \\ \mathbf{\Omega}_{12} &= E\{\mathbf{k}_1 \mathbf{k}_2^{*\mathrm{T}}\}. \end{aligned} \tag{2.78}$$

On the one hand, matrices $\mathbf{T}_{11}$ and $\mathbf{T}_{22}$ are the polarimetric coherency matrices which contain all polarimetric information of each image S_1 and S_2 separately. On the other hand, $\mathbf{\Omega}_{12}$ is a new 3×3 complex matrix which contains, in addition to polarimetric relations between both images, the interferometric information between the images for each polarization. The next step consists in making use of these 3 matrices to create complex interferograms, i.e., how we can use the matrices to yield two complex scalars which can be combined into an interferogram and extract its phase. This is done by projecting $\mathbf{k}_1$ and $\mathbf{k}_2$ onto unitary complex column vectors $\boldsymbol{\omega}_1, \boldsymbol{\omega}_2 \in \mathbb{C}^3$, hereafter denoted as *projection vectors*. By means of the projection vectors, it is possible to obtain complex backscattering

scalars $\mu_1, \mu_2 \in \mathbb{C}$ as

$$\begin{aligned} \mu_1 &= \boldsymbol{\omega}_1^{*T}\mathbf{k}_1, \\ \mu_2 &= \boldsymbol{\omega}_2^{*T}\mathbf{k}_2. \end{aligned} \tag{2.79}$$

It is straightforward that an interferogram can be generated as the standard complex product of μ_1 and μ_2,

$$\mu_1\mu_2^{*T} = (\boldsymbol{\omega}_1^{*T}\mathbf{k}_1)(\boldsymbol{\omega}_2^{*T}\mathbf{k}_2)^{*T} = \boldsymbol{\omega}_1^{*T}\boldsymbol{\Omega}_{12}\boldsymbol{\omega}_2. \tag{2.80}$$

and the interferometric phase can be directly extracted as

$$\Delta\Phi = \arg(\mu_1\mu_2^{*T}) = \arg(\boldsymbol{\omega}_1^{*T}\boldsymbol{\Omega}_{12}\boldsymbol{\omega}_2). \tag{2.81}$$

The expression of the generalized coherence is therefore given by

$$\gamma = \frac{\boldsymbol{\omega}_1^{*T}\boldsymbol{\Omega}_{12}\boldsymbol{\omega}_2}{\sqrt{\boldsymbol{\omega}_1^{*T}\mathbf{T}_{11}\boldsymbol{\omega}_1}\sqrt{\boldsymbol{\omega}_2^{*T}\mathbf{T}_{22}\boldsymbol{\omega}_2}}, \tag{2.82}$$

where its magnitude $|\gamma| \in [0, 1]$ can be used as a phase quality indicator as in the single-polarization case (Equation 2.43).

This leads us to analyze the important role that each projection vector has concerning the formation of interferograms. The first point is that the interferometric phase in Equation 2.81 should not be obtained from an arbitrary choice of $\boldsymbol{\omega}_1$ and $\boldsymbol{\omega}_2$, which could result in random phases [58]. Consequently, a first restriction has to me made to verify that

$$\arg\left(\boldsymbol{\omega}_1^{*T}\,\boldsymbol{\omega}_2\right) = 0, \tag{2.83}$$

which is directly satisfied if $\boldsymbol{\omega}_1 = \boldsymbol{\omega}_2$. This constraint is known as *Equal Scattering Mechanism* (ESM), and must be fulfilled since the selection of different scattering mechanisms (defined by each projection vector) between both images could lead to a change in the phase center. Moreover, using this approach we ensure that the coherence is only related to the interferometric contribution, which is mandatory from the interferometric point of view.

The projection vectors allow us to explore the whole polarimetric space and, hence, to generate interferograms resulting from the linear combinations of all possible polarimetric channels by the definition of the projection vectors. Table 2.2 shows some examples of scattering mechanisms (defined by the value of the projection vector) and their corresponding polarization channel [58] (index $_i$ refers to the $i-th$ element of the vector).

It is therefore intuitive to think that an 'optimum' combination of polarimetric channels can be computed by an appropriate definition of the projection vectors $\boldsymbol{\omega}_1$ and $\boldsymbol{\omega}_2$. This is the goal of PolDInSAR methods that will be detailed in Chapter 3.

Polarization	$\omega_{\{1\}}$	$\omega_{\{2\}}$	$\omega_{\{3\}}$
HH	$\sqrt{2}$	$\sqrt{2}$	0
VV	$\sqrt{2}$	$-\sqrt{2}$	0
HV	0	0	1
$HH + VV$	1	0	1
$2HV$	0	0	1

Table 2.2: Some scattering mechanisms and the associated polarimetric channel.

2.6 Image Classification

Image classification is the task of processing an input set of images with the goal of assigning to each spatial unit (either a pixel or an ensemble of pixels grouped into an object) a class. Each class belongs to a fixed set of categories (or labels) which are representative of a particular domain, such as land-cover or crop types. From our point of view, the identification of visual concepts within an image is a very trivial task due to our experience and knowledge, but it is a challenging task from a computing point of view where the information is stored as digits, as illustrated in Figure 2.17.

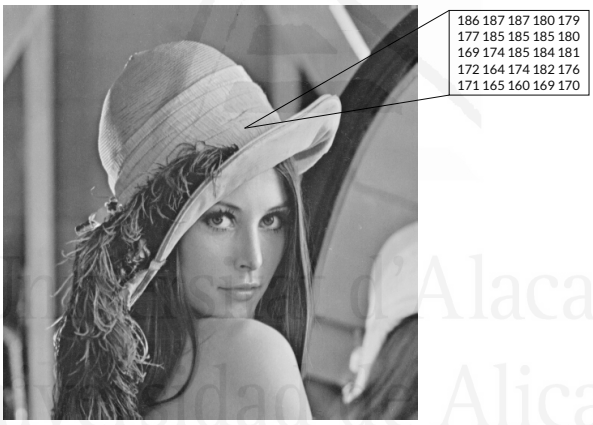

Figure 2.17: What we see and what a computer 'sees'.

However, if done properly, the benefits from automating this kind of process are evident. Automatically obtaining large thematic maps from imagery, automatic facial recognition and object identification without manual intervention are just some examples of the potential of image classification.

The automatic analysis of the input images is approached by the so-called *machine learning* algorithms, which look for patterns in data. Particularly, machine learning can be defined as the different methods which automatically recognize patterns in data, and use these uncovered patterns to predict future observations and eventually make decisions [59]. The core of a machine learning approach relies on probability, so that the main idea is that a probabilistic model enables us to describe the complex system or phenomena underlying the data.

As previously stated in Chapter 1, machine learning is split into two areas: supervised and unsupervised learning. In this PhD, we will focus on predictive or supervised learning, the goal of which

is to form a mapping from inputs X to outputs Y based on some input-output pairs. That is, supervised learning requires beforehand knowledge of the output class given some inputs. This group of known samples is called the *training set*, whereas the unknown samples we want to classify (i.e., give an output) define the *testing set*. Formerly, given a set of input-output pairs, we define the training set D as

$$D = \{(x_i, y_i)\}_{i=1}^{N} \tag{2.84}$$

where $x_i \in X$ are the input data, $y_i \in Y$ is the associated label, i.e., $Y = [Class_1, Class_2, ...Class_{NC}]$ (being NC the total number of classes), and N is the number of training samples. It is important to point out that we assume that each output class is exclusive (unique) and the *multi-label* classification case is not considered. The problem now consists in assigning an output class to the testing set D',

$$D' = \{(x_i)\}_{i=1}^{N'}, \tag{2.85}$$

by means of a probabilistic model of prediction. In other words, given an input, the machine learning algorithm will assign the 'most probable' class as output by drawing inferences from the training set. By denoting as $\mathbf{x}$ the input samples from the training set D, a model can be defined according to the probability distribution

$$p(y = y_i|\mathbf{x}, D), \tag{2.86}$$

which provides the probability of obtaining class y_i given inputs $\mathbf{x}$. According to Equation 2.86, for each class in Y we train a separate model in order to yield the most probable class label $\hat{y}$ by maximizing the likelihood

$$\hat{y} = \arg\max_{y_i=1}^{NC} \{p(y = y_i|\mathbf{x}, D)\}. \tag{2.87}$$

One way to exemplify this classification approach is by means of a simple linear model shown as follows. Let $D = \{(x_1, y_1), (x_2, y_2), (x_3, y_3)\}$ be a training set where $X = \{x_1, x_2, x_3\}$ is the input (observed) group of data and $Y = \{y_1, y_2, y_3\}$ define the known outputs. The example can be illustrated as in Figure 2.18. If we set the model to a straight line defined by equation $y = mx + b$, the goal of the algorithm is to learn model parameters m and b given the known data in D. Consequently, any new sample x_m can directly have an output according to the model. In the context of classification, this would be similar to the assignment of a class given a new or unknown observation.

In the previous example, we could easily think that the straight line model was correct simply by observing the data. However, when using real measurements, the derivation of a model that fits the known data while accurately classifying unknown inputs is rather a non-trivial task. This is therefore the real difficulty of a machine learning algorithm.

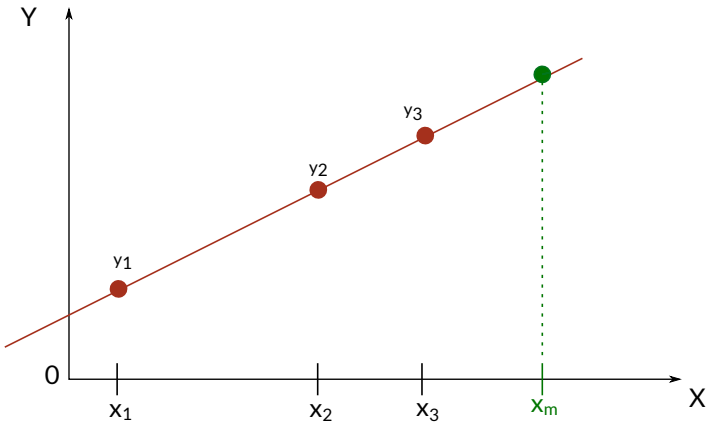

Figure 2.18: Illustration of a supervised classification with a linear model.

There exist a large variety of approaches to designing algorithms that can 'learn' and carry out the task of performing a classification given an input set of data. In this work, we will just focus on a *decision tree-based* [60] [61] classifier known as *Random Forests (RF)* [62] [63]. The idea of decision trees is to repeatedly divide input data (i.e., the training set) so that a model of decisions between inputs and outputs is built. Decisions are binary, i.e., each node of the tree is split into two new subnodes according to a condition at that node. As a consequence, when a new sample is to be classified, the tree is progressively transversed in such a way that the new input is redirected to subnodes. When the sample reaches the end of the tree, a class is automatically given. This is illustrated with the example of Figure 2.19, where we have 4 different classes (represented by 4 different colors), and a set of observations $\{X_1, X_2\}$ which define the input dataset. A decision tree can be automatically generated with the labels of the dataset (the colors), as represented in Figure 2.19(b). In this case, we impose that, if the condition of a node is verified, the input is redirected to the left branch of the tree, otherwise it is redirected to the right side. Consequently, a model of decisions which map all inputs of $\{X_1, X_2\}$ to an output class has been created. A critical aspect in decision trees is how each node is split, i.e., how we can find each threshold in Figure 2.19(b), since the goal is to create subnodes (branches and leaves) based on an optimum criterion so that we can obtain an accurate classification. This process is called *tree growing*. Accordingly, the algorithm has to seek the best 'division criterion' given by pair input-class to create new nodes in a recursive fashion (split after split). For classification purposes, the *Gini* index G_i is usually the cost function used to evaluate the quality of a split,

$$G_i = 1 - \sum_{i=1}^{NC} p_i^2 \tag{2.88}$$

where NC is the number of classes and p_i is the probability of class i.

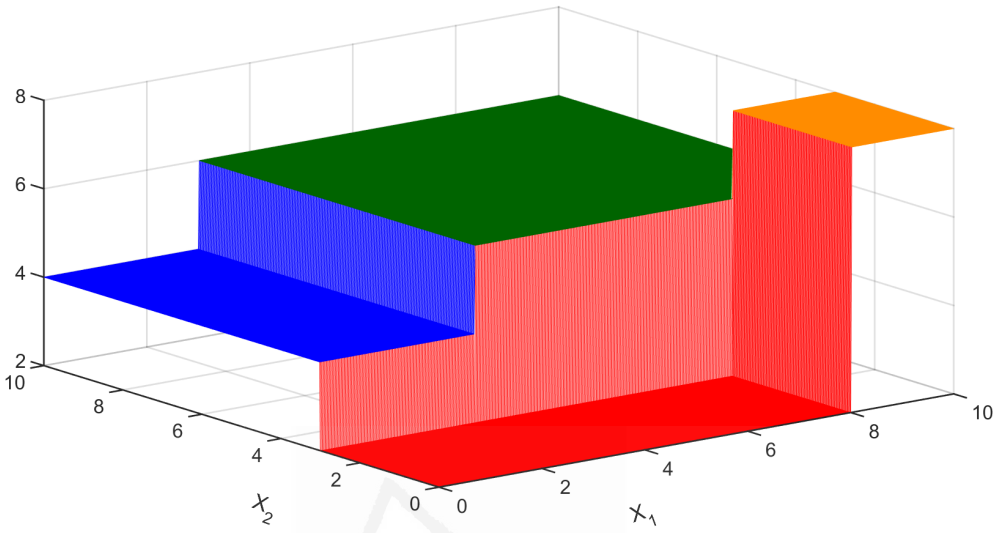

(a) Representation of input data.

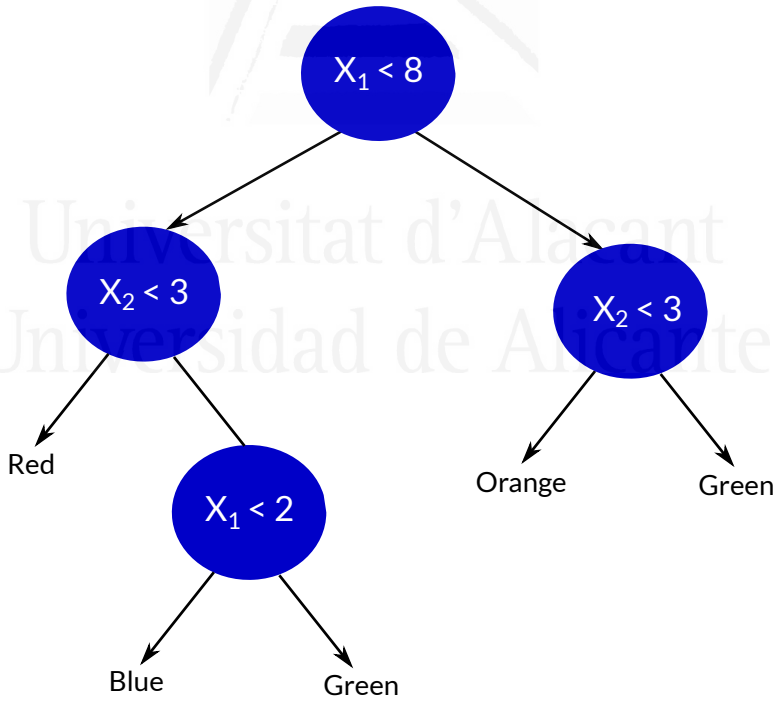

(b) Decision tree.

Figure 2.19: Construction of a decision tree based on two inputs $\{X_1, X_2\}$.

A major drawback of decision trees is the high risk of *overfitting* or *overlearning*. Overfitting appears when the model described by the decision tree is very well adapted to the training data, and, even though it seems positive, it can negatively impact on the performance of the model on new inputs. To deal with overfitting, *Ensemble Methods* are used, being Random Forests an example of such methods. The Random Forests algorithm is an improved extension of a single decision tree. It is actually a collection of n decision trees, where each tree is constructed by taking a certain number of random samples (with replacement) from the training dataset in a process called *Bagging* (or *Bootstrap Aggregating*). The number of trees used in the training step influences the final accuracy, so that the larger n is, the more accurate the prediction will be, but the computational cost increases greatly. By introducing randomness in the generation of trees, each one of them will be different and may provide a different output. A rule has therefore to be imposed to decide which one is the final class predicted by the algorithm. Usually, the final prediction of the ensemble is given as the mode of the predicted classes. A scheme of the classifier is shown in Figure 2.20. However, it is in the multitude of constructed decision trees where the robustness of Random Forests lies. Hopefully, by increasing the diversity of decision trees during the training step, the resulting model will be better adapted to new data and overfitting will be limited, which results in an improved predictive accuracy and, hence, a better overall classification of data.

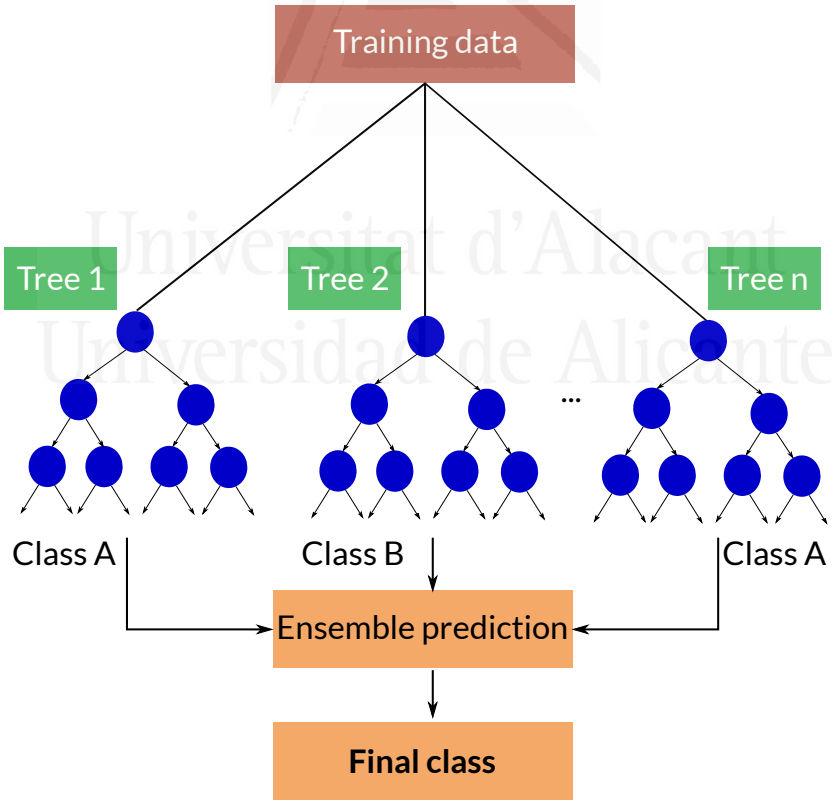

Figure 2.20: Simplified scheme of Random Forests Ensemble method.

Before applying the algorithm to a set of images, an example with 1-D data is provided to check its performance. Consider the synthetic dataset represented in Figure 2.21(a), which consists in two

different classes (red and blue colors) and two features X and Y. The total number of samples is 500. Taking into account the concepts previously explained, the samples have been divided into a training and a testing set. Specifically, 30% of samples have been used for training and the rest have been used for testing. Once the algorithm has been trained (i.e., an ensemble of decision trees has been grown), the unlabeled data from which the testing set is composed are classified according to the Random Forest method previously described.

Classification results are depicted in Figure 2.21(b). As it can be observed, the majority of testing samples have been correctly classified. In fact, a global accuracy of 80% is obtained. Note that a more detailed analysis of the accuracy of a given classification will be presented in Chapter 4. Moreover, from the results we can easily make a segmentation of the features space in order to check 'where a new sample will fall into'. That is, given a new input with features $\{x_i, y_i\}$, we can easily predict the output. For instance, a new sample with $\{x = -1, y = -2\}$ (red area) will be classified as Class 1 , whereas the classifier predicts that a sample with $\{x = -3, y = -1\}$ will belong to Class 2.

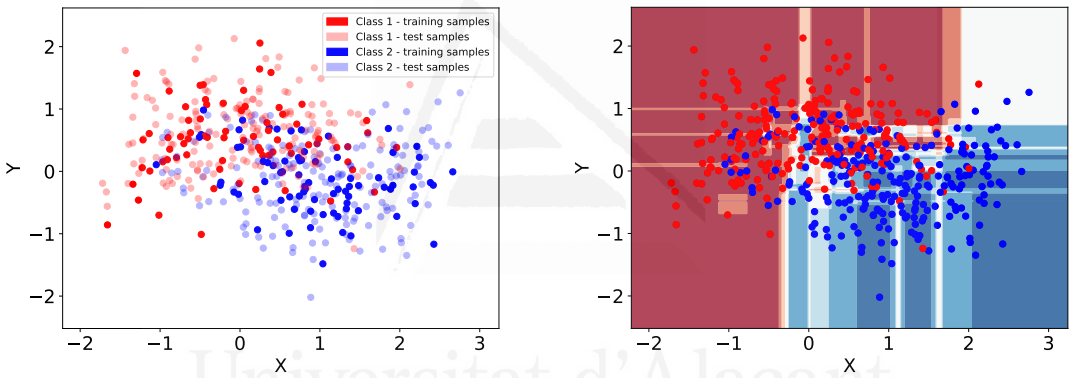

(a) Input data divided into training and testing samples.

(b) Classification results.

Figure 2.21: Example of classification with Random Forests with a 1-D synthetic dataset composed of two classes and two features.

The same methodology can be followed with images. An image can be regarded as an ensemble of individual samples which are spatially distributed. A group of pixels will be use to train the Random Forests classifier and the rest of pixels can be used as testing samples. When using remote sensed images to classify, the group of pixels that define the training set is usually called as *ground truth*, which refers to data collected on location by performing surface observation or measurements manually. An example of simulated classification is shown in the following. For simplicity, only 3 classes have been included and are represented in Figure 2.22. This image also represents the ground truth. A set of 6 observations (which could have been gathered by any particular sensor) is represented in Figure 2.23. Image values are randomly increased and decreased progressively, and a certain level of noise is uniformly added to each image.

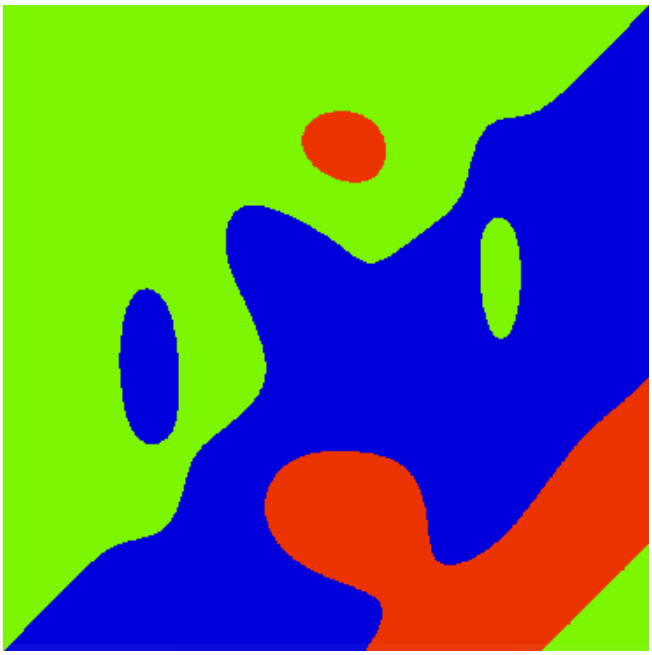

Figure 2.22: Simulated ground truth with three different classes.

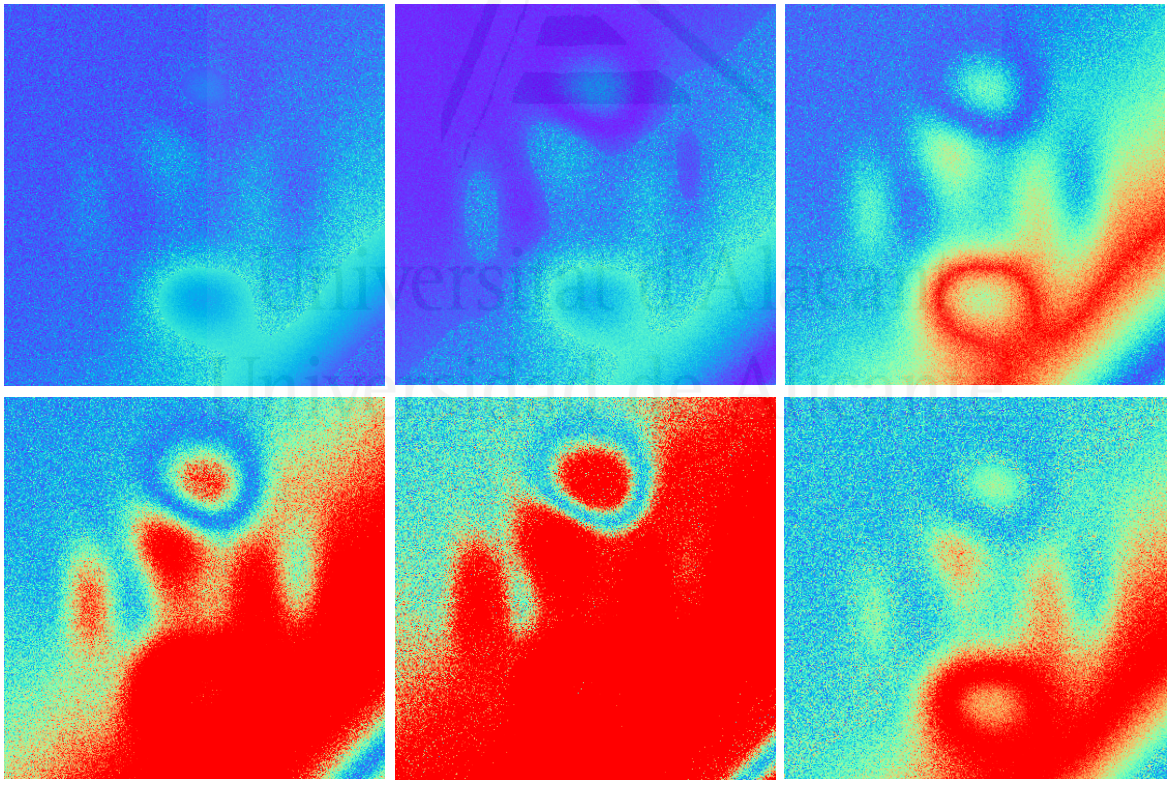

Figure 2.23: Classification example using Random Forests with a set of six synthetic images.

Concerning the classifier, different percentages of training samples have been used in order to verify the theoretical aspects of overfitting previously explained. Specifically, the algorithm is trained using 1%, 20% and 90% of samples. Results are shown in Figure 2.24.

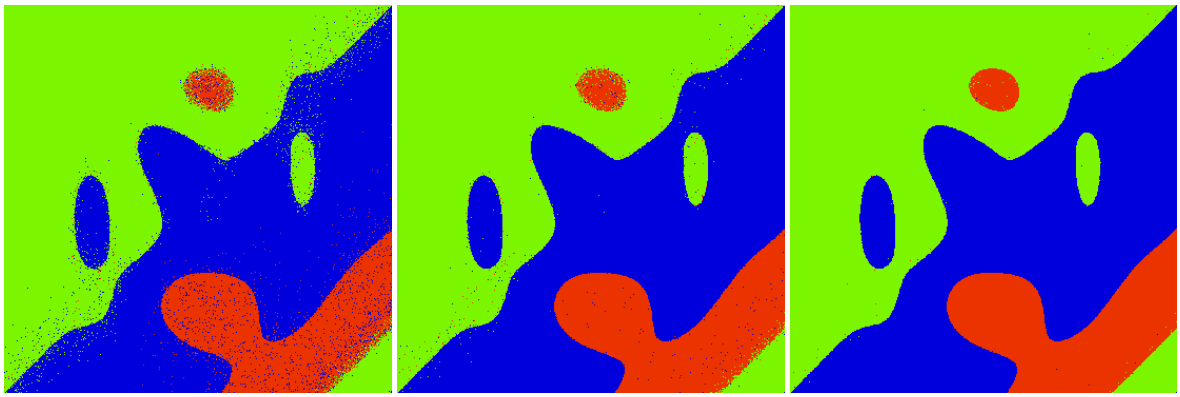

(a) Classified image using 1% of samples for training.

(b) Classified image using 20% of samples for training.

(c) Classified image using 90% of samples for training.

Figure 2.24: Classification results on synthetic images using different percentages of training samples.

It is clearly appreciated that with a larger number of training samples, the number of missclassifications reduces. In fact, by employing 90% the number of errors is almost 0 (as shown in Figure 2.24(c), the classified image is almost equal to the ground truth), showing that the algorithm is perfectly adapted to this specific set of data. In other words, the training data are very well modeled. The drawback is if new samples are to be classified, the algorithm could perform poorly, that is, the model is less portable because it was overfitted to the training set. Overfitting must therefore be avoided. To this end, the simplest strategy is to split the known data into a train and a test set (as shown in the previous example), but where the number of testing samples should be larger than the number of training samples. Another interesting strategy is to include an additional validation set, which is used to choose between different models (for instance, to select the number of decision trees or estimators to be used in the forest, etc).

3

Processing Contributions

Chapter 2 presented the theoretical aspects involved in both SAR interferometry and polarimetry, as well as their main applications. It also introduced the concept of decorrelation, which constitutes a major limitation for performing any interferometric process. This chapter is devoted to presenting processing contributions developed throughout the PhD. The main objective of each individual technique is to *improve the quality of the phase data* at different stages of the interferometric processing, by means of the suppression of disturbing effects such as decorrelation and noise which are present in every interferogram.

Chapter 3 is divided into three parts. The first one is related to range filtering. Range filtering, also known as spectral shift filtering (in range dimension), is a commonly-used preprocessing step used to remove the spectral misalignment between two images used to create an interferogram. It can be regarded as a preprocessing step in the sense that it is performed prior to interferogram formation. However, it requires that both images have been properly coregistered. Different range filtering methods are available in literature, each of them presenting different pros and cons. A deep revision of all methods will be presented in Section 3.1.1, and a refined technique developed during the PhD is proposed in Section 3.1.2.4. Results are shown in Section 3.1.3.

The second contribution consists in an advanced filter for the final interferometric phase. Unlike the previous case, this filter uses an already-formed noisy interferogram as input. At this stage, the goal is to reduce the remaining decorrelation effects that degrade the quality of the phase, and which make it unsuitable for its further processing and exploitation. A wide variety of interferogram filters have been proposed over the past years, being the well-known *Goldstein filter* [64] [65] the most

commonly-used. It is a frequency-domain filter which is based on smoothing the 2-D Fourier Transform of the interferogram. The filtering strength is controlled by a real parameter, defined between zero and one, which is usually set by visual inspection of the original phase. This constitutes its main drawback, since the filter may not be properly adapted to the local noise level of the interferogram. In this regard, a noise-adaptive version of the filter was proposed in [66]. In this *Modified Goldstein filter*, the filtering strength is adapted according to the interferometric coherence, which constitutes a direct indicator of the phase quality as highlighted in Chapter 2. This allows to strongly filter low-coherent areas while high-quality areas are barely filtered, so that the spatial resolution of the original interferogram is better preserved. A revision of the Goldstein filter and different adaptive versions is carried out in Section 3.2.1. Also, the influence of all parameters and operators involved in the filtering process will be analyzed in detail. The proposed technique developed in this thesis is explained in Section 3.2.2. The filter relies on an iterative and coherence-adaptive Goldstein approach, but it applies an innovative methodology which tries to remove the noise at all scales without over-smoothing and blurring phase details, especially useful interferometric fringe patterns. Results with both synthetic and real datasets are shown in Section 3.2.3.

The third and last processing contribution is related to PolDInSAR with single interferometric pairs (i.e., single-baseline interferometry). Although the goal is also to improve the quality of the phase, the improvement is achieved by means of algorithmic and mathematical processes which explore all the available polarimetric space, rather than with pure signal processing techniques. A revision of different polarimetric optimization algorithms is done in Section 3.3.2. Note that the optimization must be understood as a maximization or minimization of a cost function related to a phase quality criterion. Even though the coherence is the most common phase quality estimator, alternative criteria will also be considered during the optimization process. Specifically, the phase coherence (local correlation derived from phase values) and the phase standard deviation constitute two different quality criteria which can be used as cost functions. It is important to point out that all of these quality estimators require a spatial average around a pixel neighborhood, i.e., a multilook of a certain size has to be applied to the data in order to obtain values to optimize. Accordingly, after some preliminary results are shown in Section 3.3.3, an evaluation of the multilook size in the optimization is carried out in Section 3.3.4. Finally, a different formulation concerning the optimization is explained in Section 3.3.5. In this case, a variation of the conventional formulation is proposed to show the real phase quality improvement which can be obtained with the polarimetric optimization.

3.1 Range Spectral Filtering

3.1.1 Generalities

Range filtering is a common processing step in SAR interferometry, which is usually carried out right after coregistration. Specifically, the filtering addresses the loss of coherence induced by the difference between the incidence angles of master and slave images used to form an interferogram. In other words, it tries to compensate the decorrelation due to the perpendicular baseline (see Figure 2.7). Larger baselines result in higher decorrelation levels, to the extent that there is a limit from which no interferometric information can be exploited. This limit is the so-called *critical baseline* [39], which means that both images are fully uncorrelated. Its expression is derived from the system parameters as

$$B_{\perp,crit} = \frac{WR\lambda \tan(\theta - \alpha)}{c}, \tag{3.1}$$

where W is the range bandwidth, λ is the sensor wavelength, θ is the incidence angle, α is the local terrain slope and R is the ground range which can be approximated by $R = h/\cos(\theta)$, being h the satellite altitude. Taking into account Equation 2.2, the expression of the critical baseline is also given by

$$B_{\perp,crit} = \frac{\lambda R \tan(\theta - \alpha)}{\delta_r}, \tag{3.2}$$

being δ_r the slant range resolution [2].

Figure 3.1 shows an example of critical baselines for sensors ERS-1, TerraSAR-X and RADARSAT-2, the parameters of which are summarized in Table 3.1

Signal parameter	ERS-1	TerraSAR-X	RADARSAT-2
Wavelength [cm]	5.656	3.107	5.547
Altitude [km]	780	514	798
Range bandwidth [MHz]	16	150	100

Table 3.1: Determination of the critical baseline for ERS-1, TerraSAR-X and RADARSAT-2 systems parameters.

The most intuitive explanation of baseline decorrelation comes from the spectral domain. Therefore, the frequency-domain approach of interferometry is detailed in the following paragraphs. This approach gives a relation between the spectra of two SAR images and their corresponding ground-range (reflectivity) spectra defined by their ground-range wavenumbers. Accordingly, the frequency shift between two images is also denoted as *wavenumber shift*, as it was initially introduced in [67] [68]. This wavenumber shift comes from a difference between the ground-range (object) and the slant-range (data) spectra [42].

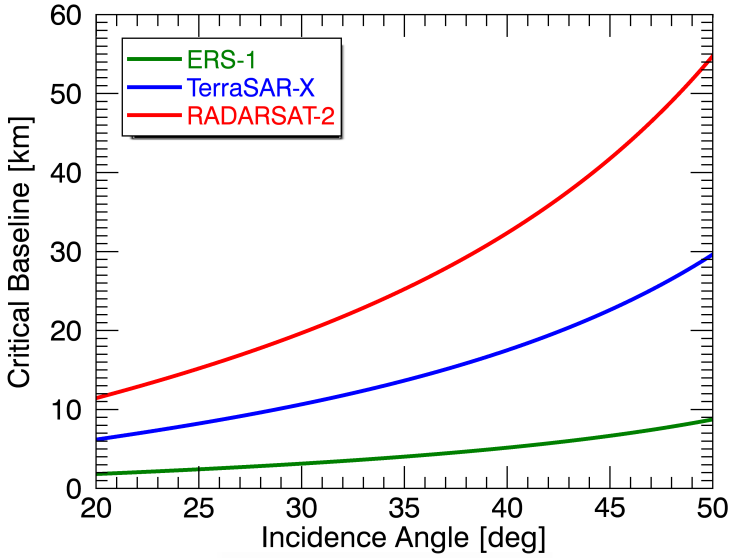

Figure 3.1: Critical baselines for sensors ERS-1, TerraSAR-X and RADARSAT-2 as a function of the incidence angle. A slope (α) of 0° is assumed for the representation.

While the ground-range spectrum is directly related to the object reflectivity, the slant-range spectrum is characterized by the SAR imaging system parameters. Formally speaking, ground-range wavenumber k_y and wavenumber in elevation k_z can be expressed as a function of the radar frequency f_0, the incident angle θ and the local terrain slope α, as

$$k_y = \frac{4\pi f_0}{c} \sin(\theta - \alpha), \tag{3.3}$$

$$k_z = \frac{4\pi f_0}{c} \cos(\theta - \alpha). \tag{3.4}$$

Since the incidence angles of master and slave images are different, ground-range wavenumbers will also differ. The wavenumber shift can be mathematically obtained by differentiating Equation 3.3 with respect to the incidence angle θ, i.e.,

$$\Delta k_y = \frac{4\pi f_0 \Delta\theta}{c} \cos(\theta_1 - \alpha). \tag{3.5}$$

being, $\Delta\theta = \theta_1 - \theta_2$ the look-angle difference and θ_1 the look-angle of the reference (master) image. Thus, as the radar is not monochromatic (each signal has a certain bandwidth centered around a central frequency f_0), Equation 3.5 states that once the ground range is projected onto the slant-range, the spectral components of the object in one image are shifted to other frequencies in the second image. A visual representation of this effect is shown in Figure 3.2.

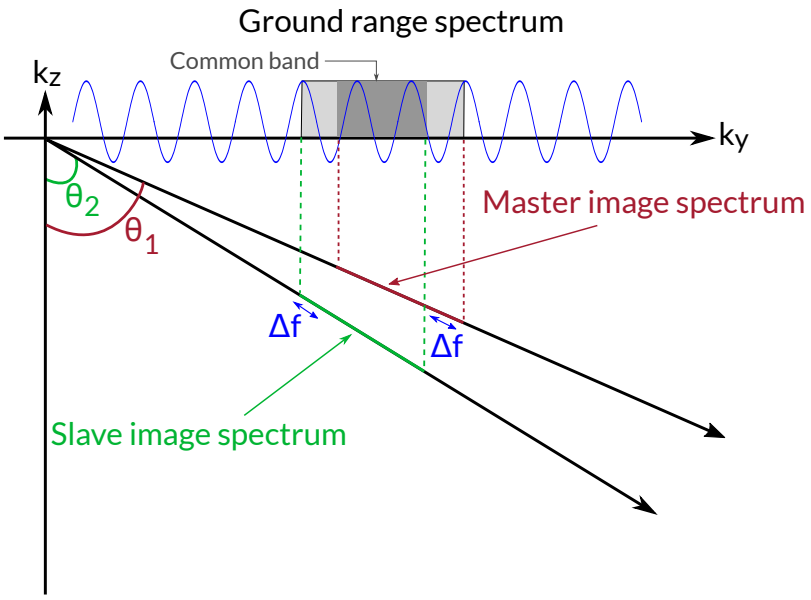

Figure 3.2: Illustration of the wavenumber shift principle.

Moreover, it is important to express this wavenumber shift in terms of frequency [68]. This allows us to really understand the impact of the baseline in interferometric processes, by comparing this shift to the system bandwidth W. Specifically, the wavenumber shift of Equation 3.5 can be expressed as an equivalent *frequency shift* as follows

$$\Delta f = \frac{f_0 \Delta\theta}{\tan(\theta_1 - \alpha)}. \tag{3.6}$$

Now, considering that the angular separation $\Delta\theta$ can be expressed, approximately, by means of the baseline $B_\perp$ and the slant range r_0, as

$$\Delta\theta \approx \frac{B_\perp}{r_0}, \tag{3.7}$$

the frequency shift between an interferometric pair of two SAR images with a given baseline $B_\perp$ is

$$\Delta f = \frac{f_0 B_\perp}{r_0 \tan(\theta_1 - \alpha)} = \frac{c B_\perp}{\lambda r_0 \tan(\theta_1 - \alpha)}. \tag{3.8}$$

The amount of spectral shift provides an indicator of the degree of decorrelation between both images and, hence, it is an indicator of the amount of useful interferometric information which can be extracted. In this regard, if the frequency shift Δf is larger than the signal bandwidth, it means that both SAR images are completely uncorrelated and cannot be used for interferometric processing, which is the same concept as the critical baseline previously explained. However, if it is less than the bandwidth, both images contain useful interferometric information and can be properly combined into an interferogram after an adequate filtering (evidently, other sources of decorrelation are not being considered). In this last case, the previous reasoning yields that the images have a *common spectral band*, which is useful from the interferometric point of view, but also a *non-common* band which in-

troduces undesired noise. Although it is not useful for interferometric use, it is worth mentioning that the non-common band allows to improve the resolution of a single SAR image by exploiting the spectral shift principle [69]. Visually, the spectral shift showing both the common and non-common bands of the images spectra is represented in Figure 3.3.

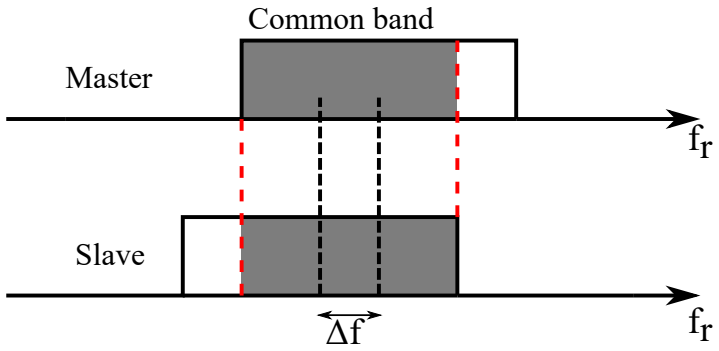

Figure 3.3: Illustration of the spectral shift between two images. Only the common band (gray) contains useful interferometric information.

It is interesting to represent the variation of the frequency shift as a function of the local terrain slope α. A particular case employing TerraSAR-X parameters (see Table 3.1) with an incident angle of 30° and a perpendicular baseline of 300 m is shown in Figure 3.4. As it can be observed, at grazing incidence, $\alpha = \theta - 90°$ ($-60°$ in this case), the frequency shift becomes exactly zero. Then, it progressively increases with the terrain slope until it is equal to the range bandwidth and no information can be extracted for interferometric use. At $\alpha = \theta$ (the slope is equal to the incident angle), the spectral shift becomes negative, causing range-reversed imaging [39] which corresponds to lay-over areas. No information can be extracted if the slope is less than the grazing incidence angle (shadow area) or if it belongs to the blind angle interval shown in Figure 3.4.

This leads to the conception of range filtering strategies in frequency domain, which have to accurately estimate the spectral shift to properly remove the non-common band of the spectra, while simultaneously preserving the useful (common) part. Without range filtering, the coherence and, hence, the global quality of interferograms drops as a function of the perpendicular baseline. The suppression of baseline decorrelation is therefore important to improve the quality of interferometric data and other products derived from this technique.

Finally, it is also important to point out that range filtering is not only of great interest for pure interferometric applications. For instance, it is compulsory in forest studies based on PolInSAR, where the local correlation (coherence) is used as an input to retrieval algorithms. Specifically, a proper removal of the geometrical decorrelation has to be carried out so that coherence values are not influenced by this noise factor, which could lead to inaccurate or erroneous results and estimations.

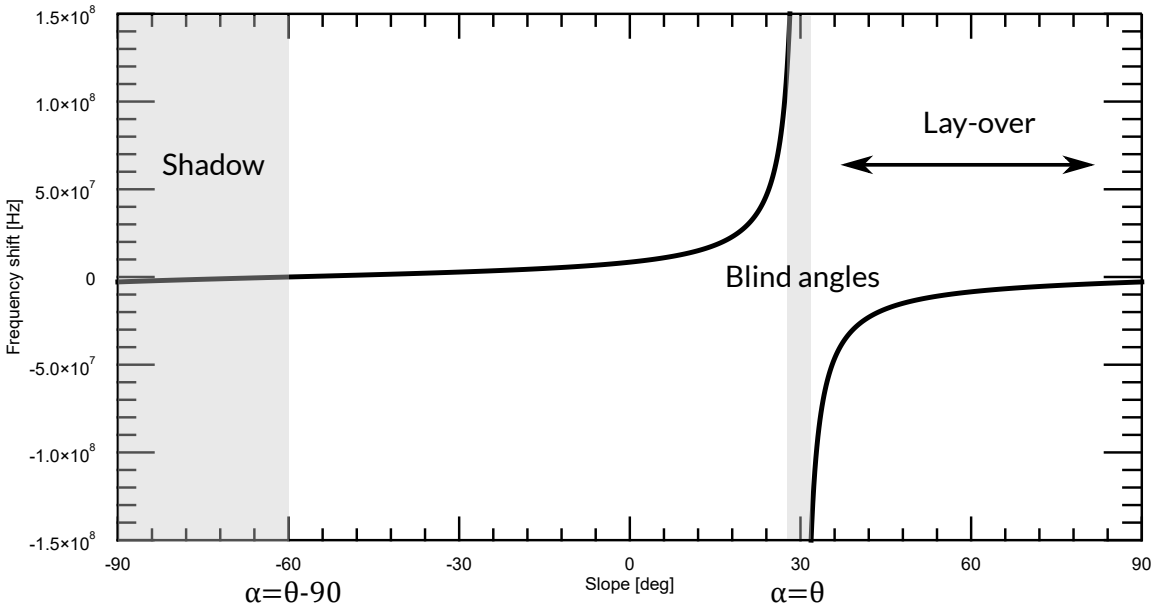

Figure 3.4: Spectral shift as a function of the local terrain slope with TerraSAR-X satellite parameters. A baseline of 300m and an incidence angle of 30° have been considered.

3.1.2 A Review of Range Spectral Filtering Methods

Different spectral filtering methods have been conceived in the past years. Evidently, the goal of all of them is an appropriate estimation of the frequency shift between a pair of coregistered SAR images which will be used to form an interferogram, as previously detailed. Once the shift is estimated, a band-pass filter is built in order to remove the non-overlapping parts of the spectra. The main aspect that varies from one method to another relies on the estimation of the shift. The rest of the filtering steps are common and can be summarized as follows. Firstly, the filtering removes the initial spectral weighting applied to each image in order to limit side-lobe contributions of strong point targets [70] [71] [72]. Side-lobe control is especially important in urban environments, where there exist a large number of strong scatterer. Also, its suppression becomes more important as the resolution increases. Each SAR sensor has a specific spectral weighting. For instance, TerraSAR-X images are weighted with a Hanning window with a coefficient $a = 0.6$ [73]. Its expression is

$$w_h(k) = a - (1-a)\cos\left(\frac{2\pi k}{N}\right), \qquad k = 1 \ldots N, \tag{3.9}$$

being N the number of samples. RADARSAT-2 images are weighted with a Kaiser-Bessel window with coefficient $\beta = 2.4$ [74]. Its expression is given by

$$w_k(k) = \frac{I_0\left(\beta\sqrt{1-(\frac{2k}{N})^2}\right)}{I_0(\beta)}, \qquad k = 1 \ldots N, \tag{3.10}$$

where I_0 is the zeroth-order modified Bessel function of the first kind. Figure 3.5 shows an example of these two spectral weighting windows with $N = 512$ samples. Note that the deweighting is, evidently, obtained with the inverse functions of Equations 3.9 and 3.11 and that it is only applied in range dimension. The azimuth window, which is usually the same, remains untouched.

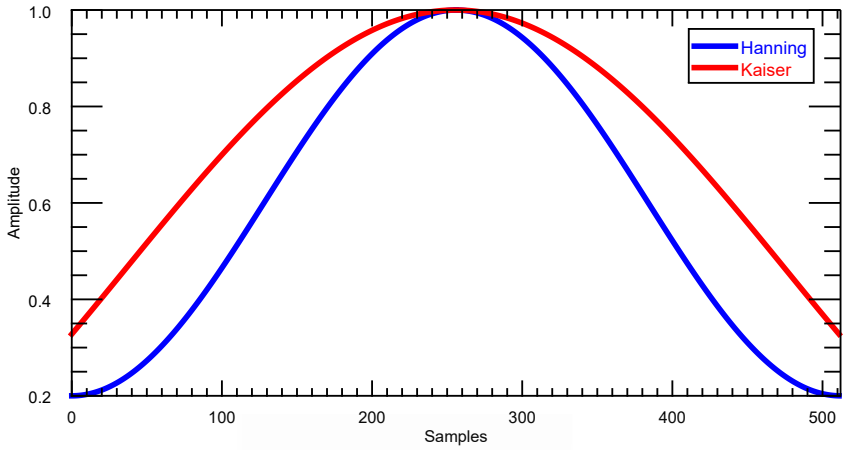

Figure 3.5: Spectral weighting windows applied to TerraSAR-X (Hanning, $\alpha = 0.6$) and RADARSAT-2 (Kaiser, $\beta = 2.4$) image products.

Secondly, the spectral shift Δf is estimated according to each method, and, once it is obtained, a new spectral weighting window is constructed according to its value. Because the spectral shift is not zero, the re-weighting window will be similar to the original but with some samples (or frequencies) set to zero. Finally, this leads to a new and reduced range bandwidth W' which is a function of Δf,

$$W' = W - |\Delta f|, \tag{3.11}$$

with a subsequent reduction of resolution in range, but with an increase in the correlation between the images.

3.1.2.1 Adaptive Method

The method known as *Adaptive* is the most widely used [42] [75] [76]. It has the advantage that is does not require any additional or external information, since the spectral shift between both images is directly estimated from the data. However, a sufficient initial degree of correlation (coherence) is required between the images, since a temporary interferogram is used to compute the spectral displacement. As a consequence, this method provides good results in coherent areas but performs poorly if other sources of decorrelation are present, especially when temporal decorrelation worsens the quality of the data.

The core idea of this method relies on computing the power spectrum of a complex interferogram and performing a peak analysis. Prior to interferogram formation, both the master and slave images should be oversampled by a certain factor to ease the peak location (usually, a factor of 2 or 4 is

enough). The spectral shift is directly provided by the location of the peak. The algorithm works in blocks, i.e., the image is divided into small patches with a given number of pixels and lines. Although each line of the block is individually filtered, a fixed number of lines inside the block is averaged in order to reduce the interferogram noise. For instance, if the block has 500 lines, 25 lines can be averaged to compute the power spectrum of the central one. Once the peak is located by the maximum value of the power spectrum, a pseudo-SNR is also calculated. This signal-to-noise ratio is directly related to the 'quality' of the peak, i.e., if it really reflects the spectral displacement between the images or, contrarily, if it is a 'false' maximum value in either a low-quality area or in an area greatly influenced by topography, as we will see. The SNR can be computed as

$$SNR = \frac{N \cdot |X_{p_{max}}|}{\sum_{k \neq p_{max}} |X_k|}, \tag{3.12}$$

where N is the number of range samples in the block, $X_{p_{max}}$ is the maximum value of the power spectrum, and $|X|$ is the averaged spectrum in range dimension of the interferogram. A threshold, which allows the filter to proceed, is therefore set. Only if the SNR is above the threshold, a range line will be filtered. Otherwise, the images should not be filtered to prevent a worse future interferogram if the estimation of the peak is not accurate. If the peak is wrong, useful parts of master and slave signals can be eliminated, hence reducing the quality of the resulting interferogram with regards to the original one.

At this point it is worth mentioning the influence of topography (represented by the local terrain slopes) in the filtering process. Since the peak corresponds to the maximum value of the Fourier transform of the interferogram, it can be regarded as the dominant frequency inside the range block. In other words, the local frequency shift is equal to the fringe frequency. Accordingly, if topography changes importantly, for instance, when the images cover a mountainous area as the one previously shown in Figure 2.9(d) in Chapter 2, the peak will inevitably widen and will not be representative of a single frequency shift.

Consequently, the filter would ideally require that inside the extracted block, the slope is either flat or perfectly constant. In this regard, the filter can be tuned so that small interferogram patches (with less pixels in range dimension) are processed. In this case, the filter would be better adapted to the local topography but there may not be enough data to yield a fine spectrum resolution, so the peak estimation would become less reliable. In practice, blocks of 128 or 64 pixels seem to perform best, whereas a smaller number of pixels is not recommended.

3.1.2.2 Method Based on Orbits

The method based on orbits employs geometrical data (the baseline) derived from the orbit state vector information to compute the spectral displacement. Then, it requires additional information since the spectral shift is directly estimated by means of Equation 3.8. In order to better adapt the filter to the local characteristics of the terrain, the filtering can be performed line by line, where each

line is in its turn divided into smaller blocks. Blocks of 128 or 256 pixels are recommended. Then, a single spectral shift within each block of the interferogram is computed. In order to improve the filtering performance, it is proposed that the largest spectral shift is selected among all obtained values (128 or 256 depending on the block size). This choice leads to better filtering results with a subsequent larger coherence improvement.

Finally, note that in this approach a flat Earth is assumed, i.e., the local terrain slope is kept constant at zero ($\alpha = 0$ in Equation 3.8). This obviously leads to a sub-optimal filtering performance in areas with a steep topography, since the local slope variations of the surface are not considered. Therefore, ignoring topography constitutes the main limitation of this method.

3.1.2.3 Slope-Adaptive Filtering

As explained in Sections 3.1.2.1 and 3.1.2.2, local topography plays an important role for determining the spectral shift. Therefore, the exploitation of a DEM, which contains information related to the terrain height and, hence, from which the local terrain slopes can be estimated to improve the performance of range filtering, becomes obvious. We will then call this method *slope-adaptive range filtering* which, in principle, is based on the orbits method (Section 3.1.2.2), but taking into account the slopes derived from an auxiliary DEM. The inclusion of elevation information was initially proposed in [77], where a coarse surface is directly estimated from the complex interferogram by means of multi-level frequency estimators followed by a phase unwrapping algorithm. Since the spectral shift is equal to the fringe frequency caused by the topography in space domain, the estimated frequencies can be used to filter in range. Although the proposed methodology has the advantage of being completely automatic (everything is derived from the pair of images), it entails the risk of not being accurate enough with low-quality and decorrelated data, where the estimation of frequencies is a very difficult task.

Nevertheless, the slope-adaptive filtering scheme proposed in [77] can be easily adapted to use an external DEM instead of estimating it from the original data. A first way of including a DEM in the filtering process relies on performing a demodulation of master and slave signals. This can be directly achieved by using the synthetic interferogram derived from the DEM and the orbits which contains the topographic phase contribution (see Figure 2.9(d)). Thus, both original SAR images S_1 and S_2 are demodulated according to

$$\begin{aligned} S_1' &= S_1 \exp\left(-j\frac{\varphi_{DEM}}{2}\right), \\ S_2' &= S_2 \exp\left(+j\frac{\varphi_{DEM}}{2}\right), \end{aligned} \tag{3.13}$$

where φ_{DEM} is the topographic phase derived from the DEM. Note that half of the topographic contribution is used for the master image, the other half for the slave image, and they are of opposite sign. The next step consists in computing the spectral displacement, which can be directly estimated from interferometric parameters (baseline and orbits). The simplest way is to globally filter the images

by a constant Δf, usually the one providing the maximum displacement. Because the images are demodulated by half of the topographic phase, their spectra are respectively symmetrically shifted and centered around the central frequency, without considering their range position. It follows that the common band between the master and the slave images is aligned, and the images can be low-pass filtered employing the same (symmetric) filter in frequency domain. Finally, the topographic phase removed in Equation 3.14 must be added back to the images by the respective conjugate operations, leading to the range-filtered images S_{1f} and S_{2f},

$$\begin{aligned} S_1 f &= S_1' \exp\left(+j\frac{\varphi_{DEM}}{2}\right), \\ S_2 f &= S_2' \exp\left(-j\frac{\varphi_{DEM}}{2}\right). \end{aligned} \tag{3.14}$$

This process is sketched in Figure 3.6.

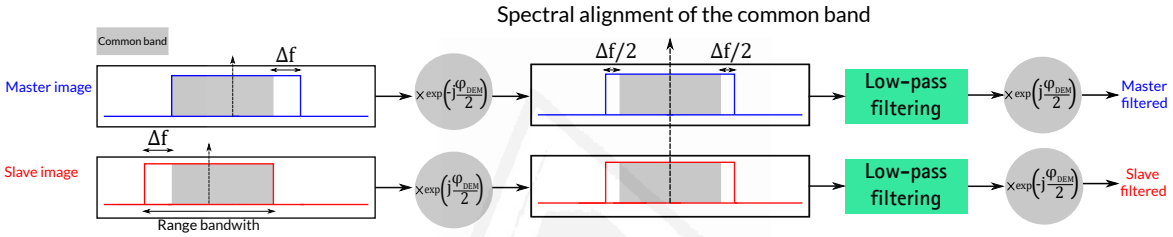

Figure 3.6: Spectral alignment of two images spectra by means of demodulation with a topographic phase, followed by a low-pass filtering.

The main limitation of this approach comes from the constant spectral shift value used to filter the whole images, which is generally not suitable since the filter may not be well matched in areas with varying topography. Moreover, another disadvantage of this method is that the DEM information remains not fully exploited.

3.1.2.4 Refined Slope-Adaptive Filtering

Once the different, state-of-the-art range filtering strategies have been reviewed, the refined method developed throughout the PhD can be explained in detail. The core idea consists in providing different methodologies to overcome the limitations of the previously explained filters by means of the complete exploitation of an external DEM. It is important to clearly state that we will focus on the problems that commonly-used filters have in areas with a steep and/or varying topography, since if the area is rather flat, most methods provide acceptable results as the spectral shift is not influenced by the terrain slope.

Firstly, the local terrain slopes (always in range dimension) must be computed. They can be easily derived since the elevation is known. Consider the SAR geometry shown in Figure 3.7 over a region with a given terrain slope a.

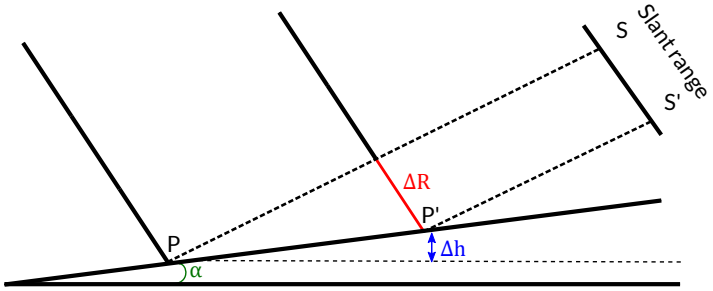

Figure 3.7: Local terrain slope (α) acquisition geometry between two adjacent points (S and S').

Two adjacent pixels in the slant-range plane receive the backscattered signals from points P and P'. The height difference Δh between both points can be directly obtained from the DEM by computing the local derivatives in range direction, i.e.,

$$\Delta h = h_2 - h_1. \tag{3.15}$$

From trigonometry, we obtain the local slope between two adjacent pixels as [78],

$$\alpha = \arctan\left(\frac{\sin\theta}{\frac{\Delta R}{\Delta h} + \cos\theta}\right), \tag{3.16}$$

being θ the incidence angle and ΔR the local slant range difference between the two consecutive pixels.

Due to the presence of topography, the filter must be very well adapted to its local variations. Therefore, it is strictly necessary to segment the images into small patches so that the variety of local slopes is always considered. However, a problem arises if we have a topography like the one represented in Figure 3.8. In this case, the selection of the slope and, hence, the estimation of the spectral displacement is not evident. Selecting the mean slope is not representative of the whole area, whereas selecting the maximum value could result in a too coarse filtering (which could cause a loss of resolution), and selecting the minimum could not be significant enough.

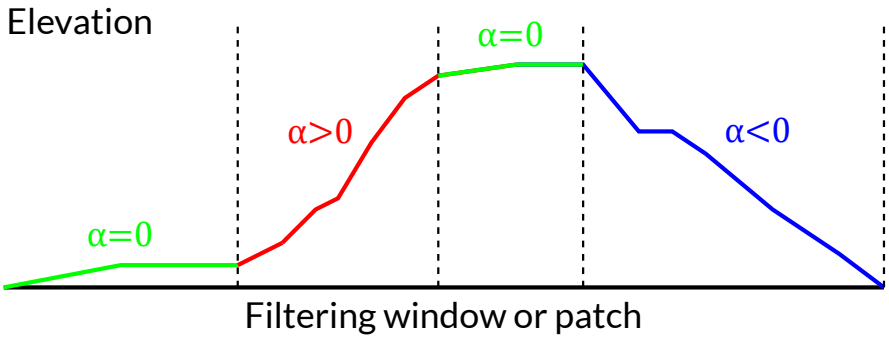

Figure 3.8: Example of filtering problem where a variety of slopes (α) is present in the same patch.

In this regard, an optimal filtering can be obtained through a subdivision of the original window into smaller sub-blocks, resulting in a *multi-scale filtering*, so that the filter is always adapted to any kind of slope. If the topography exhibits strong spatial variations, smaller windows should provide better spectral shift estimations which, consequently, result in a better filtering performance. On the contrary, flat areas benefit from larger blocks. Visually, this is represented in Figure 3.9. For simplicity, only 4 different window sizes are shown.

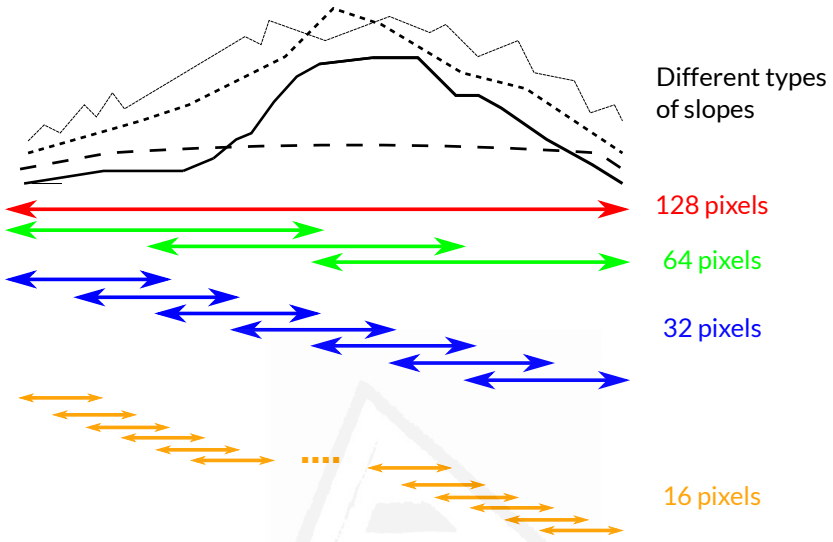

Figure 3.9: Representation of the proposed multi-scale range filtering algorithm. An overlapping factor of 50% is represented.

The proposed method is explained as follows. The algorithm works line by line by extracting a number of range pixels, i.e., a 2-D block is not used since the filter is only applied in range direction (this also allows a faster algorithm execution). Each range line is segmented into blocks of different sizes. Sizes of 128, 64, 32 and 16 pixels are proposed. Note that an overlap is fixed to avoid edge effects between adjacent filtered blocks, as represented in Figure 3.9. The spectral shift is obtained by means of geometrical parameters using Equation 3.8. The maximum displacement value is always selected. Once a given block is filtered with all window sizes, a quality criterion has to be established to determine which one performed best. The interferometric coherence provides such quality estimator. However, since the filtering is carried out only in range direction, the quality estimator corresponds to the 1-D coherence (see Equation 2.43) where only range pixels are used. It follows that the final lines of master and slave images are obtained as the ones for which the coherence is maximum. Note that to avoid the effect of the coherence estimation bias, which depends on the number of samples, coherence is always computed with a fixed window size. A general scheme of the filter is shown in Figure 3.10.

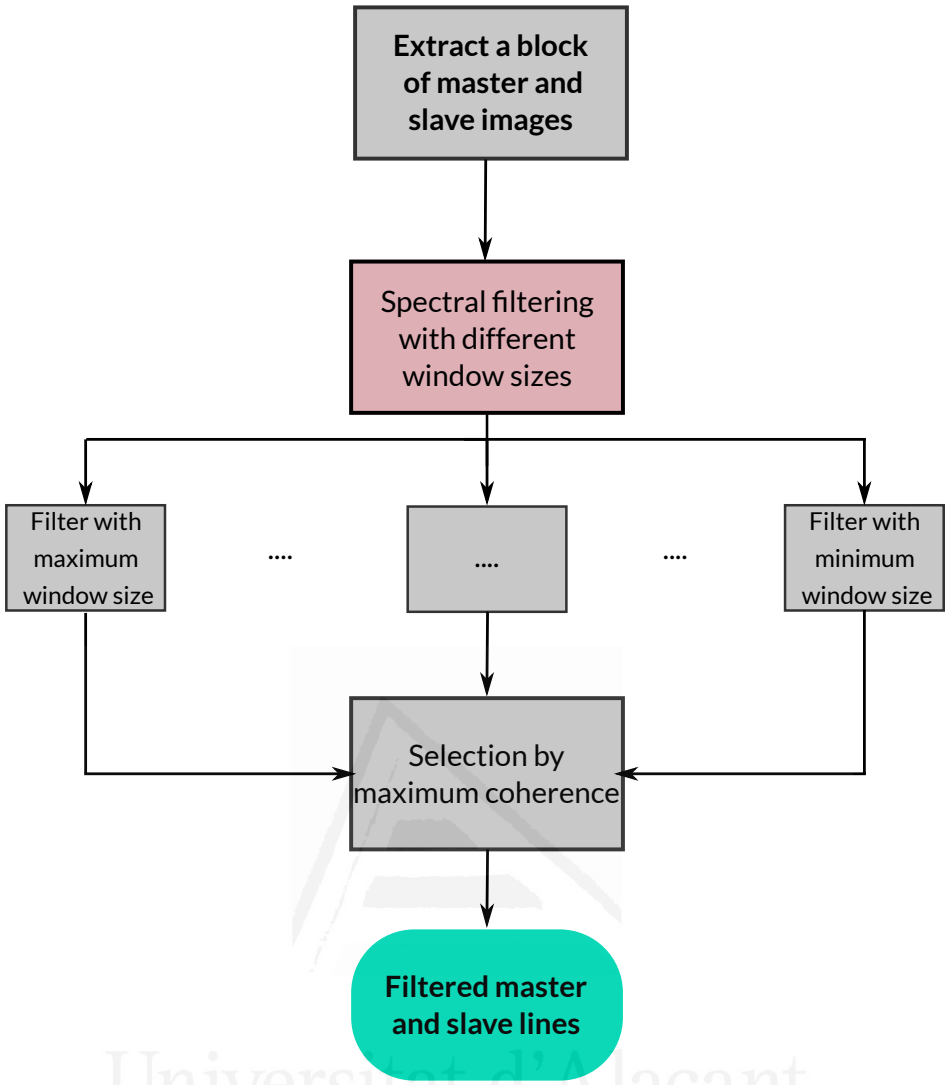

Figure 3.10: Block diagram of the proposed range filtering method.

An important aspect of the proposed method relies on the construction of the low-pass or band-pass filter. Two different, yet (almost) equivalent strategies are proposed. On the one hand, both the signals of master and slave images can be demodulated using the topographic phase according to the process described in Section 3.1.2.3.

In this case, a symmetric low-pass filter, which is identical for master and slave, is directly built according to Δf, i.e., we 'move' the signals and we keep the same filter for both images. Note that the value of Δf in pixels frequency is easily obtained by

$$\Delta f_{pixels} = \frac{\Delta f}{RSR}, \tag{3.17}$$

being RSR the sampling rate in range dimension and which depends on the sensor. This is illustrated with Figure 3.11. A Kaiser window with $\beta = 2.4$ (RADARSAT-2 spectral weighting) is used. Because the spectra are aligned, the filter keeps the useful common-band and removes the rest of each signal.

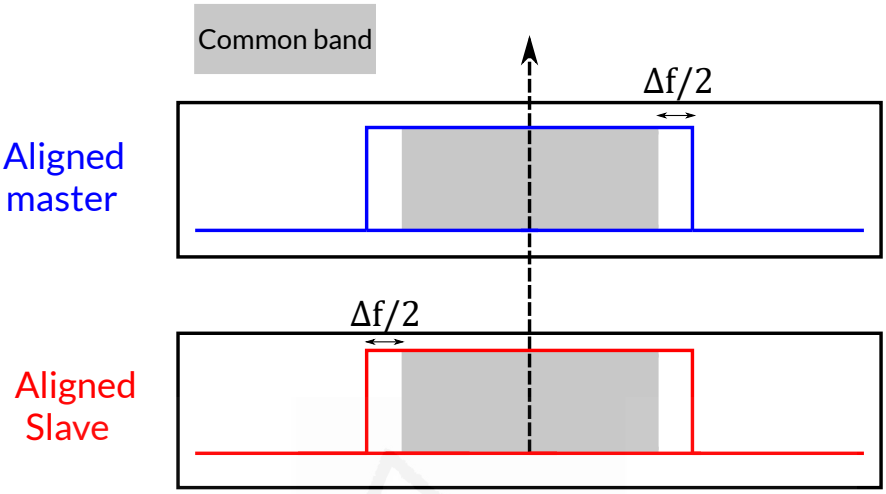

(a) Spectral alignment of master and slave images.

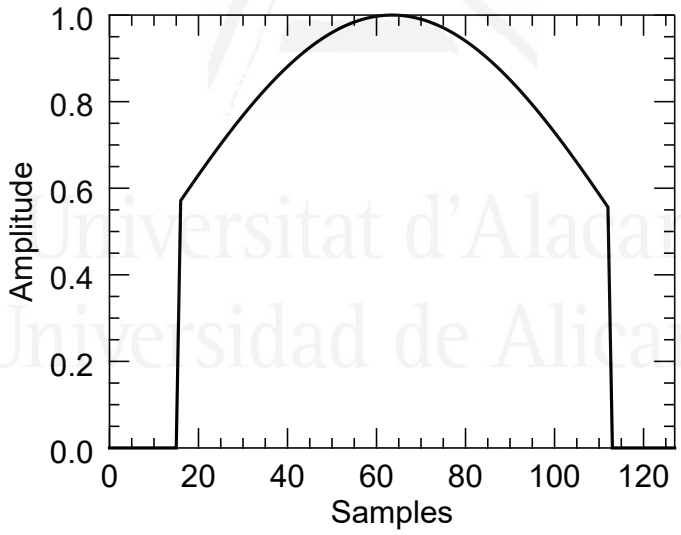

(b) Spectral shape of the low-pass filter: a Kaiser window of 128 pixels.

Figure 3.11: Low-pass spectral filtering after alignment of master and slave images. A spectral displacement of 30 pixels is assumed.

On the other hand, if both signals are not demodulated, a similar yet inverse procedure is carried out. That is, we keep the signals and we adapt the filter to appropriately remove the non-common bands. In this case, a different and non-symmetric filter is used for each signal. This is illustrated with Figure 3.12. The same Kaiser window ($\beta = 2.4$ and 128 pixels) and the same spectral shift of 30 pixels are used. Note that a reversed filter is used for master and slave images.

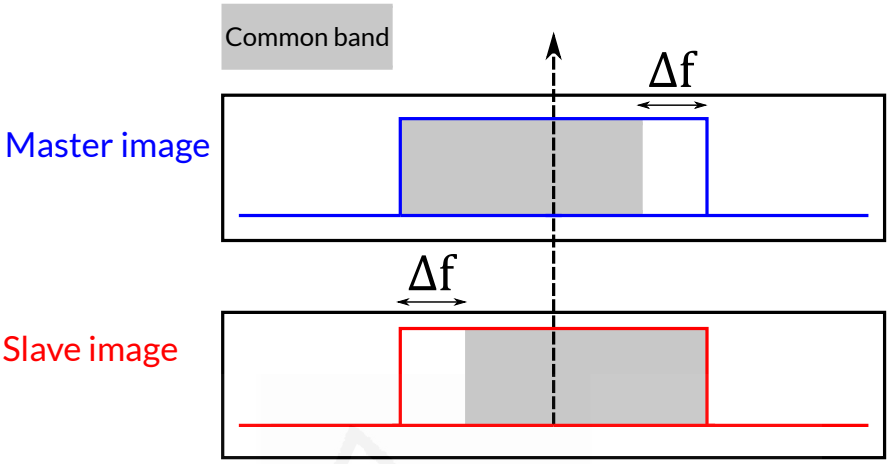

(a) Master and slave images spectra.

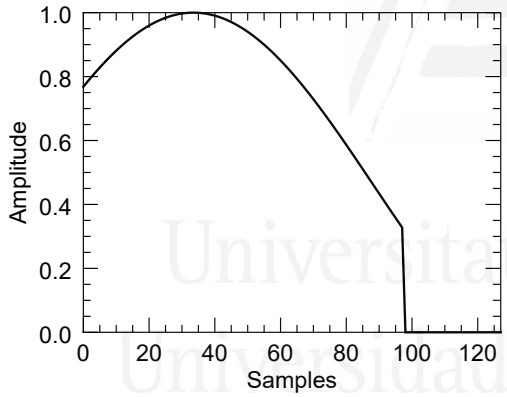

(b) Spectral shape of the band-pass filter used for master image.

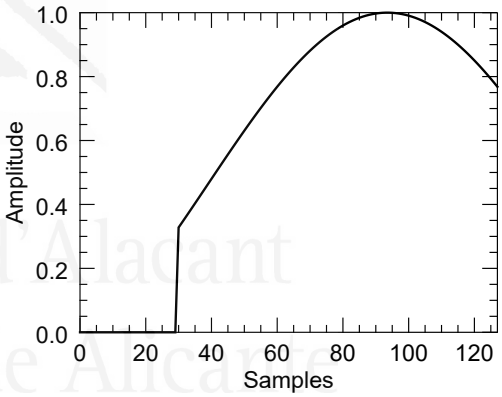

(c) Spectral shape of the band-pass filter used for slave image

Figure 3.12: Band-pass spectral filtering of master and slave images. A spectral displacement of 30 pixels is assumed.

3.1.3 Results

To verify the performance of the proposed method against the others, we have analyzed the phase quality improvement obtained after range filtering a pair of images covering the area of the Mount Etna (Sicily, Italy). A picture of the area and its geographic location are shown in Figure 3.13.

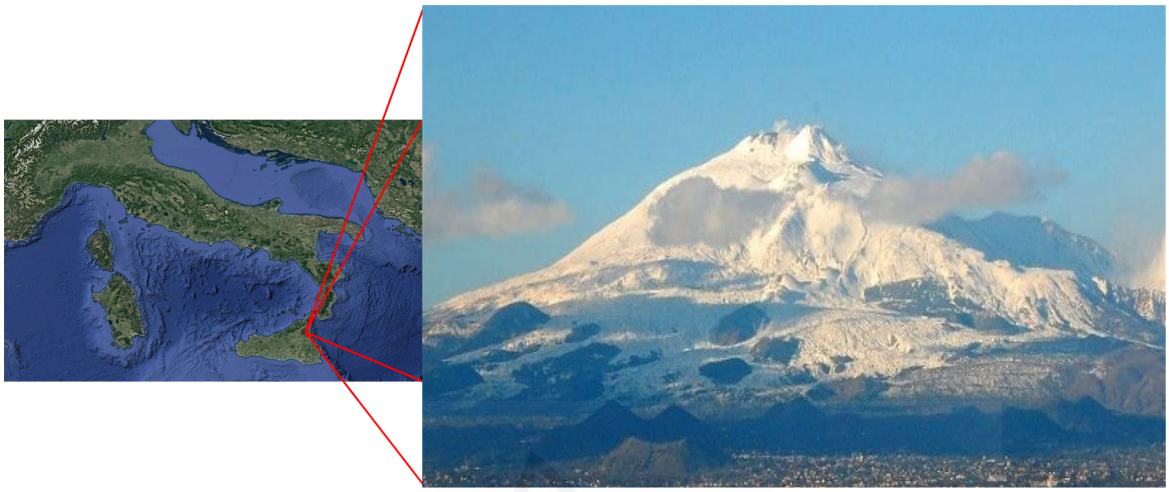

Figure 3.13: Geographic location of the Mount Etna in eastern Sicily (Italy). Images were extracted from ESA webpage and generated with Google-Earth©.

Specifically, the data set is composed of two coregistered SLC images acquired by RADARSAT-2 in May 2008. They were acquired using Fine Quad Swath 8 (FQ8) mode, the near and far range incidence angles of which are 26.9° and 28.7° respectively. The processed image size is 2000×4000 pixels (range and azimuth respectively) and the polarimetric channel is HH. The main system parameters used in the filtering process are detailed in Table 3.2. The intensity of master image is represented in Figure 3.14(a) and the DEM providing height data is depicted in Figure 3.14(b).

Master date	2008-05-05
Slave date	2008-05-29
Perpendicular baseline [m]	586.547
Range bandwidth [Hz]	$3.002442 \cdot 10^7$
DEM resolution [m]	10
Range spectral weighting	Kaiser-Bessel window with $\beta = 2.4$

Table 3.2: Processed interferometric pair characteristics.

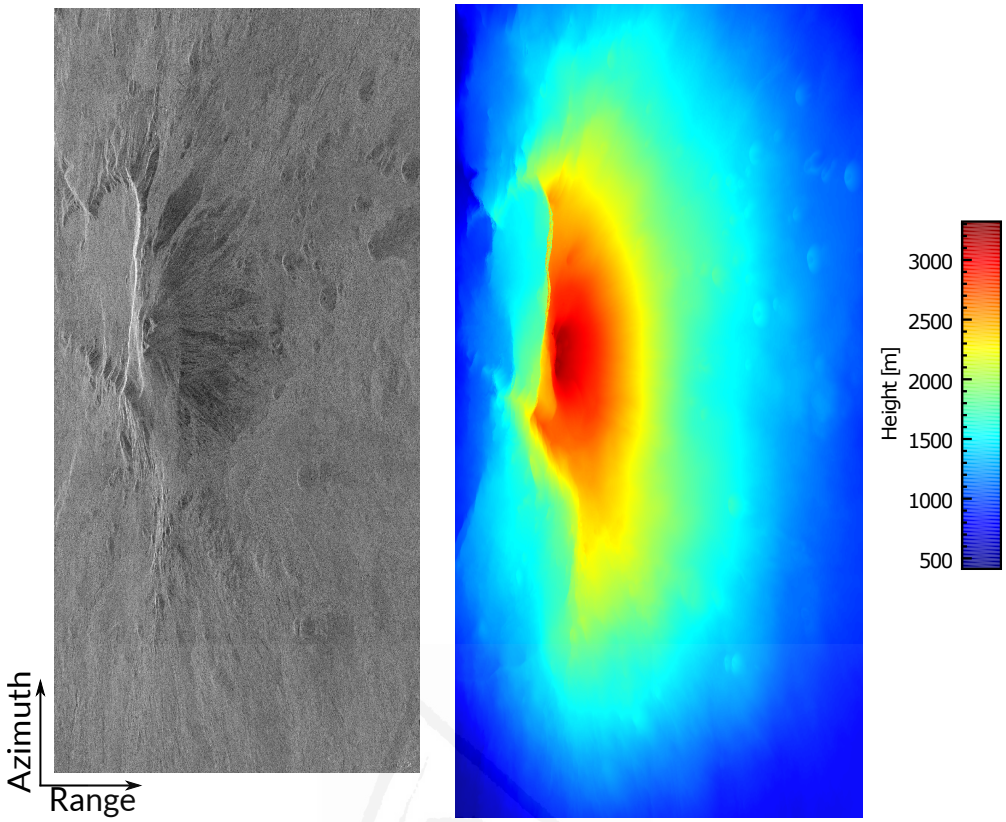

(a) Master intensity (dB). **(b)** DEM height of the processed area.

Figure 3.14: Master image intensity and DEM height of the processed area.

Moreover, slant range slopes of the test scene are represented in Fig. 3.15. It can be observed that this scene exhibits strong slopes throughout the whole area and especially around Mount Etna in the central part of the image. It is important to mention that all the results discussed in this section are only related to the range filtering process. That is, we will only show the quality improvement after removing the baseline decorrelation. Concerning the adaptive method, blocks of 128×500 pixels (in range and azimuth dimensions respectively) are progressively extracted and filtered, 35 azimuth lines in each block are averaged to compute the power spectrum, and both images are oversampled by a factor of 2 in range dimension. Additionally, a minimum signal-to-noise ratio (SNR) threshold equal to 3, allowing the filter to proceed, has been fixed. To show the impact of the window size (number of samples) on this method, its performance is also tested with a block size of 32×500 pixels and 25 lines are averaged to compute the power spectrum. Concerning the method based on orbits, each range line is divided into blocks of 128 pixels and the spectral shift is estimated with Equation 3.8 with a fixed (null) slope. Images are also filtered with the conventional slope-adaptive method after including the demodulation with the topographic phase. In this case, a global spectral displacement Δf is selected (the one providing the maximum shift).

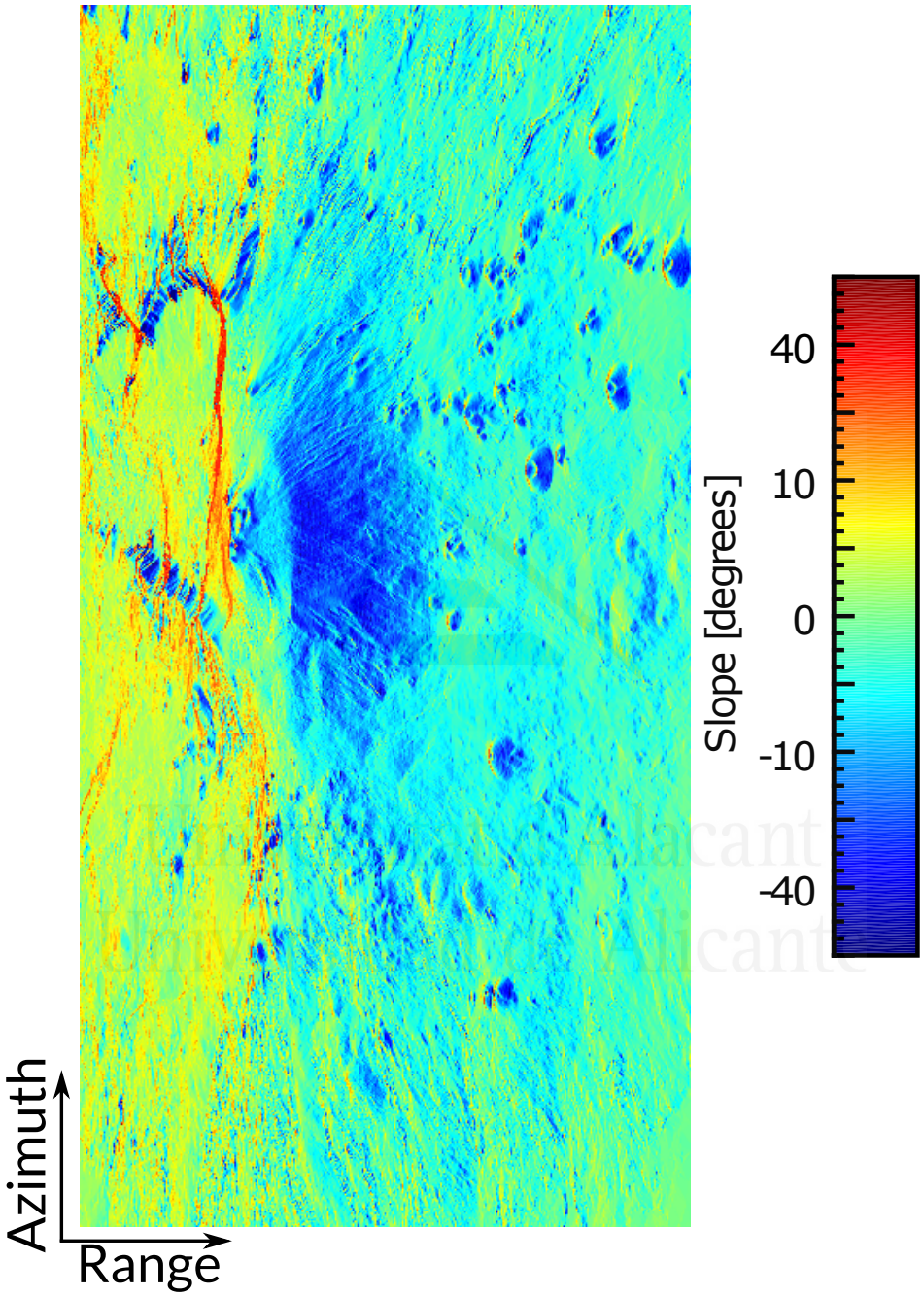

Figure 3.15: Local slopes of the terrain in slant range direction of the test area.

Furthermore, the proposed slope-adaptive multi-scale algorithm is applied as a band-pass and a low-pass filter, following both strategies described in Section 3.1.2.4. More specifically, each extracted range line is filtered four times with windows of 128, 64, 32 and 16 pixels and an overlap of 50% between adjacent blocks is set. To decide which block size performed better, the coherence of a line is estimated with 15 samples.

The overall quality improvement is assessed with the coherence histograms shown in Fig. 3.16. A multilook size of 9×5 pixels has been used for coherence computation. It can be observed that all methods produce a significant improvement with respect to not filtering, as all histograms are displaced towards higher values. This also proves that the original data were significantly influenced by geometrical decorrelation.

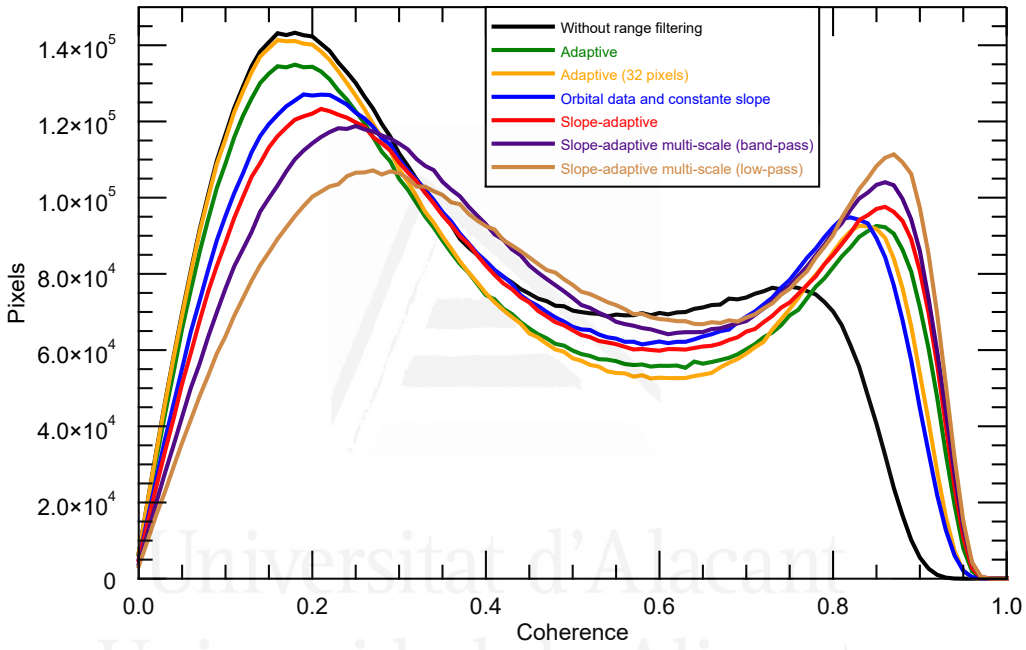

Figure 3.16: Coherence histograms after range filtering.

The adaptive method provides higher coherence values than the method based on orbits with a constant slope. This is because in high SNR areas, the computation of the power spectrum is accurate enough to yield a reliable estimate of the spectral displacement. However, it has the disadvantage that some lines are not filtered due to the reasons previously explained in Section 3.1.2.1. This can be illustrated with three different cases as follows. In the first case, when there is sufficient correlation between the images, the spectral displacement is very well determined as shown in Figure 3.17, where the slope is rather constant. Contrarily, a bad estimation of the spectral shift may come either from a flat but decorrelated area (for instance, due to the presence of vegetation) or from a correlated zone with a strongly variant topography. This is respectively illustrated with Figures 3.18(a) and 3.19(a), where it can be observed that the averaged power spectrum is noisy and a dominant peak cannot be correctly identified.

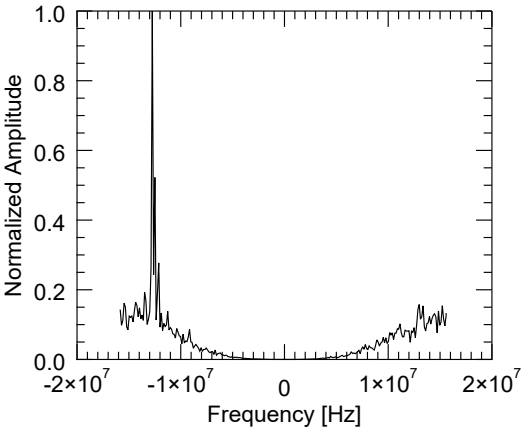

(a) Computed power spectrum with the adaptive method. A high SNR allows a clear identification of the peak.

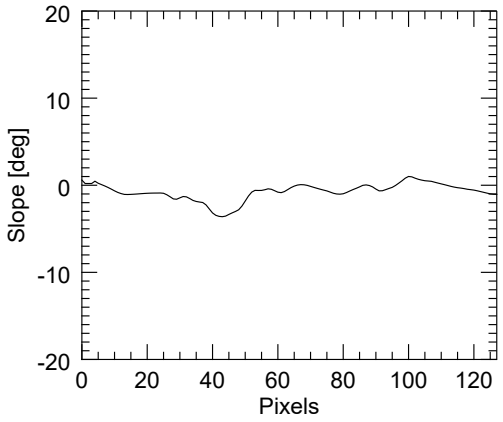

(b) Slope of the filtered line.

Figure 3.17: Spectral displacement estimated with the adaptive method in a correlated area with a flat topography.

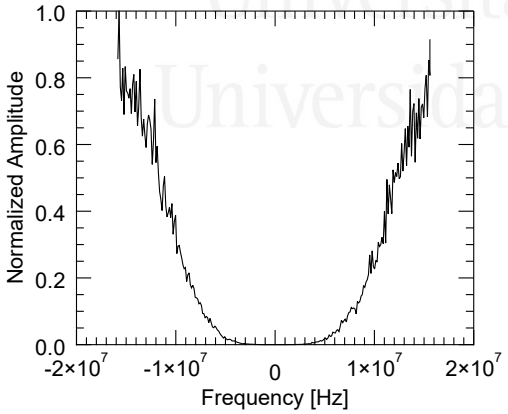

(a) Computed power spectrum with the adaptive method. A low SNR does not allow a clear identification of the peak.

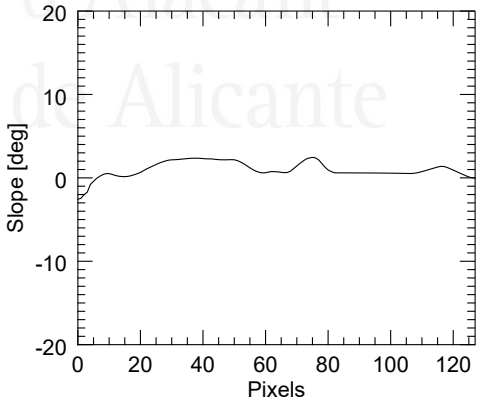

(b) Slope of the filtered line.

Figure 3.18: Spectral displacement estimated with the adaptive method in a decorrelated area with a flat topography.

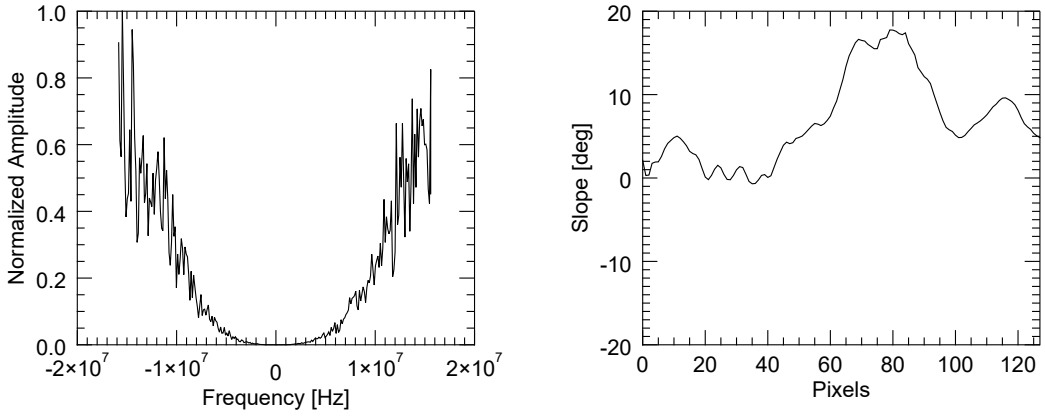

(a) Computed power spectrum with the adaptive method. A low SNR does not allow a clear identification of the peak.

(b) Slope of the filtered line.

Figure 3.19: Spectral displacement estimated with the adaptive method in a correlated area with a rapidly variant topography.

The improvement can also be observed by looking at the resulting coherence maps of the processed area, which are depicted in Figure 3.20. All methods show an overall increase in coherence throughout the whole area. However, a further gain is obtained after including the multi-scale filtering. This is better visualized by zooming into the squared area of the original coherence map in Figure 3.20(a). The coherences of this region of interest (RoI) are shown in Figure 3.21, while the corresponding interferometric phases are represented in Figure 3.22. It is clearly appreciated that fringes are sharper in the filtered data, so that the global quality of the phase is improved and, hence, the coherence is increased to a greater extent by the proposed method.

As an additional comparison, the improvement provided by each method at different coherence intervals has been evaluated. Specifically, 10 coherence intervals are selected between 0 and 1. As shown in Figure 3.23, slope-adaptive methods provide the largest improvement. However, both proposed algorithms are able to improve the coherence at all levels, outperforming the rest of the filters. The adaptive method exhibits the worst result in low-coherence areas, proving that this method is not able to filter areas strongly affected by other sources of decorrelation (improvement is almost negligible for coherence values below 0.3), for which the constant-slope orbit-based method provides some coherence improvement. On the contrary, the adaptive method performs better than the method based on orbits in highly coherent areas. In fact, it provides an improvement very similar to the slope-adaptive methods for coherence values greater than 0.8.

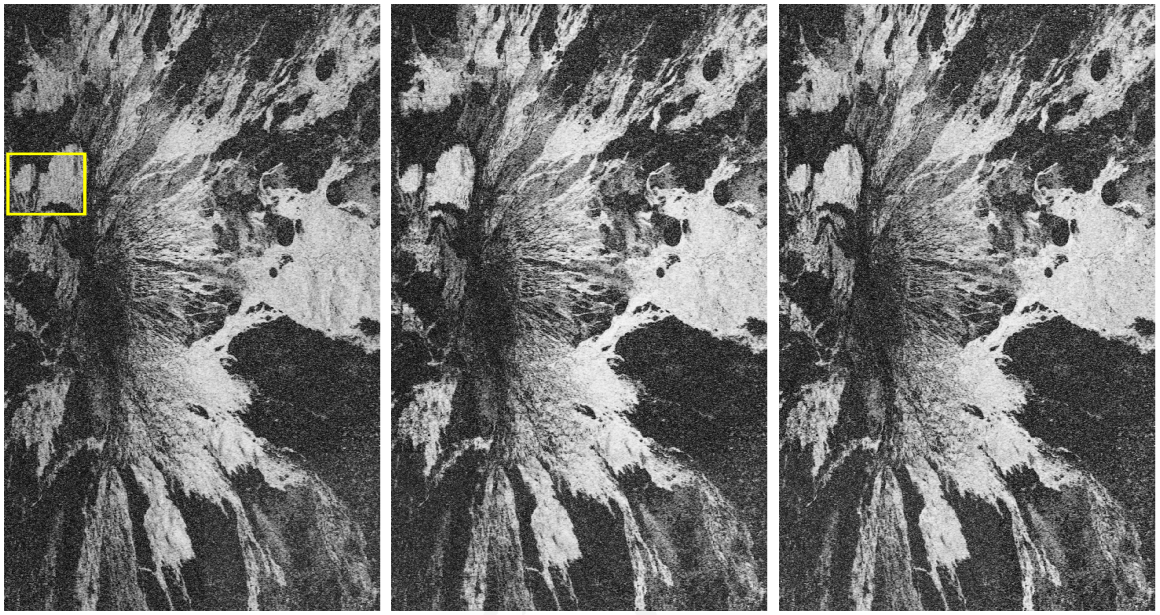

(a) Original **(b)** Adaptive method **(c)** Method based on orbits

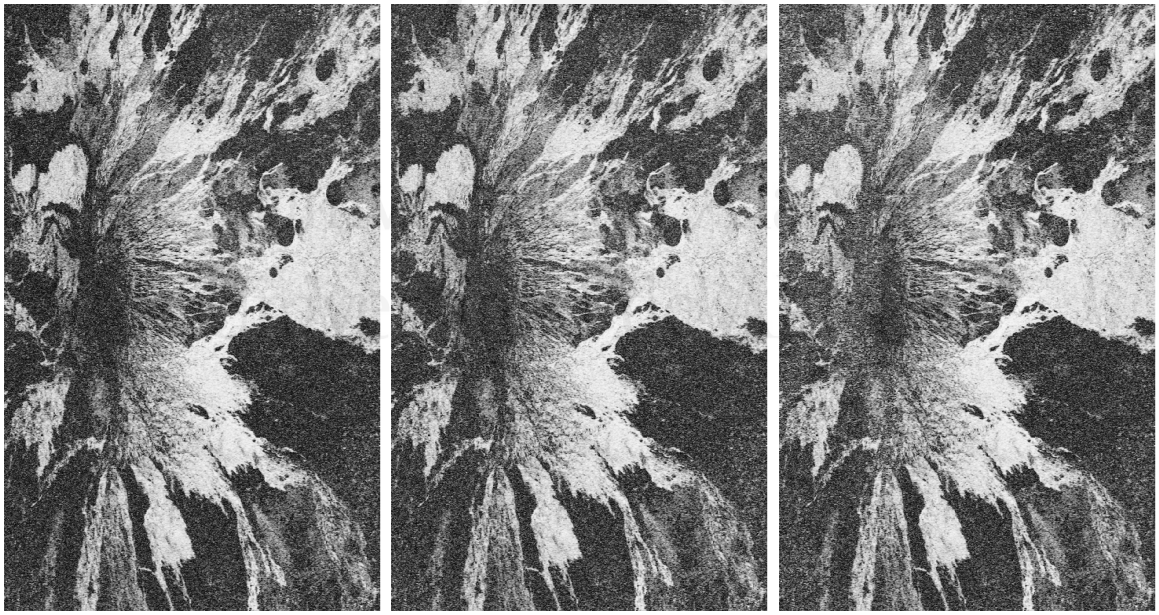

(d) Slope-adaptive **(e)** Slope-adaptive multi-scale (band-pass) **(f)** Slope-adaptive multi-scale (low-pass)

Figure 3.20: Coherence maps of the processed area after range filtering.

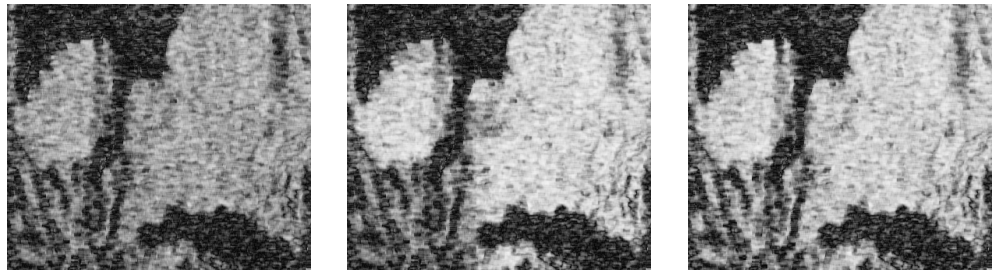

(a) Original **(b)** Adaptive method **(c)** Method based on orbits

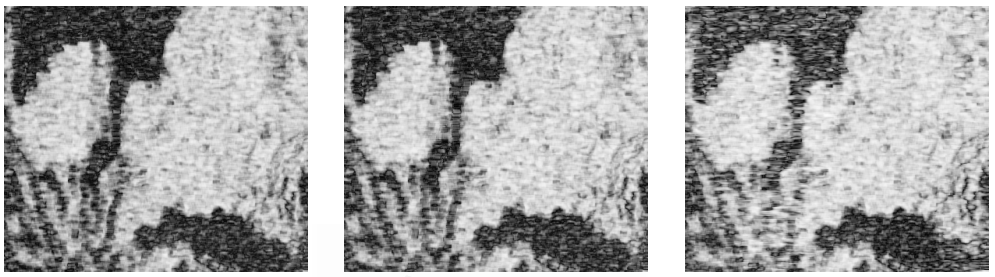

(d) Slope-adaptive **(e)** Slope-adaptive multi-scale (band-pass) **(f)** Slope-adaptive multi-scale (low-pass)

Figure 3.21: Coherence improvement after range filtering in a specific region of interest.

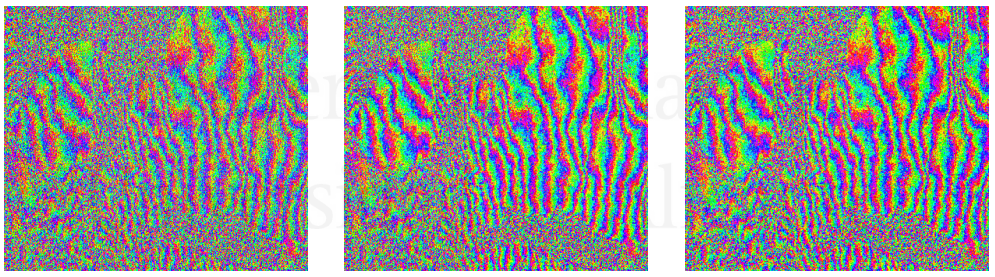

(a) Original **(b)** Adaptive method **(c)** Method based on orbits

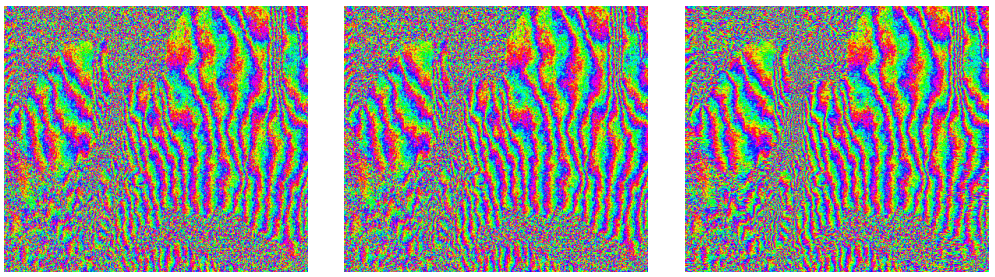

(d) Slope-adaptive **(e)** Slope-adaptive multi-scale (band-pass) **(f)** Slope-adaptive multi-scale (low-pass)

Figure 3.22: Phase quality improvement after range filtering in a specific region of interest.

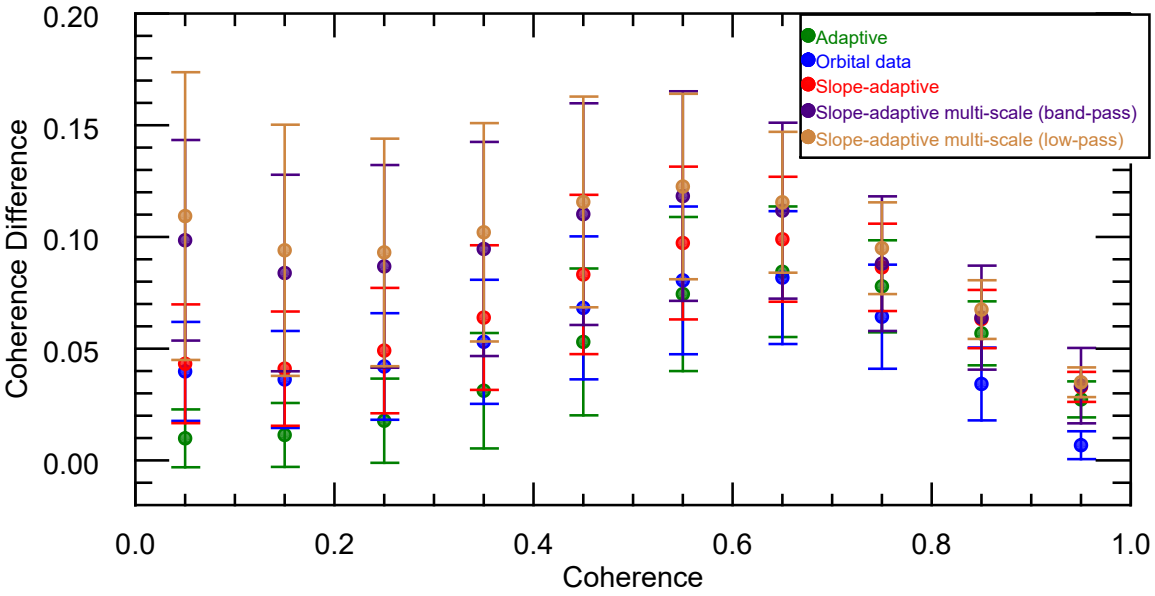

Figure 3.23: Coherence improvement for different intervals of coherence. Ten intervals are selected within $[0, 1]$.

A quantitative measurement of the improvement after range filtering is provided by the so-called *phase residues* [7]. Phase residues correspond to inconsistencies in wrapped phase values, and represent a way to identify erroneous measurements which could produce inaccuracies during the phase unwrapping step. Specifically, residues are detected by computing the local derivatives between adjacent pixels along every dimension. That is, given a phase value φ_i at spatial indexes (p, q), we evaluate:

$$\begin{aligned} r_1 &= W(\varphi_i(p, q+1) - \varphi_i(p, q)), \\ r_2 &= W(\varphi_i(p+1, q+1) - \varphi_i(p, q+1)), \\ r_3 &= W(\varphi_i(p+1, q) - \varphi_i(p+1, q+1)), \\ r_4 &= W(\varphi_i(p, q) - \varphi_i(p+1, q)), \end{aligned} \tag{3.18}$$

where W is the wrapping operator. A residue exists at position (p, q) if the sum of the previous values is not equal to 0, i.e., if:

$$\sum_{i=1}^{4} r_i/(2\pi) \neq 0. \tag{3.19}$$

Table 3.3 shows the remaining residues after range filtering with each method. Both the improvements in the whole area and in the specific RoI shown in Figure 3.22 are detailed.

	Residue number	Improvement
Full area		
Original	1512593	–
Adaptive method	1370349	9.4%
Method based on orbits (constant slope)	1317685	12.89%
Slope-adaptive	1273586	15.80%
Slope-adaptive multi-scale (band-pass)	**1113599**	**26.38%**
Slope-adaptive multi-scale (low-pass)	**1085287**	**28.24%**
Specific RoI		
Original	28960	–
Adaptive method	21524	25.67%
Method based on orbits (constant slope)	20558	29.01%
Slope-adaptive	19546	32.51%
Slope-adaptive multi-scale (band-pass)	**17460**	**39.71%**
Slope-adaptive multi-scale (low-pass)	**16998**	**41.30%**

Table 3.3: Performance analysis of the different range filtering methods in the full processed area and in the specific RoI shown in Figure 3.22.

Concerning the complete area, it is observed that the original number of residues is large, showing that the original phase was considerably degraded by the noise. This is in line with the improvement offered by the adaptive method, which is the worst among all tested range filters as a result of the low-quality original interferogram (from which every spectral displacement is computed). The slope-adaptive method exhibits a larger improvement than the method based on orbits with a constant slope, proving that the inclusion of the slope information positively influences the filtering performance. The largest improvement is clearly obtained with the proposed multi-scale strategy. By looking at Table 3.3, the number of remaining residues is greatly reduced. In fact, the improvement in terms of residues is close to the double of the one of the slope-adaptive method, showing that the multi-scale filter is completely adapted to the local topography so that the filtering performance is greatly enhanced. The major improvement of the proposed method is also obtained in the specific RoI. As shown in Table 3.3, among all filters, the proposed slope-adaptive multi-scale method offers the best result since it is able to reduce the number of remaining phase residues to a greater extent, proving that the proposed methodology maximizes the range filtering performance.

Finally, it is interesting to visualize which window size provided the best result (i.e., the best coherence) in the processed area, so that the utility of testing multiple window sizes is justified. The color map of Figure 3.24 shows the window size which provided the best filtering result in the whole processed area. By comparing Figures 3.15 and 3.24 it is deduced that there is a direct relation between the filtering window size and the local terrain slopes. In fact, it can be clearly observed that small windows (especially of 16 pixels) provide the best result throughout the scene. This was expected since the images correspond to a mountainous area where strong terrain slopes are present.

Only flatter areas benefit from larger window sizes (128 and 64 pixels).

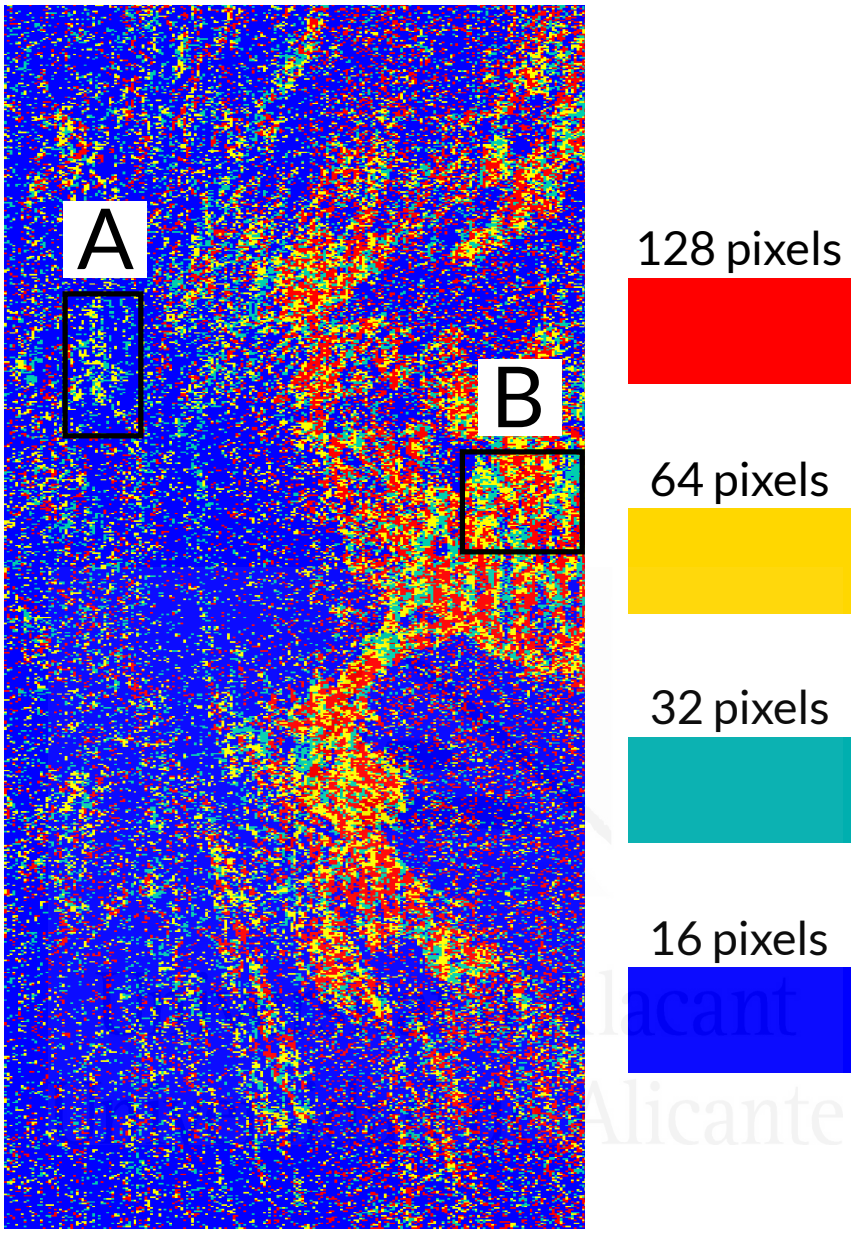

Figure 3.24: Map of the block size providing the best filtering result in the processed area.

This is better visualized if we compare the filtering window sizes and the slopes of the two regions, named as A and B in Figure 3.24. The first one (A) is located near the summit area of Mount Etna, so that strong terrain slopes are present, as shown in Figure 3.25(a). In this case, by looking at Figure 3.25(b), the best filtering results are obtained with small windows (16 and 32 pixels have a clear dominance in this area). In fact, the largest window (128 pixels) is almost never used. On the contrary, in the flat area (B) shown in Figure 3.26(a), larger window sizes (128 and 64 pixels) seems to perform better, since more image blocks have been filtered with these window sizes, as shown with Figure 3.26(b).

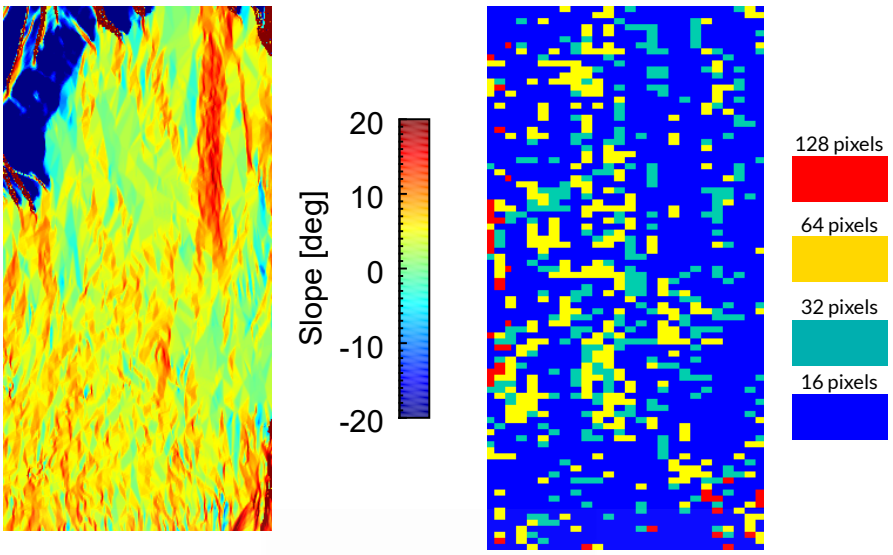

(a) Local terrain slopes in the region of interest.

(b) Window size providing the best filtering result in the region of interest

Figure 3.25: Filtering window size providing the best result in an area where strong terrain slopes are present.

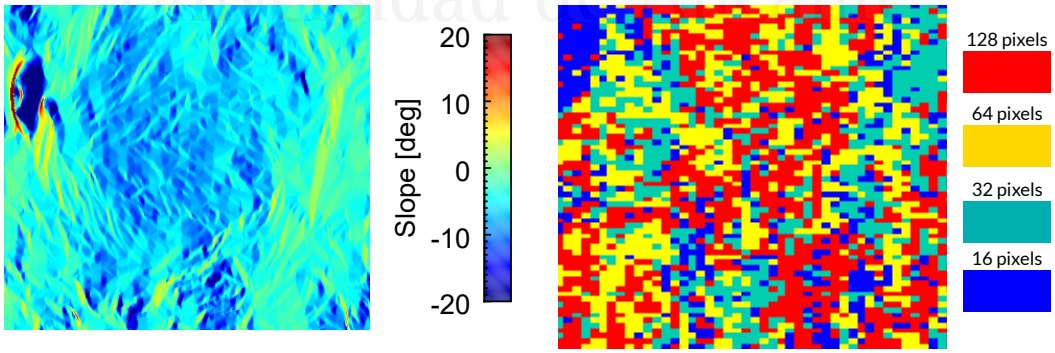

(a) Local terrain slopes in the region of interest.

(b) Window size providing the best filtering result in the region of interest

Figure 3.26: Filtering window size providing the best result in an flat area.

From this study, we have found that conventional range filtering methods are limited in areas with huge topographic variations. The adaptive method has a double drawback: besides the influence of topography, the filter is highly dependent on the original quality of the phase data. Then, the method may not be appropriate in areas as the one shown in this section, since the filtering may be either inaccurate (due to the influence of topography) or unfeasible (due to the SNR). The method based on orbits (geometrical information of the interferometric pair) is less limited, since the images will always be filtered because the spectral displacement is derived from external data. However, if a DEM is not used (i.e., the local slope of the terrain is set to 0°), its solution is not optimum in areas with a rapidly variant topography. Slope-adaptive methods are undoubtedly required. In this regard, the adaptive filter proposed in [77] (assuming that an external DEM is provided) offers overall good results. However, it only partially exploits the slope information derived from the DEM. We have proved that the number of samples used in the filtering process has an influence on the final result. The proposed method goes one step further and, simultaneously, overcomes all the disadvantages of the previous filters and fully utilizes the information derived from an external DEM. We have seen that the proposed strategy, even though it is evidently more computing-intensive than the rest of the filters, is able to completely exploit the DEM and optimize the range filtering step in this kind of complicated areas.

3.2 Interferogram Filtering

Previously mentioned applications of both InSAR and DInSAR, such as DEM generation or geohazards assessment/mapping, may become unfeasible with very deteriorated interferometric data as a result of an important decorrelation. In this context, the development of filtering methods is mandatory to improve the quality of the phase. This improvement is especially needed for the phase unwrapping step, which may be very inaccurate with low-quality and noisy phase data. Accordingly, the second processing contribution developed during this PhD deals with a final interferometric phase filter. Even though it was initially conceived for differential applications, it can evidently also be used in the context of InSAR. It is important to state that the goal of all filtering strategies relies on appropriately removing phase noise while, simultaneously, preserving fine phase details. That is, the original structure of the interferogram must remain unaltered so that useful information is not lost due to overfiltering.

3.2.1 A review of Interferometric Phase Filtering Methods

3.2.1.1 The Goldstein Filter

The well-known *Goldstein filter* [64] [65] is the most common and widely used interferogram filter. As stated in Chapter 1, it has a simple implementation, a high computational efficiency and provides good results. Its working principle consists in dividing the original noisy phase into 2-D blocks of a certain size. Then, the Fourier Transform of each block is weighted by a smoothed version of its intensity. The spectrum of the filtered interferogram is therefore obtained as

$$[\mathbf{S}_f]_{(f_x,f_y)} = |[\mathbf{S}_m]_{(f_x,f_y)}|^{\alpha} \bullet \mathbf{S}_{(f_x,f_y)}, \tag{3.20}$$

where $\mathbf{S}$ is the original spectrum of the interferogram block, $|\mathbf{S}_m|$ is the absolute value of the smoothed spectrum, (f_x, f_y) are the two-dimensional spatial frequencies (in range and azimuth directions), and symbol $\bullet$ denotes the Hadamard or element-by-element multiplication. An important parameter of the filter is α, which is a real number defined in the $[0, 1]$ interval and has the biggest impact on the effectiveness of the final filtering since it defines the weight of the smoothed spectrum with respect to the original spectrum. That is, it is directly proportional to the filtering strength. If $\alpha = 0$, the filtered spectrum will be equal to the original spectrum and no filtering occurs. However, the filtering becomes stronger as the values of α increases. Furthermore, the block dimensions are usually selected as a power of two (32×32, 64×64 pixels ...), in order to accelerate the two-dimensional Fast Fourier Transform computation of each block. Also, an overlap between adjacent patches is usually used. The overlap slows the algorithm execution but avoids discontinuities at the boundaries, which is important to avoid blocking effects in the final phase images.

The smoothing operation is also performed in frequency domain. Specifically, it is achieved by a convolution of the original power spectrum with a predefined square kernel, such as Boxcar (mean)

or Gaussian kernels of a fixed size. An example of a 15×15 Gaussian kernel is shown in Figure 3.27

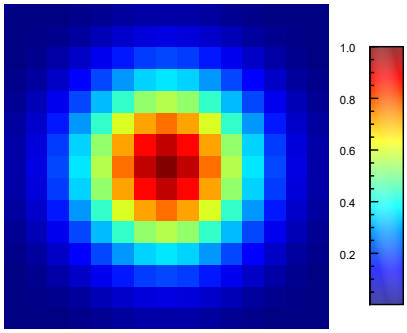

Figure 3.27: 15×15 Gaussian kernel.

The main drawback of the filter is related to the selection of parameter α, as it has to be manually chosen by visual inspection of the original noisy phase. Moreover, the same value of α is used to filter the whole phase, which is clearly non-optimum due to the non-uniform distribution of noise. In this regard, noisy areas benefit from larger values of α, but fixing a value close to 1 could cause a resolution loss, especially in correlated areas where dense fringes are present. Consequently, a value of $\alpha = 0.5$ is usually employed to ensure a balance between noise reduction and resolution preservation.

3.2.1.2 Adaptive Goldstein Filter

An adaptive Goldstein filter was proposed in [66]. In this case, the values of the filtering parameter α were adapted to the noise level of each interferogram block. Accordingly, the values of α become a function of the local coherence (Equation 2.43) as

$$\alpha = 1 - |\bar{\gamma}|, \tag{3.21}$$

where $|\bar{\gamma}|$ is the mean coherence of the effective filtering window. Note that the effective window (non-overlapped area) is always employed to compute $|\bar{\gamma}|$ in order to prevent the mean coherence from being influenced by coherence values from the overlapped and already filtered areas.

With this modification, the main drawback of the original Goldstein filter formulation is, partially, solved. Low-coherence parts of the interferogram are strongly filtered, as the values of α are larger, and high-coherence parts are filtered less, resulting in less oversmoothing effects.

3.2.1.3 Pixel-Based Filtering

Besides the adaptive values of the filtering parameter α, a window-adaptive filter was proposed in [79]. Specifically, this method proposes to individually filter each pixel in the interferogram with windows of different sizes, instead of extracting and filtering phase blocks. The size of each window is selected as a function of the coherence and the phase standard deviation of the whole scene. Note that the relationship between these two variables was previously given with Equation 2.44 and represented

in Figure 2.10. As explained in [79], the window size selected to filter a pixel corresponds to the square root of the multilook number provided by the crossing in Figure 3.28 of the coherence and the standard deviation. For instance, if a pixel's coherence is 0.4 and the computed phase standard deviation of the interferogram is 0.75 radians, the crossing point corresponds to a number of looks equal to 8. Then, the pixel will be filtered with a $\sqrt{8}$ size, which can either be a 3×3 window centered on the pixel or a non-squared window.

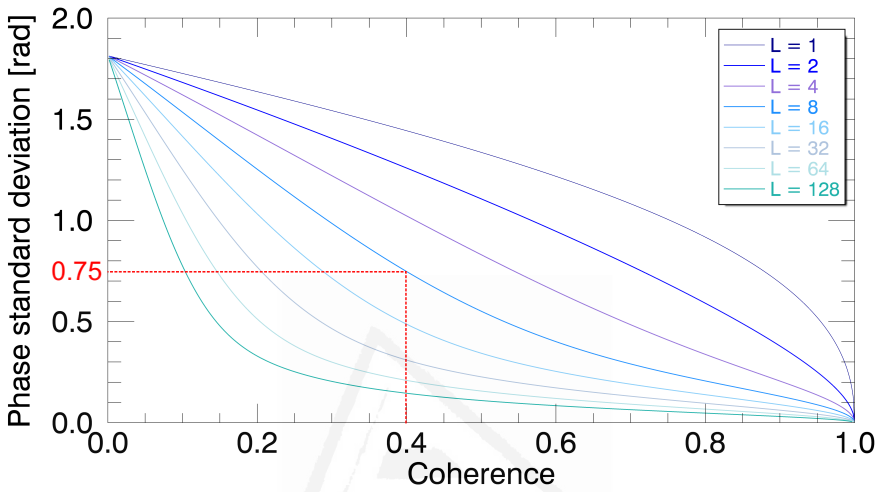

Figure 3.28: Example of selected window size as a function of the coherence and the phase standard deviation in the pixel-based filter.

Additionally, this filter introduces some modifications concerning the spectrum processing. First, local phase gradients in the filtering window are subtracted before filtering. This allows us to center the spectrum and to obtain the dominant frequencies inside the filtering window, which is useful for resolution preservation since they will be added back after smoothing the spectrum . This step will be explained in more detail in Section 3.2.2.2. Then, the spectrum of the compensated samples in the filtering window is multiplied by a 2-D *sinc* function. This allows to retain the dominant frequency components in the filtering window and to remove or greatly attenuate the rest of frequencies (which are deemed as noise). Finally, the filtering parameter is modified to

$$\alpha = 1 - |\gamma|^2, \tag{3.22}$$

being $|\gamma|$ the pixel coherence. This modification increases the filtering strength with respect to the adaptive Goldstein filter described in Section 3.2.1.2 if the same block size is used. However, over-smoothing is avoided since the size of the filtering block is small for coherent pixels as shown in Figure 3.28.

In general, this filter provides acceptable results, especially concerning the preservation of fine phase details (i.e., dense fringes). As shown in [79], the filter preserves the resolution of the original phase very clearly, even in high-density fringe areas. However, it performs worse with very noisy

interferometric phases. This is because the size of the filtering window might not be big enough with very decorrelated data, which results in either an inaccurate estimation of the local fringe frequencies or in an insufficient smoothing. It is worth mentioning that an important issue related to this filtering strategy is that the adaptive window sizes are computed with regard to the phase standard deviation of the whole scene. Unfortunately, a single value of phase standard deviation does not reflect correctly the noise level in all areas of the interferogram, as noise is not uniformly distributed.

3.2.1.4 Recursive Adaptive Spectral Filter (RASF)

In the case of very decorrelated interferometric phases, a complete removal of the noise in combination with an appropriate resolution preservation is a very arduous task. Manual tuning of the filtering parameters would be necessary to obtain an optimum performance (block size, kernel size, etc...). An interesting strategy for this purpose is to filter repeatedly the interferogram. This methodology was proposed in [80].

The core idea consists in applying the coherence-adaptive Goldstein filter with filtering windows of decreasing size in an iterative fashion. Noise suppression is more effective with larger filtering windows, since they provide a better estimate of the power spectrum of the interferogram patch as a large number of pixels are considered in the estimation. Therefore, the smoothing operation is more significant, i.e., the filter is better adapted to the signal. As a consequence, large windows are employed in the first iterations of the algorithm (for instance, a window of 256×256 pixels). Then, the window size is progressively divided in half until it reaches a minimum size, for instance, an 8×8 window. Additionally, it is proposed to use the correlation based only on phases values, usually denoted as phase coherence ρ. As in the case of the coherence estimator shown in Equation 2.43, the phase coherence requires a spatial average of M samples around a pixel neighborhood:

$$\rho = \frac{1}{M}\sqrt{\sum_{m=0}^{M-1}\cos^2(\varphi_m) + \sum_{n=0}^{M-1}\sin^2(\varphi_m)}, \tag{3.23}$$

where φ_m is the m^{th} phase sample. As explained in [80], two different phase coherence maps are computed at each iteration. The final correlation $\hat{\rho}$ value from which the filtering parameter $\alpha = 1-\hat{\rho}$ will be calculated is

$$\hat{\rho} = \begin{cases} \rho - \Delta\rho, & \text{if } \rho^* > \rho \\ \rho^*, & \text{otherwise} \end{cases} \tag{3.24}$$

where ρ is the original phase coherence, ρ^* is the phase coherence after subtraction of the local phase ramp, and $\Delta\rho = \rho^* - \rho$. As it can be deduced from (3.24), the values of the correlation coefficient $\hat{\rho}$ will be, in general, small. The subtraction of the local phase ramp will increase the values of the original phase coherence, i.e. $\rho^* > \rho$. Then, $\rho - \Delta\rho < \rho$, and consequently, the values of α will be larger in comparison to the ones of the modified Goldstein filter. Therefore, the resulting phase

is likely to be more filtered. This iterative filtering strategy has however proved to be very effective in noise reduction, even with extremely noisy interferograms [80], but overfiltering effects are more likely to occur.

3.2.2 Improved Phase Filter Based on an Iterative Method

During this PhD, an improved filter for SAR interferometry has been developed. The goal is to propose a completely adaptive, non-parametric method which is able to suppress phase noise at all levels while, simultaneously, the original spatial resolution of phase images is preserved. In other words, it has to provide a very strong filtering in decorrelated areas while high-coherent areas must remain untouched so that useful interferometric information is not lost by overfiltering. To this end, a *N-step iterative filter*, as the previously explained RASF in Section 3.2.1.4, seems to be the most attractive solution. Then, the proposed method relies on the iterative and adaptive Goldstein approach, but includes major changes which are able to overcome the previously mentioned limitations. In this regard, a specific smoothing kernel derived from the combination of a *Chebyshev interpolator* and the pseudo-inverse is proposed. Also, the subtraction of the local phase ramp is performed at two different steps of the algorithm. On the one hand, it allows to remove any remaining bias which could influence coherence estimations. On the other hand, it allows to remove useful fringe patterns prior to the filtering step, so that only the remaining noise is filtered and the original spatial resolution is preserved. Another important modification consists in smoothing the interferogram in the spatial domain, instead of doing it in frequency domain as with all the previous methods. By doing so, the filtering becomes more significant and results in a more important noise reduction. The block diagram of the developed filter is shown in Figure 3.29. The main steps of the algorithm will be explained in detail in subsections 3.2.2.1 and 3.2.2.2.

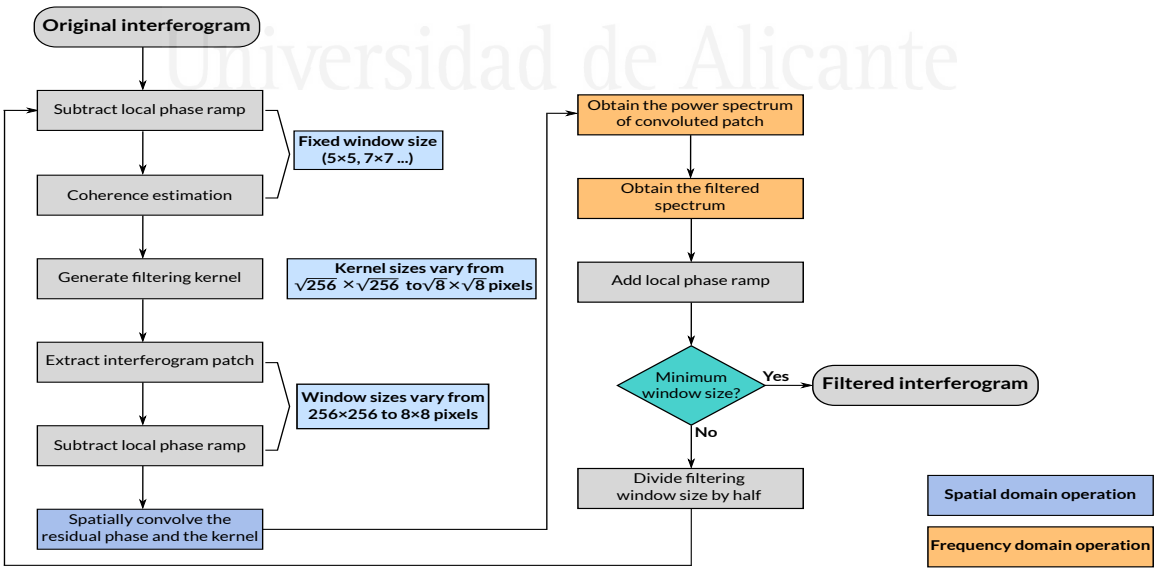

Figure 3.29: General scheme of the proposed filter.

3.2.2.1 Kernel Generation

The Goldstein filter and its variants obtain the filtered interferogram by the inverse Fourier Transform (2D-IFFT) of the product of the smoothed spectrum and the original spectrum, that is, the 2D-IFFT of Equation 3.20. The low-pass operation is also carried out in frequency domain, by means of a predefined kernel. In the proposed filter, the smoothing operation is applied in the spatial domain. Then, the original spectrum is weighted by the spectrum of the smoothed block by means of Equation 3.20, as in the Goldstein filter case.

As previously stated, the filter makes use of a specific smoothing kernel based on the combination of a Chebyshev interpolator and the pseudo-inverse. The idea of testing whether this specific kernel provides better results than others, comes from the fact that Chebyshev interpolators are widely used in Approximation Theory [81], which is concerned with how either known or unknown functions can be approximated by a set of simpler functions. Concretely, Chebyshev nodes, namely the roots of the Chebyshev polynomials of the first kind, are usually used as nodes in polynomial interpolation, due to both their good performance and their minimization of the Gibbs phenomenon [81].

For simplicity, we will start by deriving the kernel in 1-D (i.e., a regular array). Consider a generic 1-D function $F(x)$ defined in $[-1, 1]$. We assume that its value is approximately known at N abscissas x_p, i.e., there exist a set of values $\hat{f}_p$ such that

$$\hat{f}_p \approx F(x_p), \quad (p = 1, 2, \ldots, N), \tag{3.25}$$

for N points $x_p \in [-1, 1]$. The derivation of the convolution kernel is carried out by means of the following steps.

1. First, we assume that $F(x)$ can be well approximated by a Chebyshev sum of order K_x of the form

$$F(x) \approx \sum_{k=0}^{K_x-1}{}' c_k T_k(x), \tag{3.26}$$

where the prime (') indicates that the $k = 0$ summand must be multiplied by $1/2$ (halved), c_k is a set of unknown coefficients, and $T_k(x)$ is the Chebyshev polynomial of the first kind and order k, the trigonometric expression of which is given by

$$T_k(x) \equiv \cos(k \arccos x), \quad |x| \leq 1. \tag{3.27}$$

Chebyshev polynomials can also be obtained by means of the following recurrence relation,

$$\begin{aligned} T_0(x) &= 1, \\ T_1(x) &= x, \\ T_{n+1}(x) &= 2xT_n(x) - T_{n-1}(x). \end{aligned} \tag{3.28}$$

The first seven Chebyshev polynomials of the first kind ($T_0 \dots T_6$) are represented in Figure 3.30.

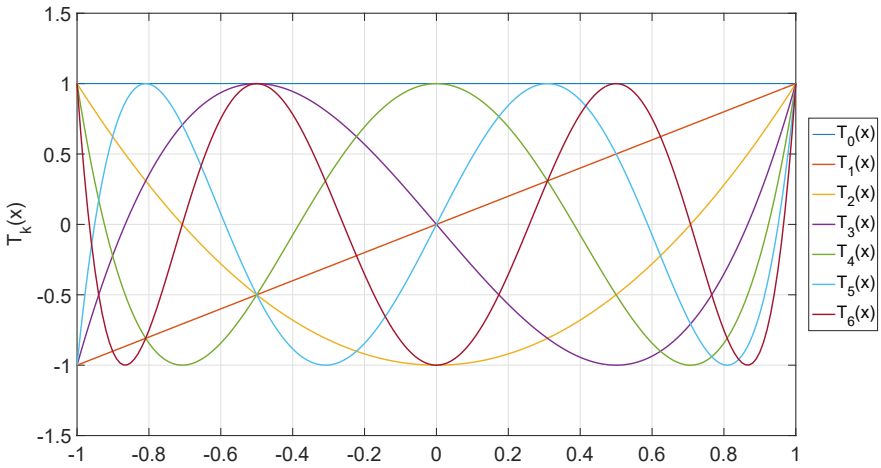

Figure 3.30: Representation of the first seven Chebyshev polynomials of the first kind.

2. Using Equation 3.25 and the model in Equation 3.26, we estimate the set of coefficients c_p using the pseudo-inverse of the linear system implicit in Equation 3.26.

3. For any x, we estimate $F(x)$ by inserting in Equation 3.26 the coefficients c_p obtained in the previous step.

4. If we fix a specific x and the abscissas x_p are regularly spaced, then the previous step delivers a convolution kernel, given that Equation 3.26 depends linearly on the coefficients c_p.

5. Note that all the previous steps can also be applied to a generic function $G(z)$ varying in any interval $[a, b]$, simply by introducing the change of variable

$$x = -1 + 2\frac{z-a}{b-a}. \tag{3.29}$$

In step 1, we have interpolated $F(x)$ using a Chebyshev sum with K_x coefficients. As previously mentioned, this interpolator is well known in approximation theory for its excellent performance. Actually, its minimax error is close to that of the minimax polynomial [81, Th. 6.13], and the interpolator converges to $F(x)$ as K_x increases just assuming that the function is continuous [81, Th. 6.5]. That is, the interpolation error goes to zero as the order increases. In addition, the interpolation allows us to view $F(x)$ as a signal the spectrum of which is the set of coefficients c_k. To see this point, we must recall the basic variable change in Chebyshev interpolation, which is

$$x = \cos\theta, \quad \theta \in [0, \pi]. \tag{3.30}$$

In terms of θ, (3.26) is

$$F(\cos\theta) \approx \sum_{k=0}^{K_x-1}{}' c_k \cos(k\theta_p), \tag{3.31}$$

being

$$\theta_p \equiv \arccos x_p. \tag{3.32}$$

Thus, we are viewing the function as a cosine polynomial. Note that since the cosine is an even function, if $F(x)$ is continuous then $F(\cos\theta)$ is continuous at all θ. In step 2., we use the pseudo-inverse to estimate the coefficients c_k. Specifically, we first combine Equations 3.25 and 3.26 into the linear model

$$\hat{f}_p \approx \sum_{k=0}^{K_x-1}{}' c_k T_k(x_p), \tag{3.33}$$

In matrix notation, the system of Equation 3.33 is of the form

$$\hat{\mathbf{f}} \approx \mathbf{T}\mathbf{c}, \tag{3.34}$$

where

$$[\hat{\mathbf{f}}]_p \equiv f_p,\ [\mathbf{T}]_p \equiv t(x_p),\ [\mathbf{c}]_k \equiv c_k, \tag{3.35}$$

and

$$\mathbf{t}(x) \equiv \begin{cases} T_k(x), & k > 0 \\ 1/2, & k = 0. \end{cases} \tag{3.36}$$

The pseudo-inverse (†) provides the estimate of $\mathbf{c}$

$$\hat{\mathbf{c}} \equiv T^\dagger \hat{\mathbf{f}}, \tag{3.37}$$

that minimizes in the coefficients c_k the quadratic error

$$\sum_{p=1}^{N} \left\| \hat{f}_p - \sum_{k=0}^{K_x-1}{}' c_k \cos(k\theta_p) \right\|^2. \tag{3.38}$$

In step 3, we may estimate $F(x)$ at any point x using coefficients $\hat{\mathbf{c}}$. This estimator is obtained by replacing c_k with the elements of $\hat{\mathbf{c}}$ in Equation 3.26. Its matrix form is

$$\hat{\mathbf{F}}(x) \equiv T(x)^T \hat{\mathbf{c}} = \mathbf{t}(x)^T \mathbf{T}^\dagger \hat{\mathbf{f}}. \tag{3.39}$$

Step 4 is a particular case of step 3, in which we take $x = 0$ and assume that the abscissas x_p are regularly spaced and sorted in increasing order. In this case, we have that the vector multiplying $\hat{\mathbf{f}}$ in Equation 3.39 is a reversed convolution kernel. In other words, if the sequence x_p is infinite, then we

may filter it using the kernel

$$[\mathbf{k}_{ch}]_p \equiv [\mathbf{t}(0)^T \mathbf{T}^\dagger]_{N-p+1}. \tag{3.40}$$

Step 5 is straight forward, given that we may estimate the function by considering the variable change of Equation 3.29,

$$F(x) = G\Big(\frac{b+a}{2} + \frac{b-a}{2}x\Big). \tag{3.41}$$

Now, we may extrapolate the previous formulation to the 2-D case. Consider a two-dimensional function $F(x, y)$, defined in $[-1, 1]$, and a set of samples $\hat{f}_p$ taken at abscissas $x_p,\ y_p, p = 1,\ 2, \ldots,\ N$, we start by introducing a bi-variate Chebyshev model for $F(x, y)$,

$$F(x, y) \approx \sum_{k=0}^{K_x-1}{}' \sum_{r=0}^{K_y-1}{}' c_{k,r} T_k(x) T_r(y). \tag{3.42}$$

We want to estimate the coefficients $c_{k,r}$ such that they verify

$$\hat{f}_p \approx \sum_{k=0}^{K_x-1}{}' \sum_{r=0}^{K_y-1}{}' c_{k,r} T_k(x_p) T_r(y_p). \tag{3.43}$$

In matrix form, this system reads

$$\hat{\mathbf{f}} \approx \mathbf{T}_{2D}\mathbf{c}_{2D}, \tag{3.44}$$

where

$$[\hat{\mathbf{f}}]_p \equiv f_p, \quad [\mathbf{c}_{2D}]_{k+(r-1)K_x} \equiv c_{k,r}, \tag{3.45}$$

and

$$[\mathbf{T}_{2D}]_{p,k+(r-1)N_x} \equiv [\mathbf{t}_x(x_p)]_k [\mathbf{t}_y(y_p)]_r. \tag{3.46}$$

As in the 1-D case, the coefficients' estimate are provided by the pseudo-inverse of $\mathbf{T}_{2D}$

$$\hat{\mathbf{c}}_{2D} \equiv \mathbf{T}_{2D}^\dagger \hat{\mathbf{f}}, \tag{3.47}$$

and the estimate $\hat{F}(0, 0)$ is given by

$$\hat{F}(0, 0) \equiv \mathbf{t}_{2D}(0, 0)^T \mathbf{t}_{2D}^\dagger \hat{\mathbf{f}}, \tag{3.48}$$

where

$$[\mathbf{t}_{2D}(x, y)]_{k+K_x(r-1)} \equiv [\mathbf{t}_x(x)]_k [\mathbf{t}_y(y)]_r, \tag{3.49}$$

and where $\mathbf{t}_x(x)$ and $\mathbf{t}_y(y)$ have respective lengths K_x and K_y, and follow the definition in Equation 3.36.

Then, we assume that abscissas (x_p, y_p) are those in a regular grid of size $N_x \times N_y$ and $N = N_x \cdot N_y$, i.e., they define a regularly-spaced and symmetric grid of points in $[-1, 1] \times [-1, 1]$ of size $N_x \times N_y$,

which corresponds to the size of the convolution kernel (in samples). Abscissas (x_p, y_p) follow the equations:

$$x_p = x_0 + \Delta x(a(p) - 1), \tag{3.50}$$

$$y_p = y_0 + \Delta y(\beta(p) - 1), \tag{3.51}$$

for a fixed position (x_0, y_0) and positive increments Δx and Δy, where $a(p)$ and $\beta(p)$ are the only non-negative integers such that $p = a(p) + N_x(\beta(p) - 1)$ with $0 \leq a(p) < N_x$. For this grid, we obtain from Equation 3.48 the convolution kernel

$$[\mathbf{k}]_{a+1,\beta+1} \equiv [\mathbf{t}_{2D}(0,0)^T \mathbf{t}_{2D}^{\dagger}]_{N-(a+N_x\beta)}, \tag{3.52}$$

where $a = 0, 1, \ldots, N_x - 1$ and $\beta = 0, 1, \ldots, N_y - 1$. In practice, we impose $N_x = N_y$, i.e., we will construct a squared kernel. Also, we assume that the polynomial order in each dimension is the same, that is, $K_x = K_y$.

It is worth mentioning that both the size of the kernel and the polynomial order have an impact on the future filtering results. However, the size of the convolution kernel is more significant. Larger kernels will provide a stronger filtering. For this reason, the size of the convolution kernel will vary in each filtering iteration, as a function of the patch size.

Finally, Figure 3.31 shows an example of some 2-D kernels based on previous formulation.

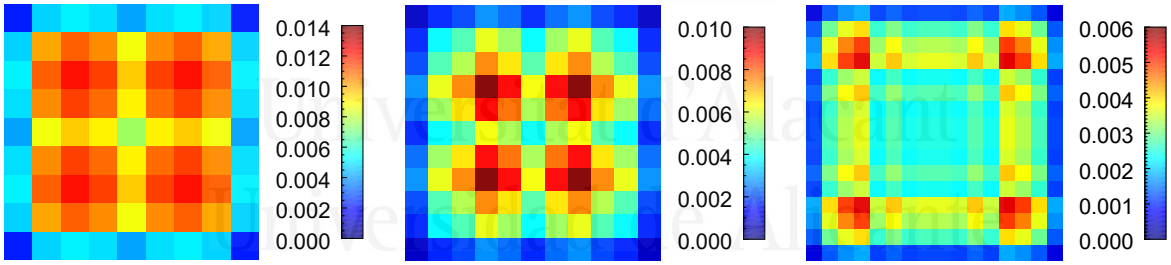

(a) 9×9 kernel of order 15. **(b)** 11×11 kernel of order 20. **(c)** 16×16 kernel of order 25.

Figure 3.31: Example of convolution kernels based on Chebyshev interpolators.

3.2.2.2 Fringe Frequencies' Estimation

Interferograms are characterized by the presence of fringes, which provide information about topography (InSAR) or about strong terrain deformations caused by geohazards (DInSAR). These fringes affect the estimation of the coherence between combined SAR images [82] [43] [55]. As a consequence, any estimation bias should be removed. A simple way to carry this out is to locally estimate the spatial frequencies of the fringes. Although different algorithms can be used [77] [83], the *Maximum Likelihood Estimator* [84] [85] provides accurate results and can be easily implemented. As

detailed in [84], the interferometric phase can be locally modeled by a 2-D sine function. Accordingly, inside a (2P+1)×(2Q+1) window, the signal is of the form

$$\mathbf{Z}_{p,q} = e^{2\pi j(f_x p + f_y q)}, \tag{3.53}$$

being $\{f_x, f_y\}$ the local two-dimensional frequencies at spatial indexes (p, q). Note that the noise term is omitted for simplicity. Then, inside the window centered on pixel (p_0, q_0), the frequency of the fringes can be estimated with

$$\{\hat{f}_x, \hat{f}_y\} = \max_{f_x f_y} \left(\left| \sum_{x=p_0-P}^{p_0+P} \sum_{y=q_0-Q}^{q_0+Q} \mathbf{Z}_{p,q} e^{-2\pi j(f_x p + f_y q)} \right| \right), \tag{3.54}$$

which corresponds to the position of the maximum value of the signal spectrum. It is important to point out that the accuracy of the estimation can be greatly improved by zero-padding the original signal, which results in a finer frequency resolution, at the expenses of a higher computational cost.

Additionally, the main phase component $\hat{\theta}_0$ can be estimated as the Fourier Transform of $\mathbf{Z}$ evaluated at $\{\hat{f}_x, \hat{f}_y\}$ spatial frequencies. That is, the argument of Equation 3.54. It follows that both the estimated 2-D frequencies $\{\hat{f}_x, \hat{f}_y\}$ and the phase θ_0 can be subtracted to obtain a *slope-compensated* or *flattened* interferogram (that is, ideally, an interferogram without fringes), as

$$\hat{\mathbf{Z}}_{p,q} = \mathbf{Z}_{p,q} e^{-2\pi j[(\hat{f}_x p + \hat{f}_y q) - \hat{\theta}_0]}. \tag{3.55}$$

In this regard, without the presence of noise, the values of $\hat{\mathbf{Z}}$ tend to zero, as any residual phase gradient has been removed and any phase offset has also been subtracted from the original phase values. However, in the presence of noise, fringe frequencies should be removed and the remaining phase values should provide a true estimate of the noise present in the original signal.

Finally, this is illustrated with the following examples. Figure 3.32(a) shows a simulated and noise-free phase (256×256 pixels) where fringe frequencies have been added. The associated coherence map, computed with Equation 3.23 and a multilook size of 15×15 pixels, is shown in Figure 3.32(b). The removal of the dominant frequencies is carried out with Equation 3.54 where a window of 8×8 pixels has been used for the estimation. The resulting flattened phase and the estimated fringe frequencies are depicted in Figures 3.32(b) and 3.32(c) respectively. Adding back the estimated fringe pattern and the main phase component yields a result equal to the original phase, as shown in Figure 3.32(d). In addition, this process increases the mean coherence from 0.7201 to 0.9996, which is a more reasonable value since there is no noise. This also clearly shows the impact of the fringes on the estimation of the coherence.

(a) True phase. **(b)** Correlation. **(c)** Flattened phase.

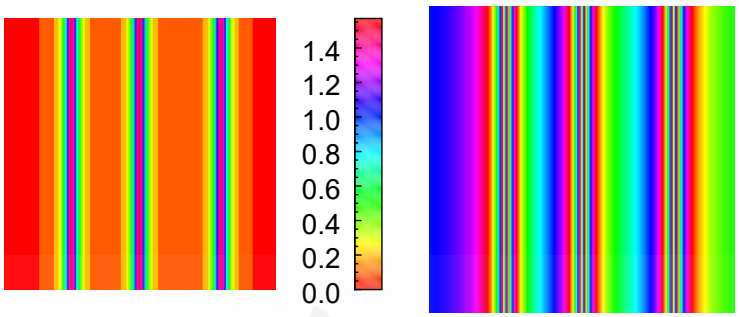

(d) Estimated fringe frequencies **(e)** Fringe frequencies added back.

Figure 3.32: Estimation of local fringe frequencies in the absence of noise. The correlation after subtraction of the local fringes is not shown since it is a completely white image.

The same process is followed in Figure 3.33 with the previous phase but some noise is included (standard deviation of 1 rad). Note how the coherence is increased in the dense fringe areas (in fact, it is globally increased from 0.42 to 0.64). Also, note that the resulting phase in Figure 3.33(d) is correctly 'defringed', even if the estimation is not as accurate as in the previous example, as shown in Figure 3.33(e). It is useful to note that the remaining values reflect the noise level of the original phase (Figure 3.33(d)).

Moreover, it is interesting to visualize that the process has a 'filtering effect' (Figure 3.33(f)), due to the fact that only one frequency is being extracted. As a consequence, a reduction of the noise is obtained if the estimation is correct. However, if the noise obscures the original signal, wrong phase ramps may be estimated (note that even pure noise will have a dominant component in its Fourier Transform). This leads to obtaining wrong fringe frequency estimates and to the appearance of different artifacts, as shown in Figure 3.34(b). Nevertheless, if appropriately integrated into the filtering process, the estimation of the local fringe frequencies is able to provide a good balance between noise reduction and resolution preservation.

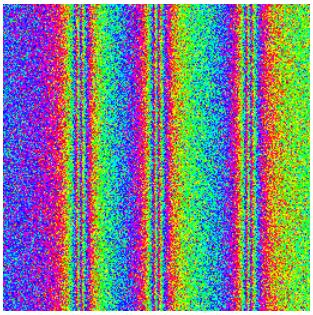

(a) Original noisy phase.

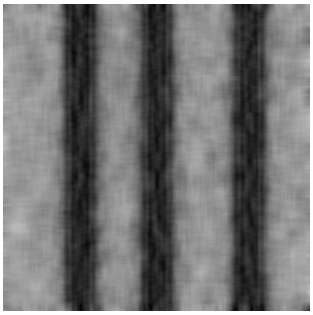

(b) Correlation.

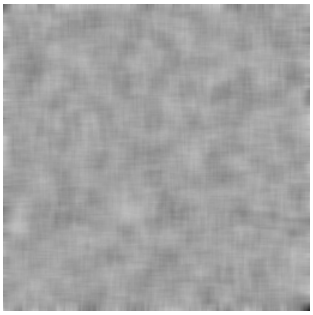

(c) Correlation after subtracting the dominant fringe frequencies.

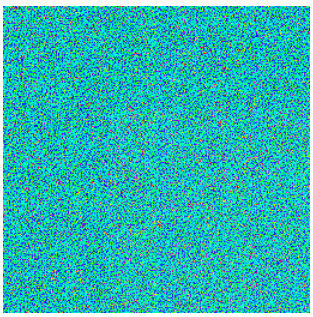

(d) Flattened phase.

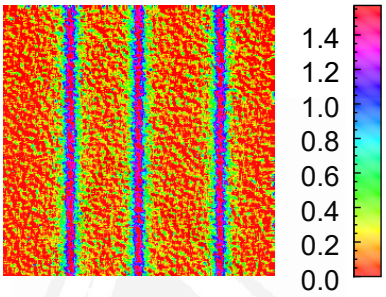

(e) Estimated fringe frequencies

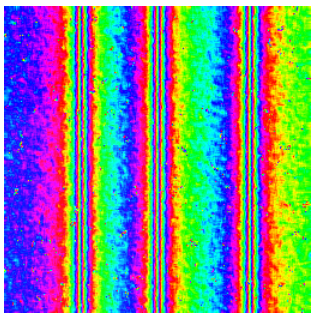

(f) Fringe frequencies added back.

Figure 3.33: Estimation of local fringe frequencies in the presence of a moderate level of noise.

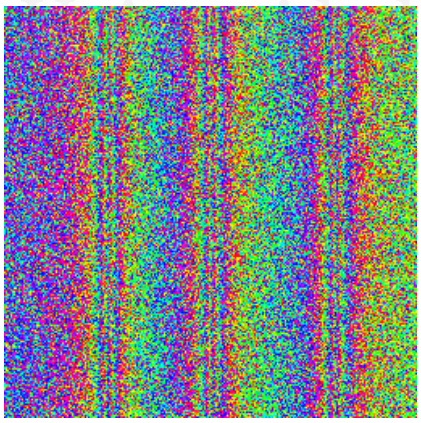

(a) Original noisy phase.

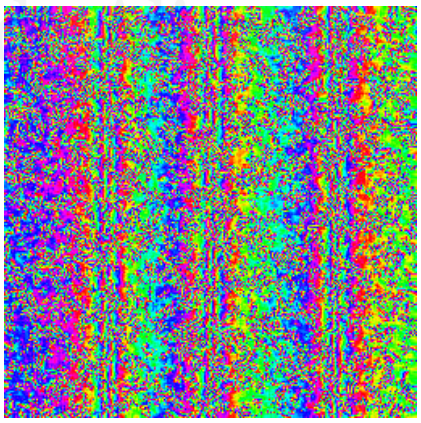

(b) Resulting phase after subtracting and adding back estimated frequencies.

Figure 3.34: Estimation of local fringe frequencies in the presence of a high level of noise.

3.2.2.3 Iterative and Adaptive Denoising

The filter has to be able to completely remove the noise in wide and low-frequency areas, and to preserve the resolution in dense (high frequency) fringe areas. To this end, an *iterative*, *non-parametric* and *completely adaptive* methodology is proposed. The original noisy interferogram is filtered a number of times with decreasing filtering windows. Large windows are employed in the first filter iterations, for instance, a 256×256 window. At each iteration, the filtering window size is reduced by half, until a minimum size of 8×8 pixels is reached. Note that both the initial and final sizes are input parameters of the algorithm, so they can be adapted according to the original quality of the interferogram. That is, more filtering iterations can be used if the original phase is very noisy, whereas a few iterations may be enough with good quality input data. In the last case, an initial size of 64×64 or 32×32 pixels should provide a very good result and has the advantage of being computationally faster.

Moreover, the filtering kernel is also adaptive, so it varies in each iteration of the algorithm. The size of the kernel is set as the square root of the size of the filtering window. Accordingly, it varies from $\sqrt{256}\times\sqrt{256}$ to $\sqrt{8}\times\sqrt{8}$ pixels (rounded to nearest integer). This allows a stronger filtering effect when larger windows are used.

Additionally, the subtraction of the local phase ramp by means of (3.54) and (3.55) is employed in two different steps of the proposed method. First, local fringes are removed from the original phase prior to coherence estimation. In this regard, the removal of the local phase ramp causes an increase in correlation and, hence, coherence values provide a more accurate estimation of the noise level, as shown with the previous simulations in Figures 3.33 and 3.34. This coherence will be used to compute the values of the filtering parameter α in each iteration.

The only parameter that is kept fixed for every iteration is the multilook size, i.e., the number of samples used to estimate the coherence. In this regard, conventional window sizes are used, for instance, 5×5 or 7×7 windows. Note that, as coherence globally increases, the values of α will be smaller than in other methods, but the iterative filtering will progressively denoise the original phase. Also, the local fringes are also removed from the original signal prior to the filtering step, i.e., when an interferogram patch is extracted. Then, only the spectrum of the remaining values (which are deemed as noise) is filtered, so the information related to the deformation fringes is better preserved.

Finally, the whole process is illustrated with Figure 3.35 where a single block of simulated phase is filtered with a single iteration. Note that the fringes are properly removed before filtering (Figure 3.35(b)) so that only the remaining noise is filtered with a spatial convolution with the kernel. The filtered phase in Figure 3.35(e) is obtained in frequency domain by applying Equation 3.20, and the final result is obtained after adding back estimated fringe frequencies from the original noisy phase.

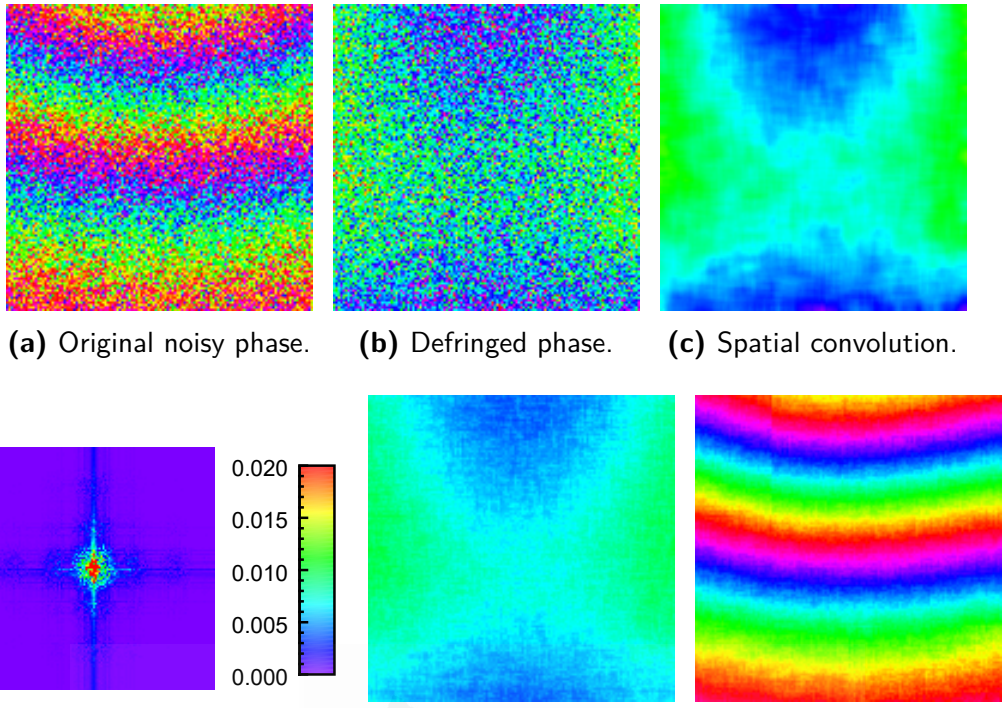

(a) Original noisy phase. **(b)** Defringed phase. **(c)** Spatial convolution.

(d) Smoothed spectrum. **(e)** Filtered phase. **(f)** Final result.

Figure 3.35: Filtering process of a single block with the proposed algorithm. The mean coherence, estimated with a 5×5 window, of the block is 0.652 and the filtering parameter α is 0.348.

3.2.3 Results

This section is devoted to validate the effectiveness of the proposed filter with different datasets. Both simulated data and real interferograms are used. The performance of the filter is compared quantitatively with different, state-of-the-art methods described in the previous Section 3.2.1.

3.2.3.1 Synthetic Datasets

A synthetic interferogram is generated as the sum of a smooth function, corresponding to a 2-D Gaussian distribution, and a highly-variant (high frequency) 2-D arctangent function. The smooth surface can be generated according to

$$S_{low} = 3(1-x)^2 \cdot e^{-(x^2)-(y+1)^2} - 10\left(\frac{x}{5} - x^3 - y^5\right) \cdot e^{-x^2-y^2} - \frac{1}{3} \cdot e^{-(x+1)^2-y^2}, \tag{3.56}$$

and the high frequency surface is simply simulated with

$$S_{high} = \arctan(x). \tag{3.57}$$

The high gradient function will be especially useful to detect overfiltering effects. Visually, the simulated phase is shown in Figure 3.36(c). The size of the data is 1000×1000 pixels.

(a) Smooth 2-D Gaussian function.

(b) Variable and increasing high frequency phase.

(c) Simulated phase.

Figure 3.36: Noise-free synthetic phase.

Then, different levels of noise are added to the original phase. For the sake of simplicity, noise is uniformly added by fixing a certain standard deviation, which is computed as a function of the coherence and the number of looks by means of Equations 2.44 and 2.45. Specifically, a number of looks $L = 9$ has been fixed and four different values of mean coherence $|\bar{\gamma}|$ are set. This yields the four noise standard deviations shown in Table 3.4, which vary from 0.509 rad and 2.569 rad. Note that the largest standard deviation has been manually set to test the performance of every method in an extremely noisy scene, since this value is out the limit derived from Equations 2.44 and 2.45, which is about 1.8 rad.

Interferogram	$\lvert\bar{\gamma}\rvert$	L	σ_φ [rad]
I_1	0.50	9	0.509
I_2	0.30	9	0.941
I_3	0.15	9	1.367
I_4	–	–	2.569

Table 3.4: Characteristics of the four simulated interferograms.

The performance of all filters is assessed by the number of residues [7], previously introduced in Section 3.1.3 Moreover, the advantage of testing simulations is that the true phase is known. Consequently, another quantitative measure of the filtering performance is given by the mean square error (MSE), which provides a quantitative measure of the difference between the true (noise-free) phase and the filtered phase. A 'perfect' filtered interferogram is obtained if $MSE = 0$, and larger MSE values indicate a poor filtering performance. This error can be calculated as

$$MSE = E\left\{|arg(e^{j(\varphi_F - \varphi_{true})})|^2\right\} \tag{3.58}$$

where φ_F is the filtered phase and φ_{true} is the noise-free phase. It is important to stress that in order to correctly compare the performance of all filters, the same parameters have been employed when

possible, i.e., when a common parameter value can be used. Accordingly, the original Goldstein, its adaptive version and the RASF filters use the same 7×7 Gaussian kernel as the smoothing operator. The spatial bandwidth of the Gaussian kernel is 2.5. Regarding the pixel-based algorithm, the power spectrum is weighted with a 3 × 3 *sinc* function, as proposed in [79]. In the proposed method, an adaptive kernel is generated at each filtering iteration, and its size varies as a function of the filtering window size, as previously mentioned. Moreover, all the block-based filters employ an overlap of 3/4 of the size of the filtering window. This means that the window advances 1/4 of its size between two consecutive patches. The rest of the filtering parameters are summarized in Table 3.5.

Filter	**Window size (pixels)**	**Coherence estimation (pixels)**	**Filter parameter α**
Goldstein	256×256	5×5	0.9
Adaptive Goldstein	256×256	5×5	Adaptive
Pixel-based	Adaptive	5×5	Adaptive
RASF	256×256 to 8×8	5×5	Adaptive
Proposed method	256×256 to 8×8	5×5	Adaptive

Table 3.5: Filtering parameters of each method.

Note that a patch size of 256 × 256 pixels has been used in both the original Goldstein and adaptive Goldstein filters. This patch size is larger than the one proposed in the original publications [64] [66], which is 32 × 32 pixels. The reason of using this patch size is to enhance the result provided by both conventional methods. As stated previously, larger filtering windows offer better results in noise reduction. Consequently, filtering results with a 32 × 32 window would have provided worse results in terms of noise reduction and residues elimination, and the comparison with the rest of the methods would not have been fair.

Figure 3.37 shows the filtering results of the interferogram named I_1 in Table 3.4, which is the one with the highest quality. All the filters show good results in this case, and the noise is almost completely suppressed. Fringe continuity is preserved with all the adaptive methods but not with the standard Goldstein filter, where oversmoothing effects are clearly visible in the dense fringe area of the central part of the interferogram. This illustrates the need of using adaptive filtering, since some fringes are lost due to the large value of α (0.9). This value of α certainly provides an optimum result in wide areas of the image, where noise reduction is almost total, and the filtered phase is identical to the true phase since the filter is strong even if the phase quality is already high. This can be observed, for instance, in the bottom right corner or Figure 3.37(b). However, a value of α of 0.9 is not suited for high-frequency areas, and the phase will be inevitably overfiltered. Table 3.6 summarizes the quantitative results according to both quality criteria previously detailed. We can see that the few residues in the original phase are reduced to 0 in all cases. Among them, the proposed filter has the best result in terms of MSE.

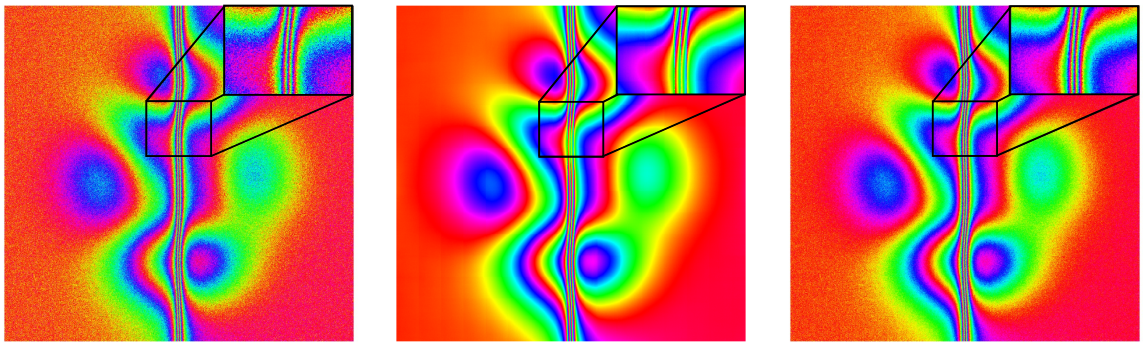

(a) Original noisy phase. **(b)** Goldstein. **(c)** Adaptive Goldstein.

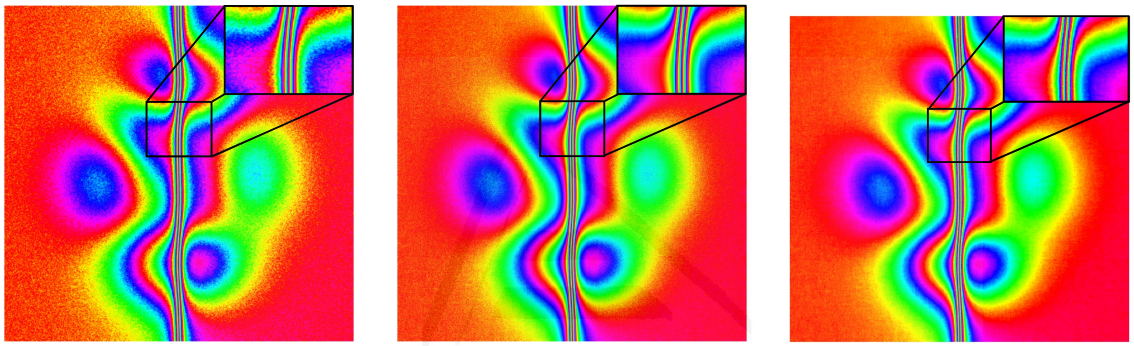

(d) Pixel-based. **(e)** RASF. **(f)** Proposed method.

Figure 3.37: Filtering results of the first simulation with different methods.

	Residue number	Improvement	MSE
Interferogram I_1			
Original	86	–	0.264
Goldstein	0	100%	0.019
Adaptive Goldstein	0	100%	0.081
Pixel-based	0	100%	0.063
RASF	0	100%	0.031
Proposed method	**0**	**100%**	**0.011**

Table 3.6: Performance analysis of different filters with the first simulation.

Results of filtering interferogram I_2 are shown in Fig. 3.38. Note that a phase standard deviation of 0.941 clearly worsens the quality of the original phase and the noise level is noticeably higher than in the previous simulation.

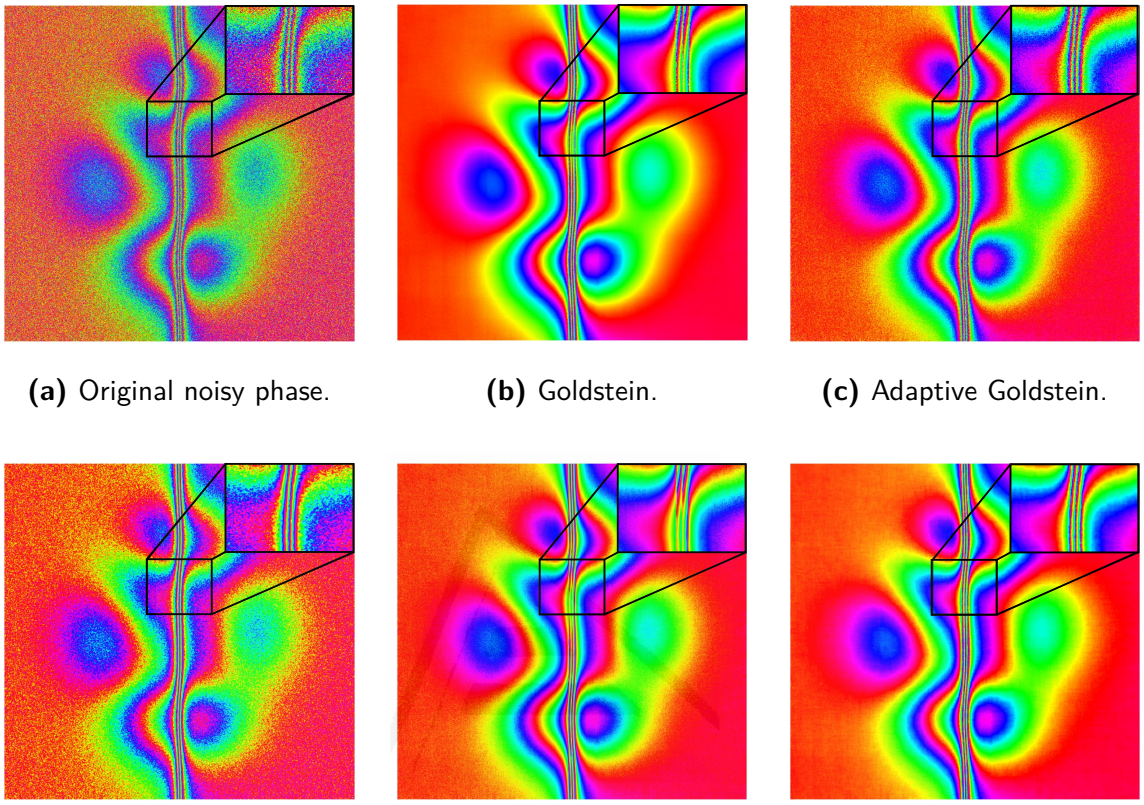

(a) Original noisy phase. **(b)** Goldstein. **(c)** Adaptive Goldstein.

(d) Pixel-based. **(e)** RASF. **(f)** Proposed method.

Figure 3.38: Filtering results of the second simulation with different methods.

Although noise is almost completely suppressed with the original Goldstein method, some fringes are lost in the central area due to overfiltering. Concerning the adaptive Goldstein and the pixel-based filters, they both show good results, especially in fringe preservation. However, noise reduction is not as effective as with the RASF and the proposed iterative method.

This simulation is also useful to prove that if not properly controlled, an iterative algorithm entails the risk of filtering too much. This can be observed by comparing Figures 3.38(e) and 3.38(f). Although both iterative methods offer the best results in noise suppression, the proposed filter is able to simultaneously preserve useful fringe information without altering the original phase structure. This optimum performance is also shown in terms of residues and MSE values in Table 3.7. The proposed method is able to completely eliminate phase residues and yields the best MSE value.

Then, according to these two simulations, we can deduce the proposed filter offers a larger improvement whenever the phase gradient or the noise are high, proving that it achieves the best balance between noise suppression and fringe preservation, in comparison with the rest of methods.

	Residue number	Improvement	MSE
Interferogram I_2			
Original	66391	–	0.941
Goldstein	164	99.75%	0.022
Adaptive Goldstein	442	99.33%	0.091
Pixel-based	2627	96.04%	0.253
RASF	12	99.98%	0.041
Proposed method	**0**	**100%**	**0.019**

Table 3.7: Performance analysis of different filters with the second simulation.

The third simulation corresponds to interferogram I_3. Filtering results are represented in Figure 3.39 and the improvement in terms of residues and MSE is summarized in Table 3.8. As shown in Figure 3.39(a), the noise level is very high and the spatial continuity of the fringes is not that clear since the noise obscures these parts of the signal. This is also reflected with the large number of residues present in the original phase.

As it can be observed in Figures 3.39(b) and 3.39(c), both the standard Goldstein and its adaptive version exhibit almost the same performance as a result of the low coherence values, which make the filtering parameter α to be large and, hence, the filtering strong. The number of residues is also similar for these two filters.

In the pixel-based filter, the size of the individual filtering windows is not enough to completely suppress the noise with just a single filtering operation, as shown in Figure 3.39(d). The number of residues of the filtered interferogram is the largest among all the filtering methods and so is the MSE, showing that the performance of the pixel-based filter is limited with very noisy input phases.

The RASF and the proposed filter show the best results in terms of residues and MSE, but none of them is able to correctly preserve the fringes of the central part of the phase. Between both, the RASF exhibits more discontinuities than the proposed method. In this regard, in the presence of a high level of noise, the estimation of the local phase ramps becomes a very challenging task, as previously mentioned in Section 3.2.2.2. Consequently, a complete noise reduction, which requires the use of larger filtering windows, along with fringe preservation, which benefit from smaller windows, is nearly unattainable and the phase is more likely to be overfiltered.

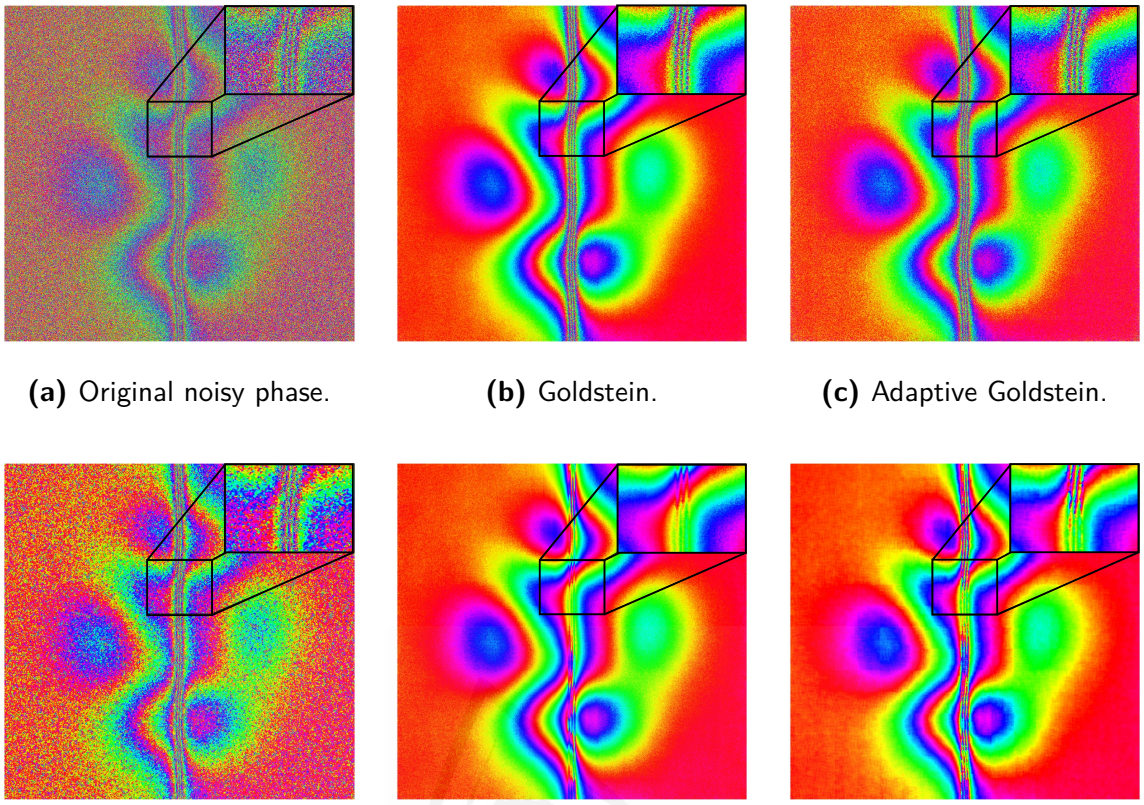

(a) Original noisy phase. **(b)** Goldstein. **(c)** Adaptive Goldstein.

(d) Pixel-based. **(e)** RASF. **(f)** Proposed method.

Figure 3.39: Filtering results of the third simulation with different methods.

	Residue number	Improvement	MSE
Interferogram I_3			
Original	264907	–	2.135
Goldstein	6600	97.51%	0.117
Adaptive Goldstein	8519	96.78%	0.228
Pixel-based	52034	80.36%	1.043
RASF	95	99.96%	0.094
Proposed method	**71**	**99.97%**	**0.080**

Table 3.8: Performance analysis of different filters with the third simulation.

The result can be enhanced by fixing a smaller initial size of the filtering window. Figure 3.40 shows the resulting phases after applying the proposed method with smaller initial window sizes. As expected, noise suppression becomes less effective with smaller windows, but the phase is less likely to be overfiltered and the fringes are better preserved. When an initial window size of 64×64 or 32×32 is used, the detailed features in the central part of the image are correctly preserved, but noise is less reduced in low-frequency areas. Nevertheless, noise reduction is still very effective and the improvement is quite remarkable, as Figures 3.40(b) and 3.40(c) show. It is worth mentioning

that the frequency of the simulated fringes by means of the arctangent function is extremely high and, in practice, such abrupt phase changes are usually not present in real SAR interferograms. However, it is convenient to test the algorithm with both extreme noise levels and strong phase gradients.

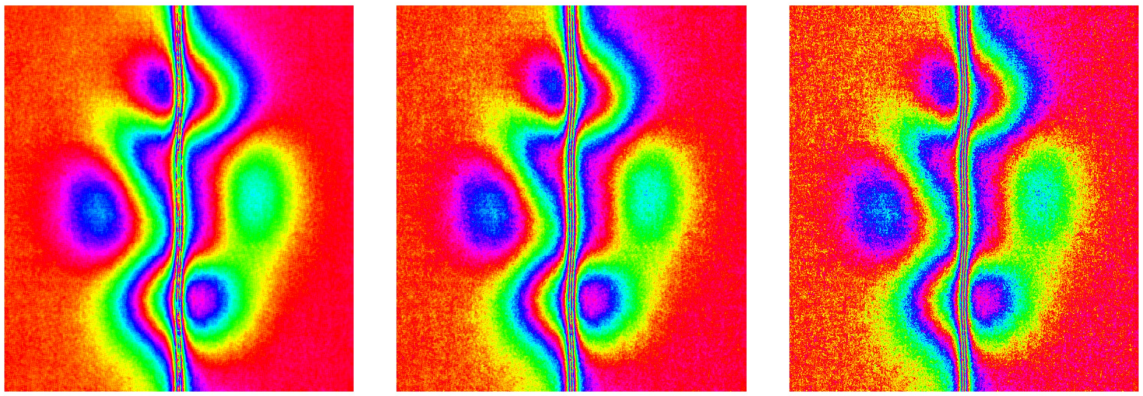

(a) 128×128. **(b)** 64×64. **(c)** 32×32.

Figure 3.40: Filtering results of the third simulation with the proposed method with different initial window sizes.

Finally, the last simulation corresponds to an extremely noisy interferogram where a very high standard deviation has been used to add noise to the original data. All the filtering results are represented in Figure 3.41. Apparently, the original phase seems to be pure noise, so that the phase structure is completely masked by the noise, as shown in Figure 3.41(a).

As in the previous simulation, the Goldstein filter and the modified Goldstein filters offer the same results, as the coherence values are close to 0, making the filter parameter α very close to 1.

However, both filters do not recover useful measurements (even with a 256×256 filtering window) and the original and filtered phases seem to be the same. Concerning the pixel-by-pixel filter, the maximum window size has been used to filter each pixel in the image. Noise reduction is almost negligible with this filter.

As it can be seen in Figures 3.41(e) and 3.41(f), both iterative filters are able to greatly suppress the noise and, at least, to recover some parts of the original signal. Moreover, the proposed method shows a better performance in the spatial smoothness of the phase values, whereas the RASF filter presents some artifacts and more discontinuities in the filtered phase. Obviously, the recovering of the detailed fringes is almost unfeasible with such a degraded original interferogram. The filtering results for this interferogram are summarized in Table 3.9. As expected, only the iterative methods present a major improvement in terms of the final number of residues. It can be observed that the proposed filter offers again the best result in terms of residues and MSE. Instead, the improvement is much less significant with the other three filters.

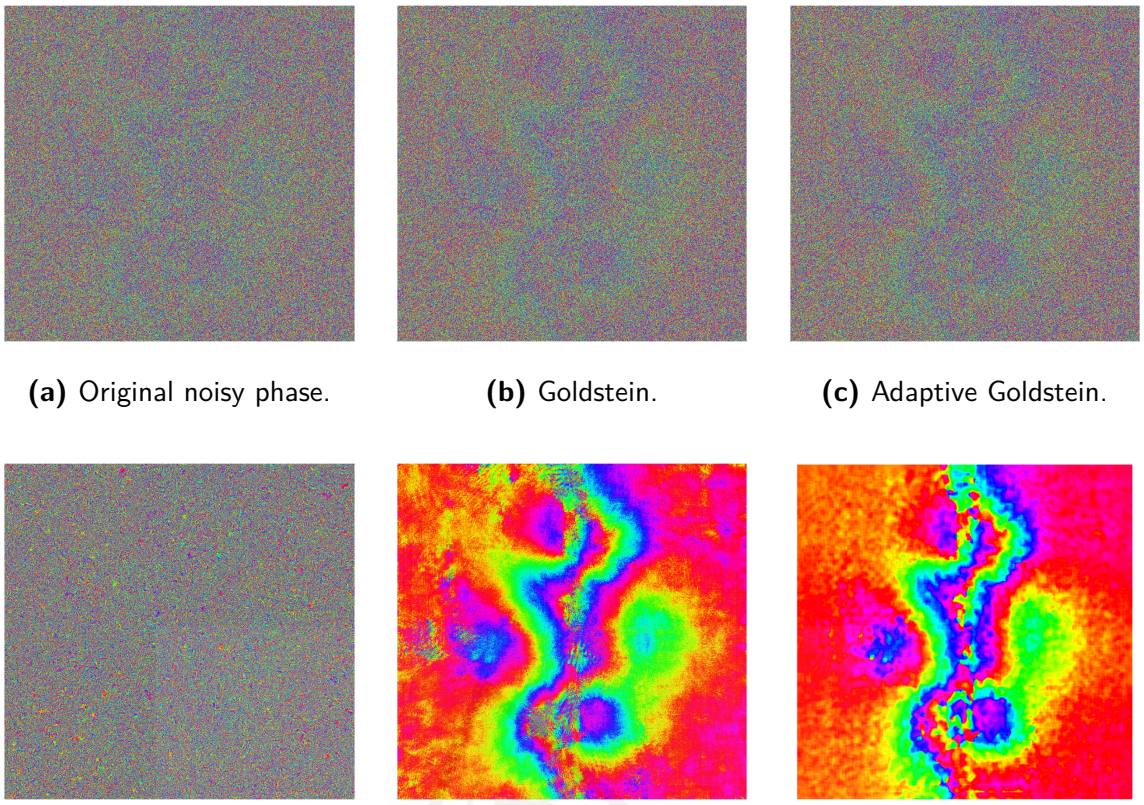

(a) Original noisy phase. **(b)** Goldstein. **(c)** Adaptive Goldstein.

(d) Pixel-based. **(e)** RASF. **(f)** Proposed method.

Figure 3.41: Filtering results of the fourth simulation with different methods.

	Residue number	**Improvement**	**MSE**
Interferogram I_4			
Original	331415	–	3.145
Goldstein	328696	0.82%	3.068
Adaptive Goldstein	328654	0.83%	3.069
Pixel-based	269945	18.55%	3.147
RASF	4293	98.71%	0.523
Proposed method	**863**	**99.73%**	**0.401**

Table 3.9: Performance analysis of different filters with the fourth simulation.

3.2.3.2 Comparison with Conventional Kernels

It is important to mention that the effectiveness of the proposed method not only relies on the use of the specific smoothing kernel. In this regard, interferogram I_3 has been filtered using the proposed scheme but with different smoothing kernels. Specifically, besides the proposed kernel based on Chebyshev polymomials, a Gaussian and a mean kernel have also been tested. To provide a better comparison, a single filtering iteration using a block size of 32×32 pixels has been used. According to the proposed formulation, the size of each kernel is 6×6 pixels (closest integer to $\sqrt{32}$). The re-

sulting phases are shown in Figure 3.42 and the quantitative results are summarized in Table 3.10. By comparing Figure 3.42(a) with Figures 3.42(b) and 3.42(c), it is clearly appreciated that the proposed kernel offers a more significant smoothing effect, which is translated into a stronger noise reduction and a better overall quality of the phase. This better performance is also reflected in terms of residues and MSE values, as shown in Table 3.10. However, it must be pointed out that conventional kernels provide an acceptable result, proving that the complete iterative strategy, involving each step of the block diagram of Figure 3.29, can also be applied with conventional kernels with similar results.

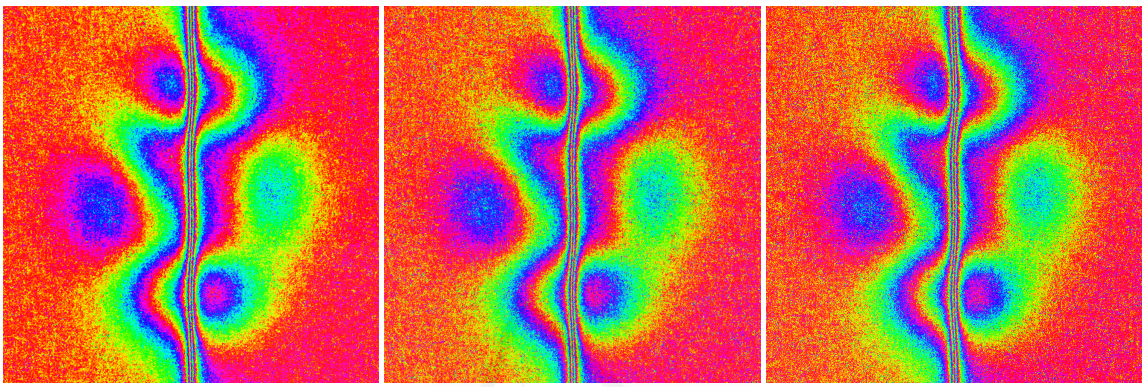

(a) 6×6 proposed kernel. **(b)** 6×6 mean kernel. **(c)** 6×6 Gaussian kernel.

Figure 3.42: Filtering results of the third simulation with three different kernels.

	Residue number	Improvement	MSE
Interferogram I_3			
Original	264907	–	2.135
Gaussian kernel	16701	93.58%	0.454
Mean kernel	13244	94.92%	0.407
Proposed kernel	**2231**	**99.14%**	**0.212**

Table 3.10: Performance analysis of the proposed method with three different filtering kernels.

3.2.3.3 Results with Real Data

Different real SAR interferograms have been processed to test the performance of the proposed method and to compare its advantage over conventional filters. It is important to point out that the filtering parameters are the same as the ones of the previous simulations, which were summarized in Table 3.5.

It is also important to note that, since a true phase is not available with real data, only phase residues provide a quantitative measure of the performance of each filter. In all cases, each filter is tested with the original interferogram at full resolution. That is, there is no previous filtering (such as a multilook) so that the noise suppression capability of each filter can be truly evaluated.

All the real data mapped a sudden geophysical event, such as a volcanic eruption or an earthquake. Accordingly, the *co-seismic* or the *co-eruption* pair will be processed. That is, we will analyze the interferogram formed by two images which embrace the earthquake or the volcanic occurrence (i.e., the first image was gathered before and the second one after the event). Consequently, each differential interferogram to be filtered reflects a strong deformation pattern of the Earth surface caused by the associated tectonic or volcanic activity.

The first real dataset corresponds to a differential interferogram mapping the Mount Etna's volcanic eruption in May 2008. Etna is the highest active volcano in Europe, located in the eastern coast of Sicily (Italy) in the Metropolitan City of Catania. Its geographic location was previously shown in Figure 3.13.

The analyzed interferogram is the result of the combination of two images which were acquired in dates 2008-05-05 and 2008-05-29 by RADARSAT-2 in beam mode FQ29. The near and far range incidence angles are 46.8° and 48.0°, respectively. The size of the processed scene is 3300×6000 pixels in range and azimuth respectively, and the polarimetric channel is HH+VV.

All filtered differential phases are represented in Figure 3.43 and the quantitative evaluation of the results is shown in Table 3.11. It can be seen in Figure 3.43(a) that the original data present a very high degree of decorrelation throughout the scene. This can be mainly due to temporal decorrelation, since the images are acquired at a revisit time of 24 days, and due to the presence of vegetation in the area. This is translated into a very large number of phase residues (almost 20% of the total number of pixels), as shown in Table 3.11.

A visual inspection of Figure 3.43(d) shows that the pixel-based method is not able to properly remove the noise with decorrelated input data. This is also deduced from the large number of residues that the filtered phase still has. Concerning the Goldstein filter and its adaptive algorithm, the filtered phases of which are shown in Figures 3.43(b) and 3.43(c), the improvement in noise reduction is noticeable but the number of phase residues remains relatively high. Furthermore, from Figures 3.43(e) and 3.43(f), it is deduced that noise can only be almost completely suppressed by filtering the original interferogram multiple times. In this regard, both the RASF and the proposed method show an extraordinary result. However, the RASF-filtered phase still has some artifacts and discontinuities whereas the resulting phase with the proposed method is cleaner, smoother and more spatially continuous, and the strong phase gradients caused by the deformation are properly preserved. This better performance is also reflected in terms of residues' suppression. As shown in Table 3.11, the proposed filter offers the best result and is able to almost completely eliminate all the original phase residues. In fact, only 1657 residues are finally detected, which is approximately 10 times less than with RASF.

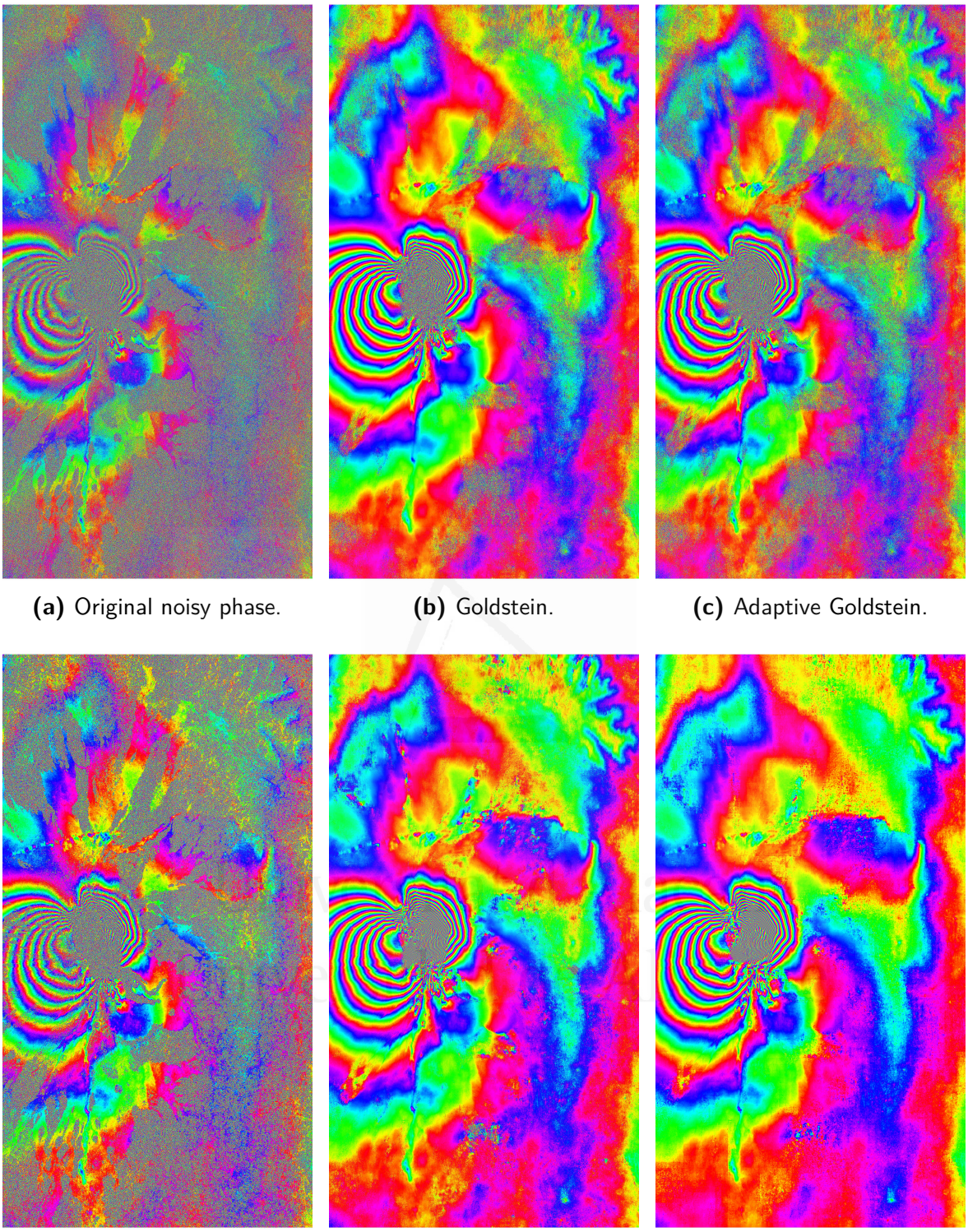

(a) Original noisy phase. **(b)** Goldstein. **(c)** Adaptive Goldstein.

(d) Pixel-based. **(e)** RASF. **(f)** Proposed method.

Figure 3.43: Filtering results of the RADARSAT-2 dataset with different methods.

Interferogram	Residue number	Improvement
Original	3794446	–
Goldstein	480836	87.33%
Adaptive Goldstein	917458	75.82%
Pixel-based	1632938	56.97%
RASF	17981	99.52%
Proposed method	**1657**	**99.96%**

Table 3.11: Performance analysis of different phase filters for RADARSAT-2 dataset.

Moreover, it is interesting to check the improvement in terms of coherence. Figure 3.44 shows the histograms of differential coherence before and after filtering with each method. The proposed method offers the largest improvement, followed by the other iterative method (RASF). In fact, before filtering, 68% of pixels had a coherence value below 0.5. After filtering with the proposed algorithm, only 0.6% of pixels (specifically, 132220 out of a total of 19800000 pixels) have a coherence below this threshold. Finally, Figure 3.45 shows the visual impact on the differential coherence maps after filtering the data with the proposed method. It can be seen that the coherence is greatly increased throughout the whole area. Only the zone around the volcano crater (in the central part of Figure 3.45(b)), still presents low coherence values due to the presence of filtering artifacts (fringes) caused by the extreme decorrelation in the original data in this specific area.

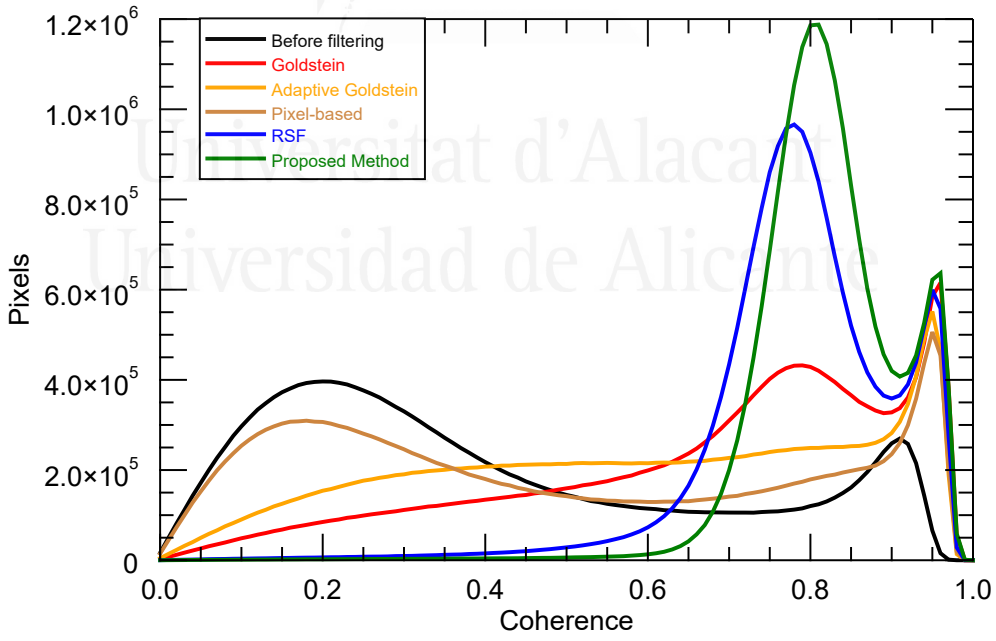

Figure 3.44: Coherence histograms of the RADARSAT-2 dataset before and after filtering with each method.

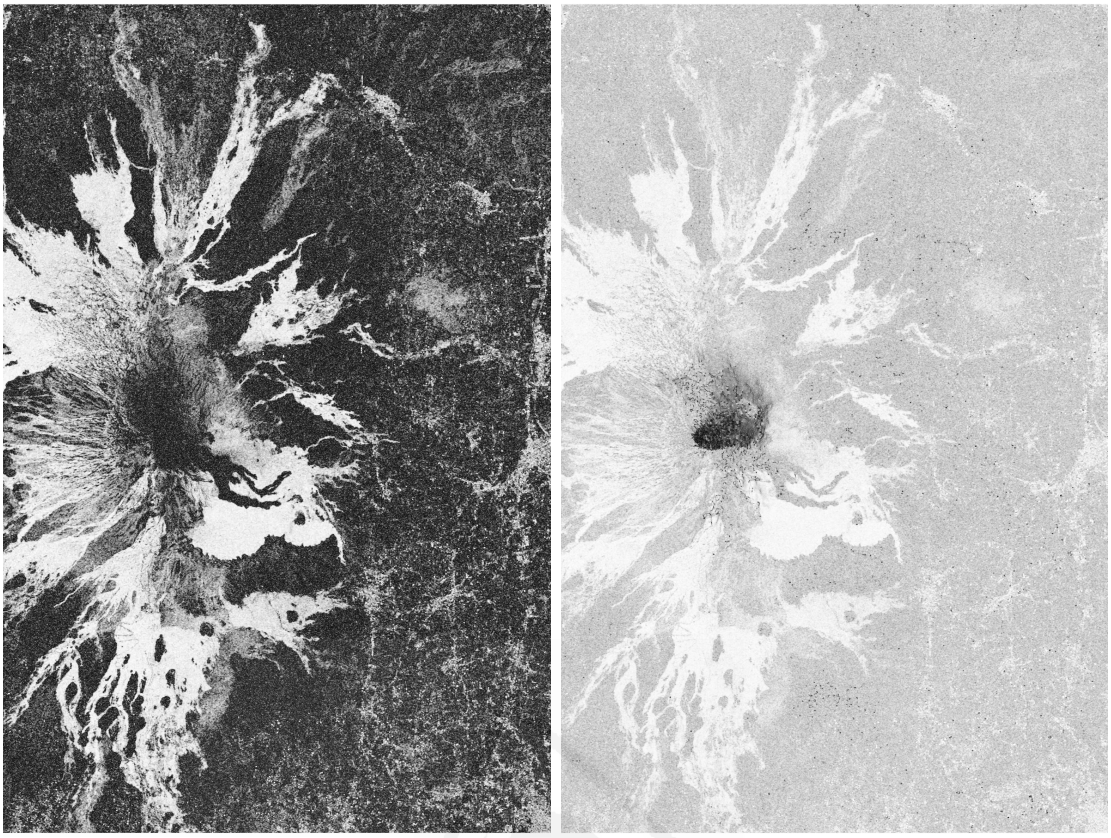

(a) Original coherence. **(b)** Coherence after filtering.

Figure 3.45: Differential coherence maps before and after filtering the RADARSAT-2 dataset with the proposed method. Coherence was estimated with a 7×7 boxcar kernel.

Another dataset from a different sensor is also shown. Specifically, an interferogram mapping the Kilauea volcanic eruption of March 2011 has been processed. Kilauea is one of the world's most active volcanoes, and it has been erupting almost continuously since 1983. Kilauea volcano on Hawaii's Big Island has been widely studied by scientists to understand volcanic eruptions for disaster preparedness and geohazards forecasting. Its geographic location is shown in Figure 3.46.

Images were acquired in dates 2010-01-06 and 2011-05-05 by the Uninhabited Aerial Vehicle Synthetic Aperture Radar (UAVSAR), which is an airbone L-band SAR operated by NASA [86]. The near and far range incidence angles are 22.37° and 66.48° respectively. The processed image size is 2300×3000 pixels (range×azimuth) and the interferogram corresponds to the HH polarimetric channel.

Filtering results are represented in Fig. 3.47 and the quantitative improvement is shown in Table 3.12. It can be observed that in this case all filters show a good performance in both noise suppression and resolution preservation.

Note that the quality of the original data, shown in Figure 3.47(a), is better than in the previous case. As a result, noise suppression by each method is better achieved. The pixel-based filter preserves the majority of deformation details, but noise suppression may not be enough in some noisy areas. For the rest of the filters, the improvement in terms of residues is remarkable.

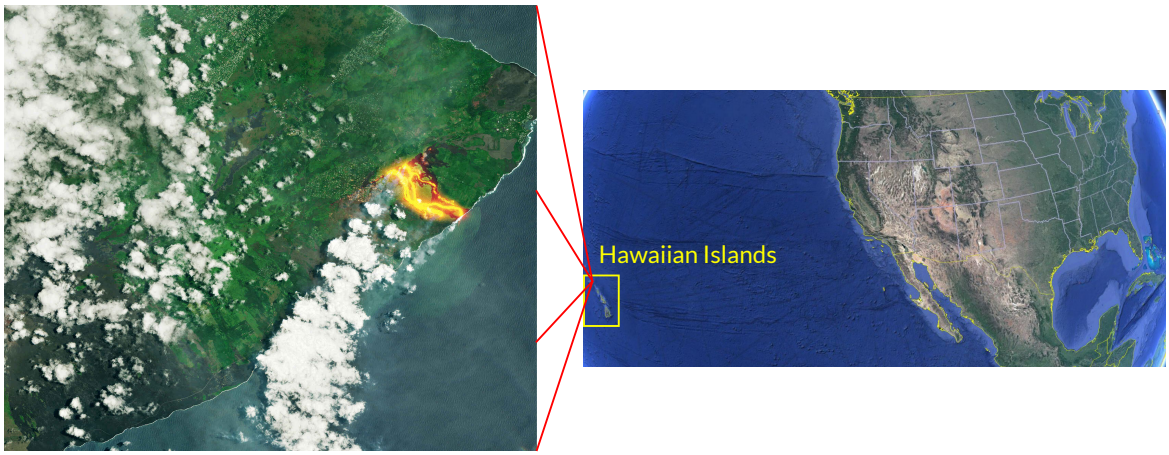

Figure 3.46: Geographic location of the Kilauea Volcano in Hawaii (USA). Images were extracted from ESA webpage and generated with Google-Earth©.

In fact, more than 93% of the residues are eliminated and the interferometric phase fringes corresponding to the deformation are well preserved. However, the proposed filter still shows the best results in terms of residues removal.

Interferogram	Residue number	Improvement
Original	773368	–
Goldstein	7785	98.99%
Adaptive Goldstein	49064	93.66%
Pixel-based	147002	81.00%
RASF	968	99.87%
Proposed method	**800**	**99.91%**

Table 3.12: Performance analysis of different phase filters for UAVSAR dataset.

As in the previous example, it is interesting to visualize the impact on the coherence. Histograms of Figure 3.48 show how the coherence is greatly improved with each filter. Note that all the methods offer good results, since the quality of the original data was significantly high. The proposed method, however, still shows the best improvement. Additionally, the increase in coherence can be visualized with the coherence maps of Figure 3.49. The coherence was estimated using a 7×7 boxcar filter. Note that some parts of the image are white since the noise was almost completely removed from the original interferogram.

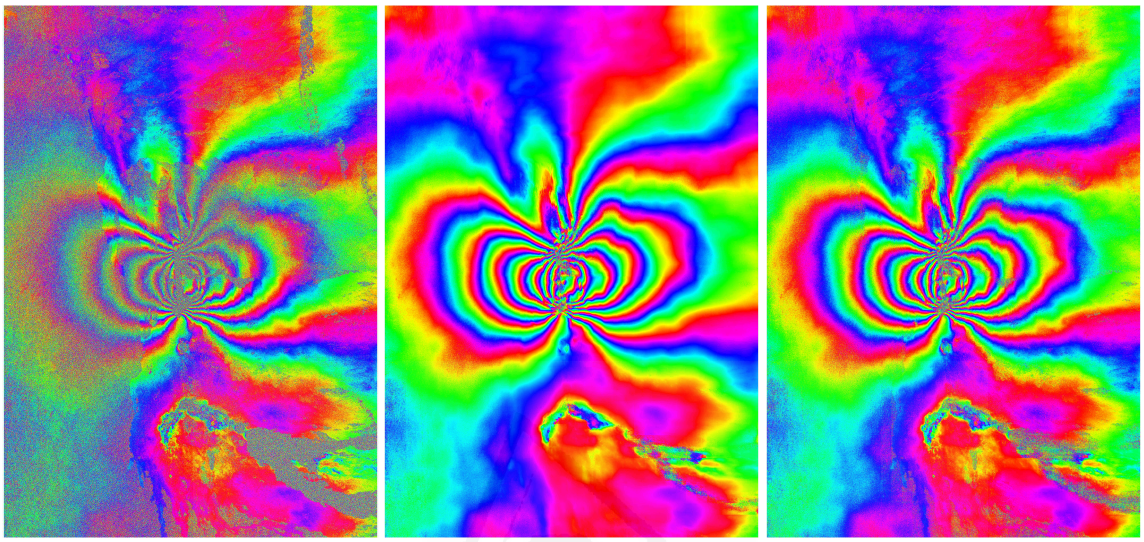

(a) Original noisy phase. **(b)** Goldstein. **(c)** Adaptive Goldstein.

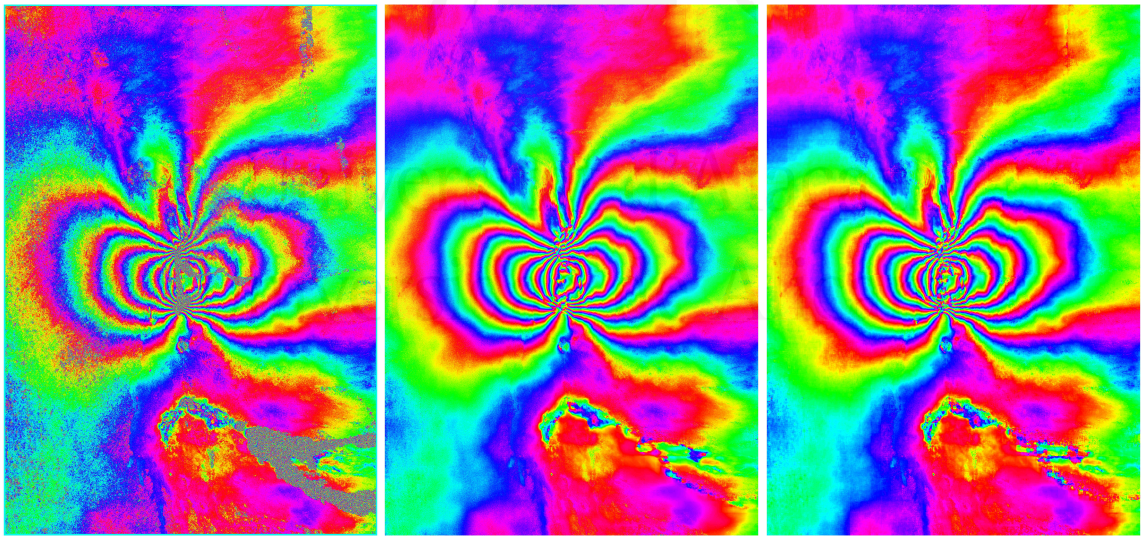

(d) Pixel-based. **(e)** RASF. **(f)** Proposed method.

Figure 3.47: Filtering results of the UAVSAR dataset with different methods.

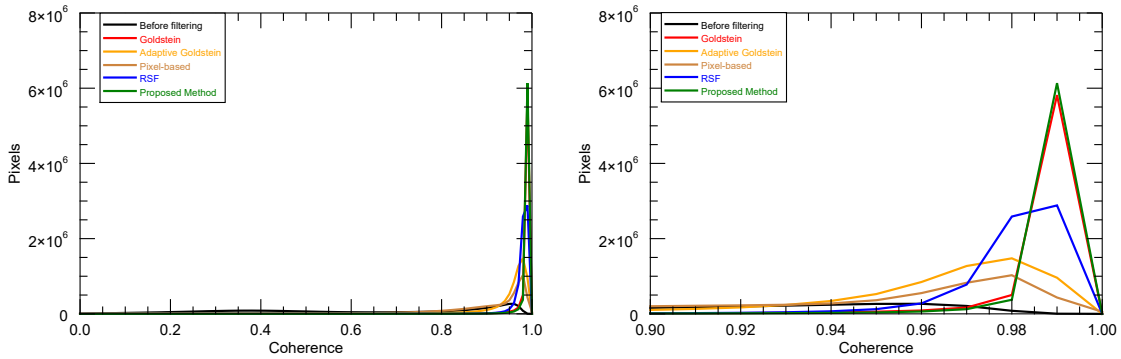

(a) Complete histograms. **(b)** Highest histogram values.

Figure 3.48: Differential coherence histograms of the UAVSAR dataset before and after filtering with each method.

(a) Original coherence. **(b)** Coherence after filtering.

Figure 3.49: Coherence maps before and after filtering the UAVSAR dataset with the proposed method. Coherence was estimated with a 7×7 boxcar kernel.

The last illustration of the filtering performance is carried out with a Sentinel-1 interferogram, which mapped again the Kilauea volcano. More precisely, it mapped a relatively recent eruption that took place in May 2018. The volcano actually experienced the largest eruption in at least 200 years [87]. Violent lava explosions followed by a massive crater collapse generated a strong earthquake on May 4.

Images were acquired in dates 2018-05-02 and 2018-05-08 by Sentinel-1 in Interferometric Wide Swath (IW) mode. The near- and far-range incidence angles are 30.89° and 36.67° respectively, and the polarimetric channel is VH. The size of the processed area is 3300×1700 pixels (range×azimuth).

The filtered differential phases are represented in Figure 3.50. Firstly, note the large number of fringes that are present in the interferometric phase as a consequence of the massive ground movement. Also note that the noise is not uniformly distributed, i.e., some areas are more affected by noise than others. In this regard, decorrelated areas in the bottom right corner of the image in Figure 3.50(a) may be due to presence of lava in the second acquisition, which changed the surface properties. Concerning the filtering results, the pixel-based method offers a poor result in noisy areas, as in the previous noisy datasets (both synthetic and real). The conventional and adaptive Goldstein filters provide approximately the same result. Both filters are able to suppress the noisy except in some very noisy areas. The best results, shown in Figures 3.50(e) and 3.50(f), are obtained with the iterative algorithms. However, the proposed filter offers a smoother and cleaner interferometric phase (for instance, in the bottom right corner of the image). The result of all filters is also evaluated with the number of phase residues in Table 3.13. As it can be seen, the proposed method offers the best result, since the cancellation of residues is almost total.

Interferogram	**Residue number**	**Improvement**
Original	752123	–
Goldstein	72255	90.39%
Adaptive Goldstein	127982	82.94%
Pixel-based	267321	64.46%
RASF	2635	99.64%
Proposed method	**714**	**99.91%**

Table 3.13: Performance analysis of different phase filters for Sentinel-1 dataset.

Finally, the improvement is also reflected with the histograms of differential coherence shown in Figure 3.51. Although the coherence is greatly increased by all methods, the proposed filter provides the largest improvement.

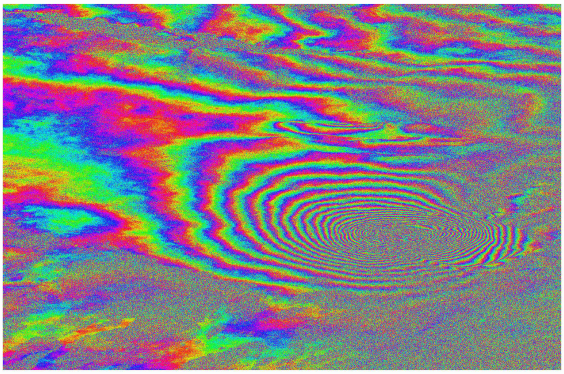

(a) Original noisy phase.

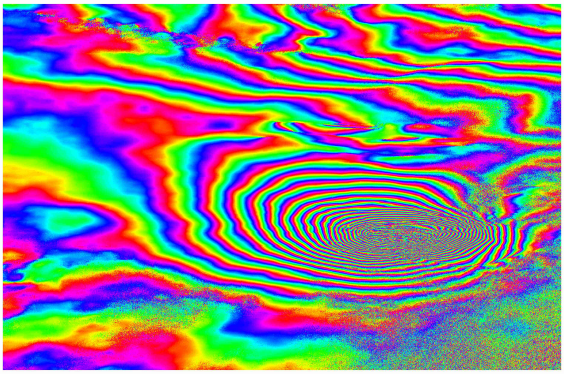

(b) Goldstein.

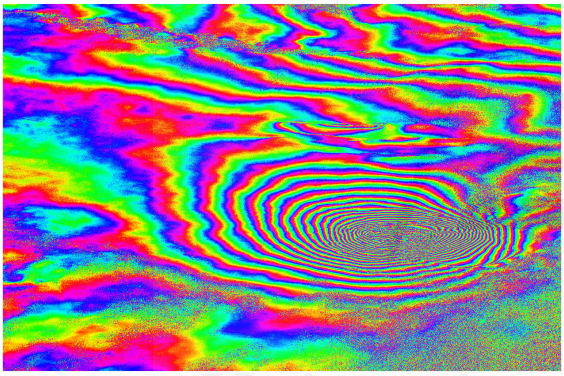

(c) Adaptive Goldstein.

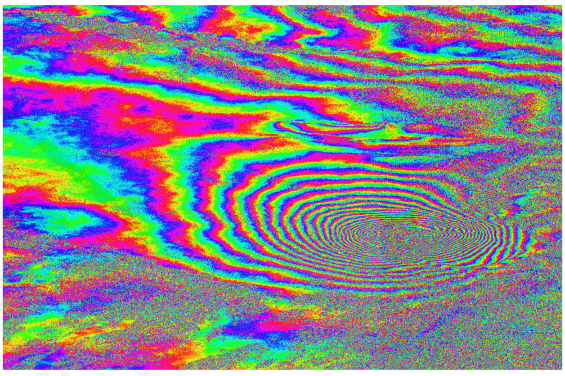

(d) Pixel-based.

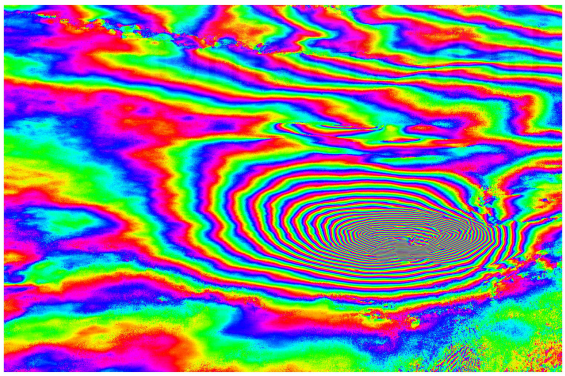

(e) RASF.

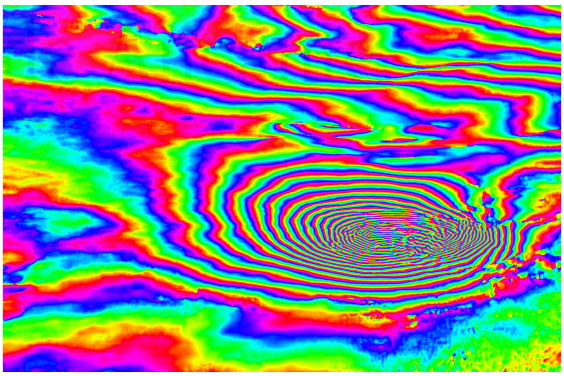

(f) Proposed method.

Figure 3.50: Filtering results of the Sentinel-1 dataset with different methods.

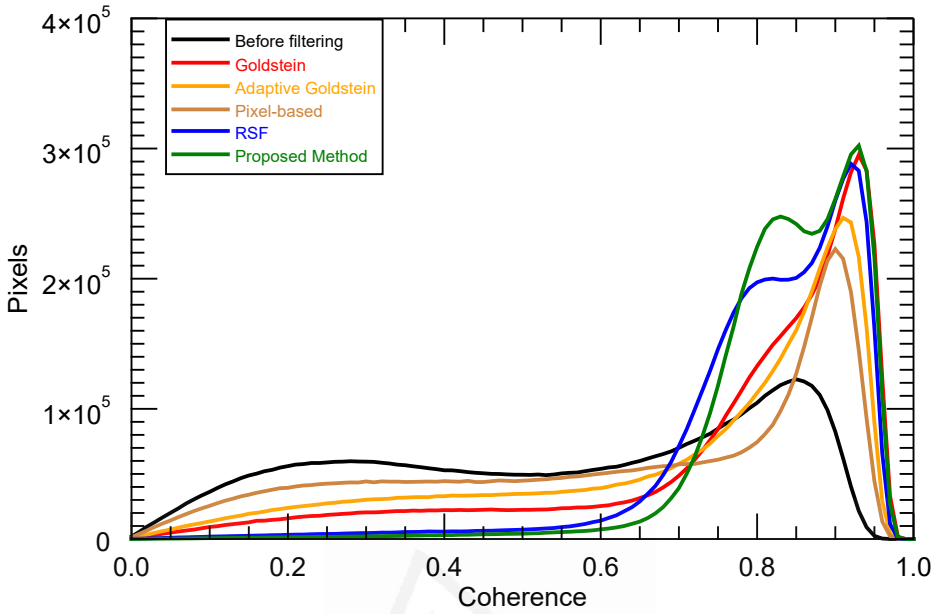

Figure 3.51: Differential coherence histograms of the Sentinel-1 dataset before and after filtering with each method.

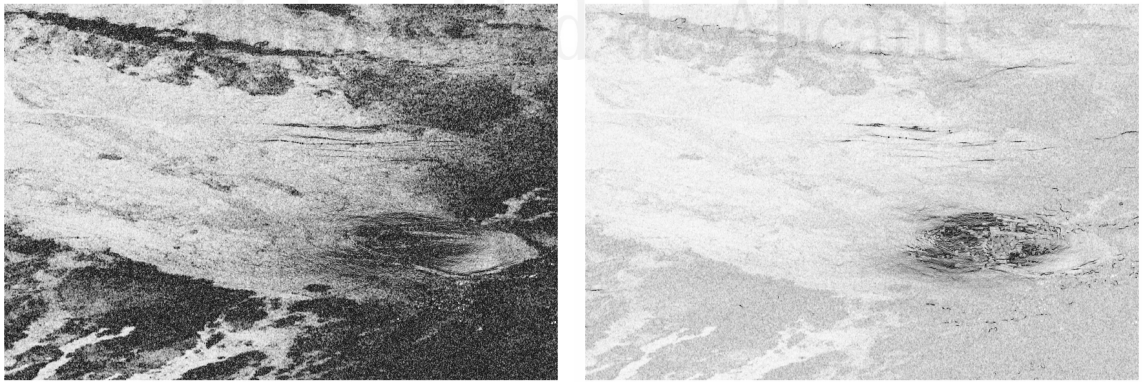

(a) Original coherence. **(b)** Coherence after filtering.

Figure 3.52: Coherence maps before and after filtering the Sentinel-1 dataset with the proposed method. Coherence was estimated with a 7×7 boxcar kernel.

3.2.3.4 Additional Filter Improvements

An evident drawback of the proposed filter is its computational cost. Obviously, since the input noisy interferogram is to be filtered repeatedly, the computation time increases with the number of iterations. To solve this inconvenience, a simple *stopping criterion* was devised. This criterion constitutes a trade-off between the algorithm performance and its computation time. Since the phase is progressively denoised, coherence is also increased after each filter iteration. The stopping criterion is directly related to this increase in coherence. Then, at any filter iteration i, the coherence difference map is computed, i.e.,

$$\Delta\gamma = |\gamma_i| - |\gamma_{i-1}|, \tag{3.59}$$

where $|\gamma_i|$ and $|\gamma_{i-1}|$ are the coherence maps obtained at iterations i and $i-1$ respectively.

Note that the criterion is block-dependent, that is, the algorithm checks if the mean coherence difference of an interferogram block is above a certain threshold (for instance, 0.1 or 0.05). If this is verified, the block is filtered. Otherwise the block is not filtered until the next iteration when the coherence difference map is computed again. In this way, the progressive denoising is automatically adapted to each resolution level.

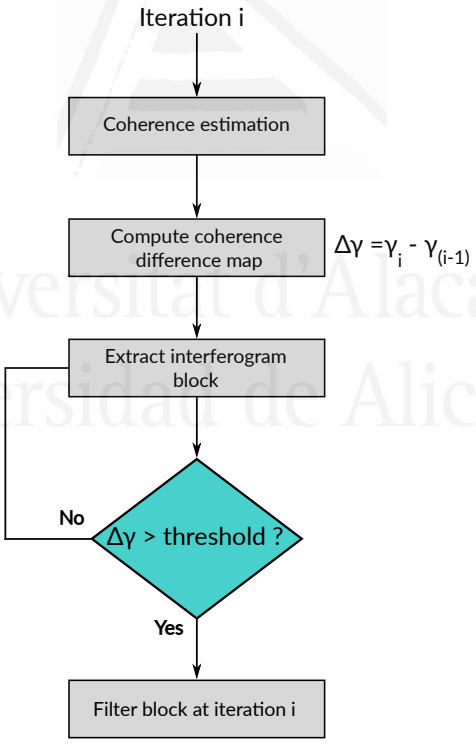

Figure 3.53: Adaptive stopping criterion diagram.

An example of the resulting improvement in computation time is provided with the simulation shown in Figure 3.54 and in Table 3.14. As it can be observed, the inclusion of this simple criterion provides almost the same filtering result but the computational time is greatly reduced.

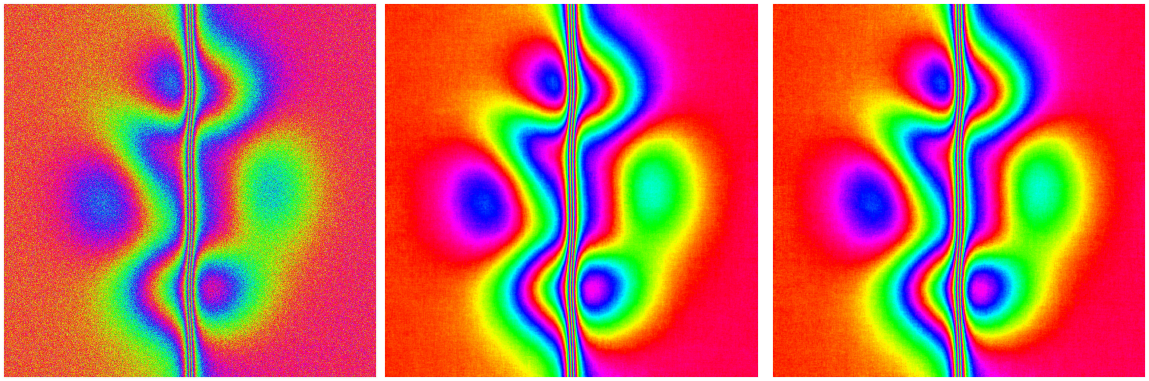

(a) Original noisy phase. **(b)** No stopping criterion. **(c)** Stopping criterion: quality threshold = 0.05.

Figure 3.54: Filtering results of a simulated interferogram with and without including the stop criterion. The noise standard deviation is 1 rad.

	Residue number	**Improvement**	MSE	Execution time (s)
Original	5709	–	0.4988	–
No stopping criterion	0	100%	0.0067	86
Stopping criterion	0	100%	0.0071	17

Table 3.14: Execution times for phase filtering with the proposed method. The filter was executed in a personal computer having an Intel Core i7-8700 with a clock rate of 3.80 GHz and 16 GB of RAM. The code is written in Interactive Data Language (IDL) and is not parallelized.

3.2.3.5 Impact on Phase Unwrapping

Even if phase unwrapping is beyond the scope of this thesis, the benefits of filtering for the unwrapping process deserve to be illustrated. In this regard, a simple simulation has been carried out. Among the different phase unwrapping methods which are available in literature [50], the efficient and simple method based on the 2-D Discrete Cosine Transform (DCT) has been used [88]. This approach is composed of the following steps.

1. Compute the local derivatives of the wrapped phase φ in both dimensions,

$$\rho_{i,j} = (\varphi_{i+1,j} - 2\varphi_{i,j} + \varphi_{i-1,j}) + (\varphi_{i,j+1} - 2\varphi_{i,j} + \varphi_{i,j-1}), \tag{3.60}$$

being $\{i, j\}$ each pixel spatial index.

2. Compute the 2-D DCT of $\rho_{i,j}$ to yield $\hat{\rho}_{i,j}$. The cosine transform C of signal x is given by

$$C_{m,n} = \sum_{i=0}^{M-1} \sum_{j=0}^{N-1} 4x_{i,j} \cos\left[\frac{\pi}{2M} m(2i+1)\right] \cos\left[\frac{\pi}{2N} n(2j+1)\right], \tag{3.61}$$

where M and N are the total number of samples in each dimension.

3. Modify $\hat{\rho}_{i,j}$ to obtain $\hat{\varphi}_{i,j}$ according to

$$\hat{\varphi}_{i,j} = \frac{\hat{\rho}_{i,j}}{2\left(\cos(\frac{\pi i}{M}) + \cos(\frac{\pi j}{N}) - 2\right)}. \tag{3.62}$$

4. Unwrapped phase values are directly provided by the 2-D Inverse DCT of $\hat{\varphi}_{i,j}$. The inverse transform can be obtained by means of

$$c_{i,j} = \frac{1}{MN} \sum_{i=0}^{M-1} \sum_{j=0}^{N-1} w_1(m) w_2(m) C_{m,n} \cos\left[\frac{\pi}{2M} m(2i+1)\right] \cos\left[\frac{\pi}{2N} n(2j+1)\right], \tag{3.63}$$

where

$$w_1(m) = \begin{cases} 1/2, & m = 0, \\ 1, & 1 \leq m \leq M-1, \end{cases} \tag{3.64}$$

and

$$w_2(m) = \begin{cases} 1/2, & n = 0, \\ 1, & 1 \leq n \leq N-1. \end{cases} \tag{3.65}$$

To visualize the impact of the filter on phase unwrapping, a simulated 2-D phase will be unwrapped and rewrapped again. Evidently, the rewrapped phase should ideally be identical to the original one. Random noise with 1 rad of standard deviation is included.

In Figure 3.55, the original noisy phase (Figure 3.55(a)) was unwrapped and rewrapped again. As shown in Figure 3.55(c), noise influences the process and an erroneous phase is obtained. It can also be observed that some fringes are lost.

Now, the noisy phase of Figure 3.55(a) was input to the proposed filter and the same process of unwrapping and rewrapping is performed. The result is depicted in Figure 3.56. It can be clearly observed that the unwrapping of the phase performed better, so that the rewrapped phase is (almost) identical to the filtered one.

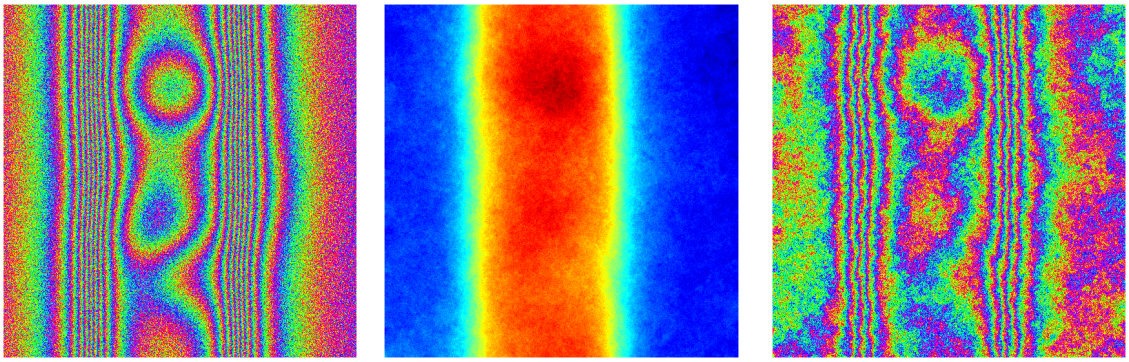

(a) Original noisy phase. **(b)** Unwrapped phase. **(c)** Rewrapped phase.

Figure 3.55: Phase unwrapping and rewrapping of a noisy phase.

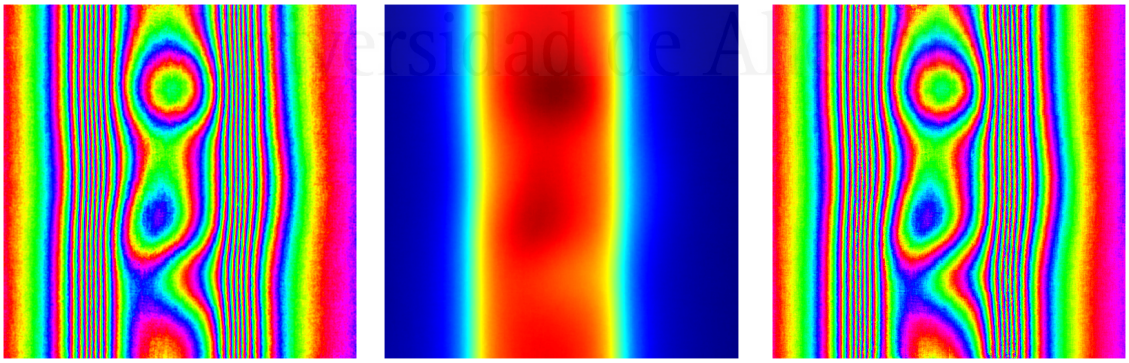

(a) Filtered phase. **(b)** Unwrapped phase. **(c)** Rewrapped phase.

Figure 3.56: Phase unwrapping and rewrapping of a filtered, cleaner phase.

3.3 PolDInSAR Optimization

3.3.1 Introduction

The recent launch of newer SAR spacecrafts with polarimetric capabilities, such as TerraSAR-X, Sentinel-1/2 or PAZ, motivated the development of a new analytical framework in which interferometric and polarimetric methods can be properly combined. In the context of differential interferometry with multitemporal datasets (i.e., time series exploiting the temporal baseline of the acquisitions) for subsidence analysis, the benefits of including all the available polarimetric information have been intensively proved [31] [33] [89] [19] [90] [91] [92]. The quality of the results is greatly improved, in terms of the number of reliable pixels, deformation measurement accuracy and spatial coverage, compared to single-polarimetric DInSAR time series.

Conversely, in this work we focus on the polarimetric optimization of *single-baseline* datasets, that is, when only a pair of images is processed. The goal of the optimization relies on improving the phase quality of interferograms, as with the filtering strategy previously detailed in Section 3.2, by exploring all the polarimetric diversity offered by modern SAR sensors. The rationale behind the optimization is to find the *optimum combination* of polarimetric channels, so that the phase quality is automatically enhanced. A wide variety of optimization algorithms are available in literature [58] [31] [33]. In the following sections, they will be described. Evidently, each method requires a quality criterion from which the optimization will be carried out. As previously stated in Section 2.3.1, the interferometric coherence is a direct indicator of the phase quality. It can be therefore deemed as the figure of merit to be maximized.

3.3.2 Algorithms

3.3.2.1 BEST

The simplest optimization algorithm is denoted as *Best* [29]. This approach selects, among the different available polarimetric channels, the one which offers the highest coherence. For instance, in a dual-pol SAR system which gathers images from channels VV and VH, the phase of each pixel is selected from the channel which provides the best coherence, i.e.,

$$\gamma_{Best} = \max\{|\gamma_{VV}|, |\gamma_{VH}|\}. \tag{3.66}$$

Note that this simple method does not use the Pol(D)InSAR formulation explained in Section 2.5. Consequently, it does not exploit the full potential that polarimetry offers, since just a discrete set of projections are tested and, hence, it does not provide an optimum solution to the optimization problem. Its implementation is, however, straightforward and its computation time is very fast since only a few comparisons are needed.

3.3.2.2 Sub-Optimum Scattering Mechanism

The Sub-Optimum Scattering Mechanism (SOM) is a more sophisticated approach which explores all possible combinations of orientation φ and ellipticity τ in the scattering matrix [93], previously introduced in Section 2.4 and defined by Equation 2.59. This method expresses the scattering matrix $\mathbf{S}$ defined in the linear polarization basis $\{\hat{h}, \hat{v}\}$ in a new orthogonal basis $\{\hat{a}, \hat{b}\}$ as a function of φ and τ, by means of the following unitary transformation [94] [58]:

$$\mathbf{S}_{ab} = \begin{bmatrix} S_{aa} & S_{ab} \\ S_{ab} & S_{bb} \end{bmatrix} = \mathbf{U}_2^T \mathbf{S} \mathbf{U}_2, \tag{3.67}$$

being the transformation matrix $\mathbf{U}_2$ given by

$$\mathbf{U}_2 = \begin{bmatrix} \cos\varphi & -\sin\varphi \\ \sin\varphi & \cos\varphi \end{bmatrix} \begin{bmatrix} \cos\tau & j\sin\tau \\ j\sin\tau & \cos\tau \end{bmatrix} \begin{bmatrix} e^{j\varphi_0} & 0 \\ 0 & e^{-j\varphi_0} \end{bmatrix} \tag{3.68}$$

and where the absolute phase φ_0 is usually set to 0 since it does not provide polarimetric or interferometric information. The optimization consists therefore in exploring all the possible values of the pair $\{\varphi, \tau\}$ and selecting the combination which maximizes the coherence, i.e.,

$$\gamma_{SOM} = \max_{\varphi,\tau} \{|\gamma_{ab}|, |\gamma_{bb}|\}. \tag{3.69}$$

where,

$$\begin{aligned} |\gamma_{aa}| &= \frac{E\{|S_{aa,1} S_{aa,2}|\}}{\sqrt{E\{|S_{aa,1}|^2\} \cdot E\{|S_{aa,2}|^2\}}}, \\ |\gamma_{ab}| &= \frac{E\{|S_{ab,1} S_{ab,2}|\}}{\sqrt{E\{|S_{ab,1}|^2\} \cdot E\{|S_{ab,2}|^2\}}}. \end{aligned} \tag{3.70}$$

$S_{aa,i}$ and $S_{ab,i}$ are the copolar and cross-polar channels in the new basis defined by the orientation and the ellipticity, for the first ($i = 1$) and second ($i = 2$) images forming the interferogram [33]. Then, the optimization is made by selecting the phase of the optimum polarimetric channel resulting for the best combination of φ and τ.

Finally, even though this method provides more accurate solutions, it remains sub-optimum since only a subspace of projections (derived from each combination of φ and τ) is tested.

3.3.2.3 Exhaustive Search Polarimetric Optimization (ESPO)

Exhaustive Search Polarimetric Optimization (ESPO) will be referred to as any algorithm which fully explores the diversity of polarimetric combinations to derive higher quality interferograms. The most intuitive idea consists in finding the projection vector $\boldsymbol{\omega}$ which maximizes the generalized coherence defined in Equation 2.82. It is important to note that the Equal Scattering Mechanism

(ESM) constraint is always satisfied. That is, we impose that $\boldsymbol{\omega}_1 = \boldsymbol{\omega}_2$ in Equation 2.82, so we only consider a single projection vector, simply denoted as $\boldsymbol{\omega}$.

Unlike the previous algorithms Best and SOM, the exhaustive search provides the most optimal solution to the optimization problem because the whole available polarimetric space is being explored. That is, this method searches the combination of polarimetric channels that provides the best coherence. To do so, it is necessary to introduce the *parameterization* of the projection vector $\boldsymbol{\omega}$.

On the one hand, for fully polarimetric data, $\boldsymbol{\omega}$ can be expressed as a function of four real parameters $(\alpha, \beta, \delta, \psi)$ [58] as

$$\boldsymbol{\omega} = \begin{bmatrix} \cos(\alpha) \\ \sin(\alpha)\cos(\beta)e^{j\delta} \\ \sin(\alpha)\sin(\beta)e^{j\psi} \end{bmatrix}, \quad \begin{cases} 0 \leq \alpha \leq \pi/2, \\ 0 \leq \beta \leq \pi/2, \\ -\pi \leq \delta < \pi, \\ -\pi \leq \psi < \pi. \end{cases} \tag{3.71}$$

On the other hand, for dual-pol images, $\boldsymbol{\omega}$ is parameterized as

$$\boldsymbol{\omega} = \begin{bmatrix} \cos(\alpha) \\ \sin(\alpha)e^{j\psi} \end{bmatrix}, \quad \begin{cases} 0 \leq \alpha \leq \pi/2, \\ -\pi \leq \psi < \pi. \end{cases} \tag{3.72}$$

At this point, the ESPO algorithm consists in finding the values of parameters α, β, δ and ψ (or only α and ψ in the dual-pol case), the ranges of which are finite and known and which provide the highest coherence. The algorithm can be implemented either with a *brute-force search* or in two steps. In the former case, a fine sampling of α, β, δ and ψ is performed and the solution is directly provided by the combination which maximizes the coherence. The major drawback of this approach is the extremely slow computation time, since a very large number of possible combinations has to be evaluated for each pixel in the interferogram. In fact, the algorithm is of *polynomial time* ($O(n^4)$ in Big-O notation). This means, for instance, that setting a fine sampling of 100 points for each parameter, i.e., a sampling of 1° for $\{\alpha, \beta\}$ and 3.6° for $\{\delta, \psi\}$, approximately 10^8 operations per pixels are needed. A more fine sampling of 1000 points per variable would require 10^{12} operations per pixel, which could result in months or years of computation.

Because of this slow computation time, a two-step approach is usually chosen. This consists in using a coarser sampling of each variable followed by a numerical method to refine the solution. Usually, the *Conjugated Gradient Method* is applied [95] [96]. In this way, the computation time is greatly reduced.

The high computational cost of ESPO is because the coherence optimization is carried out in a 4-D space (in the qual-pol case). That is, the algorithm maximizes a four-dimensional function defined by α, β, δ and ψ. Alternative methods were proposed in [97] and [98]. Specifically, the *Improved Signal-*

to-Noise Ratio Optimization (IM-SNR-OPT) [98] divides the original 4-D optimization problem into three independent and successive searches of 2-D, 1-D and 1-D, greatly accelerating the computation time. The key point of this new algorithm consists in defining a *new parameterization* of the projection vector $\boldsymbol{\omega}$. In this regard, this new definition of $\boldsymbol{\omega}$ is directly related to the SNR of the acquisitions, and can automatically be used to maximize the coherence as with the previous algorithm. However, the new parameterization does not depend simultaneously on four different variables, so that the exhaustive search is divided and the computation time is greatly reduced.

Using the Pauli basis, the information of each polarimetric channel of acquisition i can be split into a signal part and a noise part as

$$\begin{aligned}(S_i^{HH} + S_i^{VV}) &= (S_i^{HH} + S_i^{VV})_S + (S_i^{HH} + S_i^{VV})_N,\\ (S_i^{HH} - S_i^{VV}) &= (S_i^{HH} - S_i^{VV})_S + (S_i^{HH} - S_i^{VV})_N,\\ (S_i^{2HV}) &= (S_i^{2HV})_S + (S_i^{HH})_N,\end{aligned} \tag{3.73}$$

where S and N are the signal and noise parts, respectively. Each element in Equation 3.73 is therefore of the form

$$\begin{aligned}(S_i^{HH} + S_i^{VV}) &= y_0 e^{j\alpha_0} + \eta_0,\\ (S_i^{HH} - S_i^{VV}) &= y_1 e^{j\alpha_1} + \eta_1,\\ (S_i^{2HV}) &= y_2 e^{j\alpha_2} + \eta_2,\end{aligned} \tag{3.74}$$

so that, for instance, y_0 corresponds to the amplitude of channel HH+VV, α_0 its phase and η_0 is the associated noise component. According to Equation 3.74, the expression of the target vector (see Equation 2.68 in Chapter 2) is

$$\mathbf{k}_i^S = \frac{1}{\sqrt{2}}[y_0 e^{j\alpha_0}, y_1 e^{j\alpha_1}, y_2 e^{j\alpha_2}]^T, \tag{3.75}$$

and the projection vector is

$$\boldsymbol{\omega}^{*T} = \begin{bmatrix}1 & x_{01}e^{j\theta_{01}} & x_2 e^{j\theta_{02}}\end{bmatrix}, \quad \begin{cases} x_{01}, x_2 \in [0 \quad \infty] \\ \theta_{01}, \theta_{02} \in [-\pi \quad \pi]. \end{cases} \tag{3.76}$$

From Equation 3.76 we can derive the expression of the complex backscattering coefficient (equivalent to the one in Equation 2.79):

$$\begin{aligned}\mu_i^S &= \boldsymbol{\omega}_i^{*T}\mathbf{k}_i,\\ \mu_i^S &= \frac{1}{\sqrt{2}}\left(y_0 e^{j\alpha_0} + x_1 y_1 e^{j(\alpha_1+\theta_1)} + x_2 y_2 e^{j(\alpha_2+\theta_2)}\right).\end{aligned} \tag{3.77}$$

Backscattering coefficients are characterized by an amplitude A and a phase β, i.e., they can be ex-

pressed as

$$\mu_i^S = Ae^{j\beta}, \tag{3.78}$$

being its power

$$\mu_i^{S_P} = A^2. \tag{3.79}$$

Moreover, assuming that noise follows a zero-mean Gaussian distribution with variance δ^2, i.e., $\eta_1, \eta_2, \eta_3 \sim N(0, \delta^2)$, its power is

$$\mu_i^{N_P} = (1 + x_1 + x_2)\delta^2. \tag{3.80}$$

So, finally, the SNR is given by

$$\begin{aligned} SNR &= \frac{\mu_i^{S_P}}{\mu_i^{N_P}}, \\ SNR &= \frac{A^2}{(1 + x_1 + x_2)\delta^2}. \end{aligned} \tag{3.81}$$

According to Equation 3.81, noise power $\mu_i^{N_p}$ does not depend on either θ_1 or θ_2 and signal power only depends on θ_1 and θ_2 [97]. It follows that the SNR can be optimized in two steps. First, amplitude A is maximized by fixing an initial value of x_1 and x_2 and optimizing θ_1 and θ_2. Then, the SNR is improved by searching optimum values of x_1 and x_2 with the previously obtained θ_1 and θ_2.

Although the computation time of this optimization is greatly reduced (the original 4-D problem is divided into two successive 2-D optimizations), a further gain can be obtained with the following considerations [98]. Imposing the third element of Equation 3.76 to be 0, i.e., $x_2 e^{j\theta_2} = 0$, we obtain a new parameterization of $\boldsymbol{\omega}$ (denoted as $\boldsymbol{\omega}_0$) as

$$\boldsymbol{\omega}_0^{*T} = \begin{bmatrix} 1 & x_{01}e^{j\theta_{01}} & 0 \end{bmatrix}, \quad \begin{cases} x_{01} \in [0 \quad \infty], \\ \theta_{01} \in [-\pi \quad \pi], \end{cases} \tag{3.82}$$

so that Equation 3.77 is now converted to

$$\begin{aligned} \mu_{0i}^S &= \frac{1}{\sqrt{2}}(y_0 e^{j\alpha_0} + x_1 y_1 e^{j(\alpha_1 + \theta_{01})}), \\ \mu_{0i}^S &= A_0 e^{j\beta_0}, \end{aligned} \tag{3.83}$$

and a new SNR value is given by

$$SNR_0 = \frac{A^2}{(1 + x_{01})\delta^2}. \tag{3.84}$$

This allows to independently optimize x_{01} and θ_{01} so that the first 2-D optimization previously described is in its turn divided into two independent 1-D optimizations. The whole process can be summarized as follows.

1. Set the initial values of x_{01}, x_{01} and x_2.

2. Optimize θ_{01} with the initial value of x_{01} by means of Equation 3.82. θ_1 is also automatically obtained since $\theta_1 = \theta_{01}$. This is the first 1-D optimization.

3. Optimize θ_2 with Equation 3.76 with the previously obtained θ_1, x_1 and x_2. This is the second 1-D optimization.

4. Optimize x_1 and x_2 with the obtained values of θ_1 and θ_2 also with Equation 3.76. This is the 2-D optimization.

5. Optionally, the process can be iterated from step 2 to step 4. In each iteration, the new initial values of x_{01}, x_1 and x_2 used in step 1, are set to the optimized ones of the previous iteration.

Finally, as with the original ESPO, two implementation approaches can be used. On the one hand, a fine grid method can be considered at the expense of a high computational load. On the other hand, a coarse grid followed by a conjugated gradient method can be used to greatly improve the algorithm's execution time.

3.3.3 Preliminary Results

The first approach to phase quality optimization consisted in applying the previously explained algorithms to a set of quad-polarimetric SAR images. Specifically, the same pair of RADARSAT-2 images covering the Mount Etna's eruption and described in Section 3.2.3.3 has been used. The processed image size is 3700×6000 pixels. A Pauli RGB composite image of the area was previously depicted in Figure 2.16.

Once the data structures are built according to Pol(D)InSAR formulation described in Section 2.5, phase quality optimization is carried out by maximizing both the (conventional) interferometric coherence γ (Equation 2.82) and the phase coherence ρ (Equations 2.81 and 3.23). That is, both estimators are used as figure of merit in the optimization process. It is worth mentioning again that each estimator requires a spatial average of a certain number of samples, i.e., a multilook has to be applied. In this case, a boxcar filter of 15×15 pixels is selected. Moreover, the same implementation strategy has been followed for ESPO and IM-SNR-OPT algorithms, which consists in the definition of a coarse grid/sampling followed by a CGM numerical refinement. Concerning the ESPO algorithm, a sampling of 30° has been used for parameters α and β, and a sampling of 45° for δ and ψ. Concerning the SNR method, the step size for θ_1 and θ_2 is 45° and the step size for $\log x_1$ and $\log x_2$ is 2.

Figure 3.57 shows the coherence histograms for different polarimetric channels: co-polar channels HH and VV, first Pauli channels $HH + VV$ and $HH - VV$, and the optimum ones. As expected, a global increase in both $|\gamma|$ and ρ is obtained. Pixels that originally had a very low coherence (between 0 and 0.2) now present increased coherences distributed around 0.2-0.4 in the optimized channels.

Moreover, pixels with high coherences in any polarimetric channel (greater than 0.8) also have their values increased in the optimized channels, but this increase is rather small. Also, note that from the original channels, the first one in the Pauli basis, i.e., HH+VV offers the highest coherence.

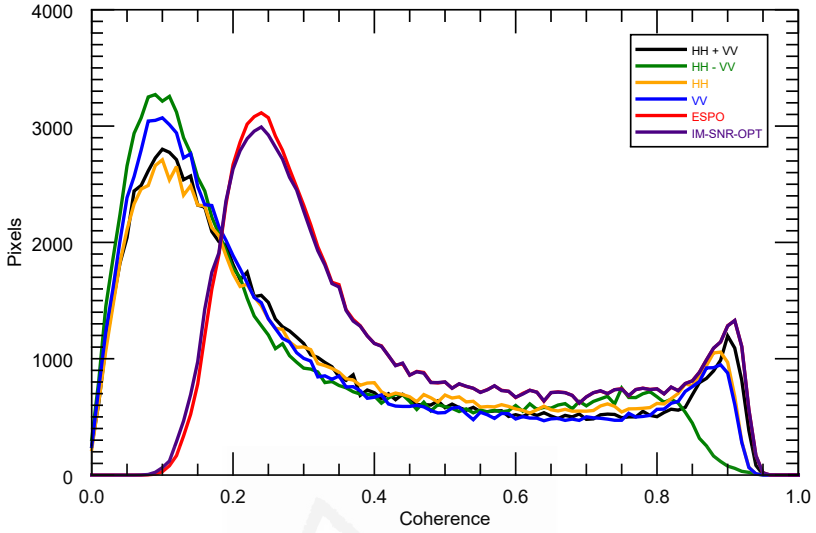

(a) Coherence optimization.

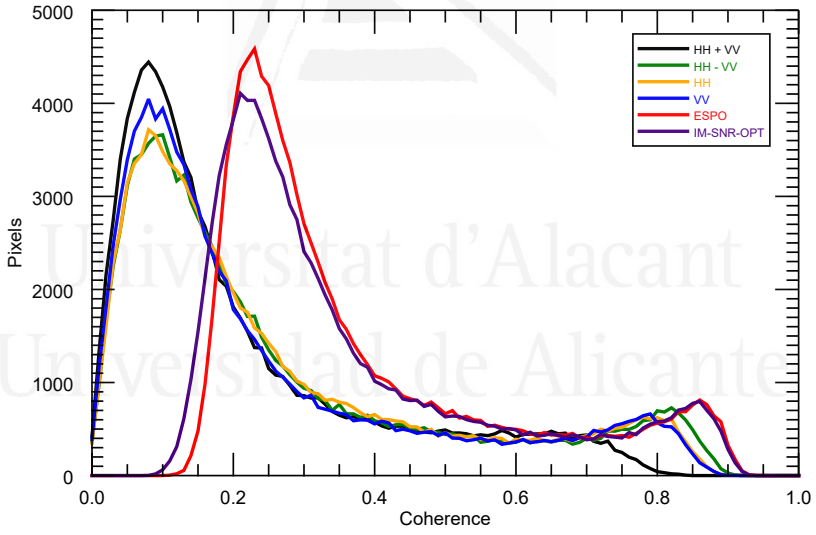

(b) Phase coherence optimization.

Figure 3.57: Histograms of coherence for different polarimetric channels, HH, VV, $HH + VV$, $HH - VV$ and optimum channels.

Moreover, looking at the histograms in Figure 3.57 it is important to point out that the performance of both polarimetric optimization algorithms is nearly the same. In terms of $|\gamma|$ optimization, the obtained optimum interferograms would be almost identical, as the histograms provided by ESPO and IM-SNR-OPT almost overlap. In terms of ρ optimization, it seems that the ESPO algorithm offers more improvement in comparison to the SNR method, especially for low values of ρ (around 0.1 and 0.3). However, as expected by the theoretical analysis of each algorithm, the SNR

method has a considerably faster execution, showing the advantage that this algorithm has against ESPO.

	Coherence optimization		Phase coherence optimization	
Algorithm	**ESPO**	**IM-SNR-OPT**	**ESPO**	**IM-SNR-OPT**
Execution time	1240 s	600 s	33933 s (≈ 9 h 20 min)	10510 s (≈ 2 h 50 min)
Mean value	0.4483	0.4469	0.3807	0.3711

Table 3.15: Computation time and global result obtained with both polarimetric optimization algorithms. Times correspond to the execution on a Dell Workstation equipped with a 12-core AMD Opteron (2.3 GHz) and 192 GB of RAM, without code parallelization.

Additionally, by observing both histograms in Figure 3.57, it seems that optimizing the phase coherence offers a larger improvement than optimizing the conventional coherence, especially for high values. This is because the initial coherence values were already higher for $|\gamma|$ than for ρ. Indeed, the final number of high coherent pixels is larger in the $|\gamma|$ optimization case. This can be verified with the histograms shown in Figure 3.58.

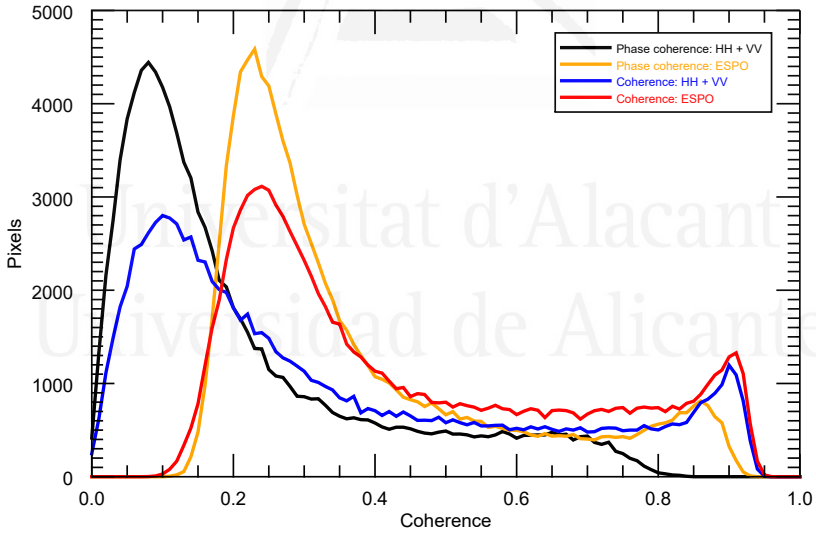

Figure 3.58: Histograms of coherence and phase coherence for channels HH+VV and the optimum channels.

The improvement is also reflected by directly looking at the coherence maps of the optimum channel. For comparison purposes, Figure 3.59 shows the coherence maps of channels HH+VV and the optimum channel. As it can be observed, the improvement is significant especially in urban and neighboring areas, where the number of coherent pixels is increased.

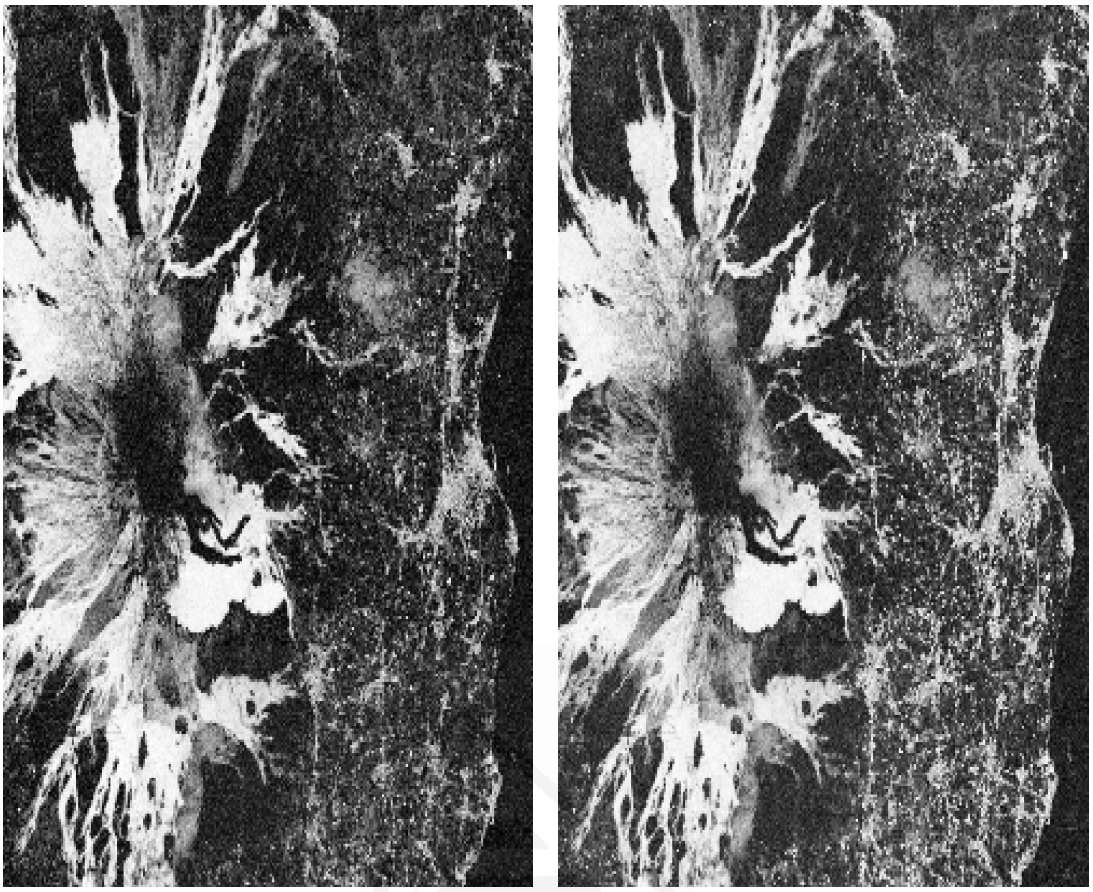

(a) Coherence map of channel HH+VV. **(b)** Coherence map of the optimum channel.

Figure 3.59: Coherence maps of channels HH+VV and the optimum channel after coherence optimization with ESPO.

Despite the promising results in terms of coherence, the real purpose of this optimization is to obtain a more reliable interferometric phase, since differential phase is the main input for geophysical analysis of ground deformation. In this regard, highly coherent areas exhibit a less noisy phase (such as the urban zones previously mentioned), but decorrelated areas (for instance, due to vegetation) are almost as noisy as in any of the original channels. This is shown with the differential phases in Figure 3.60. It can be observed that noise is slightly reduced, especially in some decorrelated areas, but in general the improvement is negligible for practical purposes. In this regard, it seems that noise reduction is mainly achieved by multilooking, and the proposed polarimetric optimization does not provide a further improvement in phase quality.

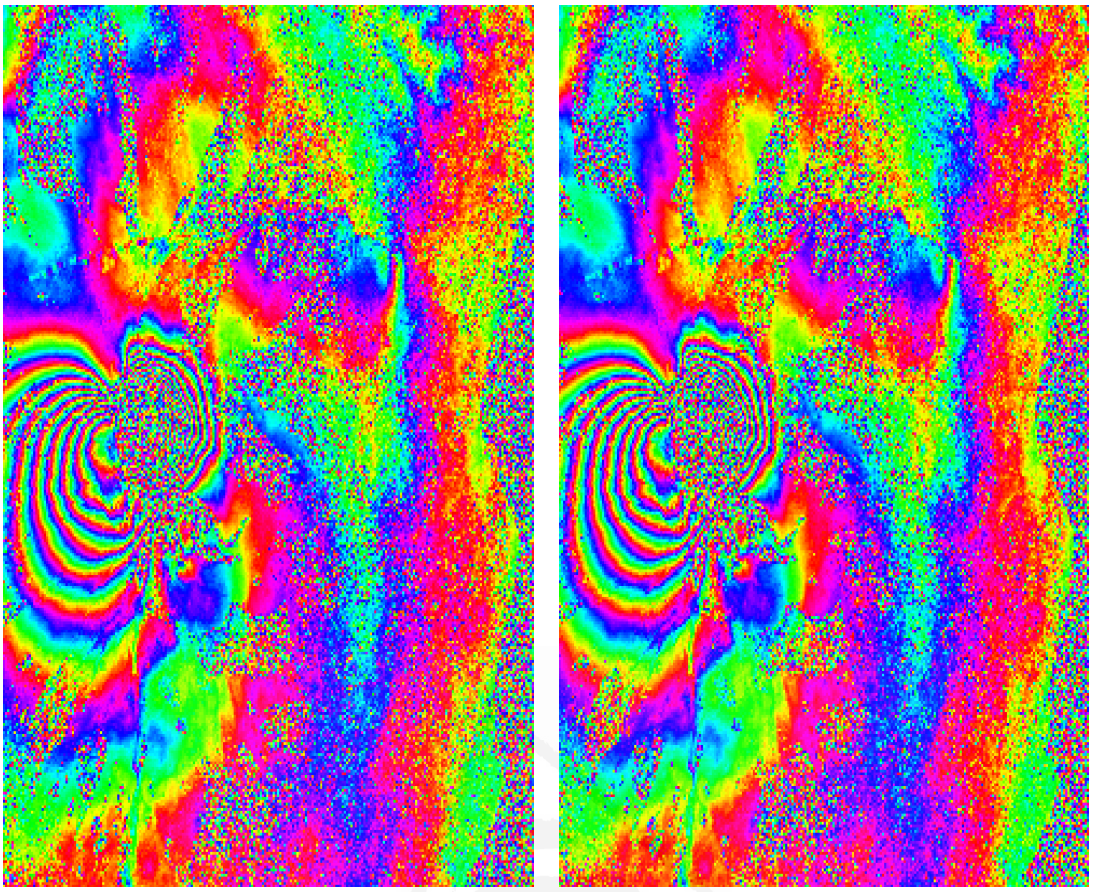

(a) Differential phase of channel HH+VV. **(b)** Differential phase of the optimum channel.

Figure 3.60: Differential phases of channels HH+VV and the optimum channel after coherence optimization with ESPO.

A possible explanation for such minor improvement lies in the optimization itself, which works on a pixel basis. That is, each pixel is individually optimized and has a specif value of the projection vector $\boldsymbol{\omega}$. Therefore, the optimum projection vector for two adjacent pixels can be different, even if they belong to the same kind of land cover. Then, the quality of the resulting phase may not be improved significantly, since different phase centers can be retrieved due to the selection of different polarimetric channels in neighbor pixels. This is assessed with the images representing the optimum values of α, β, δ and ψ (ESPO) and x_1, x_2, θ_1 and θ_2 (IM-SNR-OPT) that are shown in Figure 3.61. It is clearly observed that, from the four parameters defining the projection vector $\boldsymbol{\omega}$ in each algorithm, only the images of α and β (slightly) and x_1, x_2 resemble the scene land-cover, showing some areas with rather homogeneous values of this parameter. Instead, the other parameters are much noisier. Accordingly, the spatial variability shown in Figure 3.61 suggests that these parameters should be kept fixed during the optimization process. Finally, to test whether the spatial variation in the projection vector is the only reason for the small improvement in phase quality obtained with the optimization, a more detailed analysis of noise is carried in Section 3.3.4.

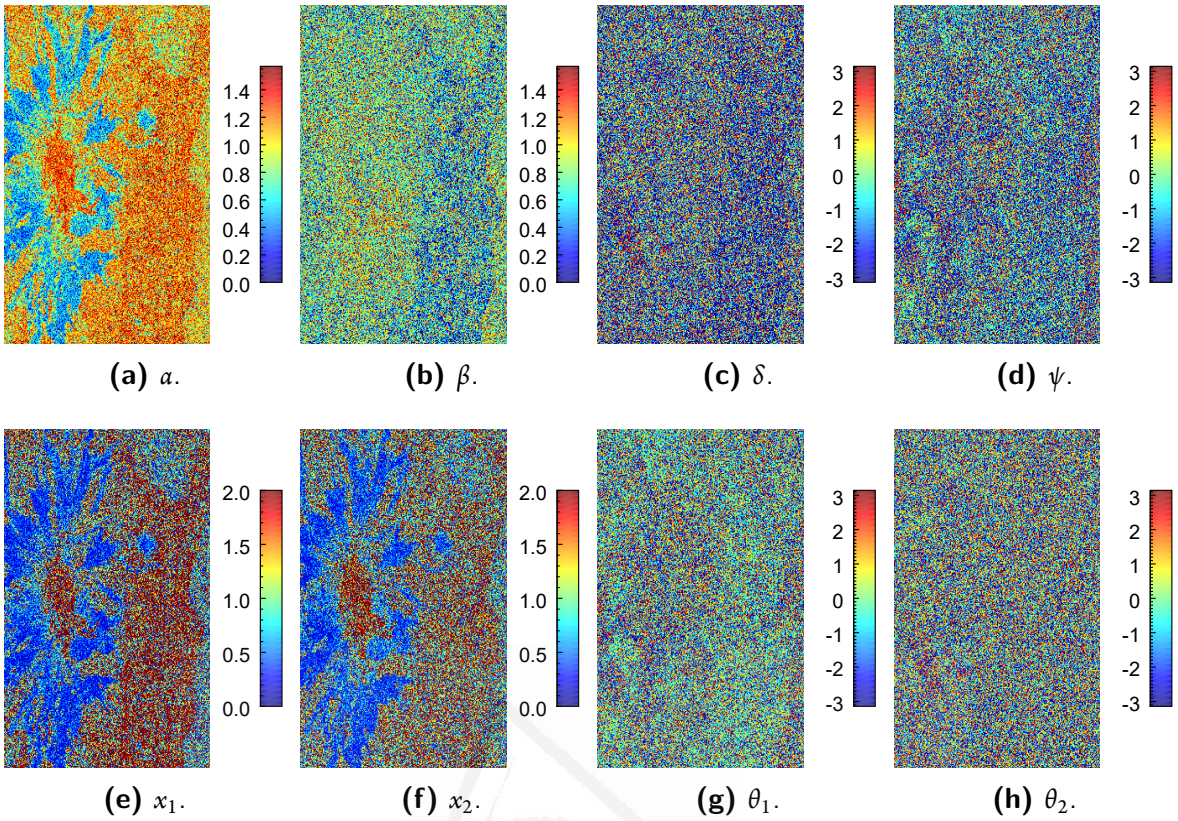

(a) α. **(b)** β. **(c)** δ. **(d)** ψ.

(e) x_1. **(f)** x_2. **(g)** θ_1. **(h)** θ_2.

Figure 3.61: Computed optimum parameters α, β, δ and ψ (ESPO) and x_1, x_2, θ_1 and θ_2 (IM-SNR-OPT) of the whole processed area.

3.3.4 Influence of the Multilook Size and Noise Analysis in Homogeneous Areas

Besides the problem of the spatial variability of the projection vectors mentioned in the previous Section 3.3.3, it is convenient to analyze the effect that the multilook size has in the optimization. Because the coherence is being used as the quality criterion, the original matrix T_6 (see Equations 2.77 and 2.78) which contains all the polarimetric and interferometric information, has to be averaged. This leads to an important noise reduction (especially if a large number of pixels are averaged) at the expenses of a significant resolution loss, as previously mentioned in Section 2.3.1. Accordingly, the effect of the *multilook size* in the optimization will be analyzed in detail. That is, we will evaluate how much coherence and, hence, how much phase quality improvement is obtained by means of this prefiltering (multilooking) followed by the polarimetric optimization process. To this end, the same optimization is performed with different multilook sizes: from 3×3 to 21×21 independent samples average. Additionally, the Non-Local SAR filter (NL-SAR) [46] is also tested. This filter has the advantage that it effectively reduces noise while preserving when necessary the spatial resolution of the original images, as non-contiguous pixels are averaged according to a similarity criterion. Moreover, the SNR method is used as the polarimetric optimization algorithm, since it provides almost the same solution as ESPO but at a reduced computation time, as shown in the previous Section 3.3.3.

Figure 3.62 shows the coherence maps of the optimum channels for a different number of looks.

Concerning the NL-SAR filtering parameters, a search window size of 25×25 pixels and a patch size of 5×5 pixels have been used. For comparison purposes, the coherence map of the 1st channel in the Pauli basis, i.e. HH+VV, is also shown.

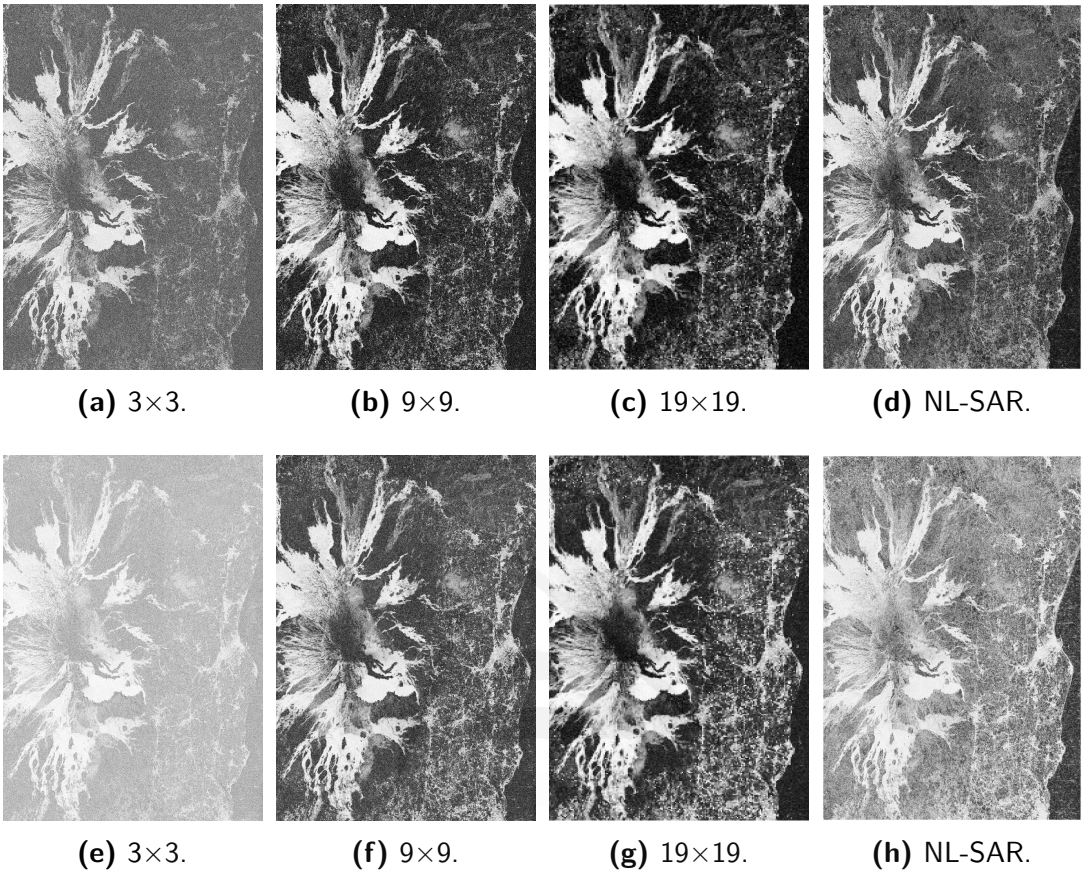

(a) 3×3. **(b)** 9×9. **(c)** 19×19. **(d)** NL-SAR.

(e) 3×3. **(f)** 9×9. **(g)** 19×19. **(h)** NL-SAR.

Figure 3.62: Coherence maps of channels HH+VV (top) and the optimum (bottom) for different number of looks.

Comparing the two rows of coherence maps in Figure 3.62, we observe that coherence is globally increased with the polarimetric optimization, especially with a 3×3 multilook. In that case, an overestimation of the coherence associated with the small number of samples averaged was expected [55] (hence the higher coherences in both rows), and polarimetry provides sensitivity to the shapes and orientations of the elements within the multilooked pixels thanks to the reduced size of the estimation window. The largest increase in coherence is obtained with this multilook size. In fact, the mean coherence of the whole area is increased by 0.31 (from 0.53 to 0.84), and the mean phase coherence is increased by 0.40 (from 0.47 to 0.87). The positively biased estimator makes coherence to be increased even in areas where it should be null theoretically, such as over the sea (right part of the image of Figure 3.62(e)). In addition, it must be stated that the bias in coherence estimation is increased when we combine two or more polarimetric channels to optimize the coherence, since the additional degrees of freedom allow us a mathematical maximization of the coherence, regardless of the scattering physics present in the scene. From Figure 3.62, we also conclude that as the multilook size increases, the initial values of estimated coherence decrease. This is due to two factors: less bias

in coherence estimation and mixing of nonhomogeneous pixels in the averaging window. Regarding the optimum values, there is an inability to find a polarimetric combination the response of which is significantly better than others, making the final improvement less evident in comparison with smaller multilook sizes. For instance, with a multilook size of 19×19 pixels, the mean coherence is only increased by 0.09 (from 0.33 to 0.42) in the whole processed area. This variable coherence increase is represented, as a function of the multilook size, in Figure 3.63. It is observed that the improvement is inversely proportional to the multilook size.

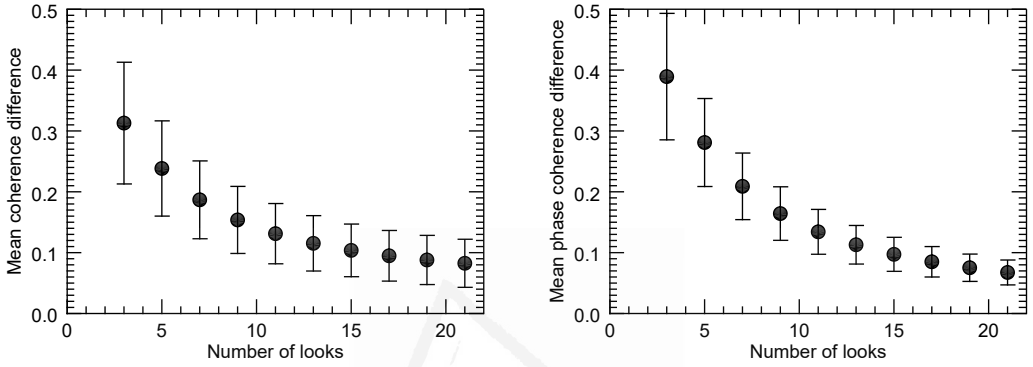

(a) Coherence optimization. **(b)** Phase coherence optimization.

Figure 3.63: Average coherence and phase coherence improvement between channels HH+VV and the computed optimum channel for different number of looks (from 3×3 to 21×21 pixels).

Moreover, concerning the optimization applied to the non-local filtered data, the improvement is quite remarkable as shown in Figure 3.62(f). Coherence is greatly increased in the whole interferogram (the mean of the scene increases by 0.20), especially in relevant areas related to surface deformation around the volcano crater and in urban areas. However, in this case it is not overestimated in decorrelated zones, as it was obtained with a 3×3 multilook. This is seen in the sea area of the right side of the images, where the coherence is not notably increased. This is in line with resolution preservation and with the mixing of only homogeneous pixels. In fact, both the optimized and non-optimized coherence maps in Figures 3.62(d) and 3.62(h) show a significant resolution preservation, in comparison with, for instance, the maps in Figures 3.62(b) and 3.62(f).

The improvement is also illustrated in Figure 3.64 with the histograms of coherence of all polarimetric channels. The largest increase is clearly observed when coherence is estimated with small windows, especially with 3×3 pixels. Pixels that originally had a very low coherence (between 0 and 0.4) now present coherences ranging from 0.45 to 0.9 in the optimum channel. Moreover, pixels with high coherences in any polarimetric channel (greater than 0.8) also have their values increased in the optimum case. As previously stated, this increase is larger with a 3×3 window and decreases progressively. Specifically, with a 3×3 multilook, 69.3% of pixels present coherence values greater than 0.8 in the optimum channel, whereas only 17.9% of pixels (difference of 51.4%) present this percentage in the HH+VV channel. However, in the 9×9 case, 16.3% of pixels have coherence values

greater than 0.8 in the optimum channel against 12.4% in the HH+VV channel (difference of just 3.9%) and this difference in high end coherence values decreases even more when larger estimation windows are used.

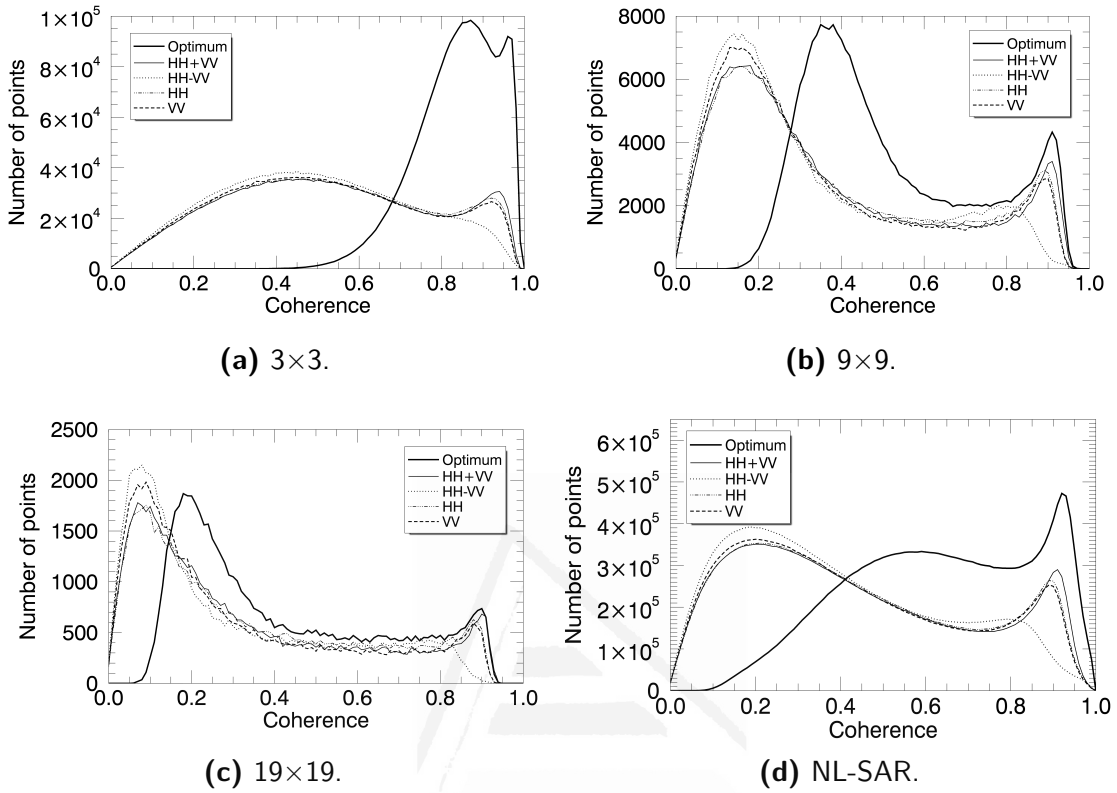

(a) 3×3. **(b)** 9×9.

(c) 19×19. **(d)** NL-SAR.

Figure 3.64: Histograms of estimated coherence for different polarimetric channels (HH, VV, HH+VV and HH-VV) and the optimum channels for different number of looks.

The same effect is observed when the phase coherence is optimized[1], as shown in Figure 3.65. That is, a major improvement is obtained for small estimation windows which decreases when large estimation windows are used.

[1]Note that the phase coherence is not optimized if the original T6 matrix is filtered with NL-SAR, since the code published in [46] does not provide the location of the neighbors of each pixel. However, the result would have been very similar to coherence optimization.

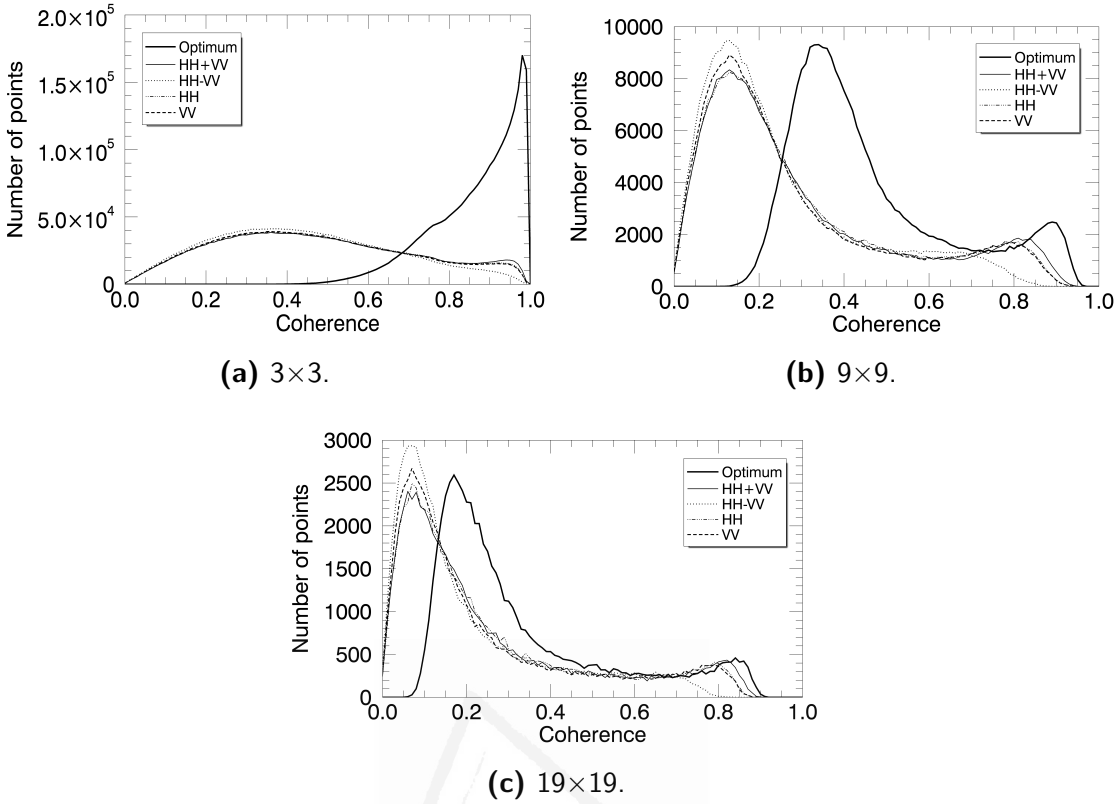

(a) 3×3.

(b) 9×9.

(c) 19×19.

Figure 3.65: Histograms of estimated phase coherence for different polarimetric channels (HH, VV, HH+VV and HH-VV) and the optimum channels for different number of looks.

Besides coherence, we need to check the phase improvement obtained at different optimization cases. The differential phases of the optimum channel and the HH+VV channel are displayed in Figure 3.66. First, we have selected the differential phases corresponding to the multilook size which provided the largest improvement, i.e., the 3×3 multilook. In this regard, comparing Figures 3.66(a) and 3.66(b), it seems that there is not a true phase quality improvement even if coherence was greatly improved throughout the area, so that noise reduction is mainly achieved by multilooking and the optimization does not provide a significant additional improvement. Then, the same is observed in the 9×9 multilook case shown in Figures 3.66(c) and 3.66(d): noise was reduced to a greater extent with the largest multilook size (and the spatial resolution was also reduced), but decorrelated zones do not present any real improvement with regards to the conventional HH+VV channel. In fact, we observe that there is almost no difference between channels, proving again that phase improvement is due to the multilook filter of the original SLC data.

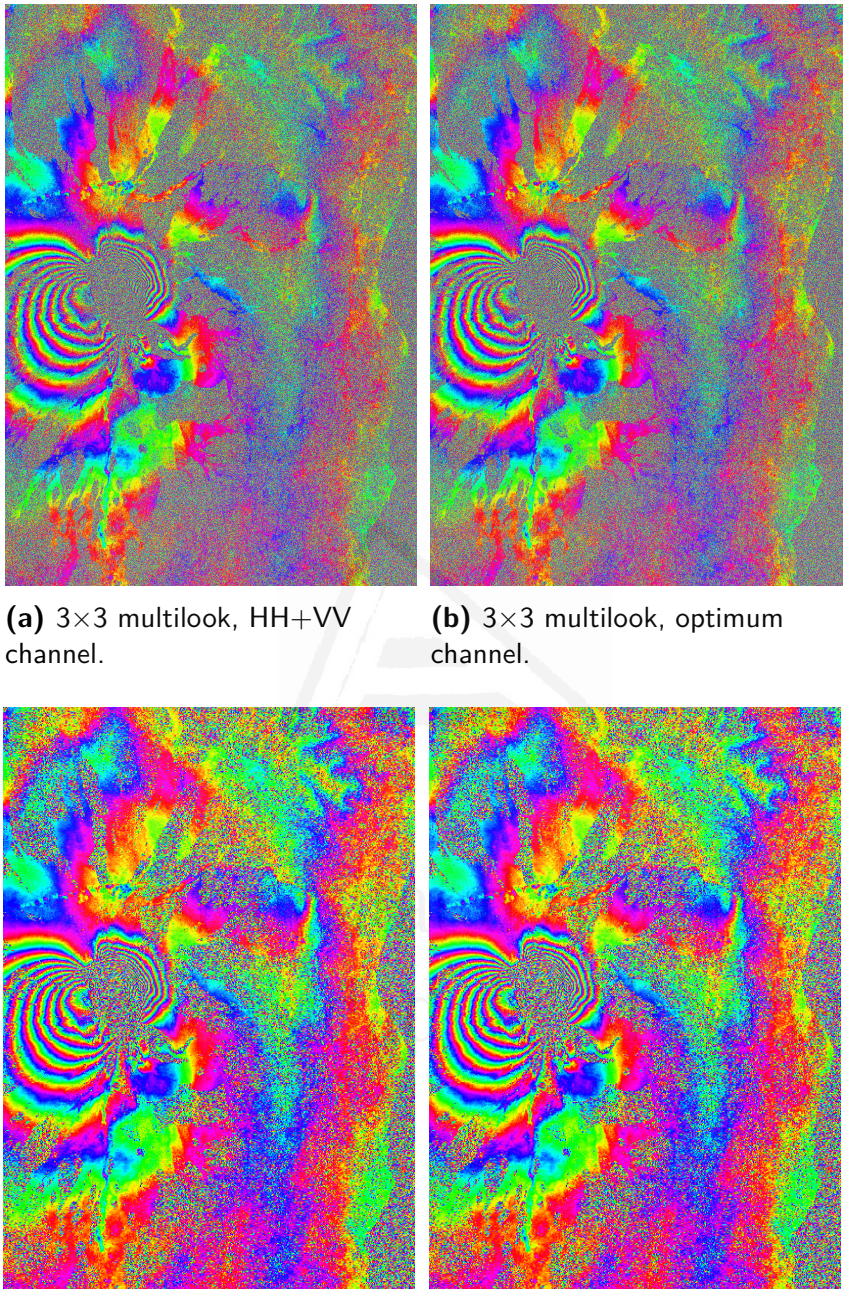

(a) 3×3 multilook, HH+VV channel.

(b) 3×3 multilook, optimum channel.

(c) 9×9 multilook, HH+VV channel.

(d) 9×9 multilook, optimum channel.

Figure 3.66: Differential phases of channels HH+VV and the computed optimum channel for two different number of looks.

Even though the global quality of the phase is not significantly improved, different conclusions can be derived from this study. It is deduced that a tradeoff between coherence improvement provided by polarimetric optimization, and noise reduction by multilooking must be considered. On the one hand, applications in which the number of coherent pixels is relevant (such as PSI [15] [31] [33]), would benefit from smaller multilook sizes since the polarimetric optimization provides a larger improvement. On the other hand, applications in which a cleaner and smoother phase is required would benefit from larger multilook sizes for a stronger noise reduction. However, unfortunately, PolDInSAR algorithms would not be able to provide an additional phase improvement. Evidently, in this last case, a direct filtering strategy is recommended since a very large multilook would worsen too much the spatial resolution of the interferogram, and more sophisticated techniques are necessary.

Apart from the multilook size, the spatial variability of the projection vectors should also be analyzed so as to test if it was the reason for the limited phase quality improvement, as previously stated. To this end, four different Regions of Interest (ROI) are selected and represented with the square polygons in Figure 3.67. Each region corresponds to a different land-cover type: a rural area, a vegetated area, an area without vegetation (i.e., a bare surface), and a changed area which was altered by the lava flow after the volcanic eruption. The size of each ROI is 200×200 pixels.

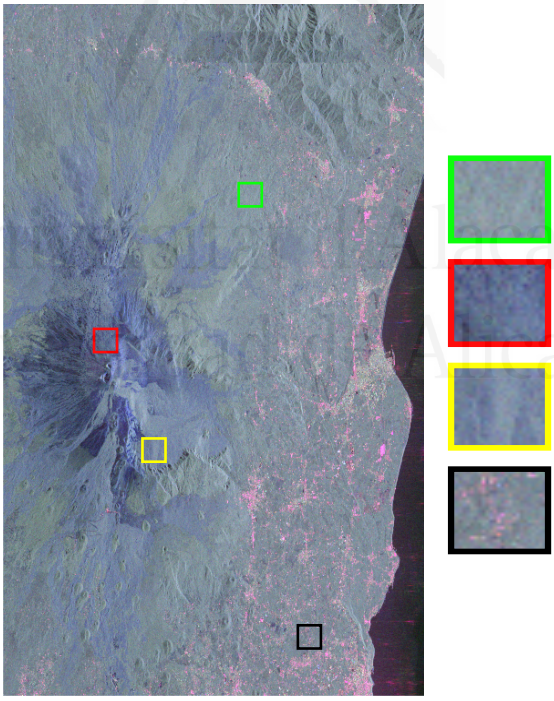

Figure 3.67: Composite RGB image of the processed area showing the four different ROIs: rural area (black square), vegetated area (green square), area without vegetation (yellow square) and changed area (red square).

The same optimization process has been carried out over the four ROIs. Instead of maximizing the coherence, the optimization consists in minimizing the standard deviation of each ROI. Note that the phase standard deviation provides a reliable estimate of the noise and can be directly estimated from the phase values, provided that the set of pixels belongs to a homogeneous area and phase gradients are eliminated prior to its computation.

Moreover, unlike the previous analysis where each pixel had a specific associated projection vector $\boldsymbol{\omega}$ (see Figure 3.61), in this case a single optimum projection is computed for the whole ROI, hence avoiding local changes in $\boldsymbol{\omega}$. That is, all pixels in each ROI will be projected onto the same combination of polarimetric channels. As in the previous coherence analysis, the process is repeated for different multilook sizes, which vary again from 3×3 to 21×21 pixels. The phase standard deviation of the non-local filtered data is also considered.

Results are summarized in Table 3.16. For comparison purposes, we have also estimated the phase standard deviation of channel HH+VV.

As it can be seen, vegetated and changed areas exhibit the highest standard deviation values, showing an extreme level of noise, which was expected due to temporal decorrelation. The rural area has a slightly lower value, and finally the bare surface area is less affected by noise. Due to the multilook processing, the initial noise is reduced for all area types, so phase standard deviation values become lower as the multilook size increases, especially for the bare surface and the rural areas which seem to be free of noise for larger multilook sizes. However, if we compare the standard deviation of the optimum channel and the HH+VV channel for any multilook size, the improvement is rather minimum. That is, there is not a significant noise reduction with regards to the conventional channel. It follows that noise suppression is mainly achieved (again) by multilooking and that the pixel-by-pixel strategy was not the reason for the minor phase quality improvement.

Phase standard deviation [rad]					
		Area type			
Multilook size	Channel	Rural	With vegetation	Without vegetation	Changed
SLC	Optimum	1.645	1.762	0.721	1.786
	HH+VV	1.657	1.769	0.788	1.789
3×3	Optimum	1.451	1.704	0.302	1.762
	HH+VV	1.461	1.712	0.303	1.769
5×5	Optimum	1.275	1.652	0.271	1.738
	HH+VV	1.285	1.663	0.272	1.745
7×7	Optimum	1.110	1.597	0.259	1.708
	HH+VV	1.123	1.611	0.262	1.718
9×9	Optimum	0.961	1.539	0.252	1.695
	HH+VV	0.972	1.557	0.254	1.702
11×11	Optimum	0.829	1.481	0.247	1.670
	HH+VV	0.840	1.507	0.249	1.695
13×13	Optimum	0.721	1.423	0.242	1.653
	HH+VV	0.734	1.459	0.245	1.676
15×15	Optimum	0.621	1.365	0.238	1.627
	HH+VV	0.647	1.409	0.241	1.657
17×17	Optimum	0.539	1.299	0.235	1.601
	HH+VV	0.578	1.355	0.238	1.633
19×19	Optimum	0.475	1.262	0.231	1.580
	HH+VV	0.516	1.301	0.235	1.618
21×21	Optimum	0.425	1.221	0.228	1.569
	HH+VV	0.468	1.248	0.231	1.598
NL-SAR	Optimum	1.276	1.657	0.248	1.686
	HH+VV	1.293	1.669	0.251	1.729

Table 3.16: Comparison of the phase standard deviation in the four analyzed areas between channels HH+VV and the optimum channel for different number of looks

Up to this point, it seems that the polarimetric optimization does not provide a significant phase quality improvement or, at least, it does not provide a further quality increase in comparison with simply multilooking the data. In order to test if PolDInSAR methods can achieve a true phase quality improvement, an alternative formulation has been tested. It is a procedure similar to the one described in [99] but where the ESM constraint is always satisfied and the expression of the generalized coherence (Equation 2.82) is considered as the cost function.

Because the coherence is to be optimized, a reduction of the spatial resolution is implicitly required. The proposed methodology consists in applying the aforementioned optimization algorithms at full resolution. That is, each pixel is individually optimized and, only during the optimization process the surrounding pixels are averaged to locally compute the coherence, but the original data are never filtered. This is illustrated with Figure 3.68. Note that there is not any previous multilooking of the original data, and the optimization is performed on a pixel basis by progressively extracting 3×3 adjacent windows.

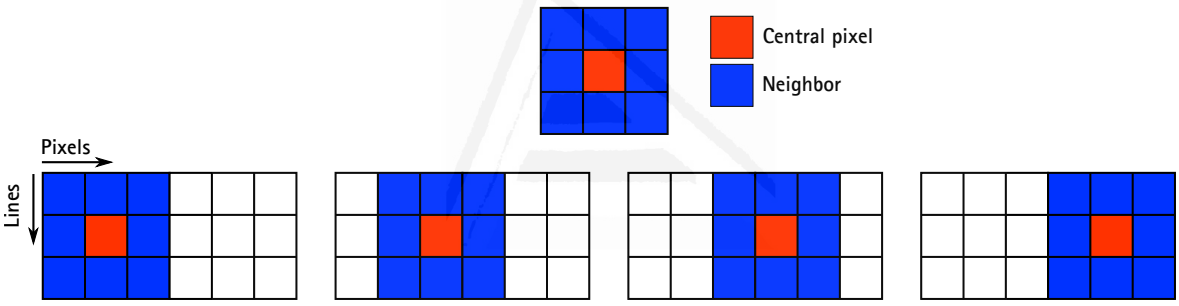

Figure 3.68: Polarimetric optimization of individual pixels.

The reason of using this window size is two-fold. Firstly, as previously analyzed in Section 3.3.4, a 3×3 multilook provided the largest coherence improvement. It is therefore preferable to use this window size. Secondly, the reduced size of the window prevents the risk of employing heterogeneous pixels during the optimization of the central one. In this way, after a pixel is optimized, it positively influences the optimization of the adjacent one, in such a way that the coherence is maximized and a cleaner phase can be obtained.

This method has been applied to the dataset of quad-polarimetric RADARSAT-2 images. Specifically, the two-step SNR method has been employed and the interferometric coherence has been used as a figure of merit. Figure 3.69 shows the differential phases of channel HH+VV and the optimum channel. Note that, unlike in the previous analysis, these phases are at full resolution. As it can be observed, even though the area is significantly affected by decorrelation and the noise level remains high, an important improvement of the phase quality is obtained by means of the polarimetric optimization. The improvement is also evaluated with the coherence histograms represented in Figure 3.70. It is clearly observed that now there is a much larger difference between the conventional and the optimum channels (comparing Figures 3.68 and 3.64) which is translated into a real phase

quality improvement. For comparison purposes, the HH+VV interferogram was filtered with the adaptive Goldstein method. Note that the same filtering parameters as the ones proposed in [66] have been used, that is, a filtering window of 32×32 pixels and a 3×3 mean kernel as the smoothing operator. As shown in Figure 3.70, even though the filter provides the highest coherence values, the optimization provides a remarkable result, which is similar to the one obtained after directly applying a filter.

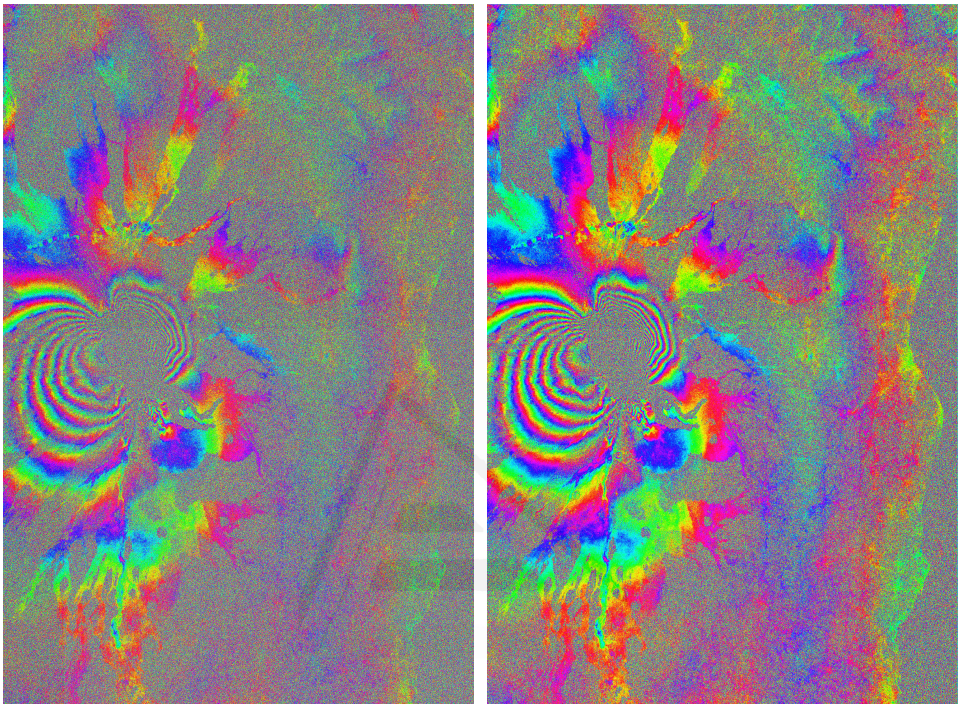

(a) HH+VV. **(b)** Optimum.

Figure 3.69: Differential phases of channels HH+VV and the computed optimum channel after applying the polarimetric optimization.

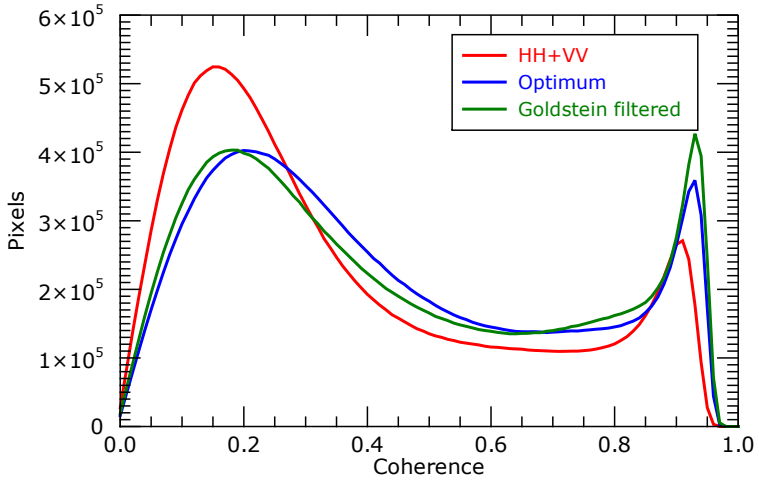

Figure 3.70: Coherence histograms of channels HH+VV and the optimum channel and the Goldstein filtered interferogram.

The associated coherence maps are shown in Figure 3.71. As expected, coherence is increased throughout the area.

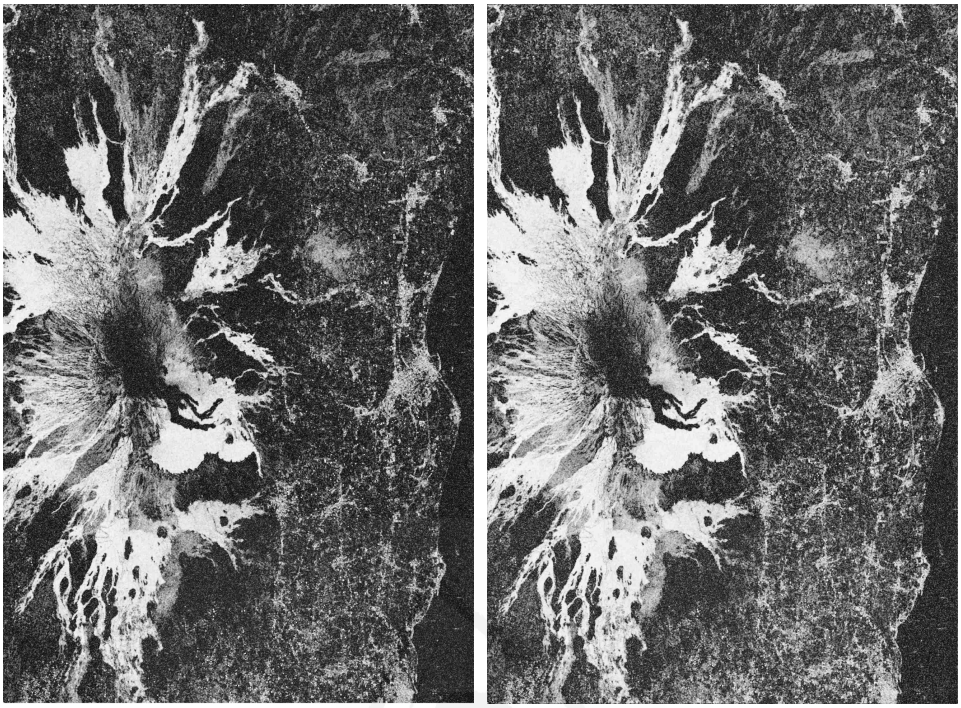

(a) HH+VV. **(b)** Optimum.

Figure 3.71: Coherence maps of channel HH+VV and the optimum channel. Coherence was estimated with a 5×9 multilook.

A more detailed visualization of the improvement is shown with the different ROIs in Figure 3.72. An urban area, a deformation area with strong phase gradients, and a correlated area (i.e., an area in which the coherence was already high) are selected. As it can be observed, a significant increase in phase quality is obtained, especially in the correlated area shown in Figure 3.72(f). The method is only limited in very decorrelated zones. In these areas, although there is an improvement, the noise remains relatively high. The major advantage of the method concerns the resolution preservation. In fact, since each pixel is individually optimized, the original spatial resolution of the interferogram is never reduced. As shown in Figure 3.72(d), fringe continuity is greatly improved and preserved.

This is an advantage with regards to filtering, where there is a higher risk of losing too much spatial resolution if not appropriately done. It is concluded that this approach finally succeeded in proving that a polarimetric optimization of the coherence can be performed to improve the quality of differential interferograms.

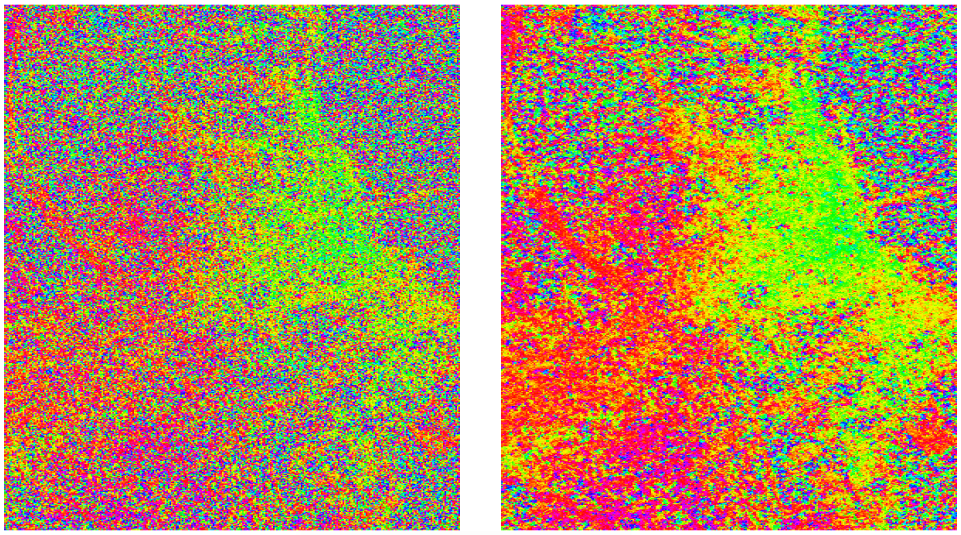

(a) Urban area. HH+VV. **(b)** Urban area. Optimum.

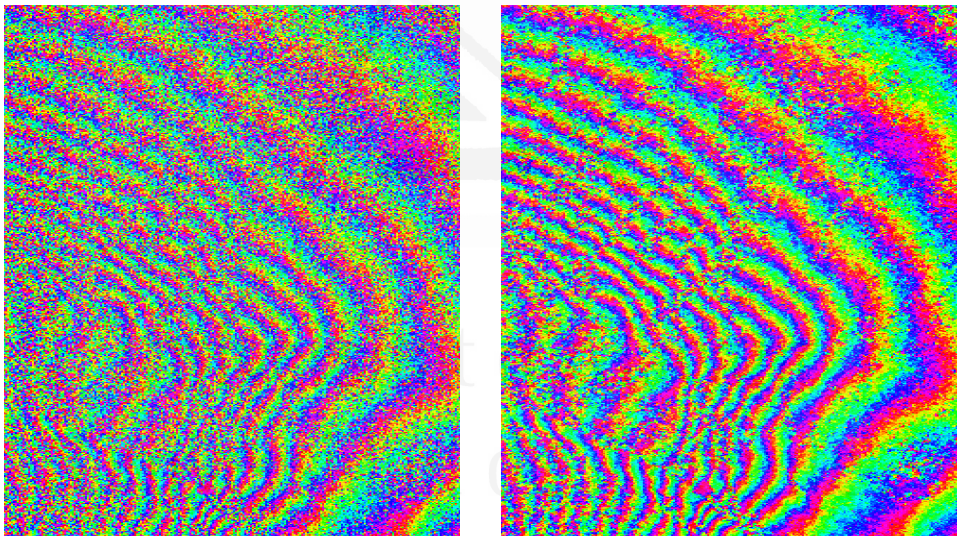

(c) Deformation area. HH+VV. **(d)** Deformation area. Optimum.

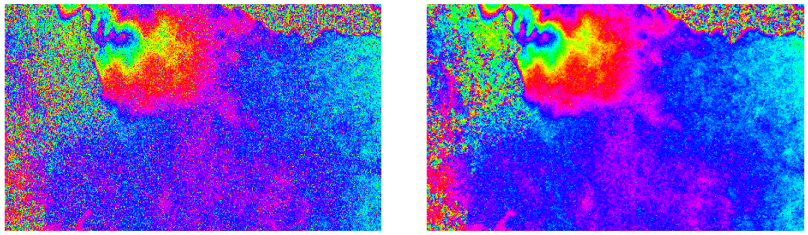

(e) Correlated area. HH+VV. **(f)** Correlated area. Optimum.

Figure 3.72: Detail differential phases of channels HH+VV and the optimum channel after coherence optimization.

4

Multitemporal InSAR for Crop Type Mapping

The last chapter of this thesis deals with an innovative exploitation of InSAR data. Specifically, this chapter concerns the *exploitation of the interferometric coherence for crop type mapping*, that is, to analyze whether the coherence constitutes a valuable feature which can be used as input to classification methods in order to construct digital crop type maps. In this regard, it is worth mentioning that in the context of SAR, the images' intensity (i.e., the backscattering coefficient) constitutes the traditional input to classification methods [100] [101]. However, InSAR data have proven effective and valuable in this context, as shown in previous works concerning the automatic mapping of the land-cover of vast areas [102] [103] [104].

As previously stated in Chapter 2, image classification is approached as a machine learning problem. The classification can be either supervised or unsupervised. In this case, we will always consider a *supervised* approach in which we have a previous knowledge of some characteristics of the area to be analyzed. That is, we have an external *ground truth* which is used to train a model with some known input-output pairs. Then, the rest of the dataset is classified according to the previously trained model. Moreover, as also indicated in Chapter 2, we will make use of a specific ensemble method denoted as Random Forests, which is an extension of the single decision tree classifier. Finally, the impact of the polarization will also be evaluated. That is, we will analyze the influence, in terms of accuracy, that different polarimetric channels have during the classification process.

In Chapter 2, the concept of the local correlation between two coregistered SAR images was introduced. Specifically, the interferometric coherence defined with Equation 2.43, represents the normalized correlation between two single SAR images. This concept can be extended to *time series*, namely, series of images spanning a certain period of time. In this regard, if a given dataset is composed by N SAR images, $S_1 \dots S_N$, we can build a $N \times N$ Hermitian, positive semi-definite *Temporal Covariance Matrix* $\hat{C}$ as

$$\hat{C} = \begin{bmatrix} E\{|S_1|^2\} & E\{S_1 S_2^*\} & E\{S_1 S_3^*\} & \dots & E\{S_1 S_N^*\} \\ E\{S_2 S_1^*\} & E\{|S_2|^2\} & E\{S_2 S_3^*\} & \dots & E\{S_2 S_N^*\} \\ \vdots & \vdots & \vdots & \ddots & \vdots \\ E\{S_N S_1^*\} & E\{S_N S_2^*\} & E\{S_N S_3^*\} & \dots & E\{|S_N|^2\} \end{bmatrix}, \tag{4.1}$$

where $E\{\}$ refers to the mathematical expectation which, in practice, is substituted by a spatial average (multilook). Note that the covariance matrix $\hat{C}$ contains the evolution of the radiometric information (that is, the series of backscatterer intensities) in its main diagonal, and all possible interferometric combinations of the dataset in its off-diagonal elements.

From Equations 2.43 and 4.1, we can easily derive the expression of the *Temporal Coherence Matrix* $\hat{\Gamma}$, which is a normalization of the previous covariance matrix $\hat{C}$,

$$\hat{\Gamma} = \begin{bmatrix} 1 & \gamma_{12} & \gamma_{13} & \cdots & \gamma_{1N} \\ \gamma_{21} & 1 & \gamma_{23} & \cdots & \gamma_{2N} \\ \vdots & \vdots & \vdots & \ddots & \vdots \\ \gamma_{N1} & \gamma_{N2} & \gamma_{N3} & \cdots & 1 \end{bmatrix}. \tag{4.2}$$

Note that $\hat{\Gamma}$ contains the complex correlation (coherence) between all possible combinations of images of the dataset. Taking the norm of each element of $\hat{\Gamma}$ directly yields the coherence coefficients of each element of the dataset. The coherence matrix is symmetric (i.e., $|\gamma_{ij}| = |\gamma_{ji}|$), so that the upper (or lower) diagonal elements provide the useful coherence data to be used as input to any classification algorithm. It is therefore easily verified that if a given dataset contains N SAR images, the number of distinct combinations is $N \cdot (N-1)/2$.

Moreover, from Equations 4.1 and 4.2, it is deduced that elements which are closer to the main diagonal of the matrices have a shorter temporal baseline. In this regard, the superdiagonal elements of $\hat{\Gamma}$ (elements located immediately above the main diagonal) correspond to the *shortest baseline* interferometric combinations.

4.2 Results

The classification process is performed in a specific agricultural area located close to the city of Sevilla (Andalucía), in the south-west of Spain. A ground truth of the analyzed area is available and is depicted in Figure 4.1. Ground truth data were provided by the Regional Government of Andalucía and FEGA (Spanish Agrarian Guarantee Fund), and they come from official cadastral information. As shown in Figure 4.1, a wide variety of agricultural crops were cultivated during the year 2017. Specifically, we distinguish 17 types of crops, being cotton and tomatoes the ones which were mostly cultivated throughout the area.

Moreover, all the results shown in this chapter have been obtained by using Sentinel-1 data. Specifically, all available SLC images of year 2017 (59 images in total) coming from orbit 154 (incidence angle of 38.7°) gathered by the two-satellite constellation Sentinel-1 A/B in interferometric wide swath mode have been considered. It is important to note that the constellation of Sentinel-1 satellites is able to provide SAR images with a reduced repeat cycle of 6 days, with respect to the original 12-day repeat cycle when just one satellite (Sentinel-1 A) was in orbit. From the interferometric point of view, this represents an advantage in terms of the quality of the data since they are less affected by temporal decorrelation.

After accurate coregistration and calibration of Sentinel-1 images [105], a large stack of interferograms corresponding to all possible master-slave combinations is obtained. In addition, data from polarimetric channels VV and VH are available and will be used either solely or jointly. Also, it is important to note that in this work we will only consider a *short-baseline* subset of the whole set of interferometric combinations. Specifically, coherences coming from 6, 12 and 18 days of temporal baselines between image-pairs will be used.

Furthermore, coherence was estimated using a conventional boxcar filter (multilook) of 4×19 pixels, which yields a pixel resolution of 60×80 meters (taking into account that the original image resolution was 3×22 meters in range and azimuth respectively). Coherence maps are then oversampled by a factor of 3×4 and geocoded[1] [106] [107] into a common reference grid (in UTM coordinates) of size 1000×1000 pixels, so that the same geometry and pixel spacing of 20m are used in the ground truth and the coherence data.

Finally, Figure 4.2 partially shows the temporal coherence matrix of the processed area (only the first 10 combinations of image pairs are shown). It is clearly observed that the coherence progressively decreases as the temporal baseline (in days) between master and slave pairs increases, as previously stated.

[1] Geocoding is the process of projecting SAR data into a standard cartographic coordinates system, such as geographic (latitude and longitude) or Universal Transverse Mercator (UTM) coordinates.

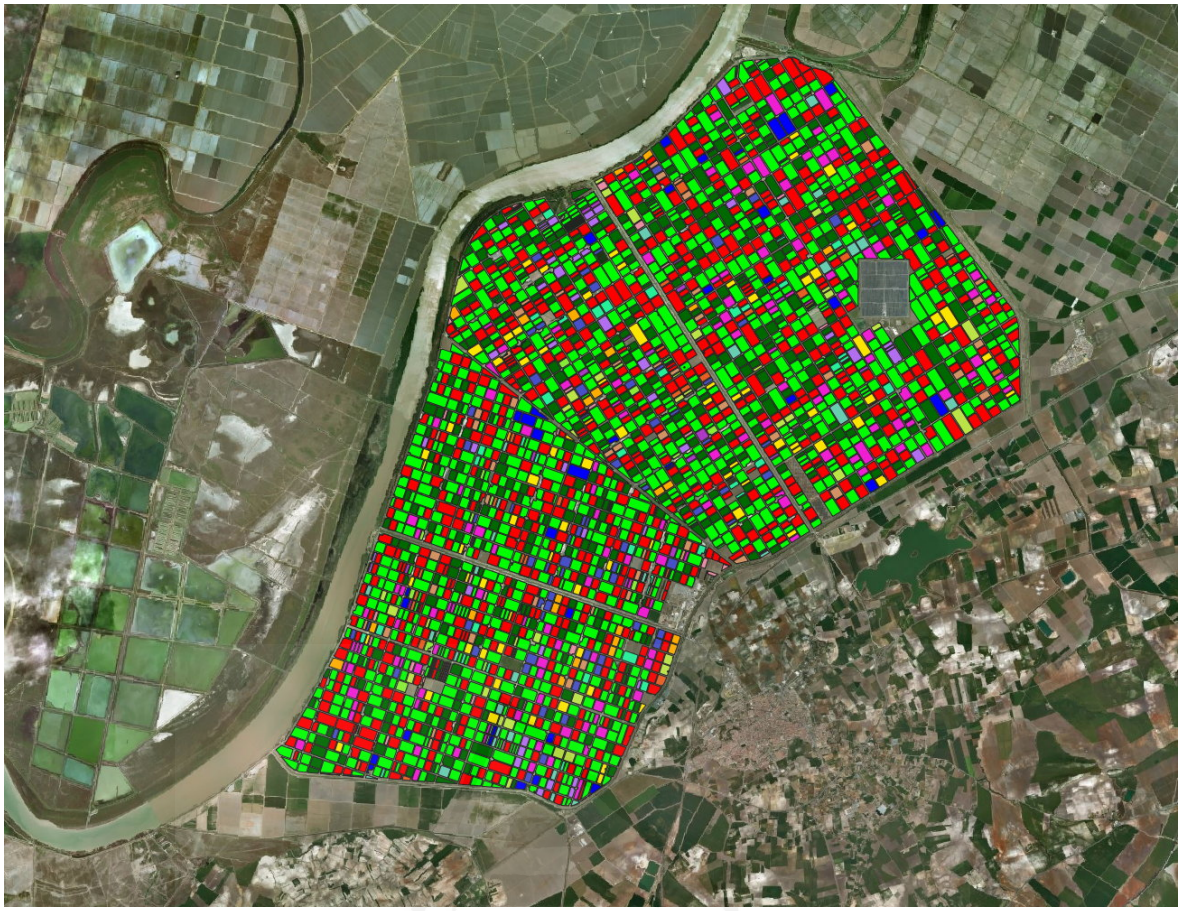

Figure 4.1: Ground truth of the processed area. Colors correspond to 17 different types of agricultural crops: **Cotton**, **Tomato**, **Sugar beet**, **Maize**, **Fallow**, **Sunflower**, **Carrot**, **Soft wheat**, **Sweet potato**, **Alfalfa**, **Hard wheat**, **Pepper**, **Quinoa**, **Pumpkin**, **Chickpea**, **Potato**, and **Onion**.

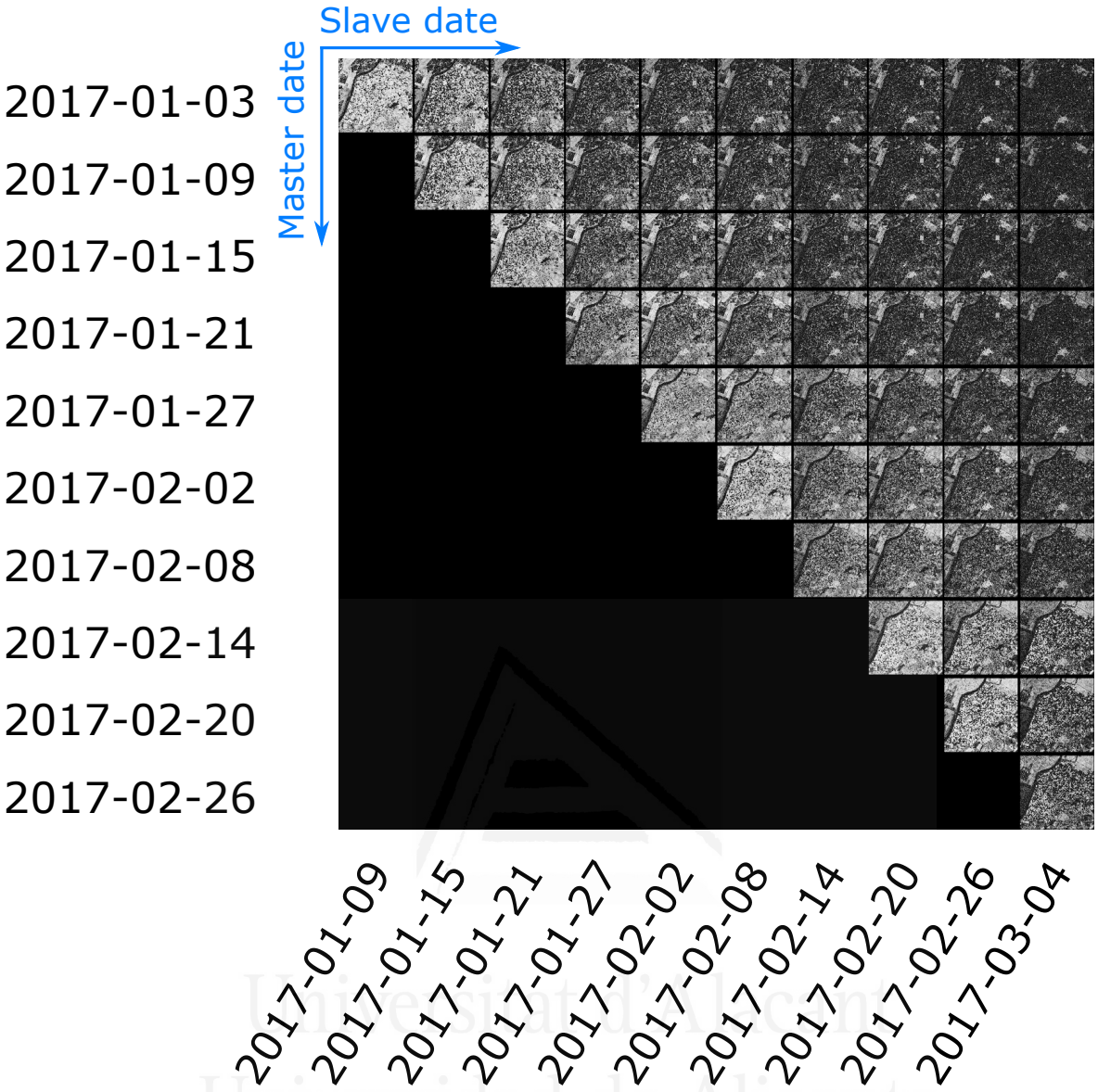

Figure 4.2: Temporal coherence matrix of the processed area between 2017-01-03 and 2017-03-04. The polarimetric channel is VV.

4.2.1 Preprocessing of Ground Truth data

In Section 2.6, we have seen the influence of the number of training samples in the classification process by means of Random Forests. In this regard, ground truth data must be correctly sampled in order to avoid undesired effects such as overfitting. The first step consists in dividing the original ground data represented in Figure 4.1 into a training set and a testing test in such a way that half of the fields of each crop type are randomly assigned to each set. This approach is followed to ensure that there is enough spatial distance between pixels of the same crop type, which is not always satisfied if just a random selection of pixels is done to build the training and the testing sets [108]. This also avoids the *spatial autocorrelation* [109] of training pixels, which positively or negatively influences

the classification of surrounding pixels in specific areas after training the model. The division of the ground truth is represented in Figure 4.3.

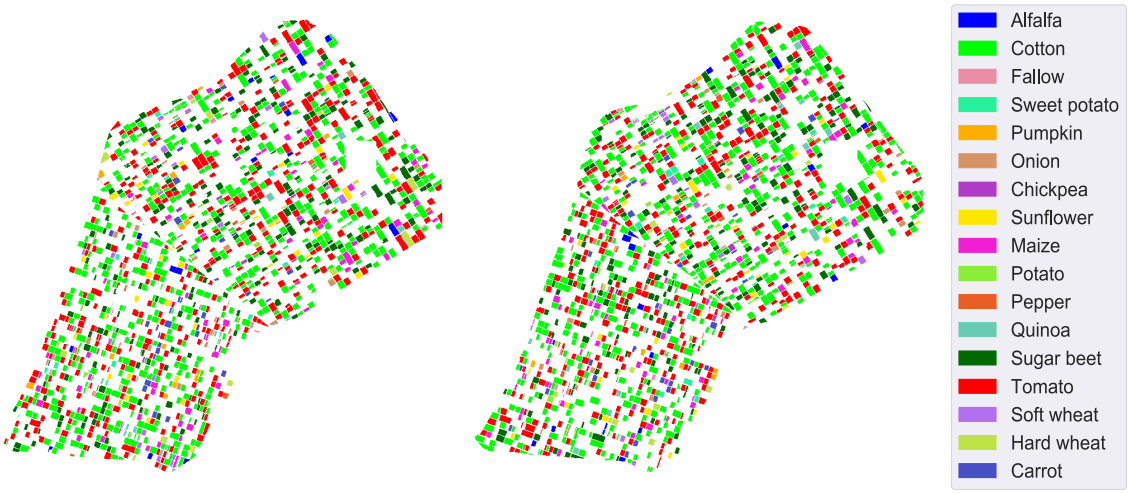

(a) Fields composing the training set. **(b)** Fields composing the testing set.

Figure 4.3: Ground truth preprocessing: for each crop type, half of the fields are used for training and the other half for testing.

By looking at Figure 4.3(a), it can be easily seen that the number of fields and, hence, the number of pixels of each crop type varies significantly among classes. Specifically, the number of samples of each set and of each crop type is shown in Table 4.1. It is deduced that some classes are *predominant* (cotton, tomato and sugar beet) whereas other classes present a reduced number of samples in the dataset (especially potato and chickpea). In other words, the training dataset is *imbalanced*. This might be a problem from the classification point of view, since an overfit towards predominant classes might happen and minority classes are more likely to be misclassified, reducing the quality of the results. To solve this inconvenience, the original training set is *equally subsampled* in such a way that the same number of samples of each crop type is used to train our model. The resulting subsampled ground truth is represented in Figure 4.4. Note that now, each of the 17 classes has the same number of pixels in the training set. Specifically, each class has 388 pixels, which is the number of samples of chickpea (which is the class with the smallest number of pixels, as shown in Table 4.1).

	Training set		Testing set		Total	
Crop type	**Number of fields**	**Number of samples**	**Number of fields**	**Number of samples**	**Number of fields**	**Number of samples**
Cotton	560	53193	560	55918	1120	109111
Tomato	391	35511	391	35943	782	71454
Sugar beet	235	18523	236	19673	471	38178
Maize	72	6004	73	6260	145	12272
Sunflower	40	3226	41	3232	81	6458
Fallow	41	604	41	808	82	1404
Carrot	35	2315	36	2505	71	4820
Onion	30	1689	30	1749	60	3456
Soft wheat	22	1608	23	1738	45	3346
Sweet potato	21	1082	21	1697	42	2779
Alfalfa	20	1890	20	2106	40	3996
Hard wheat	18	1457	18	1982	36	3439
Pepper	16	680	17	744	33	1424
Quinoa	16	936	16	1470	32	2406
Pumpkin	13	975	13	1193	26	2168
Chickpea	11	388	11	437	22	825
Potato	7	388	8	512	15	900

Table 4.1: Characteristics of the ground truth data showing the original number of training and testing samples of each crop type.

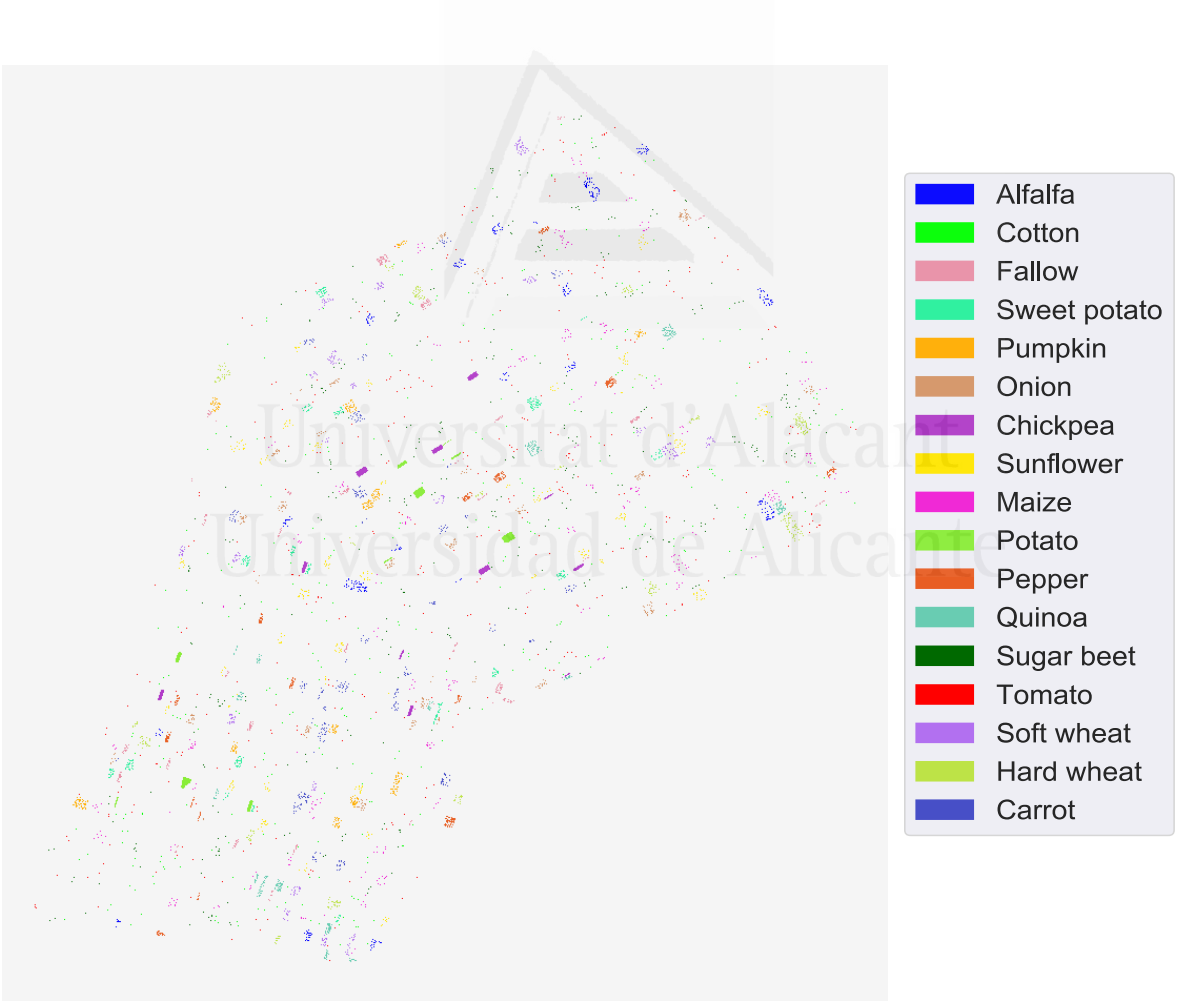

Figure 4.4: Equal subsampling of the training dataset. Each class has 388 pixels so that the total number of training samples represent around 2.5% of the total number of pixels of the ground truth data. Equal subsampling is carried out randomly.

4.2.2 Accuracy Metrics and Performance Measures

It is very important to introduce the variety of measures that will be systemically used to describe the accuracy of all classifications. Once the classification is performed and the thematic map of crop types is obtained, the testing set (shown in Figure 4.3(b)) is used to evaluate how accurate the model is performing. The following quality measures and metrics have been considered [34] [110].

- **Confusion matrix** (or contingency table). It is the most usual form of presenting the accuracy of a supervised classification. Assuming that we have K different classes, the confusion matrix is defined as

$$\mathbf{C} = \begin{bmatrix} c_{11} & c_{12} & c_{13} & \dots & c_{1K} \\ c_{21} & c_{22} & c_{23} & \dots & c_{2K} \\ \vdots & \vdots & \vdots & \ddots & \vdots \\ c_{K1} & c_{K2} & c_{K3} & \dots & c_{KK} \end{bmatrix}, \tag{4.3}$$

  where each element c_{ij} of $\mathbf{C}$ contains the number of pixels belonging to class j which are classified as class i. Therefore, it is deduced that the elements of the main diagonal of the confusion matrix correspond to correct classifications, whereas the rest are missclassifications.

- **Global accuracy**. It defines the overall proportion of correctly classified samples, and can be employed to summarize the overall accuracy of the classification. It is directly provided by the trace of the confusion matrix divided by the total number of testing samples (i.e., the sum of the whole confusion matrix).

- **Kappa score**. It is a statistic which measures the inter-observer reliability. That is, it provides a value of how closely all classified samples match the ground truth data but taking into account random chance. It can be calculated as

$$\kappa = \frac{Pr(\text{correct classification}) - Pr(\text{random chance classification})}{1 - Pr(\text{random chance classification})}, \tag{4.4}$$

  where $Pr()$ means probability of its argument.

  An estimator of κ can be derived from the rows and columns of the confusion matrix as [34]:

$$\kappa = \frac{N \sum_{i=1}^{n} m_{i,i} - \sum_{i=1}^{n} G_i P_i}{N^2 - \sum_{i=1}^{n} G_i P_i}, \tag{4.5}$$

  where i is the class label, N is the total number of testing samples, $m_{i,j}$ is the number of correctly classified samples (i.e, the trace of the confusion matrix), P_i is the number of predicted values belonging to class i (sum of row i) and G_i is the number of ground truth samples belonging to class i (sum of column i). Values of κ lie between -1 and 1. A value of 1 implies complete agreement, whereas lowers values indicate less agreement.

- **Producer's accuracy**. It is the result of dividing the number of correctly classified samples of class i by the total number of elements of class i. In terms of the confusion matrix, it corresponds to the result of dividing element c_{ii} by the total of column i. The producer's accuracy is complement of omission error.

- **User's accuracy**. It is the result of dividing the number of correctly classified samples of class i by the total number of samples that were classified as i. In terms of the confusion matrix, it corresponds to the result of dividing element c_{ii} by the total of row i. The user's accuracy is complement of the commission error.

4.2.3 Preliminary Results: Impact of an Imbalanced Training Dataset

In order to show the impact of an imbalanced dataset and the importance of a correctly sampled training set, the following preliminary test has been carried out. The Random Forests classifier[2] is applied both by using the original training set of Figure 4.3(a) and the equally subsampled training set shown in Figure 4.4. In this case, only the shortest temporal baseline has been considered (i.e., 6-day coherences) and only the data of VV polarization have been used. Note that this polarization is selected since it is known to have a SNR higher than VH.

Figure 4.5 shows the crop type maps obtained with each approach. By comparing Figures 4.5(a) and 4.5(b), it is clearly observed that the classifier has favored the majority classes. That is, the number of pixels classified as cotton and tomato is significantly larger when the model was trained without an equal sampling of the training set, as shown in Figure 4.5(a).

[2]Random Forests implementation from *scikit-learn* library [63], written in Python language, has been used in this work. The number of trees is set to 100 and the remaining parameters are set to default.

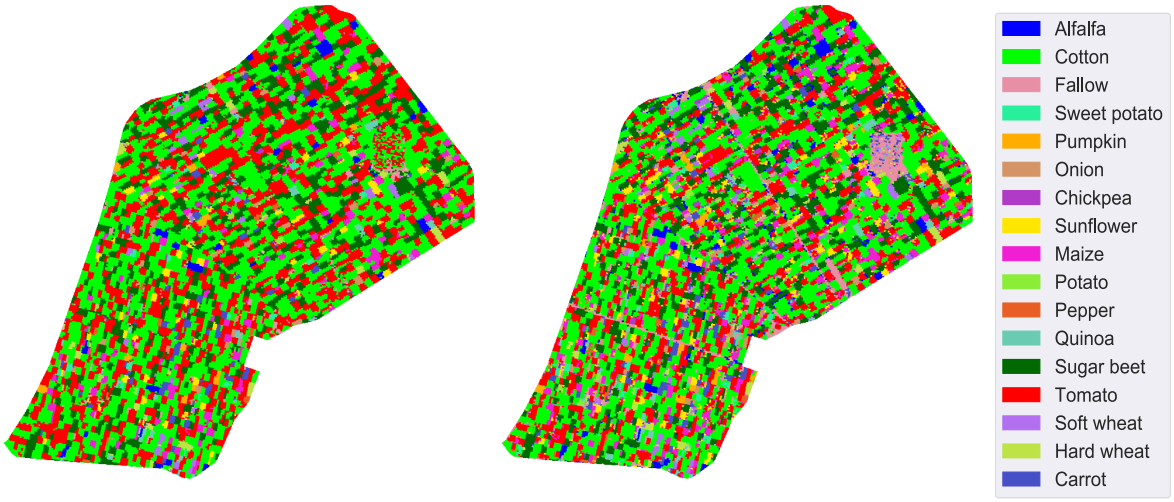

(a) Classified image obtained when the RF was trained without equal sampling.

(b) Classified image obtained when the RF was trained with equal sampling.

Figure 4.5: Classification results obtained with Random Forests using two different training models: without and with class balance. Shortest temporal baseline coherences (6 days) of channel VV were used as input to the classifier.

Moreover, the differences of accuracy become evident if we compare the confusion matrices of each case. On the one hand, Figure 4.6 shows the normalized confusion matrix obtained when the model was trained with an imbalanced number of training samples. By looking at the main diagonal of the matrix, it is clearly seen that the three majority classes (cotton, tomato and sugar beet) present the highest accuracies (which are higher than 85%). On the contrary, minority classes exhibit a very low accuracy, which is almost 0% (especially for classes sweet potato, pumpkin, chickpea and potato). It is deduced that the training model is biased towards the majority classes and that there exist an important confusion between classes. This can be verified by looking at the row (predictions) of each individual class. For instance, class sweet potato (9% of correct classifications) has been mainly misclassified as cotton (57%) and tomato (30%).

On the other hand, Figure 4.7 represents the normalized confusion matrix when the RF was trained with the same number of samples (balanced subsampling of each class). It is observed that the accuracy of majority classes remains high (86%, 72% and 90% for cotton, tomato and sugar beet, respectively), but now the accuracy of the other classes has notably improved. For instance, the accuracy of chickpea increases from 3% to 53%, and the accuracy of fallow increases from 25% to 61%. In addition, it is deduced that the confusion between classes is greatly reduced. For instance, class sweet potato presents now less confusion between cotton (it goes down from 57% to 29%) and tomato (it goes down from 30% to 21%) and the same effect is obtained for the remaining minority classes of the dataset.

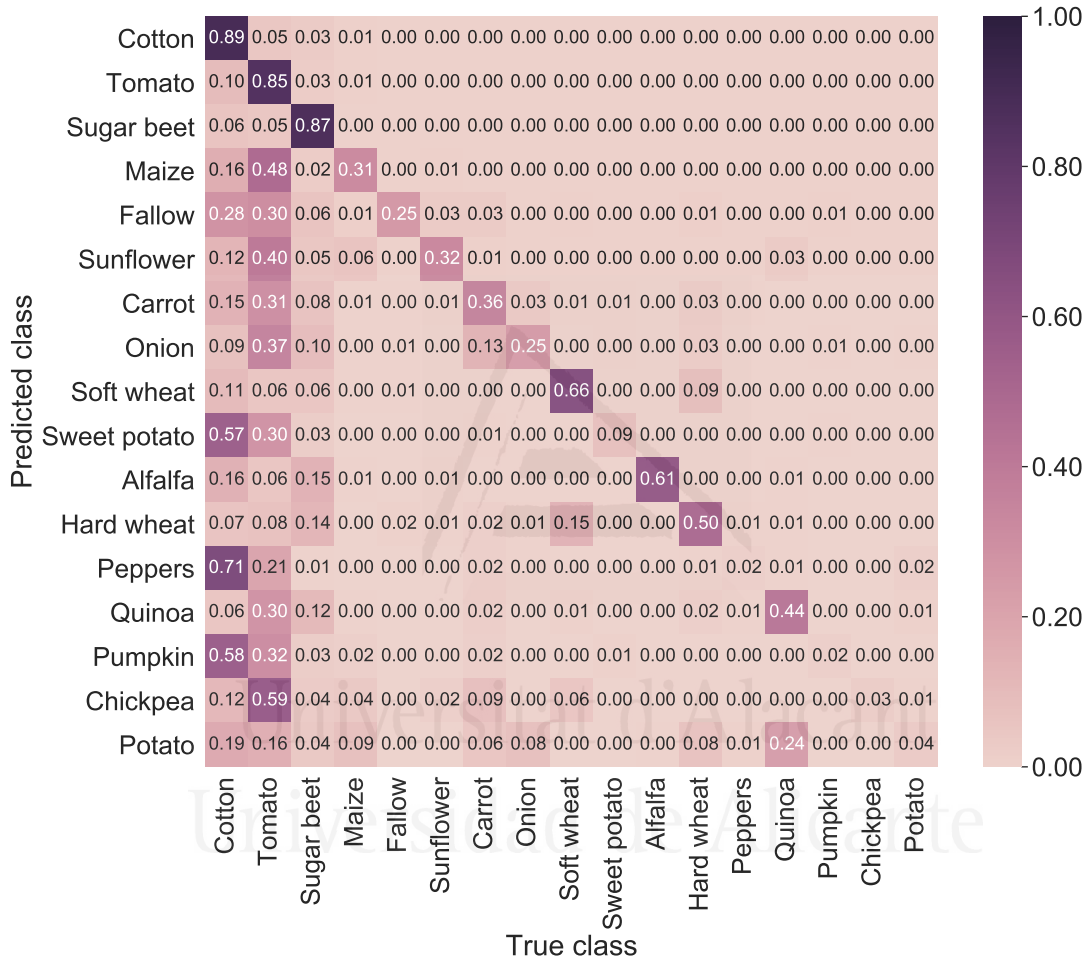

Figure 4.6: Confusion matrix obtained with Random Forests with an imbalanced sampling of the training set. Shortest temporal baseline coherences (6 days) of channel VV were used as input to the classifier.

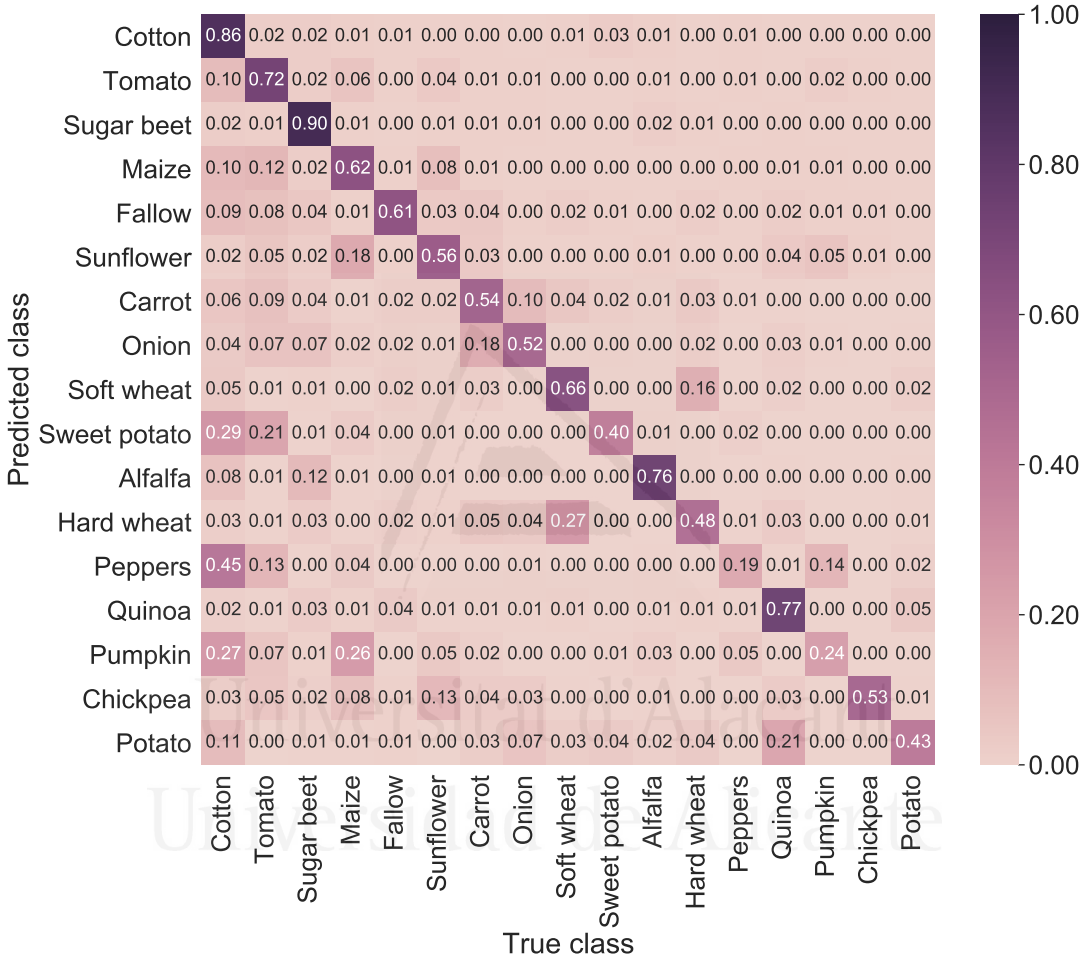

Figure 4.7: Confusion matrix obtained with Random Forests with a balanced sampling of the training set. Shortest temporal baseline coherences (6 days) of channel VV were used as input to the classifier.

The rest of accuracy measures of each approach are summarized in Table 4.2. Results show a remarkable global accuracy in both cases. In fact, it is almost the same (77.51% and 77.55%) for both imbalanced and balanced datasets. This allow us to show that the global accuracy not always provides a meaningful overview of how well a classifier is performing, and that a deeper analysis of the confusion matrix should always be carried out by computing class-level accuracies. In this regard, if the training dataset is imbalanced, a high global accuracy is obtained because the majority classes are very well classified, but it does not reflect how poorly minority classes are handled. The same conclusion is derived from the Kappa scores, which are almost identical. Note that in both cases, Kappa scores are however very good (in fact, according to [111], values between 0.61 and 0.80 indicate a substantial agreement).

Class-level accuracies are represented in Table 4.2 by both the producer's and user's accuracies. Without equal sampling of the training set, it is observed that the largest producer's and user's accuracies are obtained for the majority classes (cotton, tomato and sugar beet), while minority classes, such as maize, fallow, pumpkin or chickpea, exhibit low or very low accuracies. In fact, as shown in Table 4.2, the user's accuracy of these classes is 31.48%, 25.24%, 1.64% and 2.74%, which indicates a very poor classification. Nonetheless, user's accuracies significantly increase when the model was trained with the equally-sampled set, maximizing the accuracy of each class in a more balanced way. For instance, user's accuracy of the previously mentioned classes (maize, fallow, pumpkin and chickpea) significantly improves to 62.16%, 61.40%, 23.90% and 53.32%, respectively.

Evidently, the higher the producer's and user's accuracies are, the better the classification of a given class is. However, it is important to understand the information each accuracy is providing. Consider, for instance, maize which has, without equal sampling of the training set, a producer's accuracy of 67.14%. This means that 67.14% of pixels which are maize on the reference data (training set) have been correctly identified. However, the associated user's accuracy of such class is only 31.48%, which means that only 31.48% of pixels identified as maize actually belong to this class in the testing set. Accordingly, producer's accuracy reveals the quality of the classification of the training set, whereas the user's accuracy indicates the quality of the predictions/reality and, hence, it is a direct measure of how well the classifier performed for each class. Conversely, when a balanced training set is used, the producer's accuracy of class maize decreases to 47.28% but the user's accuracy is almost doubled to 62.16%, which indicates that this class is much better distinguished. It can also be observed that the same effect is obtained with the rest of the classes, showing that the model is better adapted.

From this study we have proven the impact that an imbalanced training set has on the classification process. We have seen that if reference data are not appropriately sampled and the number of pixels of each class varies greatly, inaccurate classifications are obtained since the model is biased towards predominant classes (classes which have more training pixels). We have also shown that the problem is solved in this case by setting a balanced subsampling for each class (exactly the same number of samples for every class). As a result, the accuracy of each individual class is greatly improved and so does the accuracy of the overall classification. Finally, it is important to mention that this strategy

will be followed for the rest of the results shown in this work, i.e., the same training data shown in Figure 4.4 will be used.

	Without equal sampling		With equal sampling	
Crop type	**Producer's accuracy**	**User's accuracy**	**Producer's accuracy**	**User's accuracy**
Cotton	83.70%	89.31%	88.55%	85.92%
Tomato	72.17%	84.82%	88.24%	72.25%
Sugar beet	80.14%	86.87%	87.48%	90.01%
Maize	67.14%	31.48%	47.28%	62.16%
Fallow	37.89%	25.24%	31.79%	61.40%
Sunflower	76.01%	32.21%	43.14%	56.42%
Carrot	52.33%	35.89%	48.67%	54.13%
Onion	51.85%	24.87%	48.94%	52.16%
Soft wheat	68.34%	66.04%	51.63%	65.86%
Sweet potato	49.17%	8.78%	28.93%	39.72%
Alfalfa	79.32%	60.69%	47.34%	76.08%
Hard wheat	56.45%	50.45%	49.47%	47.98%
Pepper	8.69%	1.61%	11.97%	19.22%
Quinoa	67.01%	43.67%	59.88%	76.87%
Pumpkin	11.19%	1.64%	15.53%	23.90%
Chickpea	13.19%	2.74%	45.96%	53.32%
Potato	13.97%	3.71%	41.24%	41.24%
Global accuracy	**77.51%**		**Global accuracy**	**77.55%**
Kappa score	**0.68**		**Kappa score**	**0.70**

Table 4.2: Accuracy assessment of crop type classification with Random Forests obtained with each approach of ground-truth preprocessing: with and without an equal sampling of training data.

4.2.4 Influence of Temporal Baseline

In previous Section 4.2.3, the Random Forests classifier was applied using 6-day coherences of polarimetric channel VV. As shown with Figure 4.7 and Table 4.2 (with equal sampling of the training set), in general good classification results have been obtained: an overall accuracy of 77.55%, a Kappa score of 0.70, and 13 out of 17 classes present an accuracy higher than 50%. In this section, the effect of the length of the temporal baseline is to be analyzed. In this regard, besides using 6-days coherences, the two second shortest baselines (12 and 18 days) will be considered, both individually and combined, so as to check if a further gain is obtained when including more data.

The first test consists in applying the classifier employing 12 and 18-day coherences individually. Note that only the data of VV polarization will be used in order to obtain a reliable comparison with the results of Section 4.2.3, in which the shortest baseline (6 days) coherence matrices of channel VV were considered. Figure 4.8 shows the normalized confusion matrix obtained in each case.

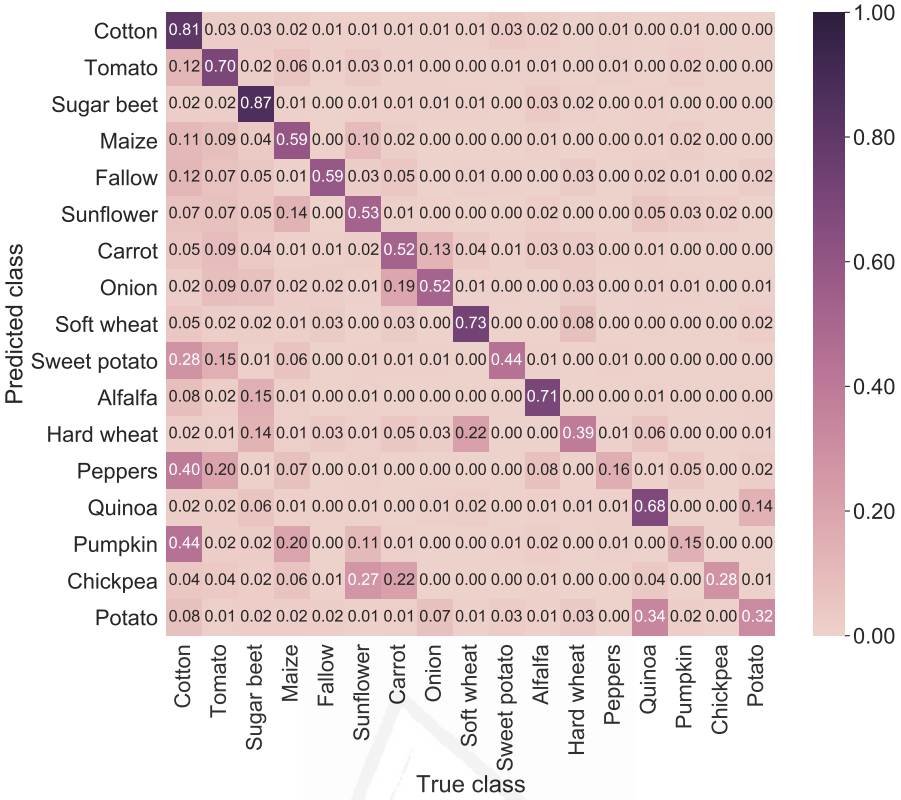

(a) 12 days of temporal baseline.

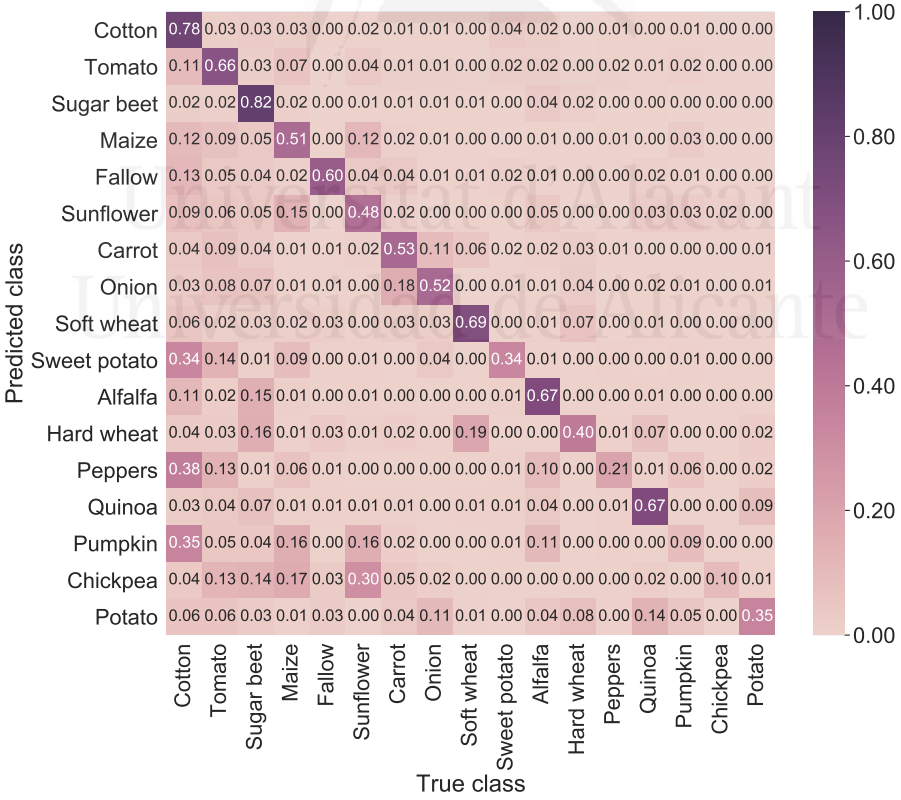

(b) 18 days of temporal baseline.

Figure 4.8: Confusion matrices obtained with Random Forests using coherences from the second and third shortest temporal baselines individually (12 and 18 days).

By comparing the main diagonals of confusion matrices of Figure 4.7 (6 days) and Figures 4.8(a) and 4.8(b), it is clearly observed that the accuracy of almost all classes progressively decreases as the temporal baseline increases. For instance, the accuracy of class alfalfa goes down from 76% (6 days) to 71% (12 days) and to 67% (18 days). Only the accuracies of classes soft wheat and sweet potato are higher when a longer baseline is used. This progressive loss of accuracy is summarized in Table 4.3, in which the accuracy differences, taking as reference the accuracy obtained using the shortest temporal baseline coherences, are calculated. It can be seen that there is a larger loss of accuracy between 6 and 18-day coherences than between 6 and 12-day coherences. This is certainly caused by the higher level of decorrelation which is present in coherence images (see Figure 4.2) when longer baselines are used, which degrade the quality of interferometric data.

	Temporal baselines	
	6 and 12 days	**6 and 18 days**
Crop type	**Accuracy difference**	**Accuracy difference**
Cotton	+5%	+8%
Tomato	+2%	+6%
Sugar beet	+3%	+8%
Maize	+3%	+11%
Fallow	+2%	+1%
Sunflower	+3%	+8%
Carrot	+2%	+1%
Onion	+0%	+0%
Soft wheat	-7%	-3%
Sweet potato	-4%	+6%
Alfalfa	+5%	+9%
Hard wheat	+10%	+8%
Pepper	+3%	-2%
Quinoa	+9%	+10%
Pumpkin	+9%	+15%
Chickpea	+24%	+43%
Potato	+11%	+8%

Table 4.3: Comparison between accuracy differences obtained when using different temporal baselines. In both cases, the accuracy obtained using 6-day coherences is selected as reference. A positive percentage indicates that the shortest temporal baseline (6 days) presents a higher accuracy, whereas a negative percentage indicates that a better result is obtained when using either 12 or 18-day coherences.

Moreover, global accuracy estimators and the rest of class-level accuracies are shown in Table 4.4. As expected, a generalized loss of accuracy is obtained when the longest temporal baseline of 18 days is used. The user's accuracy of nearly all crop types decreases, and so does the global accuracy of the classification and the associated Kappa score. However, it is worth mentioning that using longer baselines individually does not entail a dramatic loss of accuracy. In fact, the global accuracy goes

down from 77.55% (see Table 4.2), when using the shortest baseline of 6 days, to 73.82% (12 days) and to 69.66% (18 days). Also, there is not a significant difference in terms of the overall Kappa scores obtained in each case (0.70, 0.66, and 0.60 for 6, 12 and 18-day coherences respectively).

	Temporal baselines			
	12 days		**18 days**	
Crop type	**Producer's accuracy**	**User's accuracy**	**Producer's accuracy**	**User's accuracy**
Cotton	86.04%	81.13%	85.31%	77.57%
Tomato	87.58%	60.69%	88.07%	65.79%
Sugar beet	83.45%	86.78%	79.30%	81.41%
Maize	47.16%	59.38%	37.04%	49.15%
Fallow	30.06%	58.80%	33.07%	54.40%
Sunflower	36.93%	52.73%	29.10%	48.20%
Carrot	48.58%	52.46%	48.78%	52.77%
Onion	43.73%	51.81%	33.79%	52.52%
Soft wheat	54.51%	72.58%	46.95%	66.92%
Sweet potato	26.60%	44.20%	18.21%	36.95%
Alfalfa	33.93%	70.58%	26.46%	66.51%
Hard wheat	41.18%	39.40%	31.21%	30.61%
Pepper	8.15%	15.86%	8.69%	17.07%
Quinoa	51.15%	68.16%	42.70%	69.46%
Pumpkin	8.60%	14.56%	3.82%	7.28%
Chickpea	39.42%	28.15%	19.28%	16.02%
Potato	21.41%	31.84%	26.96%	37.70%
Global accuracy	**73.84%**		**Global accuracy**	**69.66%**
Kappa score	**0.66**		**Kappa score**	**0.60**

Table 4.4: Accuracy assessment of crop type classification wuth Random Forests using coherences from the second an third shortest temporal baselines individually (12 and 18 days).

Another test consists in incorporating information from the different temporal baselines to the classification process. That is, to simultaneously use coherence data coming from both 6 and 12 days, and even 6, 12 and 18 days of temporal baselines. In each case, coherences of channel VV are considered. The resulting confusion matrices are represented in Figure 4.9. It can be seen that there is almost no improvement when additional baselines are added: accuracies of each individual class are very similar to the ones obtained using the shortest baseline of 6 days (see Figure 4.7).

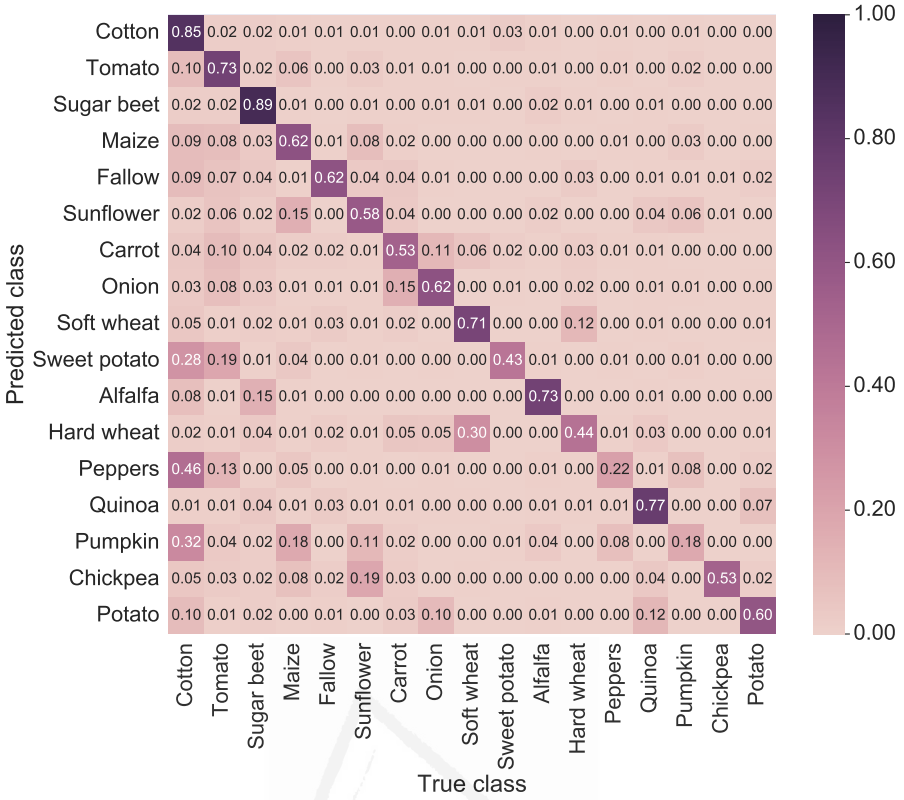

(a) 6 and 12 days.

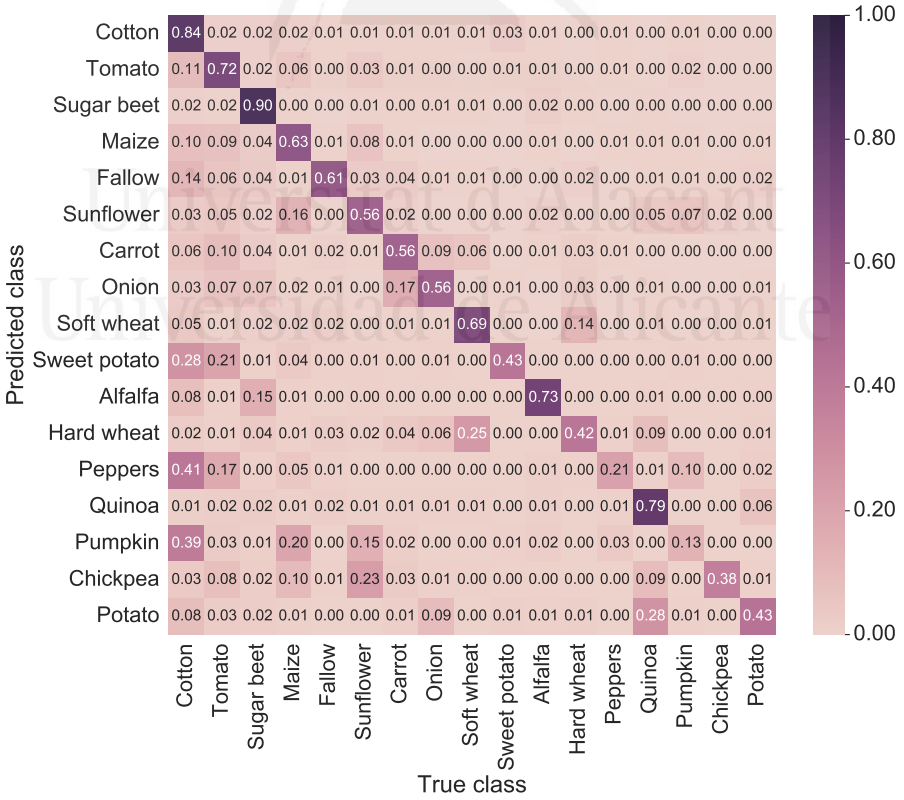

(b) 6, 12 and 18 days.

Figure 4.9: Confusion matrices obtained with Random Forests employing coherences from the first two and first three shortest temporal baselines.

The rest of accuracy measures are summarized in Table 4.5. It can be seen that the impact of including two additional baselines is very limited. As shown in Table 4.5, there is almost no difference in terms of the class-level accuracies of each crop type when all the data (three baselines) are simultaneously used. Moreover, almost the same global accuracies and Kappa scores are obtained in both classifications.

	Temporal baselines			
	6 and 12 days		**6, 12 and 18 days**	
Crop type	**Producer's accuracy**	**User's accuracy**	**Producer's accuracy**	**User's accuracy**
Cotton	88.26%	85.02%	87.59%	84.37%
Tomato	89.36%	72.59%	88.57%	71.62%
Sugar beet	86.70%	89.62%	86.07%	89.97%
Maize	47.58%	64.04%	48.55%	63.37%
Fallow	30.31%	62.54%	33.57%	61.07%
Sunflower	42.99%	55.95%	42.25%	55.70%
Carrot	53.05%	52.50%	54.36%	55.69%
Onion	48.27%	55.30%	48.85%	56.07%
Soft wheat	49.49%	69.22%	52.78%	69.09%
Sweet potato	28.33%	45.14%	25.90%	42.96%
Alfalfa	45.46%	73.65%	42.90%	72.65%
Hard wheat	44.95%	39.12%	46.21%	41.87%
Pepper	12.65%	21.64%	15.00%	21.37%
Quinoa	61.36%	74.42%	56.91%	78.71%
Pumpkin	12.75%	19.08%	8.52%	13.44%
Chickpea	37.56%	34.55%	44.44%	37.53%
Potato	38.61%	54.30%	34.58%	43.36%
Global accuracy	**77.21%**		**Global accuracy**	**76.72%**
Kappa score	**0.70**		**Kappa score**	**0.69**

Table 4.5: Accuracy assessment of crop type classification with Random Forests using coherences from the first two and first three shortest temporal baselines.

4.2.5 Influence of Polarization

The influence of polarization diversity is also to be evaluated in this work. As previously stated, among the two polarimetric channels provided by Sentinel-1, the VV component is known to have a higher SNR than the VH counterpart. As a consequence, the quality of coherence data coming from channel VV is always higher and, hence, the Random Forests classifier is expected to perform better with this polarization. A quick analysis of the classification results obtained using VH data with 6 days of temporal baseline as input effectively proves this statement. Figure 4.10 represents the normalized confusion matrix obtained for such a classification. It is observed that a clear loss of accuracy is obtained for all classes, if we compare the main diagonal of Figure 4.10 with the one of

the confusion matrix obtained using the VV component with the same baseline configuration (previously shown in Figure 4.7). The same conclusion is derived by looking at the class-level accuracies shown in Table 4.6: both the producer's and user's accuracies are lower than when the single VV polarization is used (see Table 4.2), and so is the global accuracy (decreases from 77.55% to 69.06%) and the Kappa score (decreases from 0.70 to 0.60).

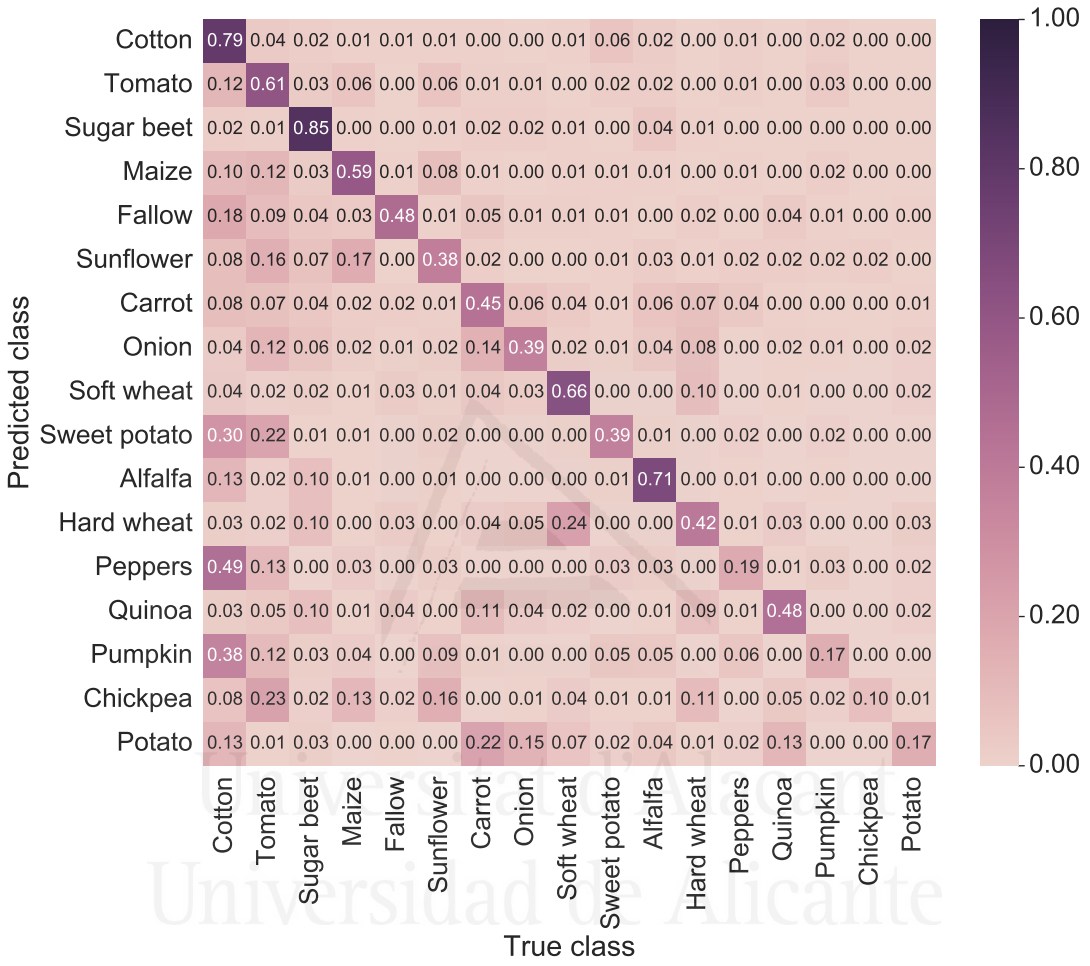

Figure 4.10: Confusion matrix obtained with Random Forests using 6-day coherences from VH polarization.

Crop type	Producer's accuracy	User's accuracy
Cotton	85.20%	78.69%
Tomato	81.84%	60.76%
Sugar beet	83.20%	84.58%
Maize	49.28%	58.78%
Fallow	24.83%	47.56%
Sunflower	26.75%	37.91%
Carrot	36.96%	44.51%
Onion	29.66%	38.84%
Soft wheat	43.89%	66.29%
Sweet potato	14.27%	38.83%
Alfalfa	28.26%	71.01%
Hard wheat	36.50%	42.21%
Pepper	7.74%	19.36%
Quinoa	57.99%	48.37%
Pumpkin	6.64%	17.03%
Chickpea	12.87%	9.84%
Potato	22.93%	16.80%
Global accuracy	**69.06%**	
Kappa score	**0.60%**	

Table 4.6: Accuracy assessment of crop type classification with Random Forests using coherences from the shortest temporal baseline (6 days) of VH polarization.

The real evaluation of the effect of polarization consists in checking if the *combination* of both polarimetric components (VV and VH) yields an additional gain of accuracy and better results. To this end, coherence data of channels VV and VH are jointly used during the classification process. Moreover, all the temporal baselines are also considered in order to check if a maximum amount of information (three baselines and two polarimetric components) provides a further gain of accuracy.

Normalized confusion matrices obtained in each case are shown in Figure 4.11. Firstly, for the same temporal baseline of 6 days, including both polarimetric channels yields a better result for almost all crop types. This can be verified by looking at the main diagonal of confusion matrices of Figures 4.7 and 4.11(a). Whilst the accuracy of predominant classes remains high (for instance, it barely varies for cotton, tomato and sugar beet), other classes are better identified. For instance, the accuracy for classes carrot, onion and soft wheat increases respectively from 54%, 52% and 66% (when single polarization VV is used) to 57%, 63% and 72% when both channels are processed.

Secondly, it seems that adding the coherences of the other two temporal baselines (12 and 18 days) along with the additional polarization does not have a significant impact on the accuracy. In fact, the best final results are obtained when the shortest temporal baseline of 6 days is exploited individually. This can be verified by comparing the main diagonals of normalized confusion matrices of Figures 4.11(a), 4.11(b) and 4.11(c).

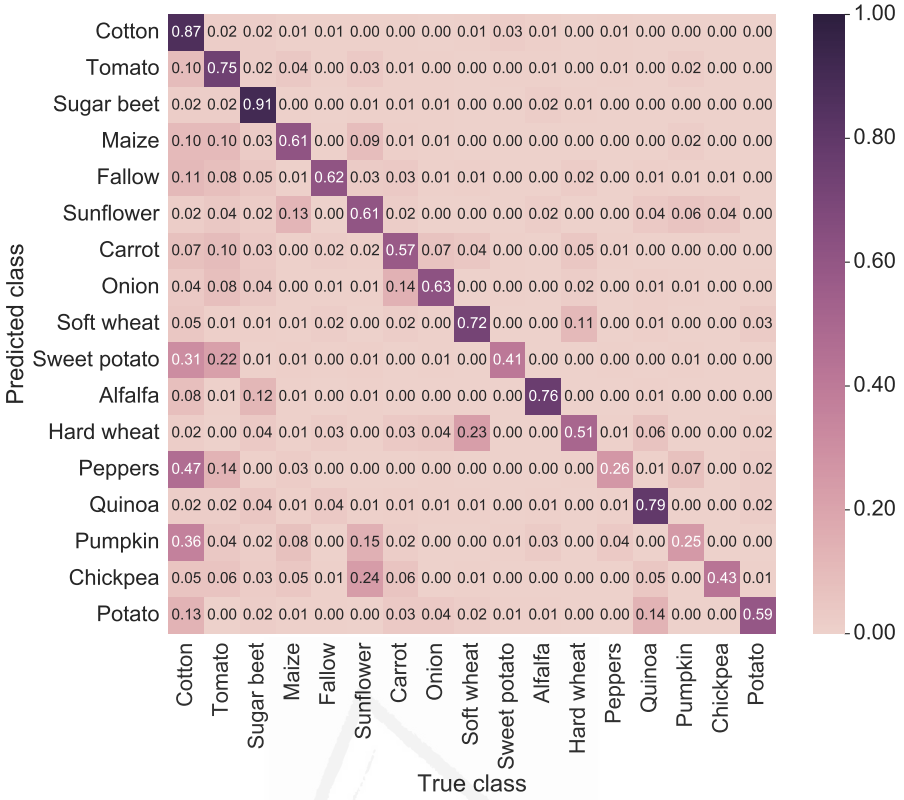

(a) 6 days of temporal baseline.

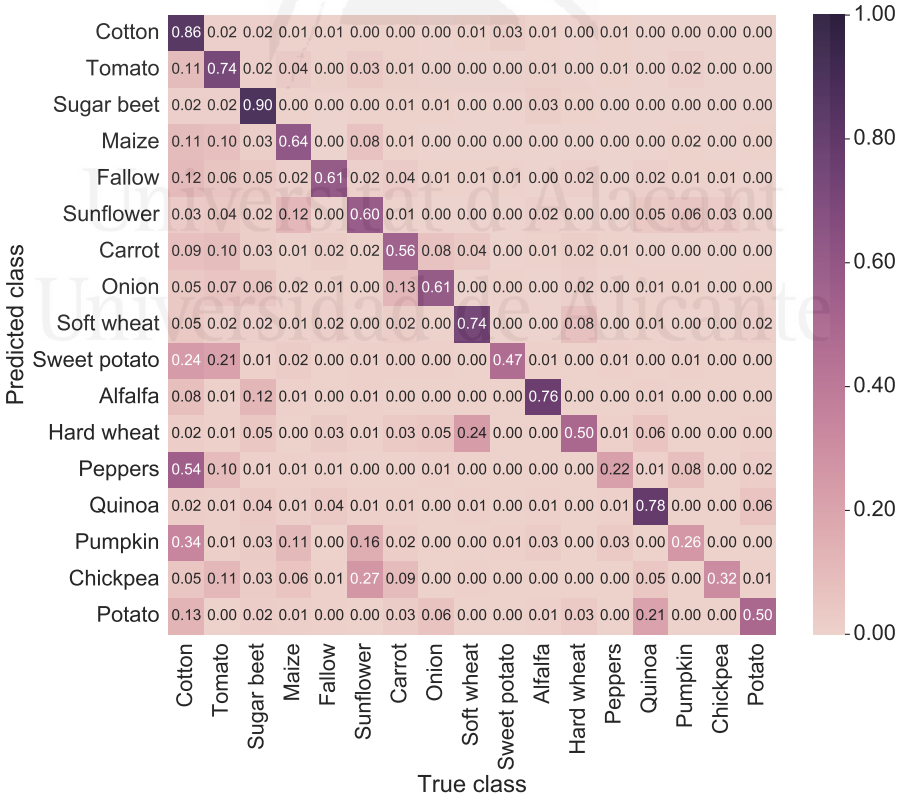

(b) 6 and 12 days of temporal baseline.

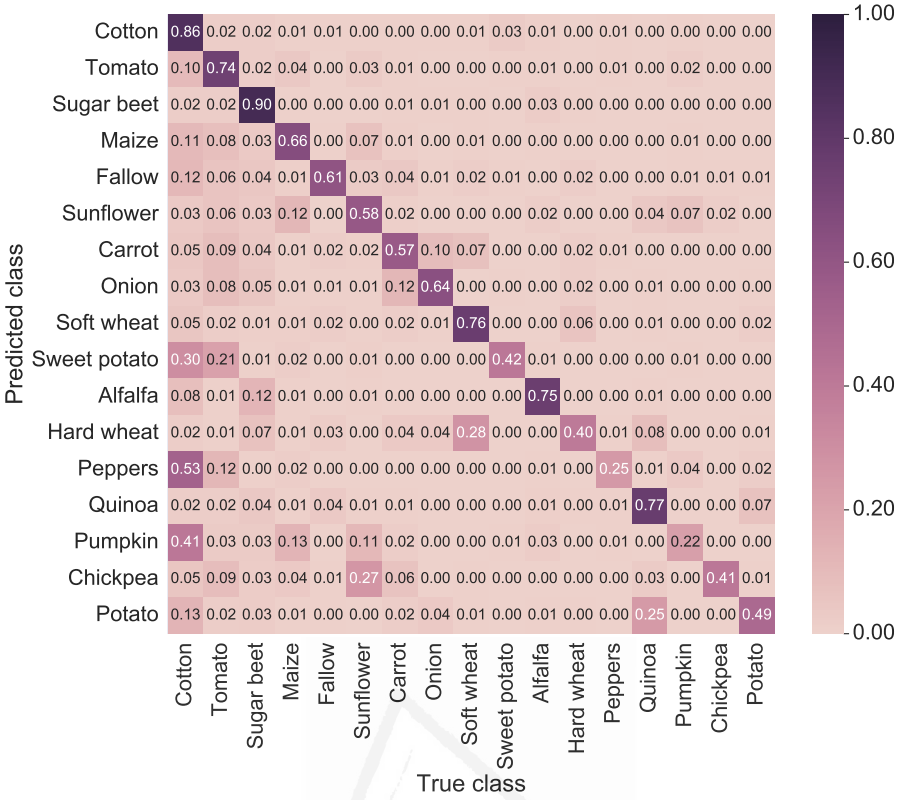

(c) 6, 12 and 18 days of temporal baseline.

Figure 4.11: Confusion matrices obtained with Random Forests employing coherences from different temporal baselines and dual polarization.

Finally, Table 4.7 summarizes class-level accuracies and overall accuracy parameters. Firstly, we can say that an increase in accuracy is obtained when dual-polarized data are jointly used. It can be observed that the best global accuracy obtained so far, which is 77.55% when using channel VV and the shortest temporal baseline, has improved to 79.19% when both polarizations are exploited and the same baseline is used. An improvement concerning the Kappa score is also obtained (from 0.70 to 0.73, as shown in Tables 4.2 and 4.7). Moreover, the producer's and user's accuracies of almost every individual class are increased, so that a better identification/classification of each crop type is attained.

Unfortunately, the inclusion of the coherences from the other two baselines does not provide an additional improvement. In fact, as shown in Table 4.7, the best classification result is obtained when only the data from the shortest baseline (6 days) are considered. The differences of accuracy are, however, very small (79.19%, 78.69% and 78.48% in terms of global accuracy, and 0.73, 0.72 and 0.71 in terms of Kappa score, and both the producer's and user's accuracies progressively decrease when more baselines are added to the classification process).

	Temporal baselines					
	6 days		6 and 12 days		6, 12 and 18 days	
Polarization	**VV + VH**		**VV + VH**		**VV + VH**	
Crop type	**Producer's accuracy**	**User's accuracy**	**Producer's accuracy**	**User's accuracy**	**Producer's accuracy**	**User's accuracy**
Cotton	88.14%	87.05%	87.56%	86.44%	87.77%	85.89%
Tomato	88.99%	74.54%	89.22%	73.73%	89.26%	74.46%
Sugar beet	86.96%	90.77%	86.73%	90.31%	85.74%	90.06%
Maize	58.24%	61.33%	57.54%	63.81%	58.27%	65.72%
Fallow	32.74%	61.56%	32.78%	61.24%	34.65%	61.40%
Sunflower	44.65%	60.82%	45.33%	59.89%	46.27%	58.49%
Carrot	53.55%	57.21%	55.85%	56.29%	57.37%	57.37%
Onion	57.97%	62.88%	57.35%	61.46%	56.81%	64.00%
Soft wheat	55.29%	72.52%	56.01%	73.63%	50.41%	76.24%
Sweet potato	29.56%	40.72%	30.81%	46.73%	27.61%	41.72%
Alfalfa	48.27%	76.19%	44.58%	75.87%	43.52%	75.40%
Hard wheat	53.73%	50.86%	57.73%	49.97%	56.28%	40.29%
Pepper	17.41%	25.54%	16.38%	21.91%	20.00%	25.13%
Quinoa	64.37%	78.91%	63.11%	77.76%	60.49%	76.67%
Pumpkin	18.28%	25.03%	15.87%	25.74%	14.42%	22.36%
Chickpea	39.29%	43.25%	38.44%	31.58%	50.28%	41.42%
Potato	54.50%	59.18%	43.44%	49.80%	42.66%	48.83%
Global accuracy	**79.19%**		**Global accuracy**	**78.69%**	**Global accuracy**	**78.48%**
Kappa score	**0.73**		**Kappa score**	**0.72**	**Kappa score**	**0.71**

Table 4.7: Accuracy assessment of crop type classification with Random Forests using coherences from different temporal baselines and dual polarization.

4.2.6 Analysis of the Temporal Evolution of the Coherence

In this section, we further analyze the results shown in previous Sections 4.2.5 and 4.2.5, so as to provide an explanation of why some classes are poorly identified. By looking at the normalized confusion matrix in Figure 4.11(a), it is seen that only 4 classes present an accuracy below 50%. These classes are sweet potato, pepper, pumpkin and chickpea. From the same confusion matrix, it is directly deduced that sweet potato is mostly confused with cotton since 31% of pixels have been wrongly identified as such (this is readily seen in the matrix by looking at the row of predictions and checking the associated column showing the true class label). Similarly, the confusion matrix shows that pepper and pumpkin are also confused with cotton (47% and 36% of misclassifications respectively) and chickpea is confused with sunflower (24% of misclassifications).

As detailed in Sections 4.2.1 and 4.2.3, ground truth data have been appropriately prepared in such a way that overfitting, underfitting and class imbalance are avoided. Accordingly, the reason for the inaccurate classification of these four crop types should be related to the coherence data themselves. Specifically, it may be due to a *similar temporal evolution* of the coherence for these classes. Figure 4.12 shows the temporal evolution of coherence values associated with every crop type throughout the whole year for each polarimetric channel. The locations of the fields of each crop type are extracted from the reference dataset. Then, coherence associated with each class is aggregated to produce a single mean and standard deviation for each date. By looking at Figure 4.12, it is observed that the evolution in time of each crop type is different. Also, note that channel VV always offers a larger

coherence than channel VH, which was expected as a result of the higher SNR of the copolar component as previously stated. However, both channels exhibit a similar trend in time.

The evolution of each class is directly related to the crop growing cycle. Accordingly, each crop has its specific growing and harvesting periods. These periods may be identified by means of the evolution of the coherence. In this regard, in the absence of crop (either because it has not been planted yet or because it has been harvested) higher coherence values are expected since parcels are bare fields, hence without volume and temporal decorrelation. Conversely, as the crop is growing, a decrease in coherence might happen since the crop is dynamically changing between successive observations. This is easily verified by looking at Figure 4.12(e), in which it can be seen that pixels belonging to class fallow have high and stable coherence values throughout the whole year. However, the rest of classes exhibit important variations during the year. Note that a significant coherence loss for all crop types is observed for the last image of November. This drop was caused by a rain event between the images.

Based on this reasoning, by looking at Figure 4.12(j) it seems that sweet potatoes start growing around May, since from this month coherence progressively decreases until it reaches minimum values during summer (July-September). Then, coherence increases till the end of the year. Now, looking at Figure 4.12(a), it is easily seen that pixels associated with class cotton have almost the same temporal evolution. Comparing Figures 4.12(m) and 4.12(o) with Figure 4.12(a), it is seen that both classes, pepper and pumpkin, exhibit also the same temporal variation as cotton. Moreover, the same is observed between classes chickpea and sunflower. In this case, coherence is relatively high during the first months of the year (January-March) and remains stable between 0.5 and 0.7. Then, it begins to decrease from April to July and from then on it increases again till December.

It can be therefore deduced that those crop types which present an important confusion (i.e., classes which are less reliably detected) exhibit a very similar temporal evolution during the year. This similar variation of coherence values is the most probable reason for getting an inaccurate identification of some crop types by means of the Random Forests classifier.

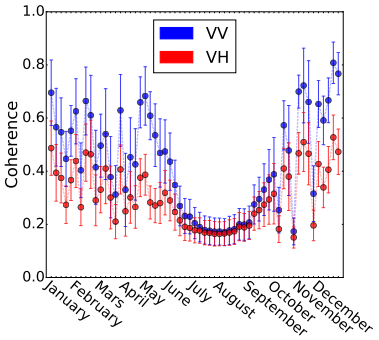

(a) Cotton.

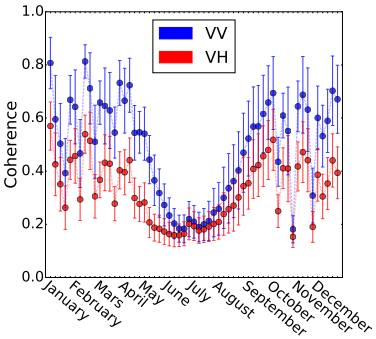

(b) Tomato.

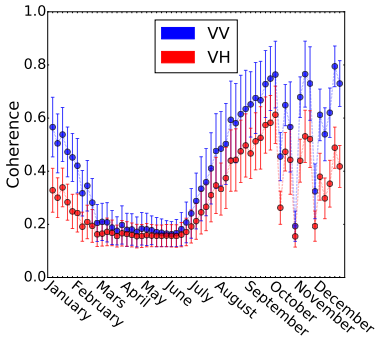

(c) Sugar beet.

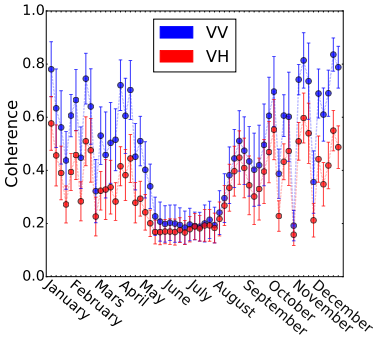

(d) Maize.

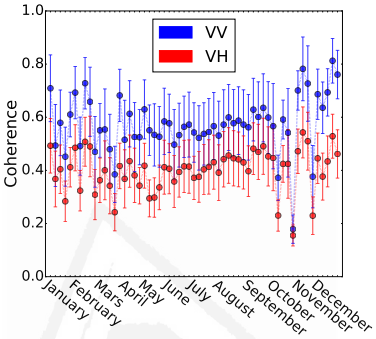

(e) Fallow.

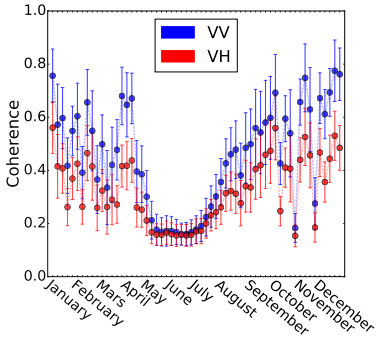

(f) Sunflower.

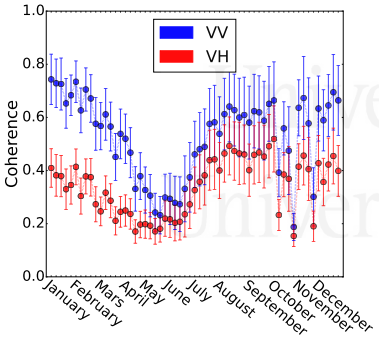

(g) Carrot.

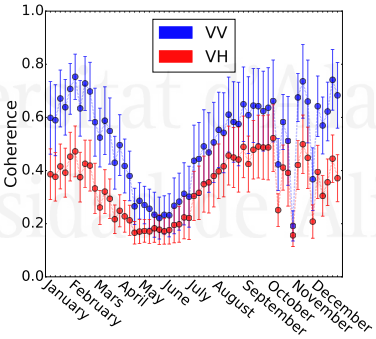

(h) Onion.

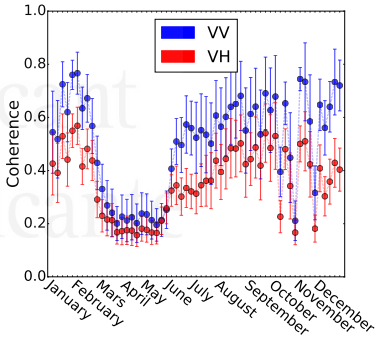

(i) Soft wheat.

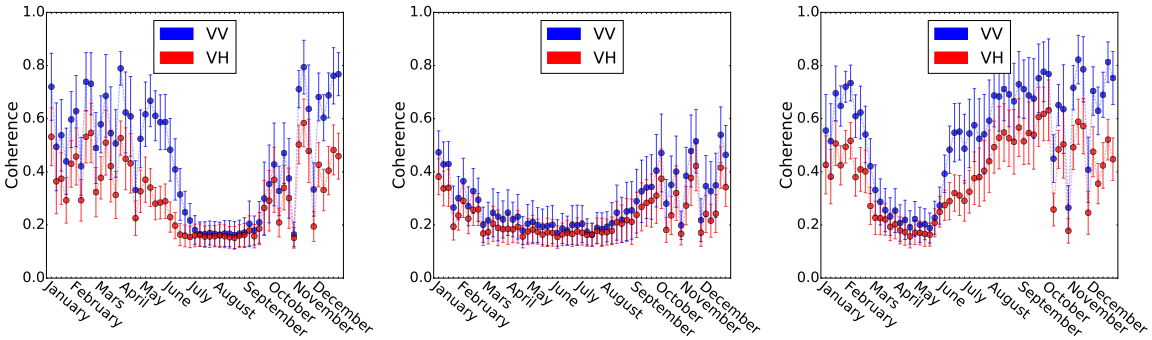

(j) Sweet potato. **(k)** Alfalfa. **(l)** Hard wheat.

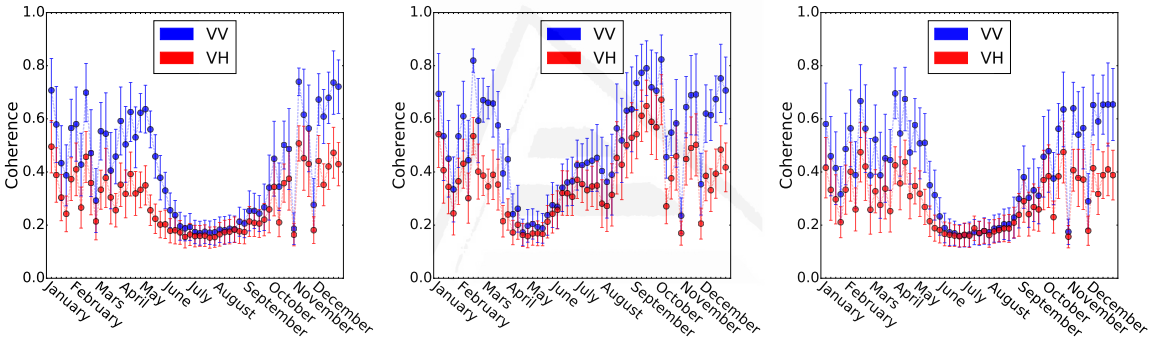

(m) Pepper. **(n)** Quinoa. **(o)** Pumpkin.

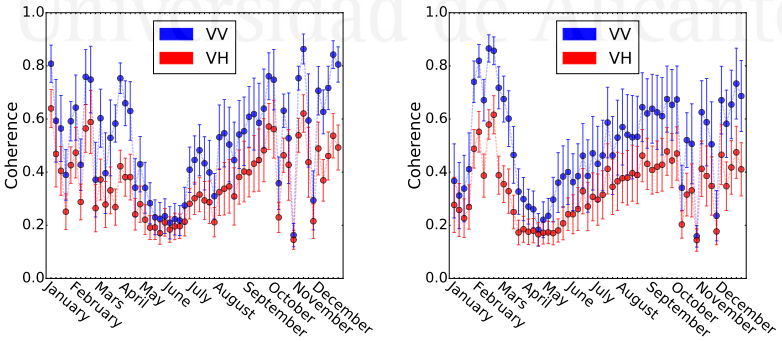

(p) Chickpea. **(q)** Potato.

Figure 4.12: Evolution in time of the coherence associated to each crop type of the dataset.

4.2.7 Summary

A summary of the most important points derived from the analysis performed in this chapter is presented in the following list.

- **Influence of the training set**. We have seen how poorly the classifier performs when an imbalanced training set is used as input, that is, when all classes are not equally represented. In this case, we have shown that the classifier is clearly biased towards predominant classes, whereas the minority classes are not correctly identified. A simple way to fix this issue consists in *undersampling* the dataset in such a way that each class is represented with exactly the same number of pixels. This leads to an unbiased classifier which is able to better distinguish every individual class. Consequently, class-level accuracies notably improve and an overall better result is obtained.

- **Temporal baseline**. From this study, it has been shown that there is not any improvement when multiple temporal baselines are jointly considered. In fact, results show that the best accuracy is obtained when just the shortest baseline (6 days) is used.

- **Polarization**. Significantly different results are obtained for the two available polarizations. It has been proved that the VV component offers better results than the ones of VH. However, the combination of both polarimetric channels performs better with an improvement of 1-2% of overall accuracy approximately with respect to the use of VV channel individually.

- **Confusion between classes and temporal variations of the coherence**. There are some classes that are not being correctly identified by the classifier. In this regard, we have seen that classes which exhibit similar temporal evolutions of coherence have a higher confusion.

5

Conclusions and Future Research Lines

This thesis dealt with different processing techniques and applications of SAR interferometry, which is based on processing and exploiting the phase difference between pairs of SAR images. In this last chapter, a revision of the main results is presented in the following paragraphs, so as to prove that the main objectives of the thesis have been properly accomplished. Moreover, some directions for future research are also proposed at the end of this chapter.

5.1 Main Conclusions

We have seen that the quality of the interferometric phase is the most crucial factor for deriving robust and precise products by means of interferometry. The major limitation of InSAR is the inevitable decorrelation which degrades the quality of phase data. Accordingly, central to this thesis was the development of innovative methods and algorithms to reduce such undesired and disturbing effects caused by multiple sources of noise. These new and improved methods were presented in Chapter 3.

Firstly, we have shown the difficulty in appropriately removing baseline decorrelation in areas strongly influenced by topography. Conventional and state-of-the-art methods may perform poorly in this kind of areas, either because the topography is not considered or because it is only partially exploited. The proposed range filter has shown how to overcome these limitations by fully utilizing an auxiliary DEM from which the local topography can be extracted. In this regard, results corresponding to the area of Mount Etna, shown in Section 3.1.3, prove that the proposed method is able

to extensively eliminate the geometrical decorrelation between both SAR images, regardless of the smoothness of the topography since the algorithm is automatically adapted to all types of surface variations. Consequently, as also shown in Section 3.1.3, the quality of the resulting interferogram is greatly enhanced: noise is better reduced in comparison with the rest of methods, which leads to an overall better phase quality and a higher correlation between the images. Moreover, the range filter has shown to be able to recover some useful interferometric fringes in some areas where the other methods are unable to achieve it.

Secondly, we have seen that almost every interferogram presents large areas where no phase measurements are possible because of remaining sources of decorrelation. Especially, the unavoidable temporal decorrelation is translated into random and noisy phases which provide no useful information and are not suitable for further processing. Filtering methods are then mandatory to remove noisy values from the original phase images. In this regard, an advanced phase filter for the final interferometric phase has been developed. The goal of the proposed method is to completely remove any remaining phase noise at all levels. To do so, a non-parametric, automatic, adaptive and iterative methodology has been followed. We have shown that the proposed filter goes one step further in terms of noise reduction and phase quality improvement. Accordingly, the goal of the filter is not only to suppress the noise, but also to ensure that the original phase structure is not modified (i.e., phase details are not blurred due to overfiltering effects). These two simultaneous objectives require a strong noise reduction along with an accurate fringe preservation (which can be understood as edge preservation in image domain). Properly carrying out both objectives is probably the most difficult task concerning interferogram filtering. As we have seen in Section 3.2, a stronger noise reduction entails the risk of loosing too much phase details and, contrarily, a better preservation of the original phase structure may lead to an insufficient noise reduction in low-coherent areas. The proposed method has shown to overcome the limitations of conventional phase filters based on the Goldstein method, since it provides a very strong noise reduction along with a good resolution preservation. A complete removal of phase noise is achieved by: 1) iteratively filtering the original noisy phase with windows of decreasing size, 2) local adaptivity to the noise level of each interferogram patch and, 3) spatial smoothing of the estimated noise by means of adaptive filtering kernels, either based on Chebyshev interpolators or conventional Gaussian/mean kernels.

All the results shown in this work prove that the proposed filter always offers the best performance, both with synthetic interferograms and real SAR data from different sensors. It has been shown that the proposed filter is able to intensively eliminate any remaining decorrelation and is able to yield a smooth and noise-free phase which is suitable for further processing. Moreover, strong phase gradients (interferometric fringes) are correctly preserved, so that the original resolution of the interferograms is appropriately retained and overfiltering effects are limited. Furthermore, we have seen that almost no phase residues are present in the filtered phase, that is, a reduction close to 100% is always achieved. This is of special interest for the phase unwrapping step, which may be impossible or very inaccurate with noisy input phases. In addition, the filtering process yields a massive increase in the

overall coherence of the processed areas.

It is important to note that the filter is completely non-parametric and does not require any manual tunning of its parameters. Only the size of the initial filtering window can be changed according to the original quality of the interferogram. In this regard, very noisy phases would benefit from a larger initial window size (for instance, 256×256 pixels as proposed) and more filtering iterations. High-quality interferograms would require less iterations. However, setting a large initial size for filtering high-quality input phases only has an important impact on the computation time and not on the final result, due to the accurate adaptivity of the filter to the local level of noise. In other words, even if a large initial size is set, the phase will not be overfiltered in the subsequent filtering iterations (in fact, it will almost remain untouched), which is an advantage of the proposed method. This led to the inclusion of a stopping criterion which evaluates the improvement after two consecutive filtering iterations. Specifically, if just a minor improvement is obtained between two iterations, the filter does not proceed since it is considered that the quality of the interferogram block is high enough, and the computation time is reduced. Evidently, this condition is adaptive and varies with the local level of noise, so that the noisiest areas are filtered at each iteration, whereas less noisy areas may be filtered only in the first iterations.

PolDInSAR analysis carried out in Section 3.3 shows that conventional polarimetric coherence optimization methods are limited with single-baseline data. In this regard, we have seen that phase improvements are mainly obtained by multilooking the original interferogram, but the optimization does not provide a significant additional gain even though coherence is globally increased. However, it is important to mention that the coherence improvement varies significantly depending on the multilook size. It has been shown that larger improvements are obtained when smaller multilook sizes are used. This is certainly because the positively biased estimator allows a mathematical maximization of the coherence. In these cases, the resulting number of high-coherent pixels is considerably larger than in conventional channels. However, we have shown that there is not a real improvement in terms of phase quality, since phase data remain very noisy and unsuitable for practical purposes. Conversely, larger multilook sizes provide a significant noise reduction, at the expenses of an important degradation of spatial resolution. In this regard, noise is effectively reduced, but the polarimetric optimization does not provide a significant improvement with respect to conventional channels. As a result, we might say that the polarimetric optimization is ineffective since the phase quality improvement is directly achieved by multilooking the original data.

A different processing approach was adopted to test if some phase improvement can eventually be obtained if the polarimetric optimization was performed without multilooking. To this end, the idea consisted in individually optimizing each pixel of the interferogram in such a way that the spatial average required for the coherence estimation was only performed during the optimization process. That is, coherence was locally computed and optimized by using the closest neighbor pixels, but the whole interferogram was never multilooked. By doing so, we are able to really evaluate if a phase quality improvement is obtained by means of the polarimetric optimization. This processing strategy

shows that a significant reduction of phase noise is globally achieved. In this regard, results show that correlated areas exhibit a much cleaner phase and that noise level remains high only in extremely decorrelated parts of the interferogram. Moreover, results also show that the spatial continuity of interferometric fringes is improved. This represents an important advantage of the method, since phase noise is effectively reduced and, simultaneously, the original resolution of the phase is never degraded. It is also worth mentioning that the process exhibits a similar improvement to the one obtained after directly applying a standard phase filter, which is very remarkable.

Finally, Chapter 4 presented a study showing the performance of interferometric SAR data for generating automatic thematic maps of crop types. Specifically, we have tested whether the multitemporal coherence constitutes a valuable feature for crop type classifications using Random Forests, one of the most popular supervised machine learning algorithms. The generic conclusion of the study is that coherence is indeed useful and provides overall highly accurate results. We have shown that global accuracies vary between 70% and 80%, depending on the input dataset provided to the classifier.

We have seen the importance of appropriately sampling the data given to the training model. It has been shown that class-level accuracies (i.e., the identification of every single class of the dataset) are very dissimilar if an imbalanced dataset is used. In this case, the model is biased towards predominant classes and the classifier is much more sensitive to detecting majority classes (the number of pixels of which is larger), whereas minority classes are poorly identified. The problem of class imbalance has been solved by resampling the input dataset. Specifically, majority classes are subsampled in such a way that every class of the training dataset presents exactly the same number of pixels. Results show that this strategy enables a much more balanced and accurate classification of every single class of the dataset.

Moreover, we have evaluated the influence of including different combinations of temporal baselines and polarizations in the classification process. On the one hand, it has been seen that including coherences coming from multiple baselines does not have a positive influence on the results. In fact, coherence data coming from the shortest temporal baseline (in this case, 6-day coherences) provides the best overall accuracy. When data from longer temporal baselines are added (12 and 18 days), the quality of the results is slightly worse. On the other hand, results show that each polarization (VV and VH) has a different sensitivity. In this regard, using the data of the VV component as input provides better results than using the ones of the VH counterpart. However, it has been shown that the information coming from both polarimetric components is somehow complementary, since jointly using the data of both polarizations as input to the classifier improves the quality of the classification. In fact, the best classification result shown in this work has been obtained when coherences of the shortest temporal baseline (6 days) and of both polarimetric channels are used.

Finally, it is important to mention that the classifier still has some difficulties in properly identifying some classes. A reason for this is the very similar evolution in time that the coherences measured at some crop types present during the year, resulting in an important confusion between such classes

and a poor discrimination of the classifier.

5.2 Future Research Lines

The last section of the PhD Thesis is devoted to providing some ideas for the continuity of this research. Firstly, some improvements and additional studies can be done to each processing technique presented in this work. Concerning the range filter, it would be interesting to test it with other data retrieved from other SAR sensors with different repeat-pass cycles and incidence angles, so as to better evaluate its performance and, eventually, verify if it presents any limitation which could be solved. It would be also interesting to develop a robust method for the automatic estimation of fringe frequencies (and hence, of the spectral shift between two images), in presence of any level of noise. Even though this is indeed a very challenging task, it would be beneficial for the range filtering step since no external information would be required. A pre-filtering of the original data followed by the frequency estimator could be studied as a possible strategy.

Concerning the final interferometric phase filter, it is planned to be improved by considering extreme noise levels and by including a minimum quality threshold (besides the already included maximum threshold) from which the filter should proceed. This is especially useful to avoid the estimation of wrong phase ramps and the appearance of associated artifacts in the filtered signal if some areas are fully uncorrelated. For instance, if an interferogram contains sea areas from which no useful phase can be recovered, it would be beneficial to directly mask out these areas without filtering them, hence avoiding wrong fringe frequencies' estimates and accelerating the filtering process. Moreover, variations of the original Goldstein filter formulation could be analyzed. Specifically, a new filter, which uses values of the filtering parameter α beyond 1, could be conceived to evaluate if a much stronger noise reduction can be obtained. The challenging task here consists in defining an adequate relation between the local level of noise in a given interferogram patch and the new values of α, in order to limit overfiltering effects. However, if appropriately designed, a few filtering iterations (or even a single iteration) would attain the same noise reduction as the method proposed in this work, which iterates several times.

Alternative ways to apply PolDInSAR optimization methods to the improvement of phase quality in single-baseline datasets could be studied. For instance, change detection techniques, based on polarimetry, could be employed to complement the interferometric coherence to evaluate the quality of the data in different areas. Furthermore, since the pixel-based polarimetric optimization at full resolution provided remarkable results, an important future research topic would be the extension of this processing technique to multitemporal datasets. Therefore, it would be interesting to apply this methodology to large stacks of interferograms in order to check if the quality of final products improves. For instance, the inclusion of this approach can be compared with conventional PSI and with different phase quality optimization methods involved in full-resolution PSI processing.

Finally, future analysis of crop type classifications must be carried out with the inclusion of addi-

tional features. The combination of radiometric (image intensities) and interferometric information should be the first choice of inputs to be evaluated. The inclusion of additional features, for instance, derived from polarimetric SAR processing (entropy, anisotropy, etc.) should also be tested to check whether a further gain of accuracy can be obtained when a classifier is provided with further information. Moreover, alternative classification approaches and, especially, deep learning algorithms (neural networks, convolutional neural networks, etc.) should be considered as a very powerful tool in this topic.

Appendix A
List of Publications

This appendix presents a list of all publications (both national and international) released during the research period of this PhD Thesis (2016-2019).

A.1 Papers in Peer-Reviewed International Journals

[1] **Mestre-Quereda, A.**, Lopez-Sanchez, J.M., Selva, J., and Gonzalez, P.J., "An improved phase filter for differential SAR interferometry based on an iterative method", *IEEE Transactions on Geoscience and Remote Sensing*, vol. 56, pp. 4471-4491, August 2018.

[2] **Mestre-Quereda, A.**, Lopez-Sanchez, J.M., Ballester-Berman, J.D., Gonzalez, P.J., Hooper, A., and Wright, T.J., "Evaluation of the multilook size in polarimatric optimization of differential SAR interferograms", *IEEE Geoscience and Remote Sensing Letters*, vol. 15, pp. 1407-1411, September 2018.

[3] Jacob, A., Vicente-Guijalba, F., Lopez-Martinez, C., Litzinger, M., Kristen, H., **Mestre-Quereda, A.**, Lopez-Sanchez, J.M., Ziolkowski, D., Lavalle, M., Notarnicola, C., Suresh, G., Antropov, O., Ge, S., Praks, J., Ban Yifang, Pottier, E., Mallorqui, J.J., Duro, J., and Engdahl, M., "Investigating Sentinel-1 InSAR coherence for land-cover mapping: a comparison of multiple feature-based classifiers", *IEEE Journal of Selected Topics in Applied Earth Observations and Remote Sensing*. Submitted in July 2019.

A.2 Papers in National and International Conferences

[1] **Mestre-Quereda, A.**, Lopez-Sanchez, J.M., Vicente-Guijalba, F., Selva, J., Gonzalez, P.J., Wright, J., and Hooper, A. "Approaches for polarimetric optimisation of single-pair differential SAR interferograms", in *Proceedings of the 8th International Workshop on Science and Applications of SAR Polarimetry and Interferometry, POLInSAR'2017*, Frascati, Italy, January 2017.

[2] **Mestre-Quereda, A.**, Lopez-Sanchez, J.M., Selva, J., Gonzalez, and P.J., "Strategies to improve the Goldstein filter for SAR interferometric phase", in *FRINGE'17: Advances in the Science and Applications of SAR Interferometry and Sentinel-1 InSAR*, Helsinki, Finland, June 2017.

[3] Lopez-Sanchez, J.M., Vicente-Guijalba, F., **Mestre-Quereda, A.**, Romero-Puig, N., and Erten, E. "Influence of incidence angle and baseline on the retrieval of biophysical parameters of rice fields by means of polarimetric SAR interferometry with TanDEM-X data", in *Proceedings of the 37th IEEE International Geoscience and Remote Sensing Symposyum (IGARSS'2017)* , pp. 926-929, Fort Worth (Texas), USA, July 2017.

[4] **Mestre-Quereda, A.**, Lopez-Sanchez, J.M., Ballester-Berman, J.D., Selva, J., Gonzalez, P.J., Hooper, A., and Wright, T.J., "Polarimetric optimisation methods applied to single differential SAR interferograms for geophysical events", in *Proceedings of the XVII Spanish Association of Remote Sensing Conference*, pp. 439-442, Murcia, 3-7, October 2017.

[5] **Mestre-Quereda, A.**, Lopez-Sanchez, J.M., Selva, J., and Gonzalez, P.J., "Iterative filtering based on adaptive Chebyshev kernel functions for noise suppression in Differential SAR Interferograms", in *IEEE International Geoscience and Remote Sensing Symposyum (IGARSS'2018)*, pp.1380-1383, Valencia, Spain, July 2018.

[6] Vicente-Guijalba, F., Jacob, A., Lopez-Sanchez, J.M., **Mestre-Quereda, A.**, Lopez-Martinez, C., Duro, J., Notarnicola, C., Ziolkowski, D., Pottier, E., Mallorqui, J.J., Lavalle, and M., Engdahl, "SInCohMap: land-cover and vegetation mapping using multi-temporal Sentinel-1 interferometric coherence",in *IEEE International Geoscience and Remote Sensing Symposyum (IGARSS'2018)*, pp.6635-6638, Valencia, Spain, July 2018.

[7] Vicente-Guijalba, F., Jacob, A., Lopez-Sanchez, J.M., **Mestre-Quereda, A.**, Lopez-Martinez, C., Duro, J., Notarnicola, C., Ziolkowski, D., Pottier, E., Mallorqui, J.J., Lavalle, M., and Engdahl, M., "Land-cover classification results and lessons learnt from the round robin consultation within the ESA SEOM SInCohMap project", in *ESA Φ-Week, Earth Observation Open Science*, Frascati, Italy, November 2018.

[8] Vicente-Guijalba, F., Jacob, A., Lopez-Sanchez, J.M., **Mestre-Quereda, A.**, Lopez-Martinez, C., Duro, J., Notarnicola, C., Ziolkowski, D., Dabrowska, K., Zbigniew, B., Antropov, O., Suresh, G., D., Pottier, E., Mallorqui, J.J., Lavalle, M., and Engdahl, M., "Land-cover classification using multi-temporal interferometric Sentinel-1 data: results from the SInCohMap project", in *ESA Living Planet Symposium*, Milan, Italy, May 2019.

Bibliography

[1] E. Zell, A. K. Huff, A. T. Carpenter, and L. A. Friedl, "A User-Driven Approach to Determining Critical Earth Observation Priorities for Societal Benefit," *IEEE Journal of Selected Topics in Applied Earth Observations and Remote Sensing*, vol. 5, no. 6, pp. 1594–1602, 2012.

[2] A. Moreira, P. Prats-iraola, M. Younis, G. Krieger, I. Hajnsek, and K. P. Papathanassiou, "A Tutorial on Synthetic Aperture Radar," *IEEE Geoscience and Remote Sensing Magazine*, March 2013.

[3] A. Moreira, "A golden age for spaceborne SAR systems," in *2014 20th International Conference on Microwaves, Radar and Wireless Communications (MIKON)*, (Gdansk, Poland), pp. 1–4, June 2014.

[4] A. S. Belward and J. O. Skøien, "Who launched what, when and why; trends in global land-cover observation capacity from civilian earth observation satellites," *ISPRS Journal of Photogrammetry and Remote Sensing*, vol. 103, pp. 115–128, 2015.

[5] L. C. Graham, "Synthetic interferometer radar for topographic mapping," *Proceedings of the IEEE*, vol. 62, no. 6, pp. 763–768, 1974.

[6] H. A. Zebker and R. M. Goldstein, "Topographic mapping from interferometric synthetic aperture radar observations," *Journal of Geophysical Research: Solid Earth*, vol. 91, no. B5, pp. 4993–4999, 1986.

[7] R. M. Goldstein, H. A, and C. L. Werner, "Satellite radar interferometry: two-dimensional phase unwrapping," *Radio Science*, vol. 23, no. 4, pp. 713–720, 1988.

[8] A. K. Gabriel and R. M. Goldstein, "Crossed orbit interferometry: theory and experimental results from SIR-B," *International Journal of Remote Sensing*, vol. 9, no. 5, pp. 857–872, 1988.

[9] A. K. Gabriel, R. M. Goldstein, and H. A. Zebker, "Mapping small elevation changes over large areas: Differential radar interferometry," *Journal of Geophysical Research: Solid Earth*, vol. 94, no. B7, pp. 9183–9191, 1989.

[10] T. G. Farr, P. A. Rosen, E. Caro, R. Crippen, R. Duren, S. Hensley, M. Kobrick, M. Paller, E. Rodriguez, L. Roth, D. Seal, S. Shaffer, J. Shimada, J. Umland, M. Werner, M. Oskin, D. Burbank, and D. Alsdorf, "The Shuttle Radar Topography Mission," *Reviews of Geophysics*, vol. 45, no. 2, 2007.

[11] C. Rossi, M. Eineder, T. Fritz, and H. Breit, "TanDEM-X Mission: Raw DEM Generation," in *8th European Conference on Synthetic Aperture Radar*, pp. 1–4, 2010.

[12] D. Massonnet, M. Rossi, C. Carmona-Moreno, F. Adragna, G. Peltzer, K. Feigl, and T. Rabaute, "The displacement field of the Landers earthquake mapped by Radar interferometry," *Nature*, vol. 364, pp. 138–142, 1993.

[13] R. Bürgmann, P. A. Rosen, and E. J. Fielding, "Synthetic Aperture Radar Interferometry to Measure Earth's Surface Topography and Its Deformation," *Annual Review of Earth and Planetary Sciences*, vol. 28, no. 1, pp. 169–209, 2000.

[14] P. Berardino, G. Fornaro, R. Lanari, and E. Sansosti, "A new algorithm for surface deformation monitoring based on small baseline differential SAR interferograms," *IEEE Transactions on Geoscience and Remote Sensing*, vol. 40, pp. 2375–2383, November 2002.

[15] A. Ferretti, C. Prati, and F. Rocca, "Nonlinear subsidence rate estimation using permanent scatterers in differential SAR interferometry," *IEEE Transactions on Geoscience and Remote Sensing*, vol. 38, no. 5, pp. 2202–2212, 2000.

[16] A. Ferretti, C. Prati, and F. Rocca, "Permanent scatterers in SAR interferometry," *IEEE Transactions on Geoscience and Remote Sensing*, vol. 39, no. 1, pp. 8–20, 2001.

[17] A. Hooper, H. Zebker, P. Segall, and B. Kampes, "A new method for measuring deformation on volcanoes and other natural terrains using InSAR persistent scatterers," *Geophysical Research Letters*, vol. 31, no. 23, 2004.

[18] M. Crosetto, O. Monserrat, R. Iglesias, and B. Crippa, "Persistent Scatterer Interferometry: Potential, Limits and Initial C- and X-band Comparison," *Photogrammetric Engineering and Remote Sensing*, vol. 76, pp. 1061–1069, 2010.

[19] R. Iglesias, J. Mallorqui, D. Monells, C. López-Martínez, X. Fabregas, A. Aguasca, J. Gili, and J. Corominas, "PSI Deformation Map Retrieval by Means of Temporal Sublook Coherence on Reduced Sets of SAR Images," *Remote Sensing*, vol. 7, pp. 530–563, 2015.

[20] G. Sinclair, "The transmission and reception of elliptically polarized waves," *Proceedings of the IRE*, vol. 38, pp. 148–151, Feb 1950.

[21] G. Deschamps, "Geometrical representation of the polarization of a plane electromagnetic wave," *Proceedings of the IRE*, vol. 39, pp. 540–544, May 1951.

[22] E. Kennaugh, *Polarization Properties of Radar Reflections*. Ohio State University, 1952.

[23] E. Kennaugh, "Effects of the type of polarization on echo characteristics," *Ohio State University, Research Fundation*, 1953.

[24] G. Deschamps, "Radar polarization power scattering matrix," *Proceedings of the IRE*, vol. 44, pp. 1290–1296, Feb 1956.

[25] J. Huynen, *Phenomenological Theory of Radar Targets*. PhD Thesis, University of Delft, The Netherlands, 1957.

[26] W. . Boerner, M. El-Arini, C.-Y. Chan, and P. Mastoris, "Polarization dependence in electromagnetic inverse problems," *IEEE Transactions on Antennas and Propagation*, vol. 29, pp. 262–271, March 1981.

[27] S. R. Cloude and K. P. Papathanassiou, "Polarimetric SAR interferometry," *IEEE Transactions on Geoscience and Remote Sensing*, vol. 39, no. 11, pp. 2352–2363, 2001.

[28] S. R. Cloude and K. P. Papathanassiou, "Single-baseline polarimetric SAR interferometry," *IEEE Transactions on Geoscience and Remote Sensing*, vol. 39, no. 11, pp. 2352–2363, 2001.

[29] L. Pipia, X. Fabregas, A. Aguasca, C. Lopez-Martinez, S. Duque, J. J. Mallorqui, and J. Marturia, "Polarimetric Differential SAR Interferometry: First Results With Ground-Based Measurements," *IEEE Geoscience and Remote Sensing Letters*, vol. 6, pp. 167–171, January 2009.

[30] V. D. Navarro-Sanchez, J. M. Lopez-Sanchez, and F. Vicente-Guijalba, "A contribution of polarimetry to satellite differential SAR interferometry: Increasing the number of pixel candidates," *IEEE Geoscience and Remote Sensing Letters*, vol. 7, no. 2, pp. 276–280, 2010.

[31] V. D. Navarro-Sanchez, J. M. Lopez-Sanchez, and L. Ferro-Famil, "Polarimetric approaches for persistent scatterers interferometry," *IEEE Transactions on Geoscience and Remote Sensing*, vol. 52, no. 3, pp. 1667–1676, 2014.

[32] V. D. Navarro-Sanchez and J. M. Lopez-Sanchez, "Spatial adaptive speckle filtering driven by temporal polarimetric statistics and its application to PSI," *IEEE Transactions on Geoscience and Remote Sensing*, vol. 52, no. 8, pp. 4548–4557, 2014.

[33] R. Iglesias, D. Monells, X. Fabregas, J. J. Mallorqui, A. Aguasca, and C. Lopez-Martinez, "Phase quality optimization in Polarimetric differential SAR Interferometry," *IEEE Transactions on Geoscience and Remote Sensing*, vol. 52, no. 5, pp. 2875–2888, 2014.

[34] M. J. Canty, *Image Analysis, Classification and Change Detection in Remote Sensing: With Algorithms in ENVI/IDL*. CRC Press, 2009.

[35] European Environment Agency, "CORINE Land Cover - Contents," *CORINE Land Cover*, pp. 1–163, 1994.

[36] M. R. Curlander, J.C., *Synthetic Aperture Radar: Systems and Signal Processing*. November 1991.

[37] R. Bamler, "A comparison of range-doppler and wavenumber domain sar focusing algorithms," *IEEE Transactions on Geoscience and Remote Sensing*, vol. 30, pp. 706–713, July 1992.

[38] R. Bamler and B. Schättler, *SAR Data Acquisition and Image Formation*, pp. 53–102. Wichmann-Verlag, 01 1993.

[39] R. Bamler and P. Hartl, "Synthetic aperture radar interferometry.," *Inverse Problems*, vol. 14, January 1998.

[40] L. Tsang, J. Au Kong, and R. T. Shin, "Theory of microwave remote sensing," *Wiley*, February 1985.

[41] M. Skolnik, "Radar handbook," *McGraw-Hill*, 1990.

[42] R. Hanssen, *Radar interferometry: Data interpretation and error analysis*. Kluwer Academic, 2001.

[43] J-S. Lee, K. Hoppel, S. Mango, and A. Miller, "Intensity and phase statistics of multilook polarimetric and interferometric SAR imagery," *IEEE Transactions on Geoscience and Remote Sensing*, vol. 32, no. 5, pp. 1017–1028, 1994.

[44] J-S. Lee, M. Grunes, and G. de Grandi, "Polarimetric SAR speckle filtering and its implication for classification," *IEEE Transactions on Geoscience and Remote Sensing*, vol. 37, no. 5, pp. 2363–2373, 1999.

[45] G. Vasile, E. Trouvé, and V. Buzuloiu, "Intensity-driven adaptive-neighborhood technique for polarimetric and interferometric SAR parameters estimation," *IEEE Transactions on Geoscience and Remote Sensing*, vol. 44, no. 6, pp. 1609–1620, 2006.

[46] C. A. Deledalle, L. Denis, F. Tupin, A. Reigber, and M. Jager, "NL-SAR: A unified nonlocal framework for resolution-preserving (Pol)(In)SAR denoising," *IEEE Transactions on Geoscience and Remote Sensing*, vol. 53, no. 4, pp. 2021–2038, 2015.

[47] A. Alonso-González, *Multidimensional and temporal SAR data representation and processing based on binary partition trees*. PhD Thesis, Polytechnic University of Catalonia, Spain, 2014.

[48] E. Sansosti, P. Berardino, M. Manunta, F. Serafino, and G. Fornaro, "Geometrical SAR image registration RID F-7297-2011," *IEEE Transactions On Geoscience and Remote Sensing*, vol. 44, no. 10, pp. 2861–2870, 2006.

[49] F. Serafino, "SAR image coregistration based on isolated point scatterers," *IEEE Geoscience and Remote Sensing Letters*, vol. 3, no. 3, pp. 354–358, 2006.

[50] D. C. Ghiglia and M. D. Pritt, *Two-dimensional phase unwrapping : theory, algorithms, and software*. Wiley, 1998.

[51] C. W. Chen and H. A. Zebker, "Two-dimensional phase unwrapping with use of statistical models for cost functions in nonlinear optimization," *Journal of the Optical Society of America A*, vol. 18, pp. 338–351, February 2001.

[52] R. Tomás, R. Romero, J. Mulas, J. J. Marturià, J. J. Mallorquí, J. M. Lopez-Sanchez, G. Herrera, F. Gutiérrez, P. J. González, J. Fernández, S. Duque, A. Concha-Dimas, G. Cocksley, C. Castañeda, D. Carrasco, and P. Blanco, "Radar interferometry techniques for the study of ground subsidence phenomena: a review of practical issues through cases in Spain," *Environmental Earth Sciences*, vol. 71, pp. 163–181, January 2014.

[53] M. Béjar-Pizarro, P. Ezquerro, G. Herrera, R. Tomás, C. Guardiola-Albert, J. M. Ruiz Hernández, J. A. Fernández Merodo, M. Marchamalo, and R. Martínez, "Mapping groundwater level and aquifer storage variations from InSAR measurements in the Madrid aquifer, Central Spain," *Journal of Hydrology*, vol. 547, pp. 678–689, April 2017.

[54] R. Bonì, C. Meisina, F. Cigna, G. Herrera, D. Notti, S. Bricker, H. McCormack, R. Tomás, M. Béjar-Pizarro, J. Mulas, P. Ezquerro, R. Bonì, C. Meisina, F. Cigna, G. Herrera, D. Notti, S. Bricker, H. McCormack, R. Tomás, M. Béjar-Pizarro, J. Mulas, and P. Ezquerro, "Exploitation of Satellite A-DInSAR Time Series for Detection, Characterization and Modelling of Land Subsidence," *Geosciences*, vol. 7, p. 25, April 2017.

[55] R. Touzi, A. Lopes, J. Bruniquel, and P. Vachon, "Coherence estimation for SAR imagery," *IEEE Transactions on Geoscience and Remote Sensing*, vol. 37, no. 1, pp. 135–149, 1999.

[56] H. Zebker and J. Villasenor, "Decorrelation in interferometric radar echoes," *IEEE Transactions on Geoscience and Remote Sensing*, vol. 30, no. 5, pp. 950–959, 1992.

[57] C. A. Balanis, *Advanced engineering electromagnetics*. John Wiley & Sons, 2012.

[58] S. R. Cloude, "Polarization Application in Remote Sensing," *Oxford University Press*, 2010.

[59] K. P. Murphy, *Machine Learning: A Probabilistic Perspective*. The MIT Press, 2012.

[60] L. Breiman, J. H. Friedman, R. A. Olshen, and C. J. Stone, *Classification and Regression Trees*. Statistics/Probability Series, Belmont, California, U.S.A.: Wadsworth Publishing Company, 1984.

[61] M. Friedl and C. Brodley, "Decision tree classification of land cover from remotely sensed data," *Remote Sensing of Environment*, vol. 61, no. 3, pp. 399 – 409, 1997.

[62] L. Breiman and Leo, "Random Forests," *Machine Learning*, vol. 45, no. 1, pp. 5–32, 2001.

[63] S. van der Walt, J. L. Schönberger, J. Nunez-Iglesias, F. Boulogne, J. D. Warner, N. Yager, E. Gouillart, T. Yu, and the scikit-image contributors, "Scikit-image: image processing in Python," *PeerJ*, vol. 2, p. e453, 6 2014.

[64] R. M. Goldstein and C. L. Werner, "Radar interferogram filtering for geophysical applications," *Geophysical Research Letters*, vol. 25, pp. 4035–4038, November 1998.

[65] J. McClellan, "Artifacts in alpha-rooting of images," in *ICASSP '80. IEEE International Conference on Acoustics, Speech, and Signal Processing*, vol. 5, pp. 449–452, Institute of Electrical and Electronics Engineers.

[66] S. Baran, P. Kampes, and Lilly, "A modification to the Goldstein radar interferogram filter," *IEEE Transactions on Geoscience and Remote Sensing*, vol. 41, no. 9, pp. 2114–2118, 2003.

[67] C. Prati and F. Rocca, "Improving slant-range resolution with multiple SAR surveys," *IEEE Transactions on Aerospace and Electronic Systems*, vol. 29, no. 1, pp. 135–143, 1993.

[68] F. Gatelli, A. Monti-Guarnieri, F. Parizzi, P. Pasquali, C. Prati, and F. Rocca, "The Wavenumber Shift in SAR Interferometry," *IEEE Transactions on Geoscience and Remote Sensing*, vol. 32, no. 4, pp. 855–865, 1994.

[69] S. Guillaso, A. Reigber, L. Ferro-Famil, and E. Pottier, "Range Resolution Improvement of Airborne SAR Images," *IEEE Geoscience and Remote Sensing Letters*, vol. 3, pp. 135–139, January 2006.

[70] B. Smith, "Generalization of spatially variant apodization to noninteger Nyquist sampling rates," *IEEE Transactions on Image Processing*, vol. 9, pp. 1088–1093, January 2000.

[71] C. Castillo-Rubio, S. Llorente-Romano, and M. Burgos-Garcia, "Robust SVA method for every sampling rate condition," *IEEE Transactions on Aerospace and Electronic Systems*, vol. 43, pp. 571–580, April 2007.

[72] R. Iglesias and J. J. Mallorqui, "Side-Lobe Cancelation in DInSAR Pixel Selection With SVA," *IEEE Geoscience and Remote Sensing Letters*, vol. 10, pp. 667–671, July 2013.

[73] German Aerospace Center, "TerraSAR-X basic product specification document," October 2013.

[74] Canadian Space Agency, "RADARSAT-2 product description," September 2018.

[75] B. M. Kampes, "Delft object-oriented radar interferometric software: Users manual and technical documentation," *Delft University of Technology, Delft*, 1999.

[76] B. M. Kampes, R. Hanssen, and Z. Perski, "Radar interferometry with public domain tools," in *Proceedings of FRINGE'03: Advances in SAR interferometry from ERS and ENVISAT missions*, (Frascati, Italy), September 2003.

[77] G. Davidson and R. Bamler, "Multiresolution phase unwrapping for SAR interferometry," *IEEE Transactions on Geoscience and Remote Sensing*, vol. 37, no. 1, pp. 163–174, 1999.

[78] T. Wang, M. Liao, and D. Perissin, "InSAR coherence-decomposition analysis," *IEEE Geoscience and Remote Sensing Letters*, vol. 7, no. 1, pp. 156–160, 2010.

[79] Z. Suo, J. Zhang, M. Li, Q. Zhang, and C. Fang, "Improved InSAR Phase Noise Filter in Frequency Domain," *IEEE Transactions on Geoscience and Remote Sensing*, vol. 54, no. 2, pp. 1185–1195, 2016.

[80] P. J. Gonzalez, "RSF: A robust non-parametric phase filtering method for automatic processing of Sentinel-1 interferograms," in *Proceedings of FRINGE'15: Advances in the Science and Applications of SAR Interferometry and Sentinel-1 InSAR Workshop*, (Frascati, Italy), March 2015.

[81] J. C. Mason and D. C. Handscomb, *Chebyshev Polynomials*. CRC Press LLC, 2003.

[82] H. Zebker and K. Chen, "Accurate Estimation of Correlation in InSAR Observations," *IEEE Geoscience and Remote Sensing Letters*, vol. 2, pp. 124–127, April 2005.

[83] U. Spagnolini, "2-D phase unwrapping and instantaneous frequency estimation," *IEEE Transactions on Geoscience and Remote Sensing*, vol. 33, pp. 579–589, May 1995.

[84] E. Trouvé, M. Caramma, and H. Maître, "Fringe detection in noisy complex interferograms.," *Applied optics*, vol. 35, no. 20, pp. 3799–3806, 1996.

[85] Z. Suo, Z. Li, and Z. Bao, "A new strategy to estimate local fringe frequencies for InSAR phase noise reduction," *IEEE Geoscience and Remote Sensing Letters*, vol. 7, no. 4, pp. 771–775, 2010.

[86] A. G. Fore, B. D. Chapman, B. P. Hawkins, S. Hensley, C. E. Jones, T. R. Michel, and R. J. Muellerschoen, "UAVSAR Polarimetric Calibration," *IEEE Transactions on Geoscience and Remote Sensing*, vol. 53, pp. 3481–3491, June 2015.

[87] C. A. Neal, S. R. Brantley, L. Antolik, J. L. Babb, M. Burgess, K. Calles, M. Cappos, J. C. Chang, S. Conway, L. Desmither, P. Dotray, T. Elias, P. Fukunaga, S. Fuke, I. A. Johanson, K. Kamibayashi, J. Kauahikaua, R. L. Lee, S. Pekalib, A. Miklius, W. Million, C. J. Moniz, P. A. Nadeau, P. Okubo, C. Parcheta, M. R. Patrick, B. Shiro, D. A. Swanson, W. Tollett, F. Trusdell, E. F. Younger, M. H. Zoeller, E. K. Montgomery-Brown, K. R. Anderson, M. P. Poland, J. L. Ball, J. Bard, M. Coombs, H. R. Dietterich, C. Kern, W. A. Thelen, P. F. Cervelli, T. Orr, B. F. Houghton, C. Gansecki, R. Hazlett, P. Lundgren, A. K. Diefenbach, A. H. Lerner, G. Waite,

P. Kelly, L. Clor, C. Werner, K. Mulliken, G. Fisher, and D. Damby, "The 2018 Rift eruption and summit collapse of Kilauea volcano," *Science*, vol. 363, no. 6425, pp. 367–374, 2019.

[88] D. C. Ghiglia and L. A. Romero, "Robust two-dimensional weighted and unweighted phase unwrapping that uses fast transforms and iterative methods," *Journal of the Optical Society of America A*, vol. 11, no. 1, p. 107, 1994.

[89] M. Neumann, L. Ferro-Famil, and A. Reigber, "Multibaseline Polarimetric SAR Interferometry Coherence Optimization," *IEEE Geoscience and Remote Sensing Letters*, vol. 5, pp. 93–97, January 2008.

[90] R. Iglesias, D. Monells, C. Lopez-Martinez, J. J. Mallorqui, X. Fabregas, and A. Aguasca, "Polarimetric Optimization of Temporal Sublook Coherence for DInSAR Applications," *IEEE Geoscience and Remote Sensing Letters*, vol. 12, pp. 87–91, January 2015.

[91] Z. Sadeghi, M. J. Valadan Zoej, and J.-P. Muller, "Monitoring Land Subsidence in a Rural Area Using a Combination of ADInSAR and Polarimetric Coherence Optimization," *IEEE Journal of Selected Topics in Applied Earth Observations and Remote Sensing*, vol. 10, pp. 3582–3590, August 2017.

[92] Z. Sadeghi, M. J. Valadan Zoej, A. Hooper, and J. M. Lopez-Sanchez, "A New Polarimetric Persistent Scatterer Interferometry Method Using Temporal Coherence Optimization," *IEEE Transactions on Geoscience and Remote Sensing*, vol. 56, pp. 6547–6555, November 2018.

[93] L. Sagues, J. Lopez-Sanchez, J. Fortuny, X. Fabregas, A. Broquetas, and A. Sieber, "Indoor experiments on polarimetric SAR interferometry," *IEEE Transactions on Geoscience and Remote Sensing*, vol. 38, pp. 671–684, March 2000.

[94] J.-S. Lee and E. Pottier, *Polarimetric Radar Imaging : From basics to applications.* CRC Press, February 2009.

[95] M. R Hestenes and E. Stiefel, "Methods of conjugate gradients for solving linear systems," *Journal cf Research of the National Bureau of Standards Vol*, vol. 49, December 1952.

[96] W. H. Press, B. P. Flannery, S. A. Teukolsky, and W. T. Vetterling, *Numerical Recipes in C: The Art of Scientific Computing.* New York, NY, USA: Cambridge University Press, 1988.

[97] B. Wu, L. Tong, Y. Chen, and L. He, "New Methods in Multibaseline Polarimetric SAR Interferometry Coherence Optimization," *IEEE Geoscience and Remote Sensing Letters*, vol. 12, no. 10, pp. 2016–2020, 2015.

[98] B. Wu, L. Tong, Y. Chen, and L. He, "Improved SNR Optimum Method in POLDINSAR Coherence Optimization," *IEEE Geoscience and Remote Sensing Letters*, vol. 13, no. 7, pp. 982–986, 2016.

[99] T. Shimada, R. Natsuaki, and A. Hirose, "Pixel-by-pixel scattering mechanism vector optimization in high-resolution PolInSAR," *IEEE Transactions on Geoscience and Remote Sensing*, vol. 56, pp. 2587–2596, May 2018.

[100] M. Craig Dobson, F. T. Ulaby, and L. E. Pierce, "Land-cover classification and estimation of terrain attributes using synthetic aperture radar," *Remote Sensing of Environment*, vol. 51, pp. 199–214, January 1995.

[101] M. Dobson, L. Pierce, and F. Ulaby, "Knowledge-based land-cover classification using ERS-1/JERS-1 SAR composites," *IEEE Transactions on Geoscience and Remote Sensing*, vol. 34, no. 1, pp. 83–99, 1996.

[102] M. Engdahl and J. Hyyppa, "Land-cover classification using multitemporal ERS-1/2 InSAR data," *IEEE Transactions on Geoscience and Remote Sensing*, vol. 41, pp. 1620–1628, July 2003.

[103] M. Santoro, J. I. H. Askne, U. Wegmuller, and C. L. Werner, "Observations, Modeling, and Applications of ERS-ENVISAT Coherence Over Land Surfaces," *IEEE Transactions on Geoscience and Remote Sensing*, vol. 45, pp. 2600–2611, August 2007.

[104] T. Strozzi, P. Dammert, U. Wegmuller, J.-M. Martinez, J. Askne, A. Beaudoin, and N. Hallikainen, "Landuse mapping with ERS SAR interferometry," *IEEE Transactions on Geoscience and Remote Sensing*, vol. 38, pp. 766–775, March 2000.

[105] N. Yague-Martinez, F. De Zan, and P. Prats-Iraola, "Coregistration of Interferometric Stacks of Sentinel-1 TOPS Data," *IEEE Geoscience and Remote Sensing Letters*, vol. 14, pp. 1002–1006, July 2017.

[106] G. Schreier, *SAR geocoding: Data and Systems*. Wichmann, 2001.

[107] D. Carrasco-Díaz, *SAR interferometry for digital elevation model generation and differential applications*. PhD Thesis, Polytechnic University of Catalonia, Spain, 1998.

[108] K. Millard and M. Richardson, "On the importance of training data sample selection in random forest image classification: A case study in peatland ecosystem mapping," *Remote Sensing*, vol. 7, no. 7, pp. 8489–8515, 2015.

[109] R. G. Congalton, "A review of assessing the accuracy of classifications of remotely sensed data," *Remote Sensing of Environment*, vol. 37, no. 1, pp. 35 – 46, 1991.

[110] S. V. Stehman, "Selecting and interpreting measures of thematic classification accuracy," *Remote Sensing of Environment*, vol. 62, pp. 77–89, October 1997.

[111] M. L McHugh, "Interrater reliability: The kappa statistic," *Biochemia medica*, vol. 22, pp. 276–82, October 2012.